



UNIVERSITA' DEGLI STUDI DI VERONA
DIPARTIMENTO DI
NEUROSCIENZE, BIOMEDICINA E MOVIMENTO
SCUOLA DI DOTTORATO IN SCIENZE DELLA VITA E DELLA SALUTE
DOTTORATO DI RICERCA IN
BIOMEDICINA MOLECOLARE, *curriculum* BIOCHIMICA
XXVIII ciclo

**Molecular analysis of the dimerization and
aggregation processes of human
alanine:glyoxylate aminotransferase and
effect of mutations leading to Primary
Hyperoxaluria Type I**

S.S.D. BIO10


Coordinatore: Prof.ssa Lucia De Franceschi

Tutor: Prof.ssa Barbara Cellini

Dottorando: Dott. Mirco Dindo

Quest'opera è stata rilasciata con licenza Creative Commons Attribuzione – non commerciale
Non opere derivate 3.0 Italia. Per leggere una copia della licenza visita il sito web:

<http://creativecommons.org/licenses/by-nc-nd/3.0/it/>

 **Attribuzione** -Devi riconoscere una menzione di paternità adeguata, fornire un link alla licenza e indicare se sono state effettuate delle modifiche. Puoi fare ciò in qualsiasi maniera ragionevole possibile, ma non con modalità tali da suggerire che il licenziante avalli te o il tuo utilizzo del materiale.



NonCommerciale -Non puoi usare il materiale per scopi commerciali.

Non opere derivate -Se remixi, trasformi il materiale o ti basi su di esso, non puoi distribuire il materiale così modificato.

“Molecular analysis of the dimerization and the aggregation processes of human alanine:glyoxylate aminotransferase and effect of mutations leading to Primary Hyperoxaluria Type I- Dott. Mirco Dindo

Tesi di Dottorato
Verona, 20 Febbraio 2017
ISBN 12324-5678-910

INDEX

ABSTRACT	p. 8
1. INTRODUCTION	p. 10
1.1 Pathogenesis of Primary Hyperoxaluria Type I	p. 11
1.2 AGT structure and function	p. 13
1.3 AGT subcellular localization	p. 16
1.4 The major and minor allelic form of AGT	p. 17
1.5 Molecular effects of pathogenic mutations in AGT	p. 19
1.6 Treatment strategies	p. 23
1.7 The chaperone role of PLP on folding-defective variants	p. 24
2. AIM OF THE RESEARCH	p. 27
3. MATERIALS AND METHODS	p. 30
3.1 Materials	p. 31
3.2 Bioinformatic studies	p. 31
3.2.1 Alanine scanning mutagenesis, molecular modeling and hydrophobic patch analysis	p. 31
3.2.2 Molecular and essential dynamics	p. 32
3.2.3 Rigid-body docking simulations	p. 34
3.2.4 Calculation of electrostatic potential maps, 2D maps and predicted pK_a	p. 35
3.3 Site-directed Mutagenesis	p. 36
3.4 Expression and purification of the AGT variants	p. 37
3.5 Preparation of apoenzyme	p. 38
3.6 Determination of the equilibrium dissociation constants for PLP ($K_{D(PLP)}$)	p. 38
3.7 Determination of the kinetic parameters	p. 39
3.8 Size exclusion chromatography	p. 40
3.9 Kinetics of the dimerization process of AGT R118A-F238S-F240S-Mi	p. 41
3.10 Spectroscopic measurements	p. 41
3.11 Dynamic light scattering (DLS)	p. 42

3.12 Aggregation kinetics: the minimalistic /“Ockham’s razor” Finke-Watzky (F-W) two-step model	p. 42
3.13 Calculation of pK_{spec}	p. 43
3.14 Limited proteolysis	p. 44
3.15 Cell culture and lysis	p. 44
3.16 Western blot analysis	p. 45
3.17 Immunofluorescence microscopy (IFM)	p. 45
3.18 Statistical analysis	p. 46
4. ENGINEERING OF A SOLUBLE MONOMERIC FORM OF AGT AND STUDY OF THE DIMERIZATION PROCESS	p. 47
Background information	p. 48
RESULTS AND DISCUSSION	p. 50
4.1 Identification of the AGT interface hotspots	p. 50
4.2 Role of the residues Arg118, Phe238 and Phe240 on AGT dimerization	p. 53
4.3 Spectroscopic features of the engineered monomeric AGT	p. 57
4.4 Kinetics of the dimerization process and role of PLP	p. 61
4.5 <i>In silico</i> analyses to explain the pathogenicity of the F152I-Mi and I244T-Mi variants	p. 63
4.6 Proposed folding and dimerization pathway of AGT-Mi and I244T-Mi and F152I-Mi variants	p. 65
CONCLUSIONS	p. 68
5. MOLECULAR AND CELLULAR EFFECTS OF PATHOGENIC INTERFACIAL MUTATIONS IN ALANINE:GLYOXYLATE AMINOTRANSFERASE AND RESPONSE TO VITAMIN B6 ADMINISTRATION	p. 69
Background information	p. 70

RESULTS	p. 71
5.1 Computational screening of the effects of pathogenic amino acid substitutions on AGT-Ma dimerization	p. 71
5.2 Intracellular behavior of the R36H, G42E, I56N, G63R and G216R variants	p. 74
5.3 Characterization of the R36H, G42E, I56N, G63R and G216R variants in the purified form	p. 78
5.4 Functional properties of the R36H, G42E, I56N, G63R and G216R variants	p. 79
5.5 Structural properties of the R36H, G42E, I56N, G63R and G216R variants in the purified form	p. 81
DISCUSSION	p. 88
6. AGGREGATION PROPENSITY OF HUMAN AGT: THE OPPOSITE EFFECT OF THE POLYMORPHIC	p. 93
Background information	p. 94
RESULTS AND DISCUSSION	p. 96
6.1 In silico analysis of the AGT surface: molecular map of the electrostatic potential	p. 96
6.2 Effect of pH and ionic strength on the aggregation propensity of AGT-Ma	p. 98
6.3 Effects of P11L and I340M polymorphic mutations on the aggregation process of AGT	p.106
6.4 Predicted effect of pathogenic mutations on the electrostatic potential of the AGT surface	p. 112
CONCLUSIONS	p. 120
7. CONCLUSIONS	p. 121
8. ADDENDUM	p. 124

9. BIBLIOGRAPHY p. 131

10. PUBLICATIONS p. 140

ABBREVIATIONS

AGT, alanine:glyoxylate aminotransferase;
AGT-Mi, minor allele of AGT;
AGT-Ma, major allele of AGT;
ANS, 1-anilino-8-naphthalene sulfonate;
APBS, Adaptive Poisson-Boltzmann Solver;
CD, circular dichroism;
CHO, chinese hamster ovary;
DLS, dynamic light scattering;
ED, essential dynamics;
FBS, fetal bovine serum;
IFM, immunofluorescence microscopy;
IPTG, isopropyl- β -D-thiogalactoside;
 $K_{D(PLP)}$, equilibrium dissociation constant for PLP;
 $K_{d(dim-mon)}$, dimer-monomer equilibrium dissociation constant;
KP, potassium phosphate buffer;
LB, Luria Bertani;
LDH, L-lactic dehydrogenase;
LOW B6, Ham's F12 medium without pyridoxine;
MD, molecular dynamics;
MOE, Molecular operating environment;
MTS, mitochondria targeting sequence;
PH1, primary hyperoxaluria type 1;
PLP, pyridoxal 5'-phosphate;
PMP, pyridoxamine 5'-phosphate;
PN, pyridoxine;
PNP, pyridoxine 5'-phosphate;
PTS1, peroxisomal targeting sequence;
SEC, size exclusion chromatography;
Uox, urinary oxalate;

ABSTRACT

Primary Hyperoxaluria Type 1 (PH1) is a rare autosomal recessive disorder characterized by the deposition of insoluble calcium oxalate crystals at first in the kidneys and urinary tract and then in the whole body. PH1 is caused by the deficiency of human liver peroxisomal alanine:glyoxylate aminotransferase (AGT). AGT is a pyridoxal 5'-phosphate (PLP)-dependent enzyme, which converts glyoxylate to glycine, thus preventing glyoxylate oxidation to oxalate and calcium oxalate formation. Only two curative therapeutic approaches are currently available for PH1: the administration of pyridoxine (PN), a precursor of PLP, which is only effective in a minority of patients (25- 35%), and liver transplantation, a very invasive procedure. AGT is encoded by the *AGXT* gene, which is present in humans as two polymorphic forms: the major allele (encoding AGT-Ma) and the minor allele (encoding AGT-Mi). PH1 is a very heterogeneous disease with respect to the clinical manifestations, the response to treatment and the pathogenic mechanisms. In fact, more than 200 pathogenic mutations have been identified so far and the molecular mechanisms by which missense mutations cause AGT deficiency span from functional, to structural and to subcellular localization defects or to a combination of them. Several lines of evidence at both molecular and cellular level, indicate that many disease-causing missense mutations interfere with AGT dimer stability and/or aggregation propensity. However, neither the dimerization nor the aggregation process of AGT have been analyzed in detail. Therefore, we engineered a mutant form of AGT stable in solution in the monomeric form and studied its biochemical properties and dimerization kinetics. We found that monomeric AGT is able to bind PLP and that the coenzyme stabilizes the dimeric structure. Moreover, the identification of key dimerization hot-spots at the monomer-monomer interface allowed us to unravel the mechanisms at the basis of the aberrant mitochondrial mistargeting of two of the most common PH1-causing variants. We also elucidated the molecular and cellular consequences of the pathogenic mutations R36H, G42E, I56N, G63R and G216R, involving residues located at the dimer

interface, and tested their *in-vitro* responsiveness to the treatment with PN. The latter results allowed us to suggest a possible correlation between the structural defect of a variant and its degree of responsiveness to PN. Finally, by combining bioinformatic and biochemical approaches, we analyzed in detail the tendency of AGT to undergo an electrostatically-driven aggregation. We found that the polymorphic changes typical of the minor allele have opposite effect on the aggregation propensity of the protein, and we predicted the possible effect/s of pathogenic mutations of residues located on the AGT surface.

Overall, the results obtained allow not only to better understand PH1 pathogenesis, but also to predict the response of the patients to the available therapies as well as to pave the way for the development of new therapeutic strategies.

1

INTRODUCTION

1.1 Pathogenesis of Primary Hyperoxaluria Type I

Primary Hyperoxaluria Type I (PH1) is a human metabolic disease with an autosomal recessive pattern of inheritance. The principal hallmark of PH1 is the formation of calcium oxalate stones that deposit at first in the kidneys and then in the whole body (1). The disease has an estimated prevalence of 1 to 3 per million populations and an overall incidence of approximately 1:120,000 live births in Europe and North America (2, 3). However, the incidence is usually higher in geographically isolated countries such as Canary Islands and in populations where consanguineous marriages are common. The disease accounts for less than 1% of paediatric patients showing end-stage renal disease (ESRD) in Europe, but this percentage increases to more than 10% in Kuwait and Tunisia (4). PH1 is the most common and severe form of primary hyperoxaluria, a group of genetic disorders characterized by the abnormal production and urinary excretion of endogenous oxalate (5, 6). PH1 accounts for approximately 80% of the cases of PH and is caused by the deficit of the hepatic peroxisomal enzyme, alanine:glyoxylate aminotransferase (AGT) (5). AGT is a pyridoxal 5'- phosphate (PLP)-dependent enzyme that catalyzes an essentially irreversible transamination reaction in which the amino group of L-alanine is transferred to glyoxylate, leading to the formation of pyruvate and glycine. In the absence of functional AGT, glyoxylate accumulates into peroxisomes and is transported to the cytosol where it is oxidized to oxalate by lactate dehydrogenase (Fig. 1).

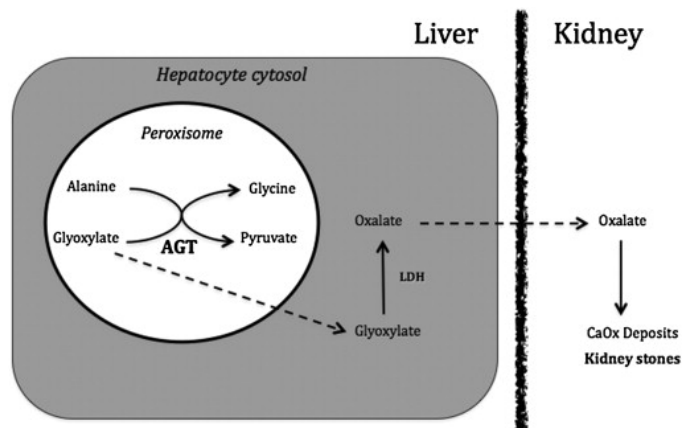


Fig. 1. Metabolic consequences of AGT deficiency. Sites and mechanisms of oxalate formation are shown.

Oxalate is an end-product of human metabolism that should be excreted by urine. In PH1 patients, very high amounts of oxalate are formed and accumulate in the urinary tract. This generates calcium oxalate (CaOx), a poorly soluble salt forming crystals when the concentration reaches the saturation limit (7). In the early and intermediate stages of PH1, CaOx crystals are deposited mainly in the urinary tract as stones (urolithiasis) or more diffused in the renal parenchyma (nephrocalcinosis). The progressive accumulation of CaOx in the kidneys eventually leads to renal failure, after which the problem of increased oxalate synthesis by the liver is compounded by the failure to remove it from the body. The resulting increased burden of oxalate allows CaOx to deposit into many organs and tissues, a potentially fatal condition named systemic oxalosis (Table 1).

Table 1. Symptoms of systemic oxalosis in PH1.

TISSUE	CLINICAL SYMPTOM
Kidney and urinary tract	Urolithiasis, nephrocalcinosis, renal failure
Bone	Bone pain, multiple fractures and osteosclerosis
Eye	Retinopathy and optic atrophy
Heart	Heart block, myocarditis and cardioembolic stroke
Nerves	Peripheral neuropathy
Deep vasculature	Vasospasm

1.2 AGT structure and function

AGT is present in human hepatocytes as an homodimeric protein, in which each subunit is composed by 392 amino acids. The crystal structure of AGT (8) reveals that it belongs to the Fold Type I class of PLP-dependent enzymes (Fig. 2, panel A). Each subunit comprises: a N-terminal extension (residues 1-21) wrapping over the surface of the neighboring subunit, a large domain (residues 22-282) containing the dimerization interface and most of the active site and a C-terminal domain (residues 283-392) containing the peroxisomal targeting information. As in all PLP-dependent enzymes, the coenzyme is covalently bound to the ϵ -amino group of a lysine residue (Lys209 in AGT) by means of a Schiff base linkage, forming a complex called internal aldimine. Other weak interactions at the active site stabilize the AGT-PLP complex including: (i) a salt bridge between the pyridine nitrogen of PLP and Asp183, (ii) a base stacking interaction between Trp108 and the pyridine ring of PLP and (iii) hydrogen bonds between the hydroxyl group of PLP and Ser158 as well as between the phosphate group of PLP and the residues Gly82, His83, Tyr260 and Thr263 (Fig. 2, panel B) (8). The active site is located in a cleft at the monomer-monomer interface and involves residues belonging to both subunits, thus suggesting that the catalytic activity is strictly related to the acquisition of the dimeric structure. The importance of the quaternary structure is also indicated by the fact that 8550 \AA^2 of each monomer surface are buried upon dimerization (9). By looking to the surface of the protein it can be noticed an asymmetric distribution of charged residues, a peculiar feature that can promote self-association processes mediated by electrostatic forces.

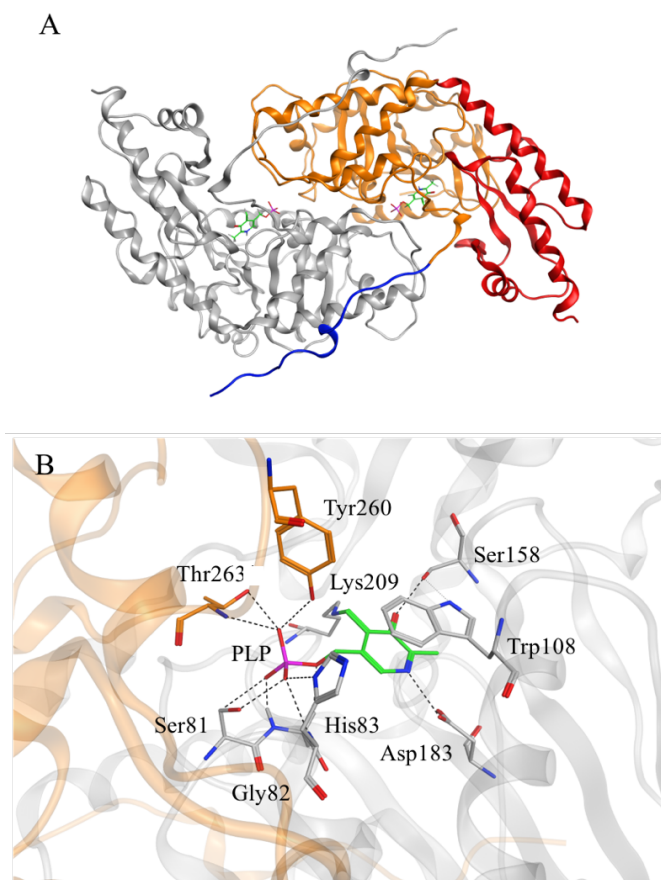
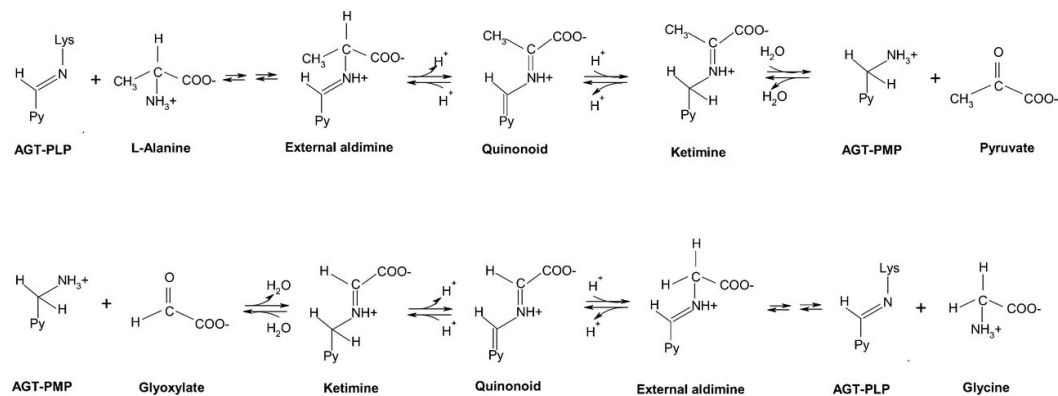


Fig. 2. Representation of AGT structure. Panel A: dimeric AGT. One subunit is colored grey; on the other subunit are indicated the N-terminal extension (blue), the large domain (orange) and the C-terminal domain (red). Panel B: detail of the active site. PLP is shown as green sticks. Residues interacting with the coenzyme are shown as grey sticks (if belong to the same subunit of the coenzyme) or orange sticks (if belong to the neighboring subunit). Oxygen, nitrogen and phosphorous atoms are colored red, blue and fuchsia, respectively.

AGT catalyzes the reversible transamination of L-alanine and glyoxylate to pyruvate and glycine by a classical ping-pong mechanism (Scheme 1). In the first half-reaction, after the binding of the substrate to the catalytic site of the enzyme in the internal aldimine form (AGT-PLP) and the formation of the Michaelis complex, the ϵ -amino group of Lys209 is replaced by the α -amino group of L-alanine, thus generating the external aldimine. The extraction of the C α -proton from the external aldimine yields a quinonoid intermediate, which is reprotonated at the C $_4$ ' of the coenzyme to give the ketimine intermediate. The latter is then hydrolyzed to pyridoxamine 5'-phosphate (PMP) and pyruvate. In the second half transamination, following the same steps of the first half-reaction but in reverse

order, glyoxylate reacts with the AGT-PMP complex and is converted to glycine, thus regenerating AGT-PLP (10).



Scheme 1. Mechanism of the transaminase reaction catalyzed by AGT.

Kinetic studies have indicated that AGT is highly specific for the glyoxylate-to-glycine conversion, in agreement with the proposed physiological role of the enzyme in glyoxylate detoxification. In fact, the equilibrium constant of the overall transamination is about 9400 and the k_{cat} for the transamination reaction of the alanine/glyoxylate pair is ≈ 150 -fold higher with respect to that of the glycine/pyruvate pair (10). Moreover, it has been shown that the enzyme has a higher affinity for PMP than for PLP, and that PMP remains tightly bound to the apoprotein during the catalytic cycle, thus making the enzyme more reactive toward oxoacids (10). The spectral changes occurring in AGT during the two half-transamination reactions have indicated that some conformational changes at the active site occurs. Through computational studies, it has been suggested that slight rearrangements of aromatic residues at the active site and a tilting of the coenzyme could take place and these structural re-orientations could be responsible for the tight PMP binding during catalysis (10).

1.3 AGT subcellular localization

During evolution the targeting of AGT has been under the influence of strong dietary selection and for this reason the localization of the protein inside the cell can vary from one species to another (11). AGT tends to be mitochondrial in carnivores, peroxisomal in herbivores and both peroxisomal and mitochondrial in omnivores. For example, in humans, rabbit and guinea pig, AGT is exclusively peroxisomal whereas in many species it could be exclusively mitochondrial (domestic cat) or both peroxisomal and mitochondrial (rat and marmoset) (12). As it occurs for the large majority of peroxisomal proteins, AGT is synthesized in the cytosol of human hepatocytes and then transported inside peroxisomes by the Pex5p carrier protein (13). The interaction between AGT and the carrier occurs through a non-canonical peroxisomal targeting sequence (PTS1), i.e. a C-terminal KKL sequence instead of the SKL sequence normally found in most peroxisomal proteins (14). The crystal structure of AGT in complex with the PTS1-binding domain of the peroxisomal carrier Pex5p (15) has shown that the stoichiometry of the complex is Pex5p-AGT-AGT-Pex5p and that the protein-receptor interface is composed by three regions: (i) the C-terminal PTS1 (residues 389-392) (ii) an extended PTS1, that includes the C-terminal part of the α -helix 13 (residues 381-388) and the loop connecting the β -strand 9 and the α -helix 12 (residues 327-330), and (iii) a region topologically separated from PTS1 formed by residues 303-307. Moreover, Mesa-Torres *et al* (16) calculated the thermodynamic binding parameters for the interaction of Pex5p-pdb with AGT by means of bioinformatics and biophysical studies. They found that the interaction is quite weak ($K_D = 1.4 \pm 0.2 \mu\text{M}$) and that the mutation of residues Ala328, Tyr330 and Lys390 can further reduce the binding affinity of AGT for Pex5p (16).

1.4 The major and minor allelic form of AGT

AGT is coded by the *AGXT* gene, located on chromosome 2q37.3, which is present in human population as two polymorphic variants, named the “major allele” and the less common “minor allele”. The frequency of the minor allele varies among different populations, ranging from 2% in the Japanese population, to the 20% of Europeans and North Americans to 28% in the Saami population (17, 18). The minor allele differs from the major one for 74-bp duplication in intron 1 and two point mutations (32C→T and 1020A→G) leading to the Pro11Leu and Ile340Met amino acid substitutions (19). Although the presence of the minor allele polymorphism is not pathogenic *per se*, it makes AGT more susceptible to the effect of several missense mutations, which are predicted to be non-pathogenic when associated with the major allele. For this reason, many investigations have been carried out to understand the differences between the two allelic forms of AGT at cellular and molecular level. In human liver, the protein encoded by the minor allele (AGT-Mi) has a specific activity of about 70% as compared with that encoded by the major allele (AGT-Ma) (20, 21). Moreover, while AGT-Ma is entirely located in peroxisomes, AGT-Mi is about 95% peroxisomal and 5% mitochondrial (20). It has been demonstrated that the partial mitochondrial localization of AGT-Mi depends on the polymorphic mutation P11L, which generates a weak putative mitochondrial targeting sequence (MTS) at the N- terminus of the protein. Despite the presence of a putative MTS, a large part of AGT-Mi is not imported to mitochondria, probably because the protein quickly dimerizes, thus avoiding the interaction with the mitochondrial import machinery that only acts on unfolded or partly-unfolded monomeric species (22). Studies performed on purified recombinant AGT-Ma and AGT-Mi have indicated that the P11L/I340M mutations do not affect either the UV-visible absorbance, dichroic and fluorescence features of AGT or the equilibrium dissociation constant for PLP ($K_{D(PLP)}$) value. This suggests the absence of gross conformational changes between the two allelic forms that share a similar active site architecture (2, 23). Nevertheless, AGT-Mi shows an approximately 30% decreased k_{cat} value for the overall transamination of the L-alanine/glyoxylate pair, in agreement with the reduced specific activity observed in human

hepatocytes. Furthermore, yeast complementation assays (24) along with pulse-chase and cross-linking experiments performed on cell-free transcription/translation products (25) have shown that AGT-Mi is less stable *in vivo* and is more susceptible to proteolytic degradation and aggregation in comparison with AGT-Ma (26). These data have been also confirmed by thermal and chemical unfolding studies, which have provided evidence for a less stable dimeric structure and a decreased overall stability of both holo- and apoAGT-Mi as compared with the corresponding forms of AGT-Ma. The structural destabilization of AGT-Mi has been exclusively attributed to the P11L mutation (26). In fact, it has been suggested that the substitution of Pro11 with a leucine residue could alter the original position and the interaction of the N-terminal arm of one subunit of AGT with the large domain of the opposite subunit, generating a less stable dimeric form of AGT (Fig. 3). Moreover, the perturbation of the N-terminal arm could also be transmitted to the AGT active site through a loop (residues 24-32), which contributes to the PLP binding site. Overall, the analyses on the differences between AGT-Ma and AGT-Mi, have allowed not only to better understand the structural features of AGT, but have also represented an important starting point to investigate the effect of pathogenic mutations associated with the major or the minor allele.

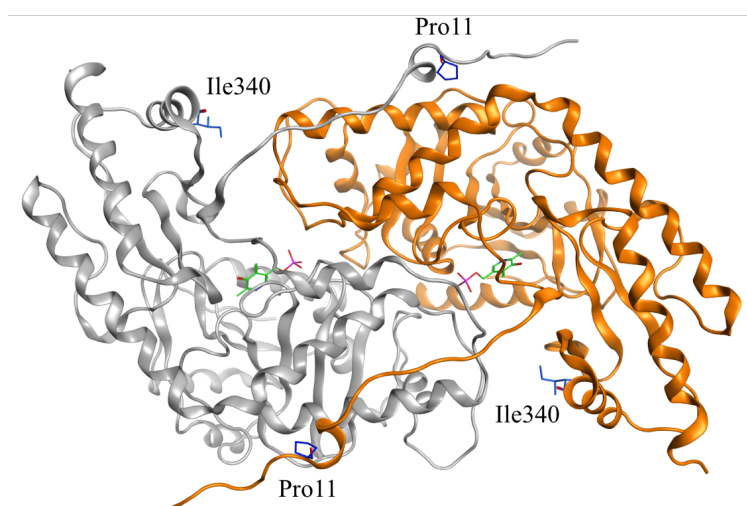


Fig. 3. Molecular representation of Pro11 and Ile340 residues in the AGT structure. The two monomers of AGT are colored white and orange. The residues Pro11 and Ile340 are represented as blue sticks.

1.5 Molecular effects of pathogenic mutations in AGT

PH1 is a loss-of-function disorder, because the symptoms are only related to the absence of functional AGT inside peroxisomes. From a genetic point of view, it can be considered a very heterogeneous disease, counting over 200 different pathogenic mutations (Fig. 4) on the *AGXT* gene, including nonsense, frameshift and missense mutations (27). While nonsense and frameshift are null mutations that lead to the synthesis of a truncated and hence non-active protein, missense mutations lead to single amino acid substitutions causing the synthesis of an aberrant gene product. Missense mutations are the most frequent ones and can co-segregate with the major allele, the minor allele or both alleles (27, 28). When a mutation is co-inherited with the minor allele polymorphism, the polymorphic changes can exacerbate the effect of the disease-causing mutation. In some cases, the synergism with polymorphic amino acid substitutions is so crucial that pathogenic mutation do not lead to PH1 if inherited on the background of the major allele (29).

In the last years, a lot of attention has been focused on the elucidation of the molecular and cellular effects of missense pathogenic mutations on AGT.

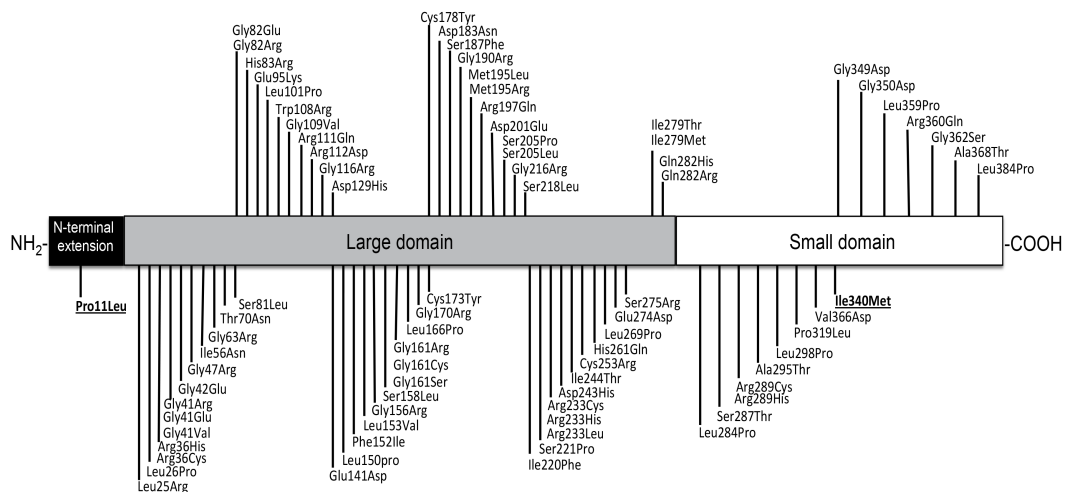


Fig. 4. AGT mutations map. The known pathogenic amino acid changes associated with PH1 are ordered on the basis of the position of the mutated residue. The underlined amino acid substitutions represent the polymorphic changes typical of the Caucasian minor allele.

These analyses have been directed to confirm the pathogenicity of each mutation, to assess its severity and to understand how it exerts a damaging effect, with the final aim of establishing genotype–phenotype correlations. Different types of *in vitro* expression systems and various forms of downstream analyses of the expressed protein have been used to shed light on the defect underlying the pathogenicity of AGT variants associated with PH1. Each approach has been used to explore a different facet of a mutation effect. Expression in mammalian cells is considered as the closest model of *in vivo* conditions and gives information on the expression level, intracellular stability and targeting of the protein. On the other hand, the purification and characterization of the variants expressed in *E. coli* is suitable to dissect and quantify the effect of a mutation on the functional properties of AGT as well as on its secondary, tertiary and quaternary structure (26, 30, 31). In addition, bioinformatic analyses allow to predict the effect of a mutation at structural level and to explain the results obtained on purified proteins.

In PH1, the combination of the approaches has shown the extreme variability of enzymatic phenotypes leading to AGT deficiency (Fig. 5) (26, 32), due to the effects of mutations on either the functional and/or the structural properties of AGT. 20% of the missense variants do not display any alteration of the expression level, but show a reduced catalytic efficiency for the transamination reaction due to a reduced k_{cat} and/or to an increased K_m for the substrate, or to an altered PLP/PMP binding mode and/or affinity (Fig. 5) (10, 33). They typically involve mutations of residues that either directly interact with PLP or are located in the proximity of the active site, such as Ser81, Gly82, His83, Trp108, Phe152, Ser158, Asp183 and Ser218. However, a remote conformational change of the active site can be also occur upon mutation of residues located far from the active site such as Ser187, Ile244 and Gly350 (32, 34). On the other hand, the reduction of the AGT expression level is a common defect shared by several variants. It has been demonstrated that in many cases PH1 can be considered a misfolding disease, because the effect of most amino acid substitutions is a conformational change that alters the folding pathway of the protein leading to various downstream effects such as:

- *a reduced stability of the dimeric unit*, as demonstrated for the G41R, G170R and F152I mutations on the minor allele, and for the G41R and G41V on the major allele (23, 31) by studies on the variants in the purified form (23, 35).

- *a higher susceptibility to proteolytic degradation*, as in the case of the G41R and I244T mutations associated with the minor allele as well as of the G41R and G41V mutations associated with the major allele. Analyses on both the pathogenic variants in the purified form and in cell-free transcription-translation systems have shown that the mutation of Gly41 increases the sensibility to degradation of AGT, while the I244T mutation strongly sensitizes AGT to trypsin treatment (31).

- *an increased aggregation propensity*, as observed for the Gly41 and Gly161 variants in the purified form by dynamic light scattering (DLS) and for the F152I-Mi variant by size-exclusion chromatography (SEC) (31, 35). While the aggregation of the F152I-Mi variant depends on protein monomerization, the aggregation of the Gly161 and Gly41 variants is driven by electrostatic interactions between dimers (31, 36).

- *the mitochondrial mistargeting*, a pathogenic mechanism peculiar of PH1 in which the protein is aberrantly targeted to mitochondria, where it is not able to perform the detoxification of peroxisomal glyoxylate. The mistargeting is due to mutations inherited on the background of the minor allele, including the most common G170R, I244T, F152I, and the G41R (32, 37, 38), and is considered the clearest example of the synergic effect of polymorphic and pathogenic mutations. In these variants the pathogenic mutation strengthens the weak MTS generated by the P11L polymorphism by populating monomeric partly-folded or unfolded intermediates able to either directly interact with the mitochondrial import receptor or strongly bind molecular chaperones and be presented to the mitochondrial import machinery (32, 37).



Fig. 5. Schematic representation of the molecular (A) and cellular (B) effects of pathogenic amino acid substitutions in AGT.

Overall, the determination of the effects of many PH1-causing mutations at molecular level has been of primary importance not only to clarify the relationship between the genotype, the enzymatic phenotype and the clinical symptoms, but also to understand the basis of the therapeutic response of the patients to the available treatments as well as to pave the way for an improved clinical management by the designing of new therapeutic approaches. Notably, it is becoming increasingly evident that many mutations affect mainly or exclusively the apo-form of AGT (as found for the G170R, F152I, G161R, G161C, G161S, I244T and A295T variants) (32, 33, 35, 36, 39, 40), thus highlighting the fact that the pathogenic mechanisms leading to AGT deficiency range probably wider than previously thought and that the study of each variant in both the holo- and apo-

forms is a necessary step for the identification of the molecular defect.

1.6 Treatment strategies

PH1 is a very difficult-to-treat disease that can remain unrecognized for years, due to a similar initial clinical presentation with idiopathic kidney stone disease (29). The time of diagnosis, which is usually confirmed by genetic testing, represents a key factor influencing treatment efficacy. In fact, an early diagnosis allows a proper treatment to be initiated as soon as possible, thus reducing the morbidity and increasing life expectancy of the patients (7). The therapeutic options currently available for PH1 patients are quite poor. Classical treatments are aimed at preventing or delaying kidney failure, or at restoring kidney function (29). They include (i) a high fluid intake to allow the hyperhydration of the patients thus preventing CaOx crystallization, (ii) the administration of crystallization inhibitors (such as magnesium and potassium citrate), (iii) the physical destruction of CaOx stones by lithotripsy, and (iv) dialysis and/or kidney transplantation procedures, to treat renal failure and the associated uremia (41).

Unfortunately, none of these approaches represents a real cure, since they focus on symptoms mitigation. Only two therapeutic approaches directed to the causes of the disease are available so far: the administration of pharmacological doses of Vitamin B6, and liver transplantation. Vitamin B6 is currently administered in form of pyridoxine (PN), which can be converted in the body to PLP (42), the essential cofactor of AGT. Clinical data indicate that only a minority of the patients is responsive to pyridoxine therapy (37, 43-46). The only curative approach available for patients unresponsive to pyridoxine is liver transplantation, a procedure aiming at replacing the entire enzymatic pool of AGT in the liver (41). Liver transplantation is usually performed in combination or in sequence with kidney transplantation, to prevent any oxalate accumulation while ensuring to the patients the ability to remove it from the body. However, this strategy is a very invasive intervention and accompanied by several side effects (such as organ rejection and the long-life administration of immunosuppressant drugs). For these reasons, many efforts have been devoted in the last years to develop new

strategies more effective and less invasive than the available treatments, able to provide long-term benefits to PH1 patients. Approaches currently under investigation include strategies to (i) improve the AGT folding efficiency, using pharmacological chaperones as B6-vitamins (see below) or substrate analogs as aminooxyacetic acid (AOA) (47), (ii) administer a functional enzyme to rescue the glyoxylate detoxification ability of the liver (48), (iii) reduce the amount of exogenous oxalate absorbed at intestinal level (e.g using oxalate degrading-enzymes) (49, 50), (iv) restore AGT expression by gene therapy or cell therapy (51) (v) reduce oxalate production by substrate reduction therapies toward glycolate oxidase or proline dehydrogenase.

1.7 The chaperone role of PLP on folding-defective AGT variants

The administration of Vitamin B6 is the first-line approach for any PH1 patient upon diagnosis (1). Vitamin B6 includes a group of six water soluble vitamins: pyridoxine (PN), pyridoxamine (PM), pyridoxal (PL) and their phosphorylated forms (PNP, PMP and PLP) (Fig. 6).

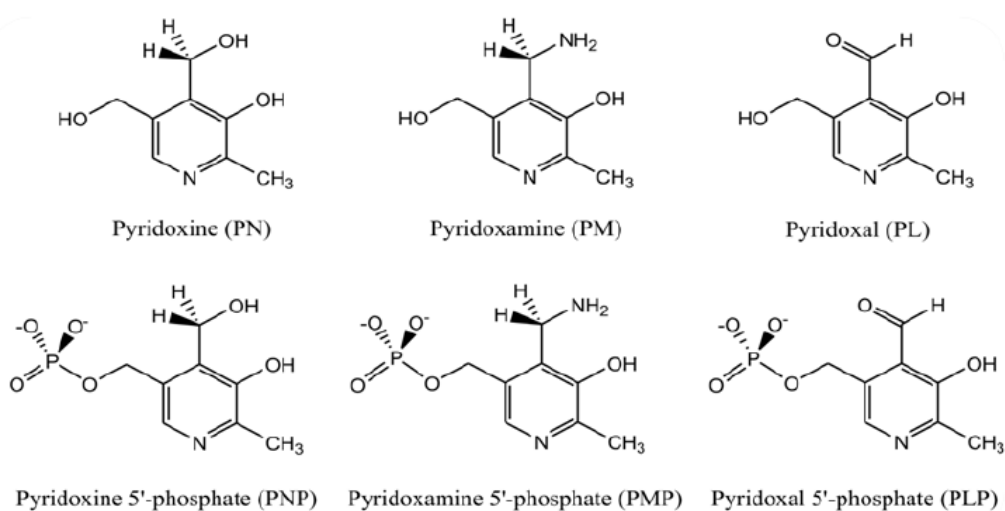


Fig. 6. Structures of B6 vitamers. The structures of PN, PM, PL and their relative phosphorylated forms (PNP, PMP and PLP) are shown.

Vitamin B6 is usually utilized in therapy as PN, which is converted to PLP inside

the cell and has proven to be effective for several disorders due to the deficit of PLP-enzymes, although the percentage of responsive patients is variable. In PH1, only 25-35% of the patients are responsive, as demonstrated by a significant reduction of the urinary oxalate levels upon a 3-months treatment with PN (10 mg/kg/day) (52, 53). Responsiveness seems to be associated with three of the most common missense variants, the G170R-Mi, F152I-Mi and I244T-Mi, which are aberrantly targeted to mitochondria and/or show an increased susceptibility to proteolytic degradation and aggregation (32, 37). In order to shed light on the molecular mechanism underlying PN efficacy, the effects of vitamin B6 have been widely investigated at both molecular and cellular level. It has been proposed that, besides its prosthetic role, PLP might improve the efficiency of the folding pathway of AGT by shifting the equilibrium from the unstable apo-form to the more stable holo-form of misfolded variants. As shown in Fig. 7, PLP can either bind a partly-folded or fully-folded monomeric form of AGT. This would generate a PLP-bound monomer that then dimerizes (pathway A). As an alternative, the folded apomonomer can dimerize and subsequently bind PLP (pathway B). Analyses of the role of the coenzyme on AGT folding and dimerization are still lacking.

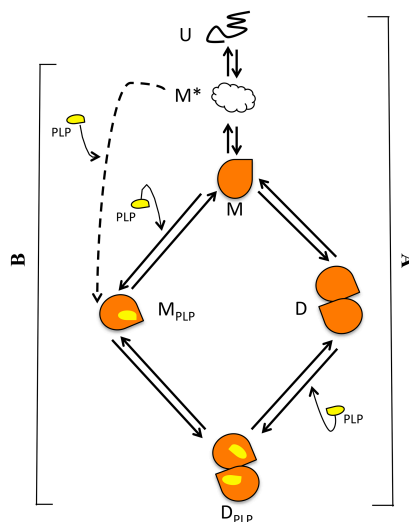


Fig. 7. Folding pathway of AGT and chaperone role of PLP. PLP could bind different folding intermediates shifting the equilibrium toward the more stable holo-form of the protein. U = unfolded monomer; M* = partially folded monomer; M = folded apomonomer; M_{PLP} = monomer-bound PLP; D = apodimer; D_{PLP} = PLP-bound dimer.

Nevertheless, recent studies have provided evidence that the coenzyme can exert a chaperone role (54). In fact, the presence of PN in the culture media of CHO-GO cells expressing F152I-Mi, G170R-Mi or I244T-Mi variants (23, 36, 37) not only improves their specific activity, but also increases the total expression level and promotes their correct subcellular localization, thus enhancing the capability to detoxify glyoxylate. These data suggest that PLP increases the productive folding of the proteins (Fig. 7) and prevents their aggregation and degradation, leading to higher amounts of active dimers imported inside peroxisomes (54).

Furthermore, recent studies performed in my research group (55), have shown that PM and PL are more effective than PN in rescuing the two PN-responsive variants F152I-Mi and G170R-Mi when expressed in a cellular model of PH1. Indeed, the administration of PN leads to the intracellular accumulation of PNP, which is able to compete with PLP for the binding to apoAGT generating an inactive AGT-PNP complex (55). On the other hand, PM or PL supplementation causes the intracellular accumulation of PLP and PMP, the two active forms of the coenzyme exerting both a chaperone and a prosthetic role, without any accumulation of PNP. Although experiments in a mouse model of PH1 have to be performed, these results support the potential use of PM and PL as a novel coenzyme administration therapy for patients bearing PH1-causing mutations that affect protein folding.

2

AIM OF THE RESEARCH

Primary Hyperoxaluria Type I (PH1) is a rare disease caused by mutations in the gene encoding alanine:glyoxylate aminotransferase (AGT), an enzyme that utilizes pyridoxal 5'-phosphate (PLP) as coenzyme to catalyze the transamination of L-alanine and glyoxylate to pyruvate and glycine. AGT deficiency allows glyoxylate accumulation and oxidation to the metabolic end-product oxalate. The high amounts of oxalate formed in PH1 patients cause the formation and deposition of calcium oxalate crystals at first in the urinary tract and then in the whole body. The only two curative treatments currently available for PH1 are the administration of Vitamin B6 in form of pyridoxine, which is effective only in a minority of the patients, and liver transplantation, which is a very invasive and problematic procedure. PH1 is a very heterogeneous disease with respect to the clinical manifestations, the response to treatment and the pathogenic mechanisms. In fact, more than 200 pathogenic mutations have been identified so far and the molecular mechanisms by which missense mutations cause AGT deficiency span from functional, to structural and to subcellular localization defects or to a combination of them. Additionally, some pathogenic mutations functionally synergize with polymorphic mutations typical of a minor allelic form of the protein. Several lines of evidence at both molecular and cellular level, indicate that PH1 can be considered a misfolding disease. In fact, most disease-causing missense mutations interfere with AGT folding leading to a variety of downstream effects that finally result in a reduced expression level. In particular, it has been supposed that the majority of them reduce the stability of the dimeric structure of the protein. However, the biochemical features of monomeric AGT as well as the equilibrium and kinetics of the dimerization process are unknown. Moreover, although it is well known that AGT is endowed with a significant tendency to aggregation, neither the molecular mechanisms underlying the aggregation process nor the possible effect of the polymorphic changes typical of the minor allele have been clarified in detail.

Based on the above considerations, the main objectives of my PhD project have been:

-engineer a mutant form of AGT stable in solution in the monomeric form, study its biochemical properties and dimerization process, as well as define the effect of the coenzyme on the stability of the dimeric structure.

-elucidate the molecular and cellular consequences of pathogenic mutations involving residues located at the dimer interface such as the R36H, G42E, I56N, G63R and G216R, and test their responsiveness to the treatment with pyridoxine.

-investigate the molecular mechanism of the aggregation process of the two polymorphic forms of AGT by means of bioinformatic and biochemical studies as the base to predict the possible effect/s of pathogenic mutations of residues located on the AGT surface.

3

MATERIALS AND METHODS

3.1 Materials

PLP, pyridoxine, L-alanine, sodium glyoxylate, rabbit muscle L-lactic dehydrogenase, isopropyl- β -D-thiogalactoside (IPTG), EDTA and imidazole were all purchased from Sigma. ANS was purchased from Molecular Probes. The Ham's F12 Glutamax medium w/o pyridoxine and G-418 were purchased from Invitrogen. All other chemicals were of the highest purity available. The rabbit polyclonal anti-AGT human and guinea-pig anti-peroxisomal proteins antibodies were kindly provided by Prof. C.J. Danpure of University College London (UK); the anti-rabbit HRP antibody was purchased from GE Healthcare. Oligonucleotides for site directed mutagenesis were purchased from MWG Biotech AG (Anzinger, Germany).

3.2 Bioinformatic studies

3.2.1 Alanine scanning mutagenesis, molecular modeling and hydrophobic patch analysis

In silico analyses for the engineering of monomeric AGT-Mi as well as the alanine scanning mutagenesis were performed by using the software Molecular Operating Environment (*MOE 2015.1001* and *MOE 2016.08*) (56) of the Chemical Computing Group using the available crystal structure of human AGT (pdb id: 1H0C) (8). Each residue present on the dimerization interface involved in either intrachain or interchain contacts was subjected to alanine scanning mutagenesis using the Unary Quadratic Optimization (UQO) under the LowMode ensemble, which uses the LowModeMD (57) to search the conformational space of the mutants. The conformations that satisfied the required energetic and geometric criteria were saved to the output database. Atoms located at a distance greater than 4.5 Å from the mutation site were marked as inert, iterations were limited to 50, and conformations were limited to ten for each mutated complex. The dStability values (kcal/mol) were calculated using the “*Protein design*” tool of *MOE 2015.1001* (56). The analysis of the interfacial hydrophobic patches and

the inspection of the AGT structure and of the interface contacts were performed by using the “*Patch analyzer*” tool of *MOE 2015.1001* (56).

3.2.2 Molecular and essential dynamics

These analyses were performed in collaboration with Dr. Giorgetti of Department of Biotechnology of the University of Verona. Molecular dynamics (MD) simulations were carried out by using the software GROMACS 4.5.5 (68) GROMOS 53A6 united atom force field (69) and the explicit simple point charge (spc/e) water model (70) were used for the simulations. The dimeric structure of human AGT was obtained by means of the PISA web server starting from the available coordinate file of the monomer (PDB id: 1H0C). In the original structure, loop residues 120-123 are missing, so the latter were modelled by a loop modelling script of the Modeller software (71). We modelled AGT-Mi by introducing the P11L and I340M mutations in the AGT protein using the Chimera software (64). The latter was also used to introduce the F152I and I244T mutations on AGT-Mi. The molecular topology and atoms parameters for PLP covalently bound to lysine 209 were taken from ATB (72). The systems were simulated in a triclinic water box, and the minimum distance between any atom of the protein and the box wall was set up to 1.0 nm. The systems were neutralized by adding Na⁺ and Cl⁻ ions using the genion program of the GROMACS 4.5.5 package (68). Each system was energy minimized in four phases. In the first two phases, 800 steps of steepest descent algorithm followed by 3000 steps of conjugate gradient were performed to gently relax the water molecule around the protein, which was constrained imposing harmonic position restraints of 1000 kJ mol⁻¹ nm⁻². In the third and in fourth phases, the protocol was repeated without using any constraint. Subsequently the minimizations steps, the systems were equilibrated in four steps. In the first stage, the systems were slowly heated up from 0 K to 300 K in 1 ns at 1 atm, followed by two stages of equilibration in isothermal-isobaric (NPT) conditions for 600 ps, in which positional constraints were applied on the solute atoms (force constant of 1000 J mol⁻¹ nm⁻²). In the last stage, a 400 ps unrestrained MD simulation was performed at 300 K and 1 atm to

assess the stability of the systems. The temperature and pressure were regulated by a Berendsen thermostat and barostat, respectively (73). The LINCS algorithm (74) was used to constrain all bonds involving hydrogen atoms and the time step was set to 2 fs. Periodic boundary conditions (PBC) were applied. The particle mesh Ewald method (PME) (75) with a cut-off length of 1 nm was used to treat long-range electrostatic interactions, and the same cut-off length was adopted for van der Waals interactions. Finally, all monomer systems were simulated for 170 ns while dimer systems were simulated for 200 ns. For the dimer systems, we decided to carry out longer MD simulations (ca. 200 ns) because the equilibrium state of the two dimer systems was reached at ca. 110 ns. To sum up, the AGT-Mi protein was simulated, in all its mutated forms, totalizing ca. 740 ns of simulation time. For the production runs, a Nosè-Hoover thermostat (76) at 300 K and an Andersen-Parrinello-Rahman barostat (77), at 1 atm were used. The trajectories were analyzed using the standard GROMACS tools. The root mean square deviations (RMSD) and the root mean square fluctuations (RMSF) were performed through GROMACS inbuilt tools. RMSD plots for the AGT-Mi and F152I-Mi mutant were calculated without considering 4-23 region, which it is extremely flexible in the monomeric form and introduces artifacts to RMSD analysis. Cutoff of 4 Å between N—O atom pairs as a definition of salt bridge formation between Arg118 and Asp243 was used (78). All the graphical displays were generated using XMGrace program. The molecular graphics shown in this work were created using UCSF Chimera (64).

Essential dynamics (ED) was performed for AGT-Mi and F152I-Mi MD simulations according to principal component analysis (PCA). ED is a standard technique able to highlight the dominant motions of the investigated systems (79). The principal components (PCs), also called eigenvectors, were calculated by using ED and represent the protein's collective motions. Here, the first eigenvector, that accounts for ca. 50% of the total motions accomplished by the system, was used to understand the dynamical differences between the AGT-Mi and the F152I-Mi systems. Therefore, RMSF along the first eigenvector for the AGT-Mi and F152I-Mi were calculated (data not shown). Covariance matrix was calculated using C α atoms and the matrix was diagonalized. The PCs were

extracted from the covariance matrix. PCA was performed in three steps: i) the covariance matrix was calculated using the C α atoms; ii) the matrix was diagonalized and iii) a set of eigenvectors and eigenvalues were extracted from the covariance matrix. The eigenvectors correspond to a direction in the multidimensional space while the eigenvalues express the amplitude of the motion of each eigenvectors. PCA was carried out by using the standard GROMACS tool i.e. `g_covar` and `g_anaeig`.

3.2.3 Rigid-body docking simulations

Since rigid-body docking simulations are based on the analysis of the monomer-monomer interface, and considering that the crystal structure of AGT-Ma the protein is in the monomeric form, we decided to use the structure of AGT in complex with the TPR domain of human Pex5p, which is in the dimeric form (pdb id: 3R9A) (15) as a template for AGT-Ma. Thus, we first performed an *in-silico* mutagenesis on both AGT monomers to obtain the three dimensional structure of mutants. We used the software Pymol (58), and we selected the most probable rotamers when multiple side chain rotamers were available.

Protein-protein docking simulations were carried out by means of the rigid-body docking algorithm ZDOCK2.3 using one of the monomers as a fixed molecule (target) and the other monomer as a probe (ligand) for roto-translational space sampling. The Fast Fourier Transform-based algorithm performs a search to optimizes the molecular complementarity between target and ligand and provides a score (ZD-s) for each docking solution, which can be summarized as a combination of three components:

$$\text{ZD-s} = \alpha S_{sc} + \beta S_{el} + \gamma S_{des} = \text{ZD}_{sc} + \text{ZD}_{el} + \text{ZD}_{des}$$

where *sc*, *el* and *des* indicate the shape complementary, electrostatic and desolvation terms, respectively, and $\alpha = 0.01$, $\beta = 0.06$ and $\gamma = 1$ are scaling factors of the energy terms (S) proposed by the ZDOCK developers (59).

Docking simulations were run to test whether mutated monomers are predicted to assemble in a wild type-like quaternary structure or if the mutation prevents the formation of a native conformation. According to a computational protocol previously developed (60), three independent and parallel docking runs were run for AGT-Ma and the pathogenic variants by randomizing the initial coordinates of the ligand, thus obtaining 12,000 solutions for each protein complex ranked according to the ZD-s. Thereafter, native-like structures were selected, consisting in all the docked complexes characterized by an alpha carbon root-mean square deviation (C_{α} -RMSD) lower than 1.0 Å from the native complex. For each docking simulation, the selected complexes resulting from the three independent runs were averaged in the resulting ZD_{avg} . The ZD_{avg} was then used to calculate the predicted relative binding affinity $\Delta\Delta G^{\circ}_{pred}$ by making use of a linear correlation equation which successfully predict the binding affinity of a variety of soluble and membrane protein systems (61). For each docked complex, the obtained $\Delta\Delta G^{\circ}_{pred}$ value was directly compared with the relative dissociation constants at equilibrium ($\ln(K_{D(mut)}/K_{D(AGT-Ma)})$), where the term “mut” indicates each pathogenic variant tested, whose values were taken from the *in vitro* studies presented on this thesis.

3.2.4 Calculation of electrostatic potential maps, 2D maps and predicted pK_a

The electrostatic potential maps of AGT-Ma and mutants were calculated by using the APBS (Adaptive Poisson-Boltzmann Solver) 1.3 tool (62), using the non-linear Poisson-Boltzmann equation and modulating the ionic strength and temperature. The graphic interface of the tool is integrated in UCSF Chimera version 1.1 (63, 64). The calculation were performed on Opal web server (65). The structures preparation and the protonation state of residues at different pH values were carried out using the PDB2PQR (66) (using CHARMM as forcefield) and PROPKA 3.0 (67) tools respectively, on Opal web service. The 2Dmaps were calculated with the tool “Patch Analyzer” of MOE 2016.08 (56). In the latter case, structure preparation and protonation were performed directly on MOE 2016.08. The calculation of the predicted pK_a of the AGT residues was obtained by using

the tool “Residue pK_a ” of MOE 2015.1001.

3.3 Site-directed Mutagenesis

The expression vectors for the polymorphic, pathogenic and artificial variants of AGT were constructed starting from the pAGT-His construct, which contains the complete open reading frame of AGT together with a C-terminal histidine-tag (AVDHHHHHH), cloned in a pTrcHis2A plasmid (Invitrogen). This vector allows to express recombinant AGT in *E. coli* under the lactose operon controller by adding IPTG to the culture broth. Moreover, the presence of a C-terminal 6-Histidine tag allows a one step purification of the protein by Immobilized Metal Affinity Chromatography. For cell biology studies, the cDNA encoding human AGT was cloned in the mammalian expression vector pcDNA3.1/V5-His-TOPO, by means of the TOPO cloning kit (Invitrogen). This expression vector contains the human cytomegalovirus enhancer-promoter sequences upstream of the multicloning site, the transcription-termination sequence of the bovine growth hormone gene (bGH) downstream of the multicloning site and the gene for neomycine resistance. The constructs for the expression of AGT P11L and I340M were already available in our laboratory. The mutations R36H, G42E, I56N, G63R, R118A, G216R, F238S and F240S were introduced on the desired vector by the QuikChange site-directed mutagenesis kit (Stratagene), which employs double-stranded DNA as a template, two complementary oligonucleotide primers containing the desired mutation, and DpnI endonuclease to digest the parental DNA template. The oligonucleotides used for mutagenesis are reported in Table 2.

Table 2. Sequence of primers used for the site-directed mutagenesis. Mutated codons are underlined.

Mutation	Primer sequence (5'-3')
R118A	GGACATCGGGGAG <u>GCC</u> ATAGGAGCCCGA
F238S	CAAGACGAAGCCCT <u>CCT</u> CCTTCTACCTGG
F240S	GAAGCCCTTCTCCT <u>CCT</u> TACCTGGACATCAAG
F238S-F240S	AAGACGAAGCCCT <u>CCT</u> CCTCCTACCTGGACAT
R36H	CAACCTGCCTCCTCACATCATGGCAG
G42E	ATCATGGCAGCCGGGGA <u>ACT</u> GCAGATGAT
I56N	GATATGTACCAG <u>ACC</u> ATGGACGAGATC
G63R	GAGATCAAGGAACGCATCCAGTACGTG
G216R	GAACGCCCTCCA <u>AGG</u> ACCTCGCTC

3.4 Expression and purification of the AGT variants

E. coli BL21 or JM109 cells transformed with the constructs encoding the AGT variants were grown in 750 ml of Luria broth at 37°C to an absorbance at 600 nm of 0.4-0.6. Expression was induced with 0.1 mM IPTG for 15 h at 30°C. Cells were harvested and resuspended in 20 mM sodium phosphate buffer, pH 7.4 containing 0.5 M NaCl, 20 mM imidazole and 100 µM PLP. Lysozyme was added to a concentration of 0.2 mg/ml and the culture was incubated for 15 min at room temperature. After a freeze-thaw, leupeptin (0.5 µg/ml) and pepstatin (0.7 µg/ml) were added and the suspension was centrifuged at 30,000 g for 30 min at 4°C. The lysate was loaded on a HisPrep FF 16/10 (GE Healthcare) equilibrated with 20 mM sodium phosphate buffer pH 7.4 containing 0.5 M NaCl and 20 mM imidazole. A linear gradient was then inserted (0-100% in 200 ml) with the same buffer containing 500 mM imidazole. Soluble AGT elutes from the Ni²⁺ resin between 300 and 400 mM imidazole. After addition of 100 µM PLP, the protein solution was concentrated; imidazole and unbound coenzyme were removed by

extensive washing with 100 mM potassium phosphate (KP) buffer, pH 7.4, using Amicon Ultra 10 concentrators (Amicon). AGT can be stored at -20 °C without loss of activity for more than 6 months. Protein concentration was determined by using the apparent molar absorption coefficient of 95400 M⁻¹ cm⁻¹ at 280 nm (80). The PLP content was determined by releasing the coenzyme in 0.1 M NaOH and by using the apparent molar absorption coefficient of 6600 M⁻¹ cm⁻¹ at 388 nm.

3.5 Preparation of apoenzyme

AGT variants in the apo-form were prepared by incubating each species (10–20 μM) in the holo-form with 500 mM L-alanine for 20 min at 25 °C, in a final volume of 2 ml. The reaction mixture was concentrated to 0.2 ml by a Amicon Ultra 4 device (Millipore), washed twice with 2 ml of KP 1 M pH 6 and then 4–5 times with KP 0.1 M, pH 7.4.

3.6 Determination of the equilibrium dissociation constants for PLP ($K_{D(PLP)}$)

The equilibrium dissociation constant for PLP ($K_{D(PLP)}$) of R36H-Ma, G42E-Ma, I56N-Ma, G63R-Ma, R118A-Mi, F238S-Mi, F240S-Mi, and F238S/F240S-Mi variants was determined by measuring the quenching of the intrinsic fluorescence of the apo-enzymes (protein concentration 0.1-0.3 μM) incubated 24 h in the presence of PLP at a concentration range of 0.01–10 μM. In the case of G216R-Ma and R118A-F238S-F240S-Mi variants, the $K_{D(PLP)}$ was determined by measuring the CD signal at 424 or 430 nm (depending on the maximum of the dichroic band of each variant) of 10 μM and 2 μM apo-form, respectively, incubated 24 h in the presence of PLP at concentrations ranging from 1 to 300 μM. The experiments were performed in 100 and 50 mM KP, pH 7.4, at 25°C, respectively.

The $K_{D(PLP)}$ values for the mutant-coenzyme complexes were obtained by fitting

the data to the following equation:

$$Y = Y_{max} \frac{[E]_t + [PLP]_t + K_{D(PLP)} - \sqrt{[E]_t + [PLP]_t + K_{D(PLP)}^2 - 4[E]_t[PLP]_t}}{2[E]_t} \quad (1)$$

where $[E]_t$ and $[PLP]_t$ represent the total concentrations of the mutant and PLP, Y refers to either the intrinsic fluorescence quenching or the 424-430 nm dichroic signal changes at a PLP concentration, and Y_{max} refers to the aforementioned changes when all enzyme molecules are complexed with coenzyme.

3.7 Determination of the kinetic parameters

The kinetic parameters for the overall transamination reaction for the pair alanine/glyoxylate of the AGT variants (0.1–20 μ M) were determined in the presence of saturating PLP concentrations by varying the substrate concentration at a fixed saturating co-substrate concentration. At different times, the reactions were stopped by adding TCA 10% (v/v). The produced pyruvate was measured by a spectrophotometric assay using the coupled lactate dehydrogenase system (10). Data of initial velocity (v) as a function of substrate concentration were fitted to the Michaelis-Menten equation:

$$\frac{v}{E_t} = \frac{k_{cat}[S]}{K_m + [S]} \quad (2)$$

where E_t is the total enzyme concentration, S is the substrate concentration, k_{cat} is the turnover number, and K_m is the Michaelis-Menten constant. The AGT enzymatic activity of CHO-GO cell clones was determined by incubating the cellular lysate with 0.5 M L-alanine and 10 mM glyoxylate for 10 or 30 min in KP 100 mM, pH 7.4. The reactions were stopped by adding TCA 10% (v/v) and pyruvate production was measured using the spectrophotometric assay coupled with lactate dehydrogenase already described (10).

3.8 Size exclusion chromatography

SEC analyses were performed on an Akta FPLC system (GE Healthcare) using the Unicorn 5.01 (GE Healthcare) software and a Superdex 200 10/300 GL column at room temperature. The injection volume was 100 μ l, the flow rate 0.5 ml/min, and the detection at 280 nm. The mobile phase was 50 mM potassium phosphate buffer, pH 7.4, containing 100 μ M PLP in the case of R118A-Mi, F238S-Mi, F240S-Mi, R118A-F238S-Mi, R118A-F240S-Mi, F238S-F240S-Mi and R118A-F238S-F240S-Mi. For the R36H-Ma, I56N-Ma, G63R-Ma and G216R-Ma variants the mobile phase was 60 mM potassium phosphate buffer, pH 7.4 to mimic the physiological conditions. To determine the dimer-monomer equilibrium dissociation constant ($K_{d(dim-mon)}$), a stock solution of enzyme in the apo- or holo-form was dissolved in 50 or 60 mM potassium phosphate buffer at pH 7.4 at different concentrations, and after overnight incubation at 25 °C (a sufficient time to reach the equilibrium between monomer and dimer) subjected to SEC. The concentration of monomer and dimer was determined by integrating the area under the curve and expressed as percent of total area of all protein-related peaks.

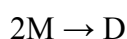
According to Manning et al. (81) the $K_{d(dim-mon)}$ value was determined by the following equation:

$$\%D = \left[(8[E] + K_{d(dim-mon)}) - \sqrt{K_{d(dim-mon)}^2 + 16 K_{d(dim-mon)}[E]^2} \right] / 0.08[E] \quad (3)$$

where %D is the percentage of dimer to total enzyme, and [E] represents the total enzyme concentration in dimer equivalents. A plot of $\log [\%D/0.04(100-\%D)^2]$ with respect to $\log[E]$ yields a straight line of slope 1. When $\log[\%D/0.04(100-\%D)^2] = 1$, $K_{d(dim-mon)} = [E]$.

3.9 Kinetics of the dimerization process of AGT R118A-F238S-F240S-Mi

The time course of AGT R118A-F238S-F240S-Mi dimerization:



induced by exogenous PLP was fitted to a simple second-order kinetics:

$$[D] = \frac{[D]_{eq}[E]k_{ass}t}{1+[E]k_{ass}t} \quad (4)$$

where $[D]$ and $[D]_{eq}$ represent the dimer concentrations at time t and at equilibrium, respectively, $[E]$ the enzyme concentration expressed as dimer, and k_{ass} the association rate constant. The equation was derived under the assumption that the reaction of dimerization is irreversible. Although this is never true, at conditions where k_{ass} is $\gg k_{diss}$ this assumption is valid and will not significantly alter the determined k_{ass} . Eq. 4 has also been used to fit the data of regain of enzyme activity and change in CD signal at 424 nm as a function of time.

On the other hand, to determine the k_{ass} of the reversible association of the apo-form, the k_{obs} of dimerization was calculated at different protein concentrations by the linear fit of the decrement of monomer concentration ($1/[M]$) versus time. k_{obs} values as a function of protein concentration were fit to a line whose slope gives the k_{ass} value.

3.10 Spectroscopic measurements

Absorption measurements were made with a Jasco V-550 spectrophotometer with 1 cm path length quartz cuvettes at a protein concentration of 1-10 μ M in 50 or 100 mM KP pH 7.4. Intrinsic fluorescence emission spectra were recorded on a Jasco FP-750 spectrofluorimeter equipped with a thermostatically controlled cell holder by using a 1 cm path length quartz cuvette. Protein emission spectra were taken from 300 to 550 nm (excitation at 280 nm) with both the excitation and the emission slits set to 5 nm. The protein concentration was 1 or 5 μ M. Spectra of

blanks, i.e. of samples containing all components except the enzyme, were taken immediately before the measurements of samples containing protein. Visible and far-UV CD spectra were recorded on a Jasco J-710 spectropolarimeter equipped with a Peltier temperature controlled compartment, by using 1 cm and 1 mm path length cells, respectively. The enzyme concentration was 1-15 μM . Routinely, three spectra were recorded at a scan speed of $50 \text{ nm}/\text{min}^{-1}$ with a bandwidth of 2 nm and averaged automatically, except where indicated. The thermal unfolding of variants was monitored by CD at 222 nm at a concentration of 1 μM or 10 μM in KP 100 mM, pH 7.4 with temperature increasing of $0.5 \text{ }^\circ\text{C}/\text{min}$ from 25 to $90 \text{ }^\circ\text{C}$ whereas for the monomeric R118A-Mi/F238S-Mi/F240S-Mi the buffer was KP 50 mM, pH 7.4.

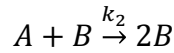
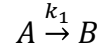
3.11 Dynamic light scattering (DLS)

DLS measurements were made on a Zetasizer Nano S device from Malvern Instruments. The temperature of sample cell was controlled by a Peltier thermostating system within $\pm 0.1 \text{ }^\circ\text{C}$ and $12.5 \times 45 \text{ mm}$ disposable cells with stopper were used. To study the aggregation propensity of the R36H-Ma, G42E-Ma, I56N-Ma, G63R-Ma and G216R-Ma variants under physiological conditions, each species was diluted to a final concentration of 4 μM in KP 60 mM pH 7.4 at $37 \text{ }^\circ\text{C}$. The aggregation kinetics of AGT-Ma, AGT-Mi, AGT P11L and AGT I340M was determined at an enzyme concentration of 10 μM in KP at different pHs and ionic strengths, at $37 \text{ }^\circ\text{C}$. The buffer was filtered immediately before use to eliminate any impurities.

3.12 Aggregation kinetics: the minimalistic/“Ockham’s razor” Finke-Watzky (F-W) two-step model

The minimalistic/“Ockham’s razor” Finke–Watzky (F–W) two-step model was routinely used to analyze protein aggregation kinetic data (82, 83). This model is characterized by nucleation and autocatalytic growth, yielding quantitative

(average) rate constants for nucleation (k_1) and growth (k_2), respectively.



where A is the monomeric protein and B is the polymeric protein i.e. in oligomers that are past the nucleation stages. The F–W 2-step model is an oversimplified, phenomenological kinetic model that consists of hundreds, if not thousands, of steps in most cases. The resultant k_1 and k_2 values are therefore averages of the true underlying steps. The classic F–W 2-step mechanism assumes an initial zero concentration of aggregate, and so the rate equation becomes:

$$-\frac{d[A]}{dt} = k_1[A] + k_2[A][B] \quad (5)$$

By mass balance,

$$[A]_0 = [A]_t + [B]_t \quad (6)$$

Combining these two equation (5 and 6), integrating and solving for $[A]_t$:

$$[A]_t = \frac{\frac{k_1}{k_2} + [A]_0}{1 + \frac{k_1}{k_2[A]_0} \exp(k_1 + k_2[A]_0)t} \quad (7)$$

where $[A]_0$ represent the initial monomeric concentrations and $[A]_t$ represents the loss of $[A]$ with time.

3.13 Calculation of pK_{spec}

The pK_{spec} was calculated with the following equation (84):

$$Y = \frac{Y_H - Y_L}{1 + 10^{pK_{\text{spec}} - pH}} + Y_H \quad (8)$$

where Y_H and Y_L are the rate constant values of k_1 and k_2 at high and low pH.

3.14 Limited proteolysis

The holo- and apo-forms of AGT-Ma and of the variants R36H-Ma and G42E-Ma (10 μ M) were treated with proteinase K in 100 mM potassium phosphate buffer, pH 7.4, at 25°C. At various times, 15 μ L of each reaction mixture were withdrawn and the protease activity was stopped by adding PMSF to a final concentration of 2 mM. Each aliquot was then subjected to SDS-PAGE and the gel stained with Comassie blue. The relative intensities of the bands were obtained by analyzing the digital image of each gel using the software ImageJ (85).

3.15 Cell culture and lysis

CHO-GO cells were cultured at 37°C under O₂/CO₂ (19:1) atmosphere in Ham's F12 Glutamax medium (Invitrogen) supplemented with fetal bovine serum (10%, v/v), penicillin (100 units/ml) and streptomycin (100 μ g/ml). When the cells were 70–80% confluent they were trypsinized, counted and re-seeded into 6-well plates or 60 mm dishes at a density of 0.3-0.6 x 10⁶ cells/well respectively. After overnight incubation at 37°C, cells were transfected with Turbofect™ Transfection Reagent (Fermentas) according to the manufacturer's instructions. After 4 hours from transfection cells were washed in phosphate buffered saline (PBS) and the medium was changed with a custom-made Ham's F12 medium without pyridoxine (PN) supplemented with fetal bovine serum (10%, v/v), penicillin (100 units/ml) and streptomycin (100 μ g/ml) (low-B6 medium). To generate stably-transformed cell clones, the selection agent G-418 at 1 mg/ml concentration was added to the medium and cells were left growing for at least 4 weeks. Where indicated, 10 μ M pyridoxine (PN) was added to the medium. Cells were harvested after 24 hours and lysed in phosphate buffered saline (PBS), pH 7.2, plus protease inhibitor cocktail (Complete Mini, Roche), by five freeze/thaw cycles followed by treatment with DNase (1 unit) at RT for 45 min. The whole cell extract was separated by centrifugation (29200 g, 10 min, 4°C) to obtain the soluble fraction. The pellets were then resuspended in an equal volume of denaturing gel loading buffer to obtain the insoluble fraction. The total protein concentration in the cell

lysate and/or in the soluble fraction, was measured using the Bradford protein assay.

3.16 Western blot analysis

10 µg of cell lysate were loaded per lane on a Mini Protean TGX™ pre-cast gel (Biorad) along with Precision plus protein Kaleidoscope™ (Bio-Rad) as molecular mass markers. Following transfer on a nitrocellulose membrane by the iBlot device (Invitrogen) the membrane was blocked in 5% bovine serum albumin (BSA) for 1 h at 37°C. For AGT detection the membrane was incubated with polyclonal rabbit anti AGT serum (dilution 1:2000), washed three times in TBST (50 mM Tris-HCl pH 7.5, 150 mM NaCl, 0.1% Tween 20) and then incubated with peroxidase-conjugated anti rabbit IgG (dilution 1:1000). Blotted proteins were detected and quantified with ECL® (Millipore), using the ChemiDoc XRS Imaging System (Bio-Rad, Hercules, CA).

3.17 Immunofluorescence microscopy (IFM)

CHO-GO cells expressing AGT-Ma and the R36H, G42E, I56N, G63R and G216R variants were grown in the absence or presence of 10 µM PN. Approximately 3×10^5 cells were seeded into each well of a 24-well plate, containing a 13-mm glass coverslip, and grown for 24 h in complete Ham's F12 medium at 37 °C under O₂/CO₂ (19:1). Cells were fixed in 4% (w/v) paraformaldehyde permeabilized with 0.3% Triton X-100 in PBS and then blocked in 3% bovine serum albumin (BSA) in PBS. For the immunolabeling, rabbit polyclonal anti-human AGT and anti-peroxisomal protein from guinea-pig were used as primary antibodies, and Alexa Fluor conjugated antibodies (Life technologies) were used as secondary antibodies. Nuclei were stained with DAPI and the coverslips were mounted over slides in AF1 medium (Dako). Images were captured using a confocal laser-scanning fluorescence microscope Leica SP5 (Leica Microsystem, Manheim, Germany) at 63× magnification and analyzed

using ImageJ (<http://rsb.info.nih.gov/ij/>). For figure preparation images were processed using Adobe Photoshop.

3.18 Statistical analysis

Experiments have been performed at least in triplicate and in any case the standard error mean (SEM) was less than 10%. Statistical analyses were performed by Origin® 7 (Origin Lab) or GraphPad Prism Version 6.0 (GraphPad software, San Diego, CA, USA).

4

**ENGINEERING OF A SOLUBLE MONOMERIC
FORM OF AGT AND STUDY OF THE
DIMERIZATION PROCESS**

Background information

Human AGT is functionally active as a homodimer in liver peroxisomes (5). The protein displays a large monomer-monomer interface (Fig. 8) as compared with other PLP-dependent enzymes. Molecular and cellular analyses have suggested that the dimerization process could be crucial for the correct folding and intracellular targeting of the enzyme. In line with this view, many pathogenic mutations leading to PH1 involve residues located at or near the dimerization interface, whose mutation strongly reduces the thermodynamic and kinetic stability of the protein, decreases its intracellular half-life, increases its aggregation propensity, and, when associated with the minor allele polymorphism, leads to the aberrant targeting to mitochondria (26, 32, 45, 86). It is also well known that patients expressing pathogenic variants of AGT showing a reduced dimer stability respond to the administration of Vitamin B6 in form of PN. PN treatment raises the intracellular concentration of PLP (32, 54), which is supposed to promote dimer formation thus increasing variants stability (54). However, neither the structural elements that govern the self-association of the AGT subunits, nor the effect of the coenzyme have been elucidated at molecular level. To fill this gap, we engineered, purified and characterized a soluble monomeric form of AGT. As a first approach, we decided to start from the minor allelic form of the protein. This choice was dictated by the fact that (i) the P11L polymorphic mutation is known to destabilize the interfacial contacts between the N-terminal arm of one subunit and the large domain of the neighboring subunit, and (ii) many pathogenic variants showing reduced dimer stability are associated with the minor allele. We then studied the kinetics of the dimerization process in the absence or presence of the PLP coenzyme. These data provided the basis to understand the responsiveness to PN administration of two of the most common PH1 mutations, F152I and I244T, associated with the minor allele.

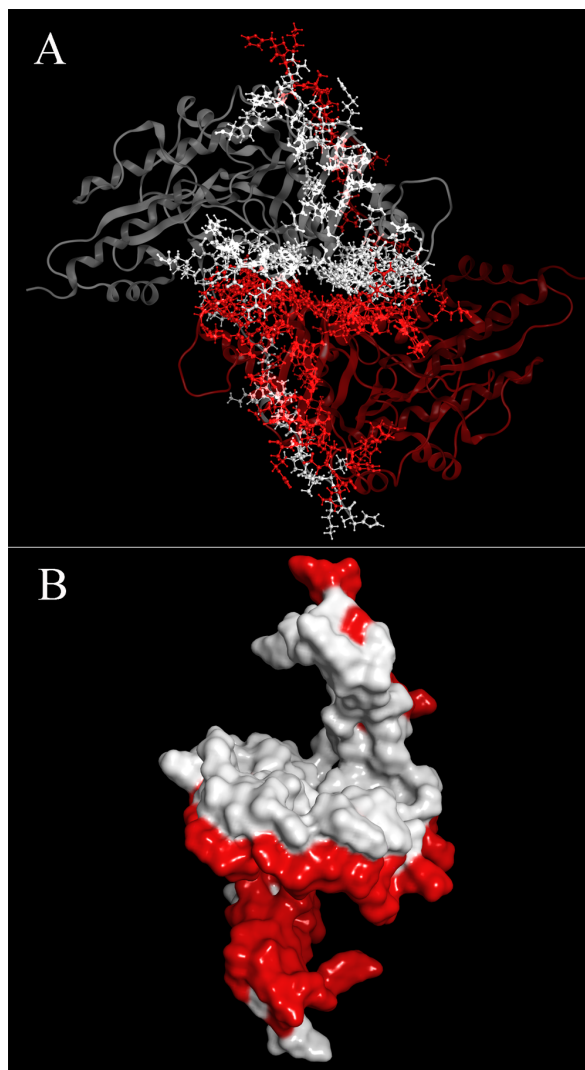


Fig. 8. Representation of the AGT dimer interface. Panel A: structure of AGT highlighting the interface residues as sticks. Panel B: surface representation of the AGT interface residues. The two monomers are coloured red and white.

RESULTS AND DISCUSSION

4.1 Identification of the AGT interface hotspots

The crystal structure of AGT reveals that 48% of the total solvent accessible area (ASA) of the protein is buried upon dimerization. Such surface comprises 110 residues per subunit, many of which are directly involved in inter-chain contacts. In particular, 15 hydrophobic patches, 40 interchain hydrogen bonds and two salt bridges contribute to the monomer-monomer interaction. Considering the high number and the different type of interchain contacts as well as their wide distribution, the identification of possible dimerization hot spot/s could be difficult. Thus, to identify residues or clusters of residues that mainly contribute to the binding free energy at the dimerization interface, we performed an *in silico* alanine-scanning mutagenesis analysis on the AGT interfacial residues using the Molecular Operating Environment software by Chemical Computing Group (56). We first constructed the model of monomeric and dimeric AGT-Mi by *in silico* mutagenesis introducing the polymorphic mutations P11L and I340M followed by an energetic minimization of the structure, as reported in the “Material and Methods” section 4.2. Then, in order to find out residues whose substitution destabilizes the quaternary structure without any significant impact on the tertiary structure of each monomer, we performed the alanine-scanning mutagenesis analysis on both dimeric and monomeric AGT-Mi.

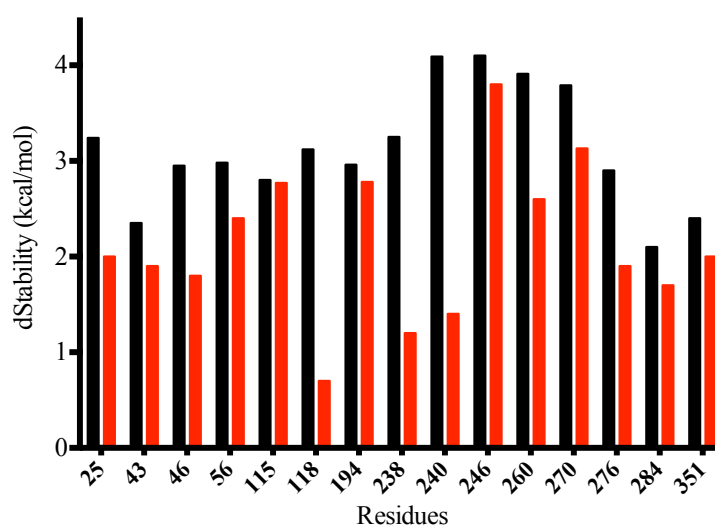


Fig. 9. Plot of the alanine scanning mutagenesis results either on the monomer (red bars) and dimer (black bars) of AGT expressed as dStability (kcal/mol) of each interfacial residue. The dStability (kcal/mol) represents the relative thermostability of each mutant with respect to AGT-Mi. Only residues with a positive value of dStability ≥ 2 kcal/mol are shown.

As shown in Fig. 9, the dStability values, representing the predicted relative thermostability of each mutant with respect to AGT-Mi, indicate that among the 15 residues predicted to play a role in stabilizing the dimeric structure (black bars), only Arg118, Phe238 and Phe240 do not significantly change the intrinsic stability of monomeric AGT (red bars). These residues are not directly involved in the binding of the coenzyme and/or of the substrate, thus suggesting that their would not affect the AGT functional properties. Arg118 forms with Asp243 of the neighbouring chain the unique salt bridge present at the AGT-Mi interface (Fig. 10, panel A). Thus, its substitution with an alanine residue could weaken the dimer interface without substantially affecting the monomer structure. Phe238 is engaged in hydrophobic base stacking interactions with the same residue of the other subunit, while Phe240 interacts with Trp246 of the same subunit as well as with Ile115, and possibly His83, of the adjacent monomer (Fig. 10, panel A). The predicted role of Phe238 and Phe240 in AGT dimerization was also investigated by the Protein Patch Analyzer tool of *MOE 2015.01*. The hydrophobic patches on the dimerization interface of AGT-Mi were ordered from 1 to 15 in the output list on the basis of a decreasing solvent-accessible surface area of the patch (\AA^2) (Fig. 10, panel B). The main hydrophobic interactions at the dimer interface are formed by patches enumerated as 1, 10, 13 and 14. It can be observed that both Phe238

(patch 13) and Phe240 (patch 1) are predicted to critically contribute to the hydrophobicity of the interface because both residues show a high ASA value when they become exposed to the solvent upon monomerization (Fig. 10, panel B). We decided to substitute the two phenylalanine residues with serine residues, in order to weaken the dimer interface and concomitantly enhance the solubility of the monomer.

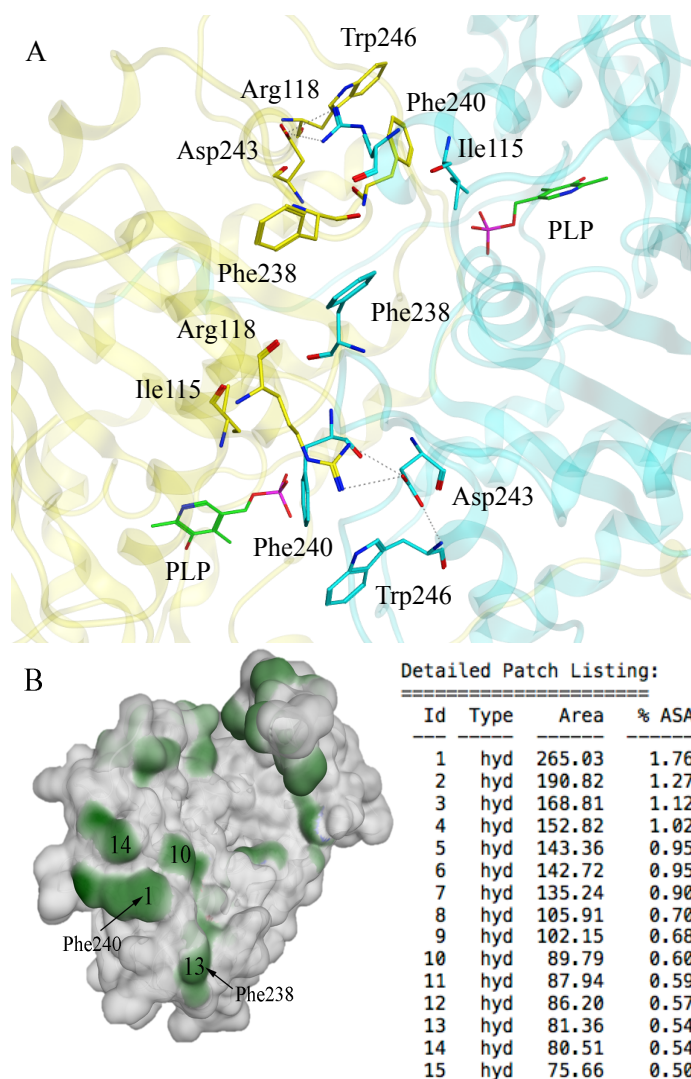


Fig. 10. The main interface hot spots and hydrophobic patches along the AGT dimerization interface. Panel A: detail of the main interface hotspots. The labelled residues are shown as yellow or cyan sticks on the basis of the colour of the belonging subunit. PLP is shown as green sticks. Panel B: interfacial hydrophobic patches of an AGT monomer shown as green areas on the grey background of AGT. The size and the energy cut-offs of each patch are 75 \AA^2 and 0.25 kcal/mol, respectively.

4.2 Role of the residues Arg118, Phe238 and Phe240 on AGT dimerization

Based on the results obtained by the computational analysis, we constructed, expressed, purified and characterized the mutants R118A-Mi, F238S-Mi, and F240S-Mi. The variants display spectral properties in the visible region analogous to those of AGT-Mi, although the R118A and the F238S mutations reduce the intensity of the 340-nm absorbance band, while the F240M mutation causes a 5-nm blue shift of the 424 nm dichroic band (Fig. 11).

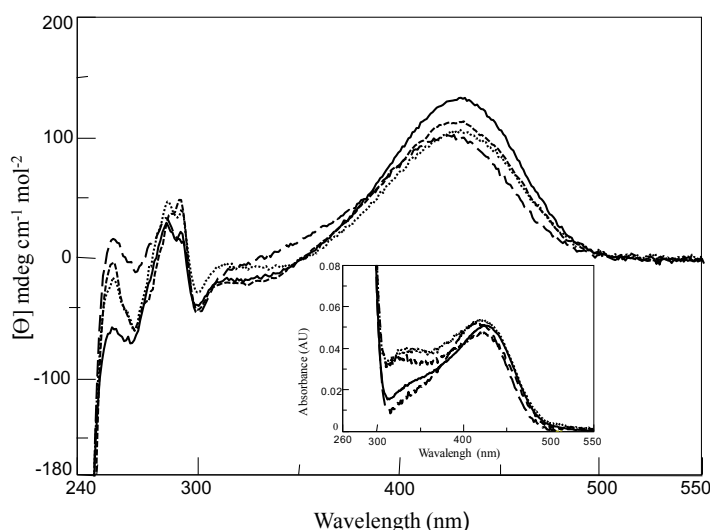


Fig. 11. CD and absorbance spectra of AGT-Mi and single variants. CD and absorbance (inset) spectra of AGT-Mi (—), R118A-Mi (·····), F238S-Mi (---) and F240S-Mi (- - -) were obtained at 10 μ M enzyme concentration in 50 mM potassium phosphate buffer, pH 7.4

These data indicate that the variants show a PLP binding mode similar to that of AGT-Mi. Moreover, as shown in Table 3, the three mutations do not significantly alter the $K_{D(PLP)}$ value of AGT-Mi as well as the steady-state kinetic parameters for the overall transamination of the alanine-glyoxylate pair. F238S-Mi shows a k_{cat} value comparable to that of AGT-Mi, while R118A-Mi and F240S-Mi display k_{cat} values reduced by approximately 50 % with respect to AGT-Mi. Thus, none of these residues is essential for catalytic activity. However, it can be suggested that the mutation of Arg118 and Phe240 could alter the proper juxtaposition of the two subunits, thus negatively influencing the catalytic power. In this regard, it should

be mentioned that a stretch of amino acids of the N-terminus called “active site loop” (residues 24-32) is present at the entrance of the AGT active site (8). Previous results indicate that interfacial mutations interfering with the interaction between the N-terminal arm and the neighboring subunit can alter the position of the active site loop and negatively influence the catalytic efficiency of the enzyme (31). Although more detailed information on the structural features of the variants would be necessary, it can be speculated that a similar phenomenon could be also caused by the R118A and F240S mutations, thus explaining their effect on catalysis.

Table 3. Steady-state kinetic parameters and $K_{D(PLP)}$ of AGT-Mi and variants obtained in 50 mM potassium phosphate buffer, pH 7.4 in the presence of 100 μ M PLP.

Enzyme	Substrate	Cosubstrate	k_{cat} (s^{-1})	K_m (mM)	k_{cat}/K_m ($mM^{-1}s^{-1}$)	$K_{D(PLP)}$ (μ M)
AGT-Mi	L-alanine Glyoxylate	Glyoxylate L-alanine	35 ± 1 39 ± 3	51 ± 7 0.20 ± 0.05	0.68 ± 0.09 195 ± 43	0.10 ± 0.01
AGT R118A-Mi*	L-alanine Glyoxylate	Glyoxylate L-alanine	21 ± 1 19 ± 1	77 ± 10 0.18 ± 0.02	0.27 ± 0.04 106 ± 12	0.20 ± 0.04
AGT F238S-Mi	L-alanine Glyoxylate	Glyoxylate L-alanine	36 ± 1 35 ± 1	46 ± 1 0.71 ± 0.06	0.78 ± 0.03 49 ± 4	0.25 ± 0.02
AGT F240S-Mi	L-alanine Glyoxylate	Glyoxylate L-alanine	22 ± 1 20 ± 1	84 ± 7 0.28 ± 0.04	0.26 ± 0.02 71 ± 15	0.19 ± 0.03

*data obtained in presence of 10% glycerol.

The impact of each single mutation on the AGT-Mi dimeric structure was investigated by SEC analyses of each variant in the holo- and apo-form at different enzyme concentrations (Table 4). HoloR118A-Mi elutes as a peak whose elution volume corresponds to that of a dimer and whose total area does not change up to 0.3 μ M, while the apo-form elutes as three peaks whose elution volumes correspond to a dimer, a monomer and aggregates at high molecular weight. The integrated area of the dimer decreases and concomitantly that of the monomer and aggregates increases as the enzyme concentration decreases from 10 to 1.25 μ M. These data strongly indicate that the apomonomer form is prone to

aggregation, as supported by DLS measurements. In fact, at 5 μM concentration, apoR118A-Mi exhibits a rapid increase in count rate typical of a fast aggregation process, leveling off after approximately 12 min (data not shown). If SEC experiments are carried out in the presence of 10% glycerol to avoid aggregation, the proportion of the apomonomer increases at the expense of the dimer as the overall enzyme concentration is lowered from 18 to 1 μM . This indicates a slow equilibrium process. A plot of the percent dimer as a function of apoR118A-Mi concentration gives a hyperbolic curve whose linear transformation yields a $K_{d(\text{dim-mon})}$ value of $9.3 \pm 0.1 \mu\text{M}$ (Table 4), a value at least 30-fold higher than that of apoAGT-Mi. Since both the apo- and holo-forms of the variants F238S-Mi and F240S-Mi maintain the dimeric structure up to 0.3 μM , it is not possible to establish if Phe238 or Phe240 play a role in the dimer formation of AGT-Mi.

Table 4. $K_{d(\text{dim-mon})}$ values of AGT-Mi and variants.

Enzymes	Apo $K_{d(\text{dim-mon})}$ (μM)	Holo $K_{d(\text{dim-mon})}$ (μM)
AGT-Mi	< 0.3	< 0.3
R118A-Mi	$9.3 \pm 0.1^*$	< 0.3
F238S-Mi	< 0.3	< 0.3
F240S-Mi	< 0.3	< 0.3
F238S-Mi/F240S-Mi	<0.3	<0.3
R118A-Mi/F238S-Mi	7.4 ± 0.4	<0.3
R118A-Mi/F240S-Mi	24 ± 1	2.4 ± 0.9
R118A-Mi/F238S-Mi/F240S-Mi	80 ± 1	9.4 ± 0.5

*data obtained in presence of 10% glycerol.

To promote AGT-Mi monomerization, double mutants were subsequently created in the following combinations: F238S-Mi/F240S-Mi, R118A-Mi/F238S-Mi, and R118A-Mi/F240S-Mi. Both the apo- and holo-form of F238S-Mi/F240S-Mi still existed predominantly in the dimeric form up to 0.3 μM , thus preventing the quantification of the effect of the combinations of the two mutations on the $K_{d(\text{dim-mon})}$ value of AGT-Mi. On the other hand, the combination of each of the mutations with the R118A substitution gave different results. In fact, the double mutant R118A-Mi/F238S-Mi in the holo-form eluted from gel filtration as a

dimer up to 0.3 μM , while the apo-form had a $K_{\text{d}(\text{dim-mon})}$ value of $7.4 \pm 0.4 \mu\text{M}$ (Table 4). The R118A-Mi/F240S-Mi double mutant demonstrated a significant shift from dimer to monomer both in the apo- ($K_{\text{d}(\text{dim-mon})} = 24 \pm 1 \mu\text{M}$) and holo-form ($K_{\text{d}(\text{dim-mon})} = 2.4 \pm 0.9 \mu\text{M}$) (Table 4). It should be noted that the $K_{\text{d}(\text{dim-mon})}$ values of the double mutants are obtained in the absence of glycerol, thus suggesting that the combination of the mutations F238S and F240S with the R118A mutation prevents apomonomer aggregation. All together, these data highlight that (i) the interacting forces between Arg118 and Asp243 of the neighboring monomer may drive dimer formation in apoAGT-Mi, (ii) Arg118 and Phe240 synergize in promoting the formation of the dimer of AGT-Mi, and (iii) substitution of both Phe238 and Phe240 with Ser could be relevant in increasing monomer solubility by reducing the hydrophobicity of the dimer interface. Therefore, we decided to construct, express, purify, and characterize the triple mutant R118A-Mi/F238S-Mi/F240S-Mi. The triple mutant displays a slow dimer-monomer equilibrium process in both the apo- and holo-form, and $K_{\text{d}(\text{dim-mon})}$ values of $80 \pm 1 \mu\text{M}$ and $9.4 \pm 0.5 \mu\text{M}$, respectively (Table 4). These results highlight that the salt bridge between Arg118 and Asp234 plays a pivotal role in stabilizing the AGT monomer-monomer interface, thus indicating that it represents a hot-spot for protein dimerization. On the other hand, both Phe238 and Phe240 take part to main hydrophobic interactions, which significantly influence the dimerization equilibrium only in the presence of the R118A mutation but represent a key factor in determining monomer stability in solution. The triple mutant R118A-Mi/F238S-Mi/F240S-Mi is stable in solution as a monomer in both the apo- and holo-form. Thus, it represents an excellent model to study the biochemical properties of AGT in the monomeric form as well as the kinetics of the dimerization process.

4.3 Spectroscopic features of the engineered monomeric AGT

The far-UV CD spectrum of the apomonomer R118A-Mi/F238S-Mi/F240S-Mi was comparable to that of apoAGT-Mi in the dimeric form, and the deconvolution revealed that they have an identical composition of the overall secondary structure. On the other hand, the comparison of near-UV CD spectra and intrinsic fluorescence spectra (both reflecting the microenvironment of aromatic side chains) as well as ANS fluorescence spectra and thermal stability data of the apomonomer and apoAGT-Mi provided evidence that a different conformation exists between the two forms. In fact, as shown in Fig. 12, the apomonomer exhibited an increase of the dichroic signals in the near-UV region and a decrease of the intrinsic fluorescence emission intensity along with a 4-nm red-shift of the maximum intensity, as well as a ~8-fold increase in ANS emission fluorescence intensity with a 4-nm red shift of the emission maximum. Additionally, unlike apoAGT-Mi which displayed a two-steps thermal transition curve with apparent mid-denaturations at 53.8 ± 0.1 °C and 66.1 ± 0.1 °C (33), the unfolding of the triple mutant in the apo-form occurred through a single step with an apparent T_m value of 47.5 ± 0.3 °C. These data indicate that the monomer is characterized by a different tertiary structure, and by an increased exposure of hydrophobic surfaces, leading to a higher sensitivity to thermal stress. Similar features were also observed for the apomonomer of the double mutant R118A-Mi/F240S-Mi.

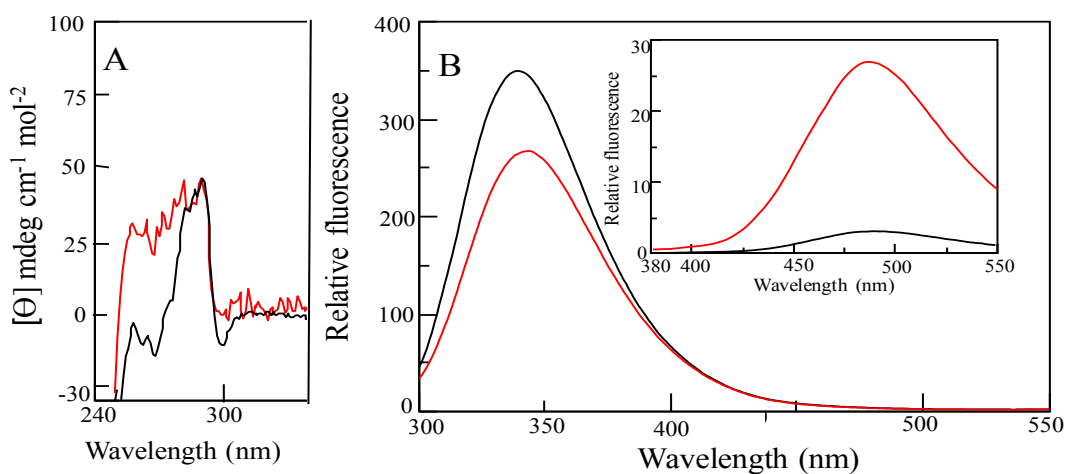


Fig. 12. Spectroscopic features of apomonomer R118A-Mi/F238S-Mi/F240S-Mi (red line) in comparison with the apodimer AGT-Mi (black line). Panel A: near-UV CD spectra at 5 μM concentration; Panel B: intrinsic fluorescence emission spectra at 1 μM concentration. Inset of panel B: ANS emission fluorescence spectra at 1 μM concentration. All measurements were obtained in 50 mM KP buffer, pH 7.4.

We then monitored the ability of the apomonomer (2 μM) to bind PLP by following the time-dependent changes in the dichroic signal at 424 nm, due to the formation of the internal aldimine complex in the presence of 100 μM PLP, i.e. under conditions in which the triple mutant is monomeric either in the apo-form and holo-form. The kinetics of PLP binding was monophasic and the process occurred with a rate constant of $2.44 \pm 0.08 \text{ min}^{-1}$. At the end of the process, the loading of the solution on a SEC column confirmed that all the protein remained in the monomeric form upon PLP binding. The prolonged incubation ($> 3 \text{ h}$) of the monomer at a concentration of 0.1 or 0.2 μM with L-alanine and glyoxylate did not lead to any pyruvate formation, thus indicating that it does not show any significant catalytic activity. When compared with holoAGT-Mi in the dimeric form, the holomonomer also revealed (i) a decrease of the dichroic band in the near-UV region, (ii) a 20-fold increase in the ANS emission intensity with a 9 nm red shifted maximum, and (iii) a mid-point denaturation reduced by 23 degrees ($50.1 \pm 0.1 \text{ }^\circ\text{C}$) (see below). In the visible region, the PLP-bound monomer showed a positive dichroic band at 424 nm whose magnitude was about half that

of holoAGT-Mi indicating a different PLP binding mode (data not shown). This is also confirmed by the fluorescence emission spectra of the NaBH₄-reduced holomonomer upon excitation at 325 nm, which displayed a 6-nm red shifted maximum and 2-fold increased intensity in comparison with that of the reduced holoAGT-Mi (Fig. 13). Moreover, while the intrinsic fluorescence emission spectrum of the reduced holodimer showed a single maximum at 341 nm, the holomonomer fluoresced not only at 342 nm but also at 393 nm, possibly due to the occurrence of an energy transfer from tryptophan(s) to the reduced coenzyme (inset of Fig. 13).

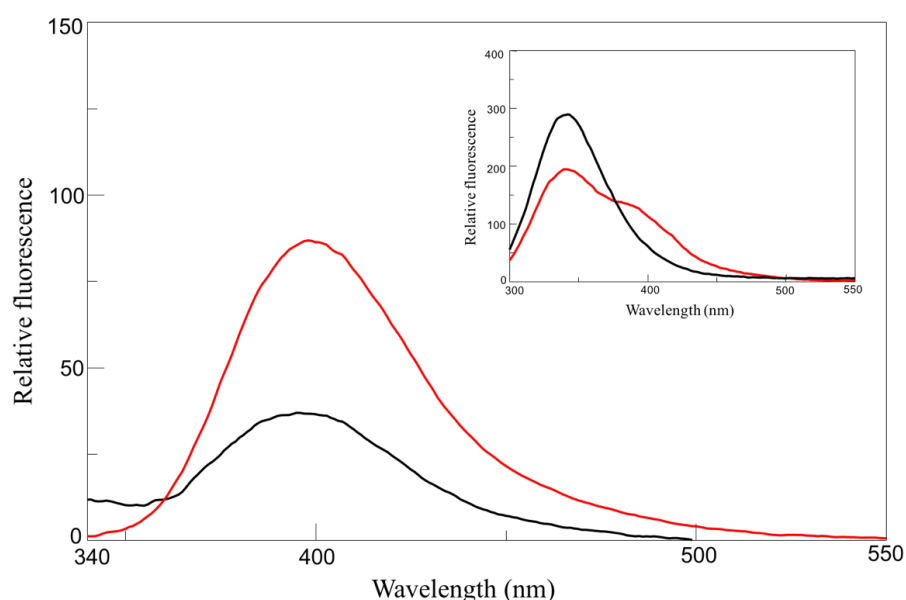


Fig. 13. Fluorescence properties of NaBH₄-reduced R118A-Mi/F238S-Mi/F240S-Mi (red line) and dimeric AGT-Mi (black line). Emission fluorescence spectra upon excitation at 325 nm. The inset show the fluorescence emission upon excitation at 280 nm. Spectra were registered at 1 μ M concentration.

When the apomonomer was treated with PLP concentrations ranging from 1 to 40 μ M, the trend of the dichroic signal values at 424 nm as a function of PLP concentration gave a $K_{D(PLP)}$ value of 4.4 ± 0.5 μ M per subunit. This value is about 17-fold higher than the $K_{D(PLP)}$ value of AGT-Mi (36). Taken together, these data indicate that the holo and apomonomer display a conformation similar to each other but different from the corresponding ones of the dimeric forms of AGT-Mi (Fig. 13 and Fig. 14), as revealed by spectroscopic properties and

apparent T_m values. Monomeric AGT is able to bind PLP, although with an affinity lower than holoAGT-Mi. The PLP-bound monomer is catalytically inactive and exhibits local structural alterations of the coenzyme microenvironment leading to a more pronounced exposure to the solvent of the PLP binding site as well as an altered spatial geometry of the functional groups in the PLP microenvironment, with respect to the holodimer.

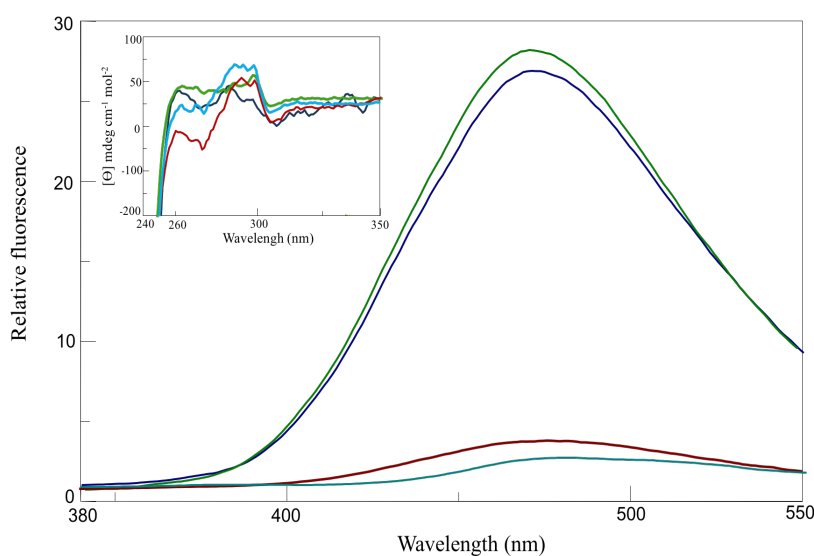


Fig. 14. Spectroscopic feature of apo and holomonomer R118A-Mi/F238S-Mi/F240S-Mi in comparison with apo and holodimer AGT-Mi. ANS emission fluorescence spectra at $1 \mu\text{M}$ concentration. In the inset: near-UV CD spectra at $1 \mu\text{M}$ concentration. Color code: cyan and red correspond to holo and apodimer of AGT-Mi, respectively, while blue and green correspond to the holo and apomonomer of R118A-Mi/F238S-Mi/F240S-Mi.

Although the vast majority of PLP-enzymes are present as dimers, only few studies until now have addressed the role of the quaternary structure on the enzyme structural and functional properties. In analogy with what already known for ornithine decarboxylase (87), bacterial diamino-pimelate decarboxylase (88) and *Treponema denticola* cystalysin (89), we found that monomeric AGT does not display transaminase activity and shows an altered active site microenvironment. This is not surprising, since residues belonging to both subunits form the protein active site. Residues of the neighboring subunit are involved in key interactions with the coenzyme, such as the hydrogen bonds

coordinated by Tyr260 and Thr263 with the phosphate group of PLP (8). Moreover, by engineering a monomeric form of the protein stable in solution, we could show that dimerization in AGT seems to be important for both the stability and the achievement of the final tertiary structure. This is in line with the finding that pathogenic mutations involving interfacial residues often lead to an increased propensity of the protein to unfolding, aggregation and degradation (90).

4.4 Kinetics of the dimerization process and role of PLP

To investigate the kinetics of the dimerization process and the effect of the coenzyme, we monitored PLP binding as a function of time at 5 μM R118A-Mi/F238S-Mi/F240S-Mi concentration, i.e under conditions in which the triple mutant is monomeric in the apo-form and mostly dimeric in the holo-form. We observed that the magnitude of the dichroic signal at 424 nm increased in a biphasic way. The fast phase, obtained by fitting the data to a single exponential process, occurred with a rate constant of $2.4 \pm 0.2 \text{ min}^{-1}$, while the slow phase, fitted to Eq. (4) (“Materials and Methods”, section 3.9), was characterized by a rate constant of $0.020 \pm 0.002 \text{ } \mu\text{M}^{-1}\text{min}^{-1}$ (Fig. 15). Aliquots withdrawn from the reaction mixture at various times were subjected to SEC and activity analyses. As shown in the inset of Fig. 15, the dimeric species increased with time at the expense of the monomeric one in a slow equilibrium process. The percentage of the dimeric form as a function of time fitted Eq. (4), yielded a rate constant value of dimerization of $0.019 \pm 0.002 \text{ } \mu\text{M}^{-1} \text{ min}^{-1}$. On the basis of this value and that of $K_{\text{d}(\text{dim-mon})}$ of the triple mutant in the holo-form, we could estimate a k_{diss} value of $0.18 \pm 0.004 \text{ min}^{-1}$. As shown in Fig. 15, the regain of transaminase activity as a function of time occurred with a rate constant of $0.021 \pm 0.002 \text{ } \mu\text{M}^{-1} \text{ min}^{-1}$, a value in excellent agreement with those of dimerization and of the slow phase of PLP binding. Thus, it is possible to suggest that the biphasic process is characterized by a fast phase representing the internal aldimine formation between the apomonomer and the coenzyme, followed by a slow phase representing dimerization and regain of transaminase activity. To obtain a realistic estimation of the catalytic activity of the triple mutant in the holodimeric form, we incubated

the apomonomer at concentrations ranging from 1.4 to 19 μM with 100 μM PLP, and we assayed the reaction mixtures both for transaminase activity and amount of formed dimer. By plotting the catalytic activity as a function of the percentage of dimer we noticed a linear relationship between the two variables (data not shown) and we calculated that 1 nmol of the triple mutant in the holodimeric form reacting with L-alanine and glyoxylate produces pyruvate with an initial rate of 4.8 nmol pyruvate/sec. Assuming that this value is close to the k_{cat} of the half-transamination, this rate is about 9-fold lower than the k_{cat} value of AGT-Mi.

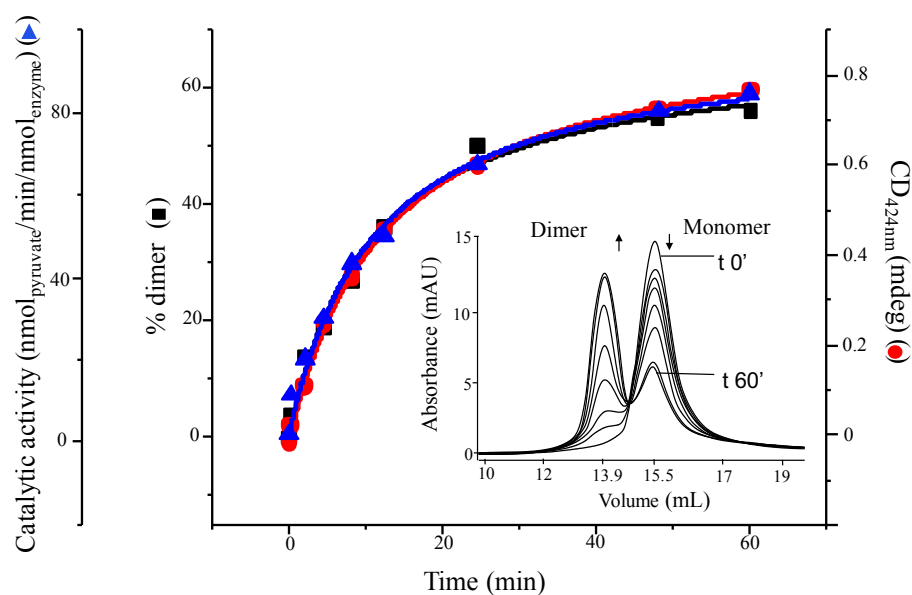


Fig. 15. Second-order kinetic plots for data of dimerization (\blacklozenge), increase of magnitude of the CD signal at 424 nm (\bullet), and catalytic activity (\blacktriangle) according to Eq. (4). Inset: SEC profiles of the apomonomer after addition of 100 μM PLP at the indicated times.

We also investigated the kinetics of the dimerization of the triple mutant in the apo-form by SEC experiments. We found a value of k_{ass} equal to $7.9 \pm 0.6 \times 10^{-6} \mu\text{M}^{-1} \text{min}^{-1}$ and, on the basis of the $K_{\text{d}(\text{dim-mon})}$, we estimated a k_{diss} value of $6.4 \pm 0.4 \times 10^{-4} \text{min}^{-1}$. Thus, the apomomer is able to dimerize even if with rates of association and dissociation about 2700- and 280-fold lower respectively, than the corresponding ones of the PLP-bound monomer.

Overall these data show that PLP binding shifts the equilibrium toward the dimeric form of AGT mainly by accelerating the dimerization process. This implies that, in line with previous evidences, the coenzyme does not only play a prosthetic role for the enzyme, but also a chaperone role by promoting the achievement of the native structure. A similar behavior has been also suggested for other B6 enzymes such as *Treponema denticola* cystalysin, Dopa decarboxylase (DDC) and delta-Aminolevulinate Synthase (ALA Synthase) (54).

4.5 *In silico* analyses to explain the pathogenicity of the F152I-Mi and I244T-Mi variants

Studies performed on both purified proteins and cellular systems have suggested that some of the most common pathogenic mutations could reduce the stability of the dimeric structure of AGT leading to various effects (32). Based on the results reported above indicating that Arg118 is a hot-spot interfacial residue playing a relevant role in the dimerization of AGT-Mi, we wonder if some PH1-causing mutations could play their effects by directly or indirectly interfering with Arg118. Taking into consideration in the crystal structure of AGT an ideal sphere of 15 Å radius whose center is the C α of Arg118, we noticed the presence of several residues of the large domain whose mutation is associated with PH1. Among them, we focused our attention on Phe152 and Ile244, because the mutations F152I and I244T are two of the most common and studied. Molecular and cellular analyses have suggested that both the Phe152-to-Ile and the Ile244-to-Thr substitutions could synergize with the P11L polymorphism and destabilize the AGT dimer leading to a various effect including in particular the mitochondrial mistargeting of the protein. To analyze the effects of the F152I and I244T mutations on AGT-Mi we carried out MD simulations on the modeled structures of AGT-Mi, I244T-Mi and F152I-Mi in the dimeric form in collaboration with the group of Dr. Giorgetti of the Department of Biotechnology of the University of Verona. By visual inspection, we observed that the salt bridge formed by Arg118 and Asp243 was maintained for about 87.3% of the time in AGT-Mi, while it remained stable for only 17.5% of the time in the I244T-Mi

mutant. Thus, we hypothesized that the I244T mutation could have a direct influence on the formation of a key interface contact. Indeed, we observed that the breaking of the Arg118-Asp243 salt bridge coincided with the formation of a hydrogen bond between Thr244 and Asn92, which forced a backbone conformational change (Fig. 16).

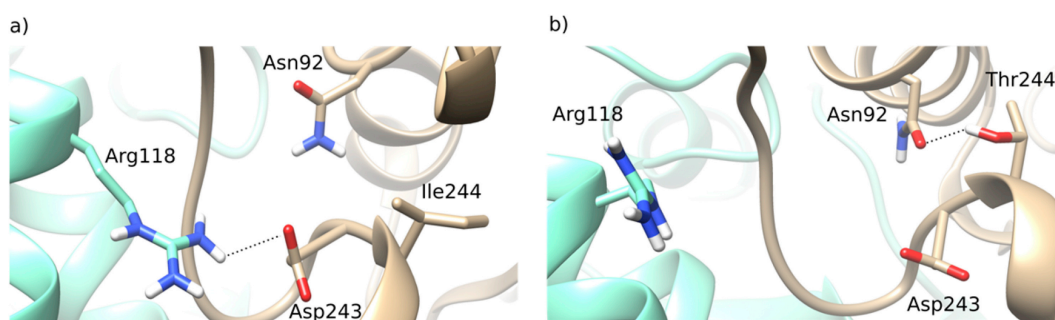


Fig. 16. Perturbation of the microenvironment of Arg118. Panel A: Arg118-Asp243 salt bridge, together without Asn92-Thr244 hydrogen bond interaction. Panel B: breaking of Arg118-Asp243 salt bridge, together with Asn92-Thr244 hydrogen bond interaction; the two monomeric subunits are displayed in aquamarine and brownish. Depicted hydrogen atoms were added within the setup of the simulations.

This was not possible in AGT-Mi because the isoleucine at position 244, which cannot form H-bonds with neighboring residues, guaranteed the stability of the Arg118-Asp243 salt-bridge. Conversely, we did not observe any significant difference between the interface contacts of dimeric AGT-Mi and F152I-Mi. Thus, we conducted MD simulations for 170 ns on the monomeric structure of both AGT-Mi and F152I-Mi. However, neither these analyses nor visual inspection revealed significant changes at the dimer interface regions between the two proteins. Thus, we decided to calculate the ED on the MD simulations. The ED technique allows not only to highlight the dominant motions of the system, which are often meaningful and correlated with protein function, but also to reduce the complexity of the data. Fluctuations analysis by ED revealed that the F152I mutation could influence the dynamics of several amino acid stretches of AGT-Mi, i.e., 95-97, 118-121, 141-145, 171-176 and 281-290, with peaks for residues 97, 118, 143, 175 and 281. These results suggest that the latter residues

have a different behavior in terms of flexibility in F152I-Mi as compared with AGT-Mi. In particular, one of the stretches exhibiting a different behavior in the mutated system was formed by residues 118-121, located at the dimerization interface (data not shown). On these bases, we can suggest that the F152I mutation could affect dimer formation by increasing the flexibility of the region 118-121, thus possibly reducing the complementarity between the two monomers.

4.6 Proposed folding and dimerization pathway of AGT-Mi and I244T-Mi and F152T-Mi variants

The aberrant targeting to mitochondria is a pathogenic mechanism leading to PH1 that deserves particular attention (46). The import into peroxisomes mainly acts on the fully-folded dimeric state of AGT (26), while that in mitochondria requires a monomeric state of the enzyme provided with a mitochondrial targeting sequence resulting from the P11L polymorphism. It follows that the dimerization and the correct subcellular localization of AGT are correlated events for this PLP-enzyme. It has been suggested that the combined effect of some mutations with P11L could result in a destabilization of the dimeric structure of AGT-Mi, thus allowing the population of monomeric folding intermediates that are compatible with the mitochondrial import. However, no structural explanations for these effects have been provided until now. In this study we engineered for the first time a mutant form of AGT stable in solution as apomonomer and holomonomer. We used this form to analyze how the quaternary structure influences the spectral features of the protein. Moreover, we demonstrated that the coenzyme PLP is able to bind monomeric AGT and promotes protein dimerization. This confirms previous hypothesis on the chaperone role of PLP for AGT (54). Moreover, the analysis of the AGT dimerization process as well as the MD experiments reported above can allow to understand how the F152I and I244T mutations can lead to folding defects as well as explain their functional synergism with the polymorphic mutation P11L.

A possible pathway of AGT folding has been already proposed (8) in which the

unfolded monomer is converted to a partly unfolded monomer, and then to a folded monomer which finally dimerizes (8). Based on the finding that AGT is endowed with a large core dimer interface and that a truncated form of the protein devoid of the first 21-N-terminal residues is able to dimerize (91), it can be advanced the proposal that dimerization could start by means of core dimer interfacial interaction and not by the N-terminal extension (Fig. 17, pathway 1).

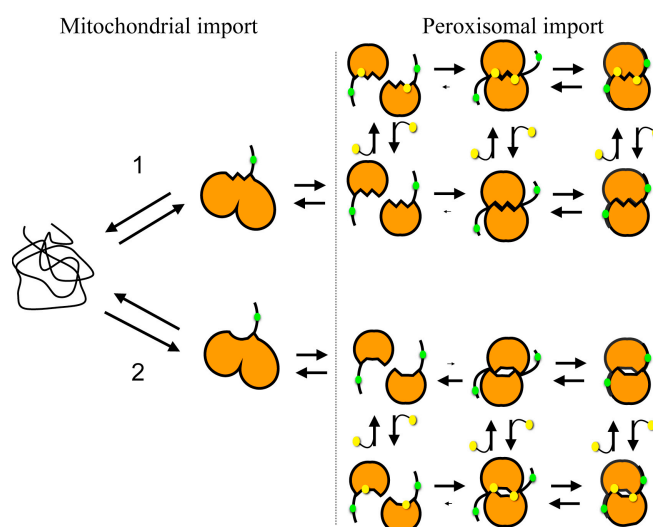


Fig 17. Proposed folding and dimerization pathway of AGT-Mi (1) and of the I244T-Mi and F152T-Mi variants (2). The green dots indicate the P11L polymorphism. The yellow dots represent the PLP coenzyme.

Following this view, the N-terminal extensions, containing the P11L polymorphism generating a putative MTS, should be exposed and flexible and not tightly bound to the surface of the neighboring subunit. Since MD simulations predict that the mutations I244T and F152I interfere with dimerization, the formation of the dimeric structure of the variants I244T-Mi and F152I-Mi should be greatly impaired, while the formation of the partly unfolded and unfolded monomeric forms should prevail. Thus, the partially unfolded monomers of the variants I244T-Mi and F152-Mi containing the P11L polymorphism, could be imported into mitochondria, possibly with a rate higher than that of their conversion to the corresponding folded monomers (Fig. 17, pathway 2). Nevertheless, here we have demonstrated that the dimerization of the

apomonomer of the triple mutant occurs with k_{ass} and k_{diss} remarkably lower than the corresponding ones of the PLP-bound monomer. These findings indicate that high levels of PLP could shift the equilibrium from the PLP-bound monomer of the variants F152I-Mi and I244T-Mi to the dimeric form, thus preventing their mislocalization. This could explain why the F152I-Mi or I244T-Mi variants have been found to be responsive to pyridoxine administration, a therapeutic strategy that increases the intracellular level of PLP (37).

CONCLUSIONS

In this work, by combining *in silico* analyses with biochemical studies on purified proteins, we were able to: (i) identify the interfacial residues, Arg118, Phe238, and Phe240, which are not essential for catalytic activity of AGT-Mi but have a relevant impact on its dimerization process, (ii) engineer and characterize a folded apomonomer and holomonomer, both able to dimerize (iii) demonstrate that dimerization is critical for catalytic activity, and (iv) outline the possible structural basis of the functional synergism between the mutations I244T or F152I and the mutation P11L responsible for the aberrant targeting to mitochondria of the variants I244T-Mi and F152I-Mi associated with PH1. These results are significant not only for the AGT folding and dimerization processes as well as for the effect of mutations interfering with dimer stability, but they can also provide useful insights to understand the behavior of other PLP enzymes for which the coenzyme can play a similar role.

5

**MOLECULAR AND CELLULAR EFFECTS OF
PATHOGENIC INTERFACIAL MUTATIONS IN
ALANINE:GLYOXYLATE AMINOTRANSFERASE
AND RESPONSE TO VITAMIN B6
ADMINISTRATION**

Background information

Dimerization is considered a crucial event for AGT, because it is supposed to influence the overall stability of the protein and its intracellular fate, including in particular the correct peroxisomal localization (32). The binding of the PLP coenzyme favors the attainment of the dimeric structure, as previously claimed by various authors (9, 37, 45, 54, 55) and demonstrated in the previous chapter of this thesis. This would imply that PH1 patients bearing missense mutations that cause a destabilization of the AGT dimeric structure could be responsive to Vitamin B6 administration. Clinical data have demonstrated that this is true for two of the most common mutations, the G170R and the F512I associated with the minor allele (43). Both amino acid substitutions interfere with AGT dimerization leading to the increase of population of monomeric folding intermediates that undergo aggregation and/or intracellular degradation and/or mitochondrial mistargeting (32).

Among the 79 missense mutations known to be associated with PH1, 26 involve residues directly located at the monomer-monomer interface. The effects of many of them have not been analyzed in detail, as well as their possible response to Vitamin B6. On these bases, we carried out an *in silico* analysis to rank the interface destabilization caused by each amino acid substitution. Then, we analyzed the molecular and cellular effects of a selected group of mutations and we tried to correlate the defect of each variant with the *in vitro* responsiveness to PN administration. We limited the study to missense mutations associated with the major allele because the polymorphic P11L mutation typical of the minor allele (i) is known to influence AGT dimerization and can functionally synergize with pathogenic interfacial mutations (32, 92), and (ii) generates a putative targeting sequence for mitochondria (37), thus possibly making more difficult the interpretation of the results obtained in the cellular system.

RESULTS

5.1 Computational screening of the effects of pathogenic amino acid substitutions on AGT-Ma dimerization

We applied a rigid body docking-based screening to predict the effects of AGT pathogenic mutations involving residues located at the dimerization interface on the monomer-monomer binding affinity (8). The method was applied to 12 dimeric variants prepared *in silico*, corresponding to mutations associated with either the major allele or an unknown locus. The results of docking simulations of AGT-Ma and pathogenic variants are reported in Table 5 and show that on average 11 native-like solutions out of 12,000 total solutions from the three independent sets of docking runs were found. Moreover, in all cases, the native-like conformations are comprised within the first ten solutions of each run. This guarantees the efficacy of the method. The final output of the analysis is the ZD score of each single run. The arithmetic mean between the three ZD score gives the ZD average (ZD_{avr}) from which we obtained the predicted $\Delta\Delta G^\circ$ ($\Delta\Delta G^\circ_{pred}$) (“Materials and Methods”, section 3.2.3), that represents the difference in the predicted ΔG° of dimerization between each variant and AGT-Ma, thus providing a possible quantification of the stabilizing or destabilizing effect of each amino acid substitution on the monomer-monomer interaction.

Besides the L25R variant, for which no significant difference in dimer stability was predicted as compared with AGT-Ma, and the S275R-Ma, predicted to have an increased stability of the dimeric structure (Table 5), all the other variants show a negative value of $\Delta\Delta G^\circ_{pred}$, indicating a probable destabilization of the dimeric structure, though to a different extent.

Predictions generated by docking-based simulations were then combined with information derived from the inspection of the AGT structure and from previous knowledge of the structural properties of the protein. Three of the mutations (D243H, R111Q, R233L) involve residues that directly or indirectly interact with dimerization hot-spots already identified in previous studies (this thesis). Asp243 and Arg118 form a ionic bridge that is the only one present on the dimerization

interface, thus explaining the significant destabilization of the dimeric structure predicted by docking analyses ($\Delta\Delta G^{\circ}_{\text{pred}} = -2.30$ kcal/mol) (Table 5). Arg111 interacts with the main chain of the residues His261 and Tyr260. Its replacement by a glutamine residue could destabilize the orientation of His261 that forms a hydrogen bond with the main chain of Phe240, an important dimerization hotspot already described (this thesis). Finally, the replacement of Arg233 with a leucine residue interrupts the hydrogen bond between Arg233 and the main chain of Lys236 and destabilizes the orientation of the loop composed by residues Phe238, Phe240 and Asp243 involved in the formation of an interface hotspot.

Table 5. Results of docking simulations for AGT-Ma and pathogenic variants.

Enzyme	Allele	#native-like solutions	ZD _{avg}	ZD _(mut) - ZD _(AGT-Ma)	$\Delta\Delta G^{\circ}_{\text{pred}}$ (kcal/mol)
AGT	Ma	12	195.6 ± 7.0	/	/
L25R	Unknown	11	195.3 ± 6.4	-0.3	-0.11
R36H	Ma	10	191.8 ± 5.7	-3.8	-1.48
G42E	Ma	12	192.2 ± 6.3	-3.4	-1.32
I56N	Ma	9	193.3 ± 5.5	-2.3	-0.89
G63R	Ma	9	186.6 ± 6.5	-9.0	-3.51
R111Q	Unknown	11	192.6 ± 6.2	-3.0	-1.17
G216R	Ma	10	170.9 ± 6.2	-24.7	-9.62
R233L	Unknown	12	192.3 ± 6.4	-3.3	-1.28
D243H	Unknown	12	189.7 ± 6.2	-5.9	-2.30
H261Q	Unknown	13	191.8 ± 6.7	-3.9	-1.52
S275R	Ma	10	204.6 ± 6.6	+9.0	+3.51

Based on the above considerations, in the present study we focused our attention on the mutations R36H, G42E, I56N, G63R and G216R (Fig. 18) because they are all supposed to have a destabilizing effect on the dimeric structure (Table 5) although involve residues far from the AGT interface hot-spots. Within the pool of selected mutants, it is of note the predicted destabilization of the dimeric structure induced by the mutations G63R and G216R, leads to a decrease in affinity of 3.5 and 9.6 kcal/mol respectively (Table 5), thus suggesting an important role of these residues in the stability of the dimeric structure.

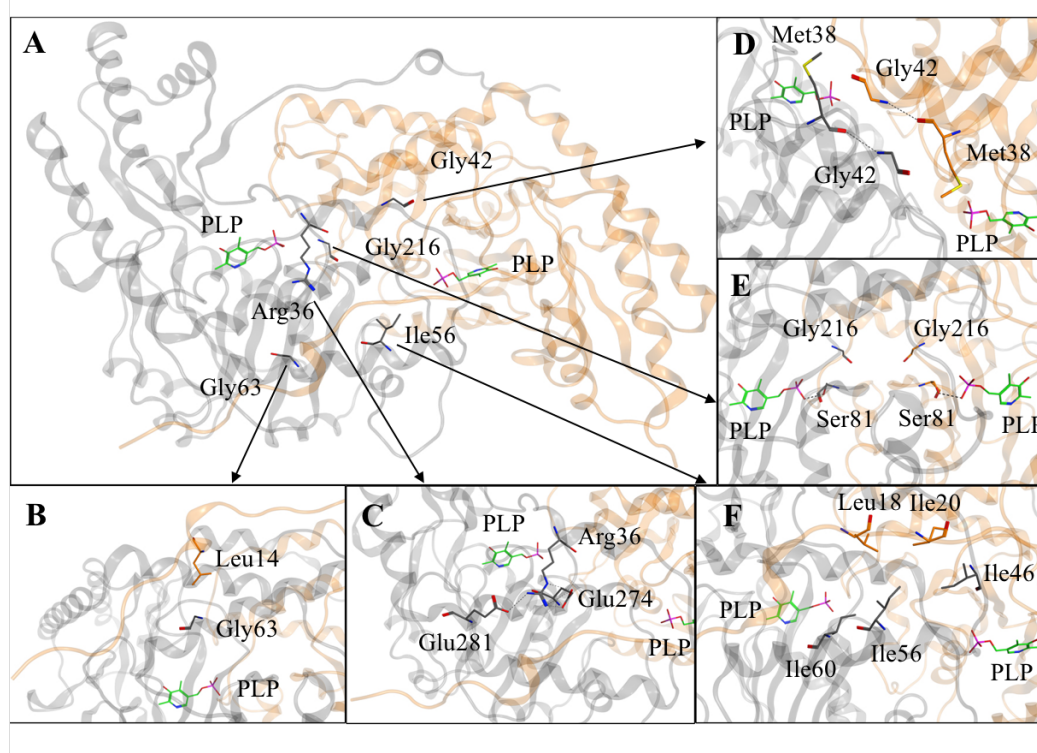


Fig. 18. Tridimensional representation of the mutation sites. Ribbons representation of the crystal structure of human AGT (PDB :1H0C). Monomers are colored grey and orange. PLP is colored green. A) Overall dimeric structure of holoAGT with all the mutation sites, represented as grey sticks. B, C, D, E and F) Residues subjected to pathogenic mutations (grey or orange sticks) and their main contact residues belonging to both subunits, colored as the belonging monomer.

As reported in Fig. 18, all the mutation sites are located in the large domain of AGT. Arg36, Gly42, Ile56 and Gly63 interact with residues located at the N-terminal domain of the adjacent subunit while Gly216 is located in the proximity of the active site and it interacts with Gly216 of the other subunit and Ser81, an important residue involved in the binding of the PLP phosphate group (chapter 1.2 of this thesis).

5.2 Intracellular behavior of the R36H, G42E, I56N, G63R and G216R variants

We introduced the R36H, G42E, I56N, G63R and G216R mutations in the AGT cDNA cloned in a pcDNA 3.1 vector suitable for the expression in mammalian cells. Then, we transfected Chinese Hamster Ovary (CHO) cells expressing glycolate oxidase (GO) (CHO-GO), a well-recognized disease model for PH1 (32, 55), with the resulting constructs. We selected cells stably expressing each species and we adapted them for growing in a custom-made medium containing a Vitamin B6 concentration mimicking that present under physiological conditions (low B6) (“Material and Methods”, section 3.15). Thereafter, we compared the AGT expression level and specific activity of the cells before and after treatment with 10 μ M PN, a condition mimicking that of treated patients (52).

The results shown in Fig. 19 panels A and B indicate that all the mutations caused a structural defect in AGT.

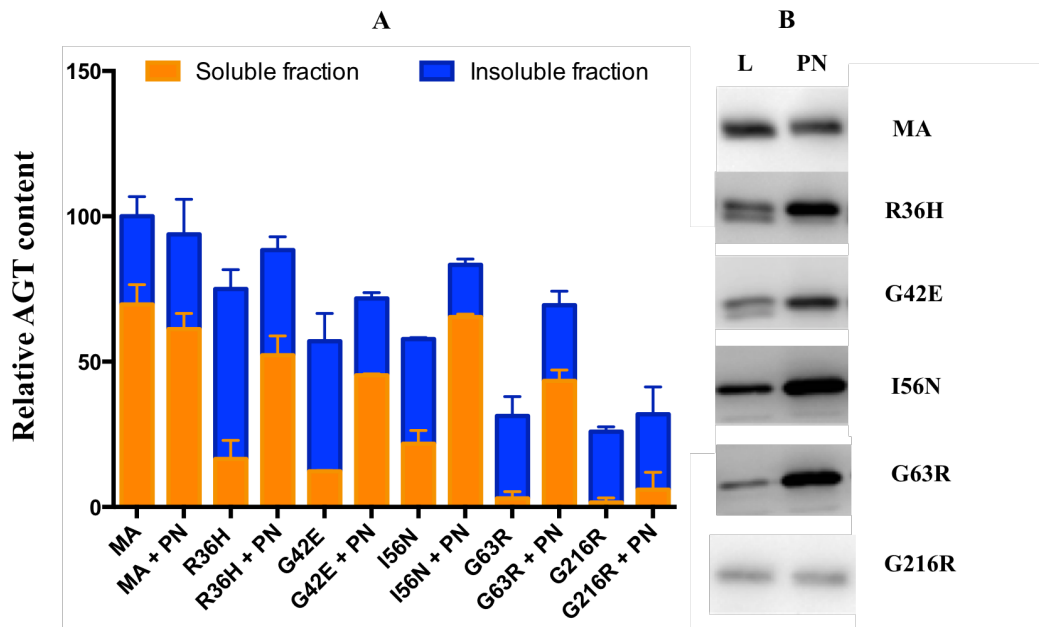


Fig. 19. Effect of PN on the expression level of AGT-Ma and variants. CHO-GO cells expressing the indicated enzymatic species were grown in the presence or absence of 10 μ M PN.

Cells were harvested and lysed, 2 μ g of soluble lysate were subjected to SDS-PAGE, immunoblotted with anti-AGT from rabbit (1:6000) and detected by chemiluminescence. Bar graphs represent the mean + SEM. Panel A: histograms representative of the immunoblot band

volume. The color code is the following: soluble fraction colored orange while the insoluble fraction colored in blue. Panel B: immunoblot of the soluble fraction; lanes are coded as follows: cells grown in low-B6 (L) and cells grown in presence of 10 μ M PN (PN).

In fact, as compared with AGT-Ma, the amount of soluble protein was 24, 21, 39, 9, and 11%, for R36H, G42E, I56N, G63R and G216R, respectively. Conversely, the relative amount of protein present in the insoluble fraction increased of 30% for AGT-Ma to 76, 79, 61, 91, and 89% of R36H, G42E, I56N, G63R and G216R, respectively, thus possibly suggesting an increased aggregation propensity. We also observed that R36H and G42E variants were prone to proteolytic degradation, as shown by the presence of a faster migrating band in western-blot (Fig. 19, panel B), thus indicating that the two mutations could increase the flexibility of exposed regions of the protein that become susceptible to the cleavage by proteases (31). As compared with wild-type AGT, the specific activity of R36H, G42E, I56N and G63R was 10, 12, 9 and 3%, respectively. No transaminase activity was detected for the G216R variant, even at high protein concentration and incubation time, thus suggesting that the Gly216-to-Arg substitution could also alter the AGT functional properties. The presence of PN in the culture medium did not change the levels of AGT-Ma in the soluble fraction, but increased by 3.2-, 3.7-, 4.8-, 13.2- and 1.4-fold that of R36H, G42E, I56N, G63R and G216R, respectively. This effect was also accompanied by a reduction of the relative amount of protein present in the insoluble fraction. Notably, no significant changes in the expression level of G216R were observed, even after treatment of the cells with PN at millimolar concentrations, taking into account the high value of $K_{D(PLP)}$ of the variant (see below). PN treatment also counteracted the proteolytic cleavage of the R36H and G42E variants, as indicated by the presence of a single band in western-blot. The specific activity of AGT-Ma decreased by 75% in the presence of PN, in agreement with previous reports (55), due to the intracellular accumulation of PNP that competes with PLP and generates an inactive AGT-PNP complex. On the other hand, PN treatment increased the specific activity of R36H, G42E, I56N and G63R by 1.7-, 2.5-, 2.5-, and 2.6-fold, respectively (Fig. 20).

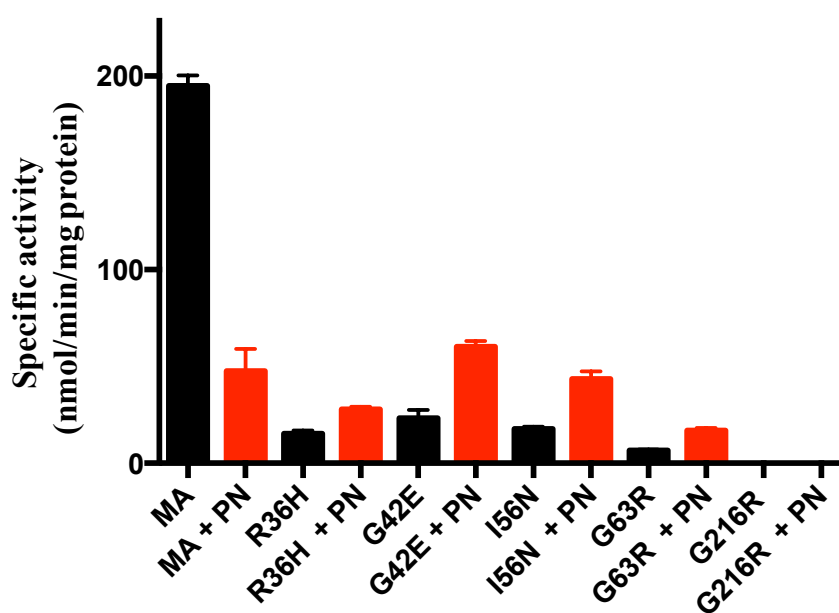


Fig. 20. Effect of PN on the specific activity of AGT-Ma and variants. CHO-GO cells expressing the indicated AGT species were grown in the absence or presence of 10 μ M PN. The AGT transaminase activity was detected by incubating the soluble lysate with 0.5 M L-alanine, 10 mM glyoxylate and 200 μ M PLP at 25°C in 100 mM KP buffer, pH 7.4. Bars are colored as follows: cells grown in low-B6 in black and cells grown with 10 μ M PN in red.

We also investigated the influence of the pathogenic interfacial mutations under study on the subcellular localization of AGT. In the absence of PN added to the culture medium, all the variants displayed a peroxisomal localization, as shown by the colocalization between the signal of AGT and that of the peroxisomal marker (Fig. 21).

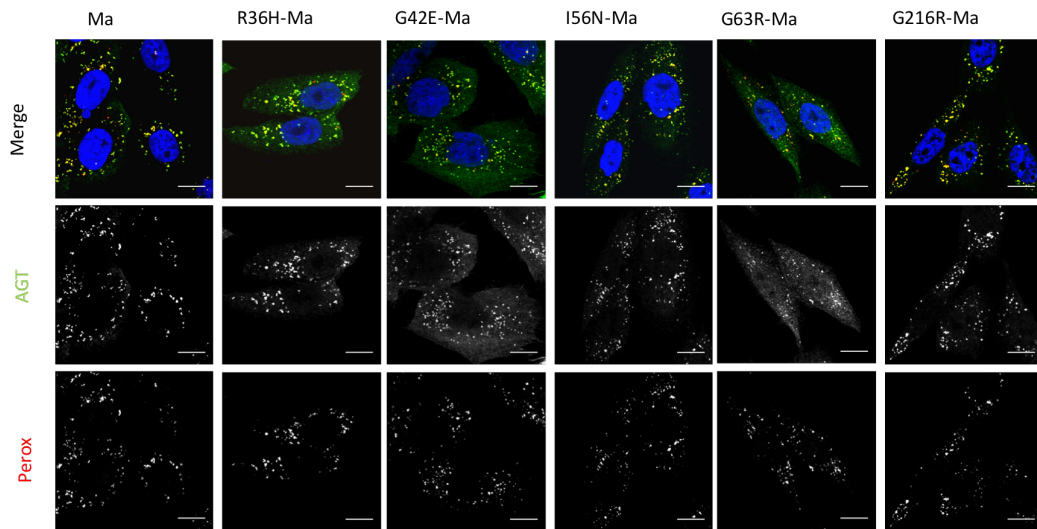


Fig. 21. Subcellular localization of AGT-Ma and pathogenic variants grown in low-B6 medium. CHO-GO cells expressing each species were fixed and colored as follows: anti-AGT (red) and anti-peroxisomal GO (green). Nuclei were stained with Dapi (blue). Merge and single-channel images come from a single z-plane. Scale bar: 10 μ m.

The partial cytosolic localization of R36H, G42E and G63R suggested that their structural alteration could somehow influence the peroxisomal import of the protein. The treatment with PN redirected all the variants to peroxisomes, as shown by the complete correspondence between the pattern of AGT and that of the peroxisomal marker (Fig. 22).

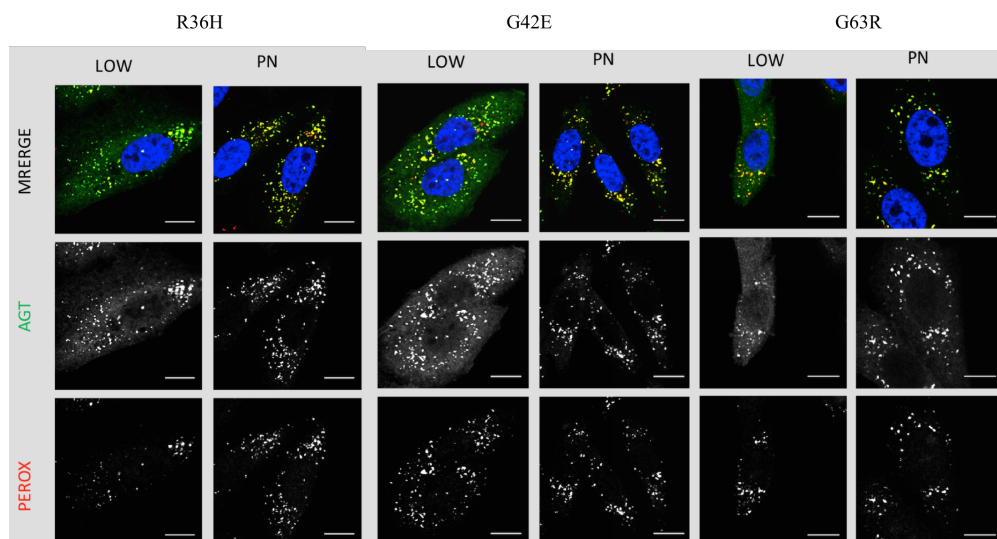


Fig. 22. Subcellular localization of the pathogenic variants R36H, G42E and G63R upon treatment with 10 μ M PN. CHO-GO cells expressing the pathogenic variants were fixed and colored as follows: anti-AGT (red) and anti-peroxisomal GO (green). Nuclei were stained with Dapi (blue). Merge and single-channel images come from a single z-plane. Scale bar: 10 μ m.

All together, these data lead to conclude that (i) all the analyzed mutations should cause a structural defect, which probably increases the aggregation propensity of AGT in the cell and, in some cases, makes the protein more susceptible to proteolytic degradation and/or affects its peroxisomal import; (ii) PN treatment is able to partly rescue for the effects of interfacial mutations, although to a different extent.

5.3 Characterization of the R36H, G42E, I56N, G63R and G216R variants in the purified form

In order to define how each interfacial mutation affects the biochemical properties of AGT, the R36H, G42E, I56N, G63R and G216R variants were expressed in *E. coli*, purified and characterized. SDS-PAGE analyses revealed that the proteins were homogeneous as indicated by a single band with a mobility identical to that of AGT-Ma. The far-UV dichroic spectrum of each variant was identical to that of AGT-Ma indicating no gross structural alterations of the secondary structure of the protein. Therefore, we investigated how each mutation affects (i) the functional properties of AGT, including the PLP binding mode and affinity as well as the kinetic parameters for the overall transamination reaction, and (ii) the structural properties of the protein in the holo- and apo-form, including the tertiary and quaternary structure, the aggregation propensity and the susceptibility to proteolytic cleavage.

5.3.1 Functional properties of the R36H, G42E, I56N, G63R and G216R variants

The values of the equilibrium dissociation constant for PLP ($K_{D(PLP)}$) of each species show a slightly altered of the PLP binding affinity, the only exception being the G216R-Ma that displays a $K_{D(PLP)}$ value ≈ 400 -fold higher than that of AGT-Ma.

Table 6. Equilibrium dissociation constants for PLP ($K_{D(PLP)}$) and optical activity of AGT-Ma and variants.

Enzymatic species	$K_{D(PLP)}$ (μM)	Optical activity
AGT-Ma	0.27 ± 0.03^a	97 mdeg/Abs 420 nm ^b
R36H	0.36 ± 0.04	95 mdeg/Abs 417 nm
G42E	0.40 ± 0.04	104 mdeg/Abs 424 nm
I56N	0.74 ± 0.10	102 mdeg/Abs 422 nm
G63R	0.85 ± 0.13	93 mdeg/Abs 422 nm
G216R	110 ± 14	n.d.

n.d., not determined

^aFrom reference (10)

^bFrom reference (33)

Coenzyme binding to AGT gives typical absorbance bands at 430 and 340 nm associated with a positive and negative dichroic signal, respectively, at the same wavelength (10). We calculated the optical activity from the UV-visible absorbance and CD spectra of the R36H, G42E, I56N, G63R variants at 10 μM concentration in the presence of saturating PLP (Table 6). We did not notice significant changes of the coenzyme binding mode. The high value of $K_{D(PLP)}$ of the G216R variant did not allow to register the absorbance and CD spectrum at saturating PLP concentration.

The steady-state kinetic parameters for the overall transamination of the alanine-glyoxylate pair of the variants are reported in Table 7. The R36H, G42E, I56N, G63R variants do not show a strong alteration of catalytic efficiency value. However, we noticed an approximately 70% reduction of the k_{cat} value for the R36H. Moreover, the k_{cat}/K_m value of G216R obtained in presence of saturating

PLP was decreased by ~254-fold with respect to AGT-Ma, mainly driven by the decrease in the k_{cat} value.

Therefore, the G216R is the only interfacial mutation causing a significant functional defect in AGT among those analyzed, while the other variants should mainly display a structural defect.

Table 7. Steady-state kinetic parameters of AGT-Ma and the pathogenic variants for the overall transamination reaction.

Enzyme	Substrate	Cosubstrate	k_{cat} (s^{-1})	K_{m} L-Alanine (mM)	K_{m} Glyoxylate (mM)	$k_{\text{cat}}/K_{\text{m}}$ ($\text{s}^{-1}\text{mM}^{-1}$)
AGT-Ma	L-Alanine Glyoxylate	Glyoxylate L-Alanine	^a 45 ± 2 ^a 45 ± 3	^a 31 ± 4	^a 0.23 ± 0.05	^a 1.40 ± 0.20 ^a 196 ± 44
R36H	L-Alanine Glyoxylate	Glyoxylate L-Alanine	12 ± 1 13 ± 1	20 ± 3	0.23 ± 0.03	0.41 ± 0.06 56 ± 5
G42E	L-Alanine Glyoxylate	Glyoxylate L-Alanine	40 ± 1 42 ± 2	86 ± 6	0.48 ± 0.08	0.46 ± 0.04 89 ± 15
I56N	L-Alanine Glyoxylate	Glyoxylate L-Alanine	30 ± 1 29 ± 1	59 ± 3	0.37 ± 0.01	0.50 ± 0.04 78 ± 8
G63R	L-Alanine Glyoxylate	Glyoxylate L-Alanine	28 ± 1 32 ± 2	36 ± 3	0.50 ± 0.10	0.77 ± 0.07 64 ± 13
G216R	L-Alanine Glyoxylate	Glyoxylate L-Alanine	0.160 ± 0.007 0.171 ± 0.003	60 ± 10	0.22 ± 0.03	0.0026 ± 0.0004 0.77 ± 0.15

^aFrom reference (10)

5.3.2 Structural properties of the R36H, G42E, I56N, G63R and G216R variants in the purified form

-Tertiary structure. The near-UV CD and ANS emission fluorescence spectra shown in Fig. 23 panels A and C, indicate that the variants in the holo-form do not show significant variations as compared with holoAGT-Ma. We observed a small increase of the ANS fluorescence only for the holoR36H and holoG63R. In contrast, all variants in the apo-form we show a remarkable reduction of the dichroic signal at 280 nm in comparison with AGT-Ma, although to a different extent (Figure 23, Panel B) In addition, the ANS emission fluorescence spectra of the apo variants (Figure 23, Panel D) revealed an enhanced emission intensity (from 3.5- to 15-fold) and a blue shift of the emission maximum (from 10 to 18 nm). These data indicate that all the mutations cause structural changes mainly on the apo-form of AGT, consisting in a different microenvironment of aromatic residues as well as in an increased exposure of hydrophobic surfaces. Notably, the alterations of the tertiary structure seem to be especially marked for the apo variants R36H, G63R and G216R.

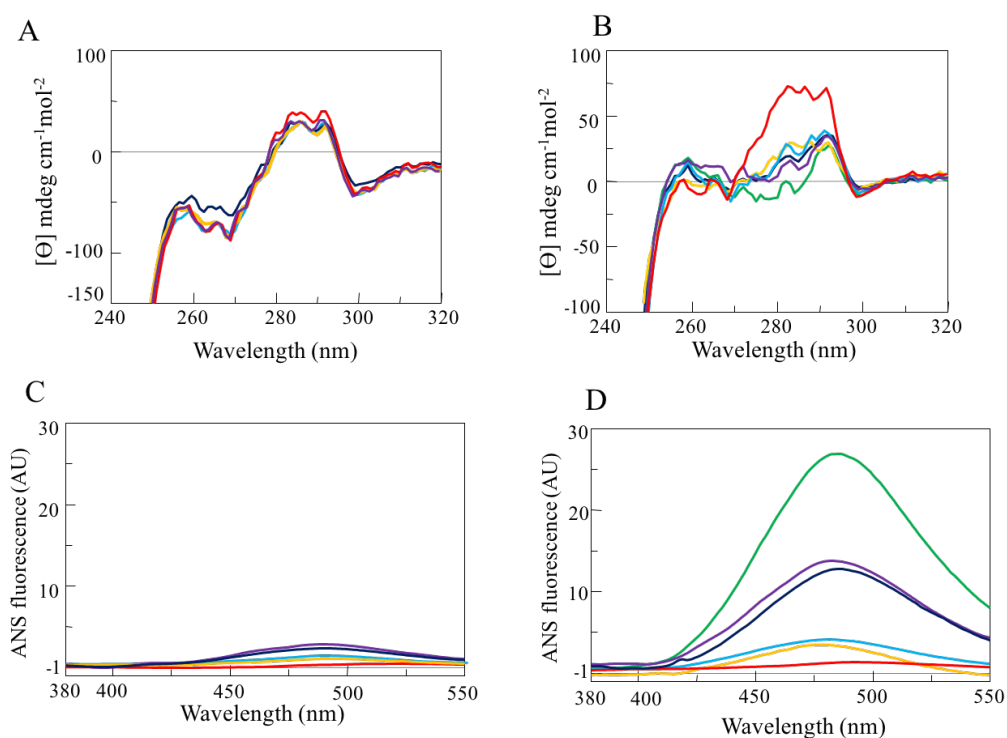


Fig. 23. Circular dichroism and ANS emission fluorescence spectra of the variants in the holo- and apo-form. Panels A and B: near-UV CD spectra of the variants in the holo- (A) and apo-form (B). Panels C and D: ANS emission fluorescence spectra (λ_{exc} 365 nm) of the variants in the holo- (C) and apo-form (D). For each panel, the spectrum of AGT-Ma is shown for comparison. The color code is: red, AGT-Ma; yellow, I56N; cyan, G42E; blue, R36H; purple G63R; green, apoG216R. Protein concentration was 10 μ M for the CD-spectra while for the ANS-binding experiments was 1 μ M in KP buffer 0.1 M, pH 7.4.

-Quaternary structure. All the mutations under study involve residues located at the monomer-monomer interface and, as predicted by the rigid-body docking simulations reported above (paragraph 5.1), they should destabilize the dimeric structure of AGT. We investigated the impact of each mutation on the quaternary structure of both apo and holoAGT by SEC. The results obtained are reported in Table 8. The holo- and apo-form of AGT-Ma as well as the holo-forms of the R36H, G42E, I56N, and G63R variants eluted as a single peak with a retention volume corresponding to a dimer from 5 to 0.3 μ M concentration (the latter value being the detection limit). On the other hand, holoG216R and all the variants in the apo-form, except G42E, displayed a destabilized dimeric structure. ApoR36H, apoI56N, apoG216R and holoG216R exhibited an elution profile consisting in two peaks whose elution volume correspond to a dimer and a monomer. The proportion of the dimer decreased while that of the monomer increased as the

enzyme concentration was lowered from 15 to 0.3 μM , thus indicating a slow equilibrium process. In the same concentration range, apoG63R eluted as a single peak whose position varied between the dimeric and monomeric forms of the protein, thus indicating a rapid equilibrium process. From the % of dimer at each enzyme concentration we calculated the $K_{d(\text{dim-mon})}$ value of each species (Table 8).

Table 8. $K_{d(\text{dim-mon})}$ of AGT-Ma and the pathogenic variants.

Enzymatic species	$K_{d(\text{dim-mon})}$ (μM)	
	Apo-form	Holo-form
AGT-Ma	< 0.3	< 0.3
R36H	1.4 ± 0.2	< 0.3
G42E	< 0.3	< 0.3
I56N	1.2 ± 0.3	< 0.3
G63R	1.6 ± 0.3	< 0.3
G216R	4.8 ± 0.5	0.9 ± 0.2

Taken together, these data clearly indicate that the R36H, I56N, G63R and G216R mutations destabilize the dimeric structure of AGT. The effect is mainly related to the apo-form of the protein, except for the G216R variant, for which we observed a strong impact on both the holo- and the apo-form. This is in line with spectroscopic data indicating a structural effect of the mutations mainly on the apo-form of the protein, and further confirms the stabilizing effect of PLP on the AGT quaternary structure demonstrated by the study of the dimerization process (chapter 4.4 of this thesis). At present, it is not possible to establish if the G42E mutation affects the quaternary structure of AGT, since the $K_{d(\text{dim-mon})}$ values of the variant are below the detection limit of the technique, as already observed for AGT-Ma.

With the aim of defining if there was any correlation between the results obtained in solution and those obtained by docking simulations, we performed a combined analysis of the $\Delta\Delta G_{\text{pred}}^{\circ}$ values predicted *in silico* and the $K_{d(\text{dim-mon})}$ determined *in vitro* for the variants under study (Fig. 24). We noticed a striking linear correlation ($R^2 = 0.98$), which suggests interesting implications related to the AGT

folding/dimerization mechanism. Indeed, the general assumption underlying rigid-body protein-protein docking is that neither the target, nor the ligand protein undergo major conformational changes upon binding. As shown previously (61), under these circumstances, a rigid-body docking algorithm (that describes with sufficient accuracy all the energetic terms virtually making up the Gibbs free energy, except those related to conformational and entropy changes) may be used to predict the effect of point mutations on the binding affinity, provided that an exhaustive sampling of the roto-translational space of the ligand with respect to the target is performed (60). Therefore, the strong correlation observed for the AGT variants simulated in the present study (Fig. 24) suggests that dimerization could occur in a rigid body-like fashion, i.e. without involvement of major conformational changes in each of the monomers, and that the monomer folding and dimerization processes might constitute two separate steps in the AGT folding pathway.

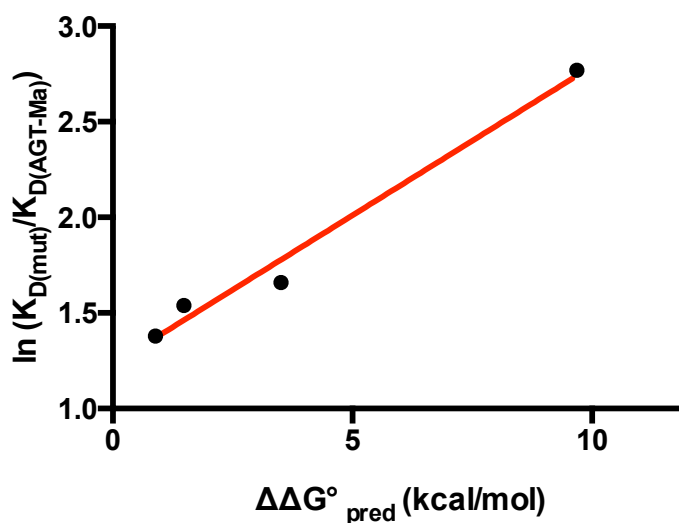


Fig. 24. Plot of the relative affinities predicted by docking simulations ($\Delta\Delta G^{\circ}_{\text{pred}}$) versus the $\ln(K_{d(\text{mut})}/K_{d(\text{AGT-Ma})})$ obtained *in vitro* for the AGT pathogenic variants. The linear fitting of the data is shown. R^2 is equal to 0.98.

-Aggregation propensity. One of the effects caused by the R36H, G42E, I56N, G63R and G216R interfacial mutations at cellular level is the increased amount of AGT found in the insoluble fraction of the lysate, which suggests an increased aggregation propensity of the variants. Therefore, we analyzed the aggregative

behavior of each variant under physiological conditions (37°C, pH 7.4 at $I = 150$ mM). Fig. 25 shows the change in the total count rate in DLS (a parameter that depends on the size of the particles in solution) as a function of time for the apo and holo variants. In the case of G216R, only the apo-form is shown, due to the high $K_{D(PLP)}$ value. In agreement with previous evidences (31), no changes of the count rate were observed for apo and holoAGT-Ma. The holo-forms of the R36H, G42E and I56N variants showed a very low increase in count rate, while holoG63R underwent a significant aggregation process, with count rate leveling off after approximately 30 min. Notably, all variants in the apo-form were highly prone to aggregation, with count rate levelling off after 15-70 minutes depending on the species. On the basis of the aggregation rate and extent, the apovariants can be ranked in the order: G63R>G216R>I56N>R36H>G42E. The aggregation extent of the apovariants increased as the protein concentration increased (from 5 to 25 μ M) and decreased as the ionic strength increased (from 0.1 to 1 M), thus suggesting that the aggregating species is probably a dimer and that aggregation is mediated by electrostatic forces. Based on previous results obtained on AGT variants bearing mutations at Gly41 (31) as well as on those reported in chapter 6 of this thesis, it can be speculated that the conformational change induced by each interfacial mutation could alter the electrostatic potential of the AGT surface, thus enhancing the intrinsic propensity of the protein to electrostatic aggregation. The finding that holoenzymes are less susceptible to aggregation with respect to apoenzymes suggests that bound PLP is able to prevent or limit the conformational change caused by the mutations and shifts the equilibrium from the apo- to the more stable holo-form. This can contribute to explain why PN administration to cells expressing the variants increases the amount of protein in the soluble fraction of the lysate.

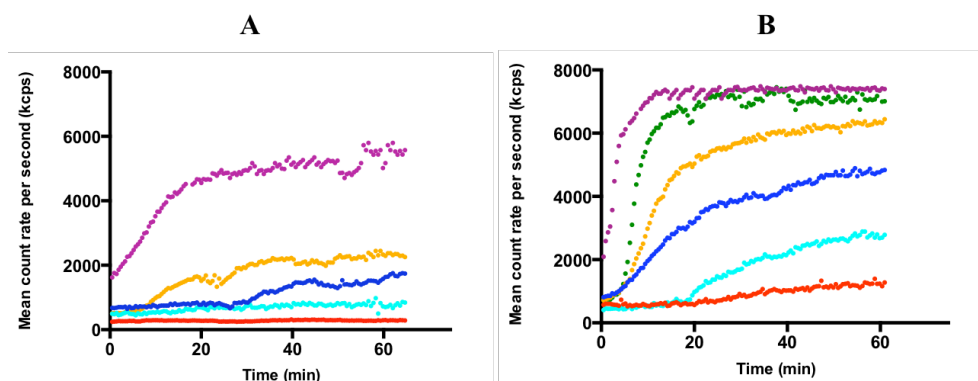


Fig. 25. Time-dependence of the total count rate (measured as kilo counts per second) of AGT-Ma and variants in the holo- (A) and apo-form (B). Measurements were performed at 10 μ M enzyme concentration at 37°C, pH 7.4 and $I = 150$ mM. The color code is the following for both apo and holoenzymes: red, AGT-Ma; yellow, I56N; blue, R36H; cyan, G42E; purple, G63R; green, apoG216R.

-Susceptibility to proteolytic cleavage- Based on the data obtained in CHO-GO cells indicating that the pathogenic variants R36H and G42E were prone to proteolytic degradation, we analyzed the behavior of the two variants by limited proteolysis experiments. AGT-Ma and the pathogenic variants in the apo- and holo-form were incubated with proteinase K at an AGT/protease weight ratio of 50/1 and subjected to SDS-PAGE analysis, as described in the “Materials and Methods” section 3.14. No proteolytic events were detectable for the apo- and holo-forms of AGT-Ma up to 2 hours as well as for the R36H and G42E variants in the holo-form. On the other hand, apoR36H and apoG42E underwent a very fast cleavage, as shown by the progressive disappearance of the band corresponding to the intact monomer and the concomitant appearance of a faster migrating band at ≈ 40 kDa. By determining the percentage of dimer as a function of time, we calculated a cleavage rate of $0.10 \pm 0.02 \text{ min}^{-1}$ and $0.07 \pm 0.01 \text{ min}^{-1}$ for the R36H and G42E, respectively (Fig. 26). Moreover, western blot analyses of the proteolysis mixture revealed that the cleaved protein is not detectable by an antibody specific for the AGT N-terminus.

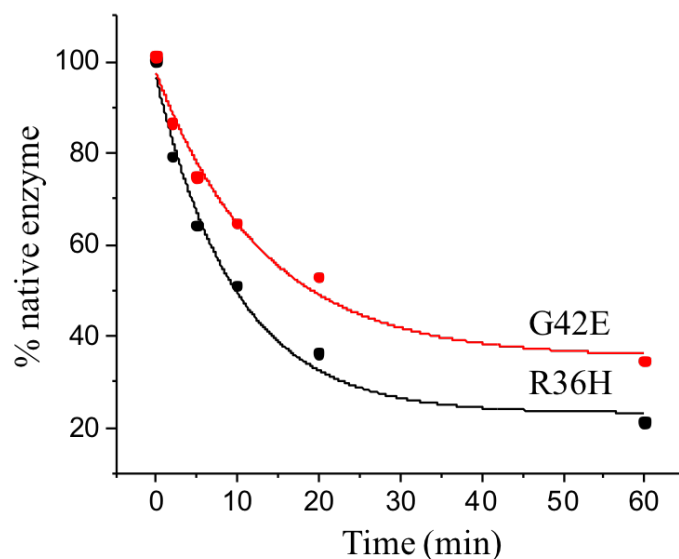


Fig. 26. Proteolytic cleavage of the apoR36H and apoG42E variants. Kinetics of proteolysis of apoR36H and apoG42E at 10 μ M incubated at 25 $^{\circ}$ C in 100 mM KP, pH 7.4, at a 500:1 (w/w) mutant:proteinase K ratio. At the times indicated, aliquots were removed, treated with 2 mM PMSF and subjected to 12% SDS-PAGE. The band intensities were analyzed using the ImageJ software (Rasband, WS). The rate of proteolysis was determined by plotting the percentage of native apoR36H (black dots) and apoG42E (red dots) vs time and by fitting the data to a first-order equation.

This indicates that, as already reported for other AGT pathogenic variants (92), the cleavage occurs within the N-terminal domain, which probably becomes more flexible and/or exposed to the solvent as a consequence of the mutations. These data well agree with the partial proteolytic degradation of the variants observed in the cellular system. Moreover, the fact that only the apo-forms are susceptible to proteolysis explains why no cleavage occurs in the cell upon PN administration when the equilibrium is shifted toward the holoenzymes (32).

DISCUSSION

One of the open questions related to inherited disorders caused by enzymatic deficits is the relationship between the genotype of the patients and the metabolic phenotype, including in particular the responsiveness to the available treatments. This is particularly true for genetically heterogeneous diseases, such as phenylketonuria, where hundreds of disease-causing mutations are known, but the effects of many of them have not been extensively clarified (93). In the case of PH1, the genetic heterogeneity is compounded by the high frequency of missense mutations and by the variety of different mechanisms by which they can lead to the deficit of AGT (32). In fact, while null mutations are expected to completely abolish the enzyme expression and activity, the cellular and molecular consequences of single amino acid substitutions are not directly evident. Furthermore, although the solved crystal structure of holo-AGT has greatly supported the interpretation of *in vitro* results, it is becoming clear that many pathogenic mutations mainly affect the apo-form of the protein, whose structural features are probably different with respect to those of holoAGT, as suggested by spectroscopic data (35). It follows that the establishment of solid genotype/phenotype correlations should pass through the analysis of the consequences of each mutation at protein and cell level. Nevertheless, the administration of Vitamin B6 in form of PN is the only pharmacological approach currently available for PH1. Patients bearing the common mutations G170R and F152I on the minor allele are generally responsive, but no clear evidences have been provided for the other mutations. Since various studies support a role of PLP in the stabilization of the AGT dimeric structure (26, 37, 54), and considering the predicted importance of dimerization for the correct folding and localization of the protein (9, 92), we focused our attention on AGT variants bearing mutations involving residues located at the monomer-monomer interface. The main aims of our study were (i) to unravel the molecular and cellular defect(s) of each variant, and (ii) to look for possible correlations between the biochemical features of the variants and their degree of responsiveness to PN administration *in vitro*.

-Molecular and cellular effects of pathogenic interfacial mutations in AGT. Based on a preliminary *in silico* simulation of the possible interfacial destabilization caused by known pathogenic mutations involving interfacial residues, we decided to analyze in detail the molecular and cellular effects of the mutations R36H, G42E, I56N, G63R and G216R, all associated with the major allele. We found that they do not merely interfere with the dimerization process, but also affect the structural and/or functional properties of the protein. A global analysis of the results obtained allows us to conclude that:

-the G216R variant is the only one showing remarkable functional (reduced PLP binding affinity and catalytic activity) and structural (altered tertiary and quaternary structure, aggregation propensity) defects. The latter features explain the very low levels of soluble protein in the cell as well as the undetectable transaminase activity. The inspection of the AGT crystal structure (8) reveals that the Gly216-to-Arg substitution could generate a high steric hindrance in the active site pocket, thus possibly explaining the effects on PLP binding and catalysis. In fact, the Arg side chain would probably interfere with the orientation of Ser81 and Gly82 that are involved in the PLP binding (chapter 1.2 of this thesis).

-among the variants displaying only structural defects, the G63R shows the greatest changes consisting in an altered tertiary structure, a reduced apodimer stability, and an enhanced aggregation propensity mainly related to the apo-form. It can be speculated that the insertion of an Arg residue at position 63 could induce a significant conformational change of apoAGT, possibly due to a destabilization of the hydrophobic pocket composed by Leu14, Ile60, Val77, Leu269 and Leu276 that could stabilize both the dimeric structure and the native monomer conformation of AGT.

-the R36H, G42E and I56N mutations seem to give rise to milder structural defects on AGT consisting in an alteration of the tertiary structure and an increased aggregation propensity. Both the R36H and the G42E variants are susceptible to proteolytic degradation both in the cell and in the purified form. Unexpectedly, while the R36H mutation destabilizes the AGT dimer, the G42E variant does not show any change of the K_d (dim-mon). Molecular modeling studies on dimeric AGT reveal that a Glu residue at position 42 is not predicted to

generate steric hindrance between the subunits. Furthermore, the mutation does not alter intra- and inter-chain contacts. On the other hand, the presence of an His residue at position 36 interfere with the formation of ionic bridge between Arg36 and the Glu274 of the same subunit but in proximity of the monomer-monomer interface (see Fig. 18 panel C of the chapter 4.1) probably destabilizing the region explaining the dimer destabilization. The I56N mutation destabilizes the apoAGT quaternary structure and makes it particularly prone to aggregate under physiological conditions. The latter effect is almost undetectable in holoI56N, thus indicating that the binding of PLP is able to rescue for the conformational change caused by the mutation. The substitution of Ile56 to Asn interferes with inter-chain hydrophobic attractions between Ile56 and Leu18 and Ile20 of the other subunit, thus probably explaining dimer destabilization.

-Correlation between the molecular properties of the variants and the in vitro responsiveness to PN. We observed that all the analyzed mutations cause a structural defect mainly related to the apo-form of the variants, as already reported for other pathogenic forms of AGT. Considering the demonstrated role of the coenzyme in promoting AGT dimerization, we hypothesized that it could be effective in the rescue of interfacial mutations. Indeed, except for G216R, we found that the presence of PN in the culture medium of cells expressing the analyzed variants is able to increase their expression level and specific activity, although to a different extent. Thus, we wonder if there is any relationship between the molecular features of the apovariants and their responsiveness upon PN administration. We used the increase in the $K_{d(\text{dim-mon})}$, the increase in the ANS emission fluorescence and the decrease of the CD signal at 280 nm with respect to AGT-Ma, as parameters indicative of the structural alterations of the apovariants. To quantify the response to PN, we used two different parameters: the increase of the amount of soluble protein and the increase of specific activity. The first reports the levels of protein without any indication of its functionality. The second reports the levels of functional enzyme, but could be influenced by the inhibitory effect of PN (55).

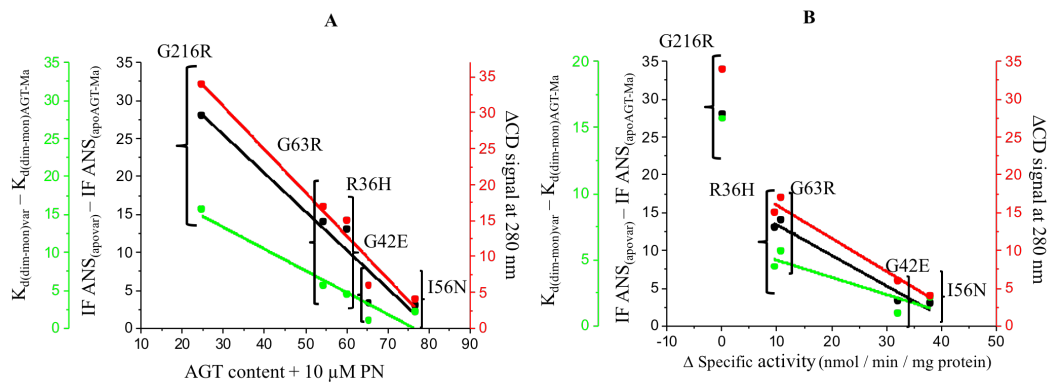


Fig. 27. Correlation analyses between the structural alteration of the apovariants and the expression level (A) and the specific activity (B) upon PN treatment. A) Plot of the ratio between the ANS emission fluorescence of the apovariants and that of apoAGT-Ma (black dots), the ratio between the $K_{d(dim-mon)}$ of the apovariants and that of apoAGT-Ma (green dots) and the magnitude of the near-UV CD signal at 262 nm (red dots) as a function of the increase in the expression level (A) and specific activity (B) of the variants upon PN treatment.

The resulting correlation analyses shown in Fig. 27, panel A and B, suggest that the degree of structural alteration of the apo-form of the variants could inversely correlate with the response to PN treatment. In particular, a remarkable difference can be observed between G216R and the other species, in agreement with the strong structural and functional alterations typical of this variant and with its complete absence of response to PN. Among the responsive variants, G63R and R36H have more evident structural alterations and a lower level of responsiveness with respect to G42E and I56N. This would imply that lower is the structural alteration of an enzyme, higher is the expected chaperone effect of the coenzyme. Although these results should be interpreted with caution considering the small number of analyzed variants, they would indicate that the response to PN administration could be higher for mutations causing milder effects on AGT. Nonetheless, our preliminary data suggest that it could be possible to identify a relation between the biochemical features of AGT variants and the degree of responsiveness to PN administration in a cellular model of PH1. The integration of our correlation analysis with data obtained from PH1 patients, could be considered an excellent starting point to predict PN responsiveness at clinical level. Further analyses are currently ongoing to widen the number of analyzed mutation, as well as to test the effect of B6 vitamers that not lead to inhibitory effect (pyridoxamine and pyridoxal).

-Possible implications of the results for AGT folding. The analysis of the significance of the data obtained from the AGT perspective allows to draw some interesting hypotheses. In particular, the finding that a high degree of structural alteration reduces the chaperone effect of the coenzyme, could support the view that PLP binding is a late event during AGT folding. This would mean that PLP binds partly-folded or quasi-folded monomers. Moreover, the strict correlation between the rigid-body protein-protein docking results and the degree of destabilization of the dimeric structure measured *in vitro* (Fig. 24) suggests that AGT dimerization could occur upon the interaction of monomers in a folded or quasi-folded conformation. However, it should be taken into account that *in silico* data are obtained based on the structure of the holo-form, while *in vitro* experiments are related to the apo-form of the protein. Nonetheless, these considerations support the view that AGT folding passes through the first collapse of the unfolded chain into a partly-folded monomer, which should then acquire a native or quasi-native conformation to bind the PLP coenzyme and form the final dimeric and functional structure. Although this would be in agreement the AGT folding pathway previously proposed on the basis of denaturation studies performed with the purified protein (23), a more detailed analysis of the role of coenzyme binding and dimerization for the intracellular fate of the protein will be necessary.

6

**AGGREGATION PROPENSITY OF HUMAN
AGT: THE OPPOSITE EFFECT OF THE
POLYMORPHIC MUTATIONS P11L AND
I340M**

Background information

The propensity to aggregation is an inevitable issue for many proteins. This phenomenon has important implications for pharmaceutical industries, in particular for the formulation and manufacturing of therapeutic proteins (94). Moreover, the abnormal formation of protein aggregates has been identified as one of the leading causes of several diseases. Aggregation can occur through different pathways, including the formation of partly-folded intermediates exposing sticky patches, or the self-association of native-like states under conditions that favour protein-protein interactions. In most cases, protein aggregation is nucleation-controlled, because it depends on the formation of a critical nucleus (a lag phase in which no large particles are detected) followed by the rapid growth of insoluble aggregates until a plateau phase when all the protein is in the aggregated state (95). Research efforts devoted to the understanding of protein aggregation have been mainly focused on the identification of critical factors that influence the aggregation extent as well as of the forces governing protein-protein interactions (96). Among them, the interaction of protein folding intermediates exposing hydrophobic patches is a well-known mechanism (97). However, theoretical (98) and experimental (99) evidences suggest that also electrostatic forces can play an important role in inducing or enhancing protein aggregation. The process of electrostatic aggregation is based on the attraction between complementary charged domains of a protein surface and it usually decreases at high ionic strength, due to screening effects (99). One of the key factors governing electrostatic aggregation is protein charge anisotropy, i.e. the asymmetric distribution of charged residues on the exterior of a particular protein. Although in many cases the aggregation occurs at a pH close to the isoelectric point, it has been reported that a difference can exist between pI and the pH of maximum aggregation (99). Some data suggest that electrostatic interactions can also contribute to the stabilization of protein-protein complexes, by influencing the binding rate and/or equilibrium (100).

The propensity to self-association is also a problem for AGT. Data obtained in prokaryotic and eukaryotic models as well as by analyses on variants in the

purified form, indicate that many mutations reduce the folding efficiency of AGT by promoting its aggregation (31, 35). In some cases the aggregation is due to a low dimer stability, which allows the formation of monomers exposing hydrophobic surfaces and prone to self-association (9, 36). In other cases however, an aggregation driven by electrostatic interactions between folded dimers showing an increased surface charge anisotropy has been reported (31). Interestingly, some differences between the two polymorphic forms of AGT have been reported. In fact, although AGT-Mi is not disease-associated, it shows an increased aggregation propensity and a reduced stability with respect to AGT-Ma, both *in vitro* and in the cell (23). Between the two amino acid substitutions typical of AGT-Mi, the P11L mutation seems to be the main actor in reducing the stability of the protein, while the I340M mutation has been supposed to mitigate the effects of the Pro11 substitution (30).

Since the aggregation tendency of AGT has not been investigated in detail, during my PhD I studied the aggregation propensity of dimeric AGT in the recombinant purified form by means of bioinformatic and biochemical studies, with particular emphasis on the role of electrostatic interactions between exposed surfaces of opposite charge as well as on the effect of the polymorphic substitutions P11L and I340M.

RESULTS AND DISCUSSION

6.1 *In silico* analysis of the AGT surface: molecular map of the electrostatic potential

Based on the known 3D structure of AGT-Ma in the holo-form (Pdb id:3RBF), we evaluated the distribution of hydrophobic surfaces as well as the electrostatic map, in order to understand the physical/chemical features of the protein that could govern its aggregation process. As reported in Fig. 28, AGT-Ma shows only few hydrophobic patches on its surface, mainly located along the dimerization interface (8), in line with the finding that the native monomeric form of AGT tends to aggregate probably driven by hydrophobic attractions (9, 23).

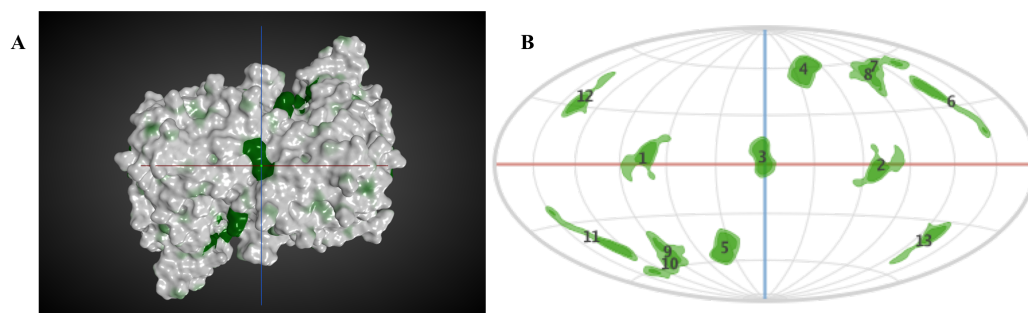


Fig. 28. Distribution of the hydrophobic patches around AGT-Ma. Panel A: hydrophobic patches of dimeric AGT shown as green areas on the grey background of AGT. The area and the energy cut-offs of each patch are 100 \AA^2 and 0.25 kcal/mol , respectively. Panel B: representation of the hydrophobic patches around AGT as 2D maps. Patches are enumerated in decreasing order based on their area. The red and blue lines indicate the equatorial and central meridians projection axes, respectively.

Interestingly, the electrostatic map of AGT-Ma reveals an asymmetric distribution of negative and positive charges on the dimeric surface. In particular, as shown in Fig. 29 panels A and C, four main negative patches are present in one face of the dimer, mainly formed by residues Asp331, Asp334, Asp341 and Asp344 (patch 1 and 2, size 351 \AA^2) Glu281, Glu371, Asp374 and Glu378 (patch 3 and 4, size 175 \AA^2). On the other hand, as shown in Fig. 29 panels B and D, four main positive patches are present on the other side composed by Arg289, Arg292, His299, Arg301, Lys312, Arg333, Lys357, His386, Lys389 and Lys390 (patches 5 and 6, size 522 \AA^2) and by Arg122, His124, His146, His174, Arg175, Arg197, Lys225, Lys227, Arg233, Lys234 and Lys236 (patches 7 and 8, size 568 \AA^2). We

compared the electrostatic map of AGT with those of other PLP-dependent aminotransferases belonging to the Fold type I family such as human cytosolic aspartate aminotransferase (PDB: 3WZF, to be published), human ornithine aminotransferase (101) and human tyrosine aminotransferase (PDB: 3DYD, to be published) as well as of proteins sharing a sequence similarity $\geq 30\%$ with AGT. We found that all the latter proteins (except alanine: glyoxylate aminotransferase from *Aedes aegypti* that displays some positive patches), show an unvarying negative potential on their surface (data not shown). These analyses led us to hypothesize that the aggregation propensity of AGT could depend on the peculiar distribution of charges on its surface. Following this view, parameters such a pH and ionic strength should critically influence its aggregation rate and/or extent. Moreover, mutations of surface residues could change the charge distribution and negatively or positively influence the self-association process.

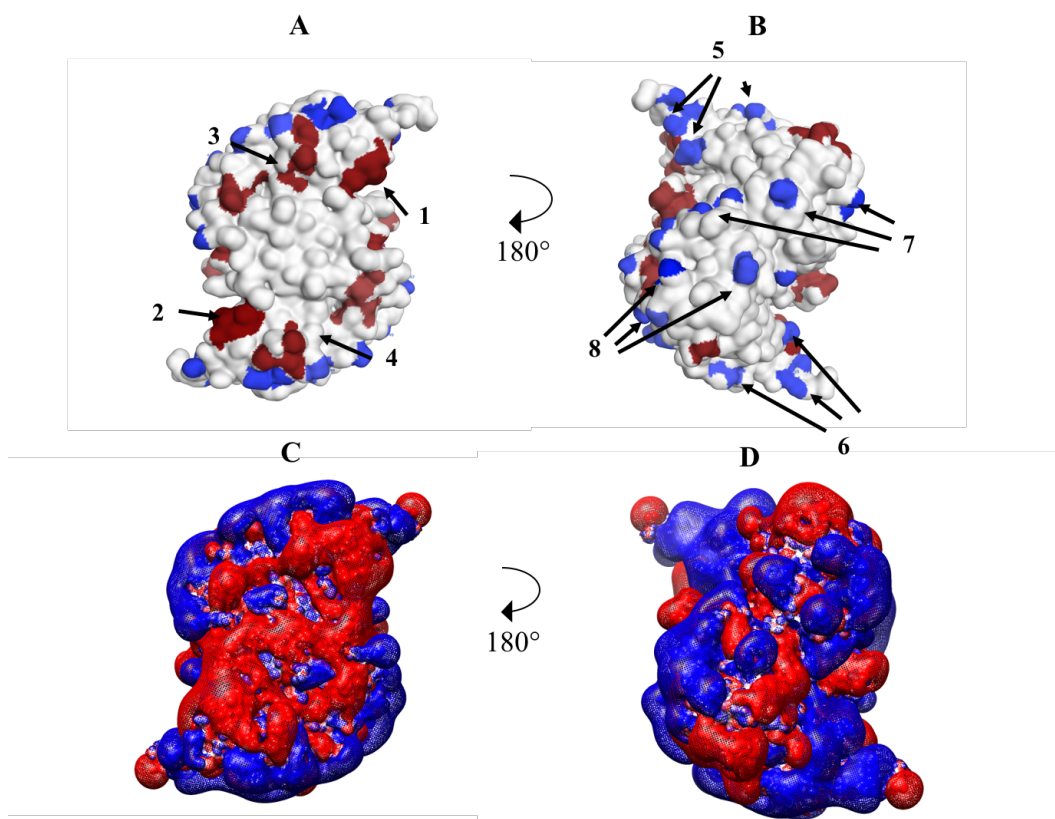


Fig. 29. Charged patches and electrostatic potential around AGT. Panel A and B: positive (blue) and negative (red) patches of dimeric AGT on a grey background. The size and the energy cut-offs of each patch are $> 100 \text{ \AA}^2$ and 50 kcal/mol , respectively. Patches characterized by an high potential are rendered in a dark color and indicated by numbers and arrows. Panel C and D: electrostatic potential contours showed as mesh (-0.5 (red) and $+0.5$ (blue) kT/e) around AGT obtained by using the PDB2PQR tool for structure preparation, PROPKA 3.0 for the protonation state of the residues of AGT at different pH values and APBS tool to generate the electrostatic potential map. Each tool was run on an Opal web-service. The visualization of the potential electrostatic map was performed by using UCSF CHIMERA 1.11 program at $I = 0.06 \text{ M}$, at pH 7.4, at $37 \text{ }^\circ\text{C}$.

6.2 Effect of pH and ionic strength on the aggregation propensity of AGT-Ma

To have insights into the forces involved in the aggregation process of AGT-Ma, we evaluated the aggregation propensity of the protein by dynamic light scattering (DLS) experiments performed at various pH and ionic strength. All the analyses were performed at the physiological temperature of 37°C and at a protein concentration of $10 \text{ }\mu\text{M}$, to guarantee that no monomerization occurred (23). We monitored the increase in mean count rate, a parameter that represents the average

scattering intensity during the measurement and is related to the amount and the size of the species present in solution (102). To determine the aggregation rate, data on the time-dependent increase in count rate were fitted using the analytic equation (7) proposed by Morris *et al* (83) (see “Material and Methods”, section 3.12). This equation is related to the minimalistic/”Ockham’s razor” Finke-Watzky (F-W) two-step model, which has been used to analyse the aggregation data of a wide set of protein (83), giving averaged rate constants for nucleation (k_1) and autocatalytic growth (k_2). Moreover, we analysed the species present in the aggregating solution and accounting for the scattering signal, taking into account that the DLS signal is proportional to the sixth power of a particle diameter, hence the presence of the signal related to the dimer indicates that it should be by far the most abundant species in solution.

Many proteins tend to have decreased solubility near the isoelectric point, often referred to as isoelectric precipitation, where the low net charge of the protein corresponds to the loss of aggregation inhibiting repulsion. AGT has a predicted isoelectric point (pI) of 8.59. We incubated the apo- and holo-form of the protein at 37°C the KP buffer 0.1 M in the pH range 5.5-8.0, to avoid protein unfolding due to strong acid or alkaline conditions. HoloAGT-Ma does not show any significant increase in count rate from pH 8 down to 6.5, while slight aggregation propensity can be seen at pH 5.5 and 6 (Fig. 30, panel A).

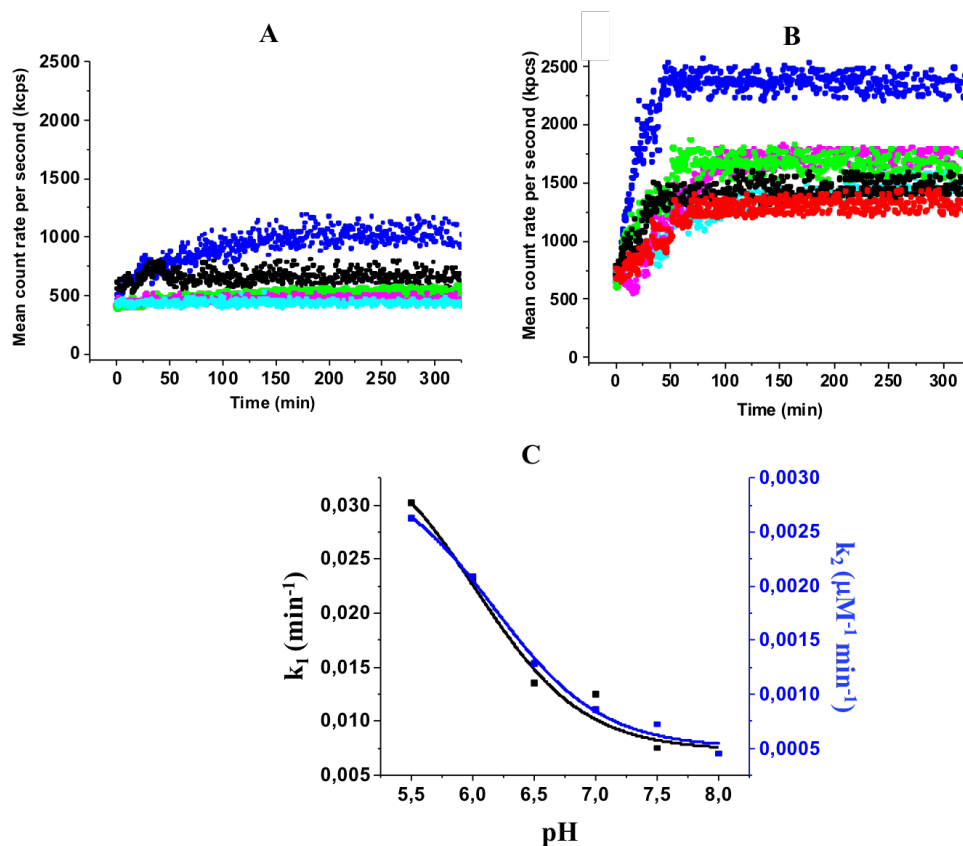


Fig. 30. Aggregation profiles of holoAGT-Ma (A) and apoAGT-Ma (B) and plot of rate constants values of k_1 and k_2 of apoAGT-Ma (C). Panel A: time dependence of total count rate (measured as kilo counts per second) of holoAGT-Ma. Panel B: time dependence of total count rate (measured as kilo counts per second) of apoAGT-Ma. Panel C: plot of the k_1 (black dots) and k_2 (blue dots) rate constants (obtained using Eq. 7) as a function of pH. The lines represent the fitting of each set of data to Eq. 8. Measurements were performed at 10 μM enzyme concentration, 0.1 M ionic strength in potassium phosphate buffer, at 37°C. The color code of the panel A and B is the following: blue, pH 5.5; black, pH 6.0; green, pH 6.5; purple, pH 7.0; red, pH 7.5 and cyan pH 8.0.

At pH 5.5, the values of k_1 and k_2 were equal to $1.7 \cdot 10^{-2} \pm 2.0 \cdot 10^{-4} \text{ min}^{-1}$ and $7.3 \cdot 10^{-4} \pm 5.0 \cdot 10^{-5} \text{ min}^{-1} \mu\text{M}^{-1}$, respectively. On the other hand, apoAGT-Ma showed an increase in count rate along the whole pH range, with extent and rate of aggregation higher than the corresponding of holoAGT-Ma (Fig. 30, panel B). The estimated values of k_1 and k_2 increase as the pH is lowered from 8 to 5.5, giving values of pk_{spec} of 6.03 ± 0.13 , and 6.18 ± 0.09 , respectively (Fig. 30, panel C). Thus, holo- and apoAGT-Ma do not undergo an isoelectric precipitation, because the aggregation extent is higher at pHs where the protein net charge shows the highest values. It should be mentioned that the aggregation process leads to the formation of aggregates of size spanning from 400 to 800 nm (data

not shown), with a rate that fits very well that of the increase in count rate. However, the signal of the dimer is always visible in the whole pH range. Thus, although aggregates are the main responsible for the scattering signal, the dimer still remains the more represented species in solution and it is probably the form of the protein that primes aggregate formation. The fact that the dimer is the aggregating species is also shown by the linear increase of the aggregation rate constants at increasing AGT concentrations (Fig. 31).

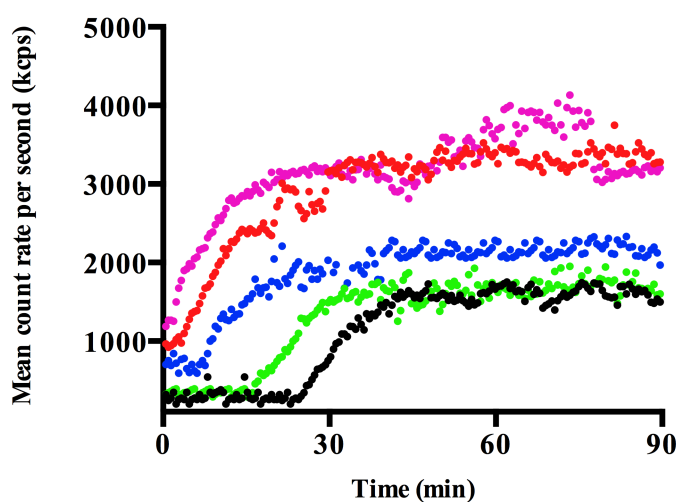


Fig. 31. Aggregation profiles of apoAGT-Ma at different protein concentrations. Time dependence of total count rate (measured as kilo counts per second) of apoAGT-Ma. Measurements were performed at 2 μM (black), 5 μM (green), 10 μM (blue), 15 μM (red) and 20 μM (purple dots) protein concentration, 0.1 M KP buffer, at pH 5.5, at 37 $^{\circ}\text{C}$.

We then monitored the aggregation process of apoAGT-Ma at pH 5.5 at ionic strengths varying from 0.05 to 1 M, to include values below and above the physiological one (0.15 M corresponding to 0.06 M potassium phosphate). As reported in Fig. 32, the aggregation propensity of apoAGT-Ma increases at decreasing ionic strength of the buffer. In particular, the aggregation is completely prevented at values equal or higher than 0.2 M, and occurs with k_1 values of $3.1 \cdot 10^{-2} \pm 3.0 \cdot 10^{-3} \text{ min}^{-1}$ and $2.2 \cdot 10^{-2} \pm 2.0 \cdot 10^{-3} \text{ min}^{-1}$, and k_2 values of $2.9 \cdot 10^{-3} \pm 3.0 \cdot 10^{-4} \text{ min}^{-1} \mu\text{M}^{-1}$ and $2.0 \cdot 10^{-3} \pm 2.0 \cdot 10^{-4} \text{ min}^{-1} \mu\text{M}^{-1}$, at values of 0.05 M and 0.1 M, respectively. These data indicate that aggregation is not due to

hydrophobic attractions, which would have been enhanced by increased salt concentrations. Rather, it depends on electrostatic interactions, which are reduced or suppressed at high ionic strength due to screening effects (99).

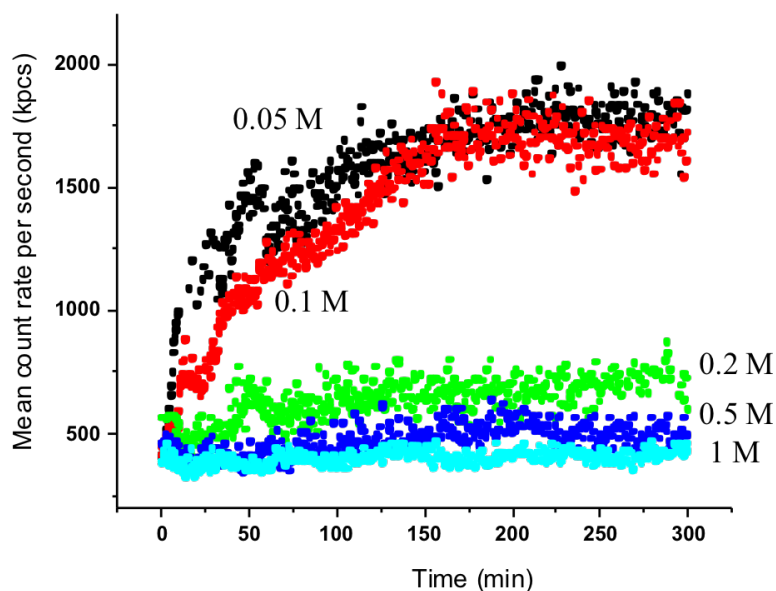


Fig. 32. Aggregation of apoAGT-Ma at different ionic strength. Time dependence of total count rate (measured as kilo counts per second) of 10 μ M apoAGT-Ma at 37°C in KP buffer pH 5.5 at the indicated ionic strength.

We asked if aggregation was accompanied by an unfolding process by monitoring the dichroic signal at 222 nm, indicative of the secondary structure content, of 10 μ M apoAGT-Ma in 0.05 M potassium phosphate buffer pH 5.5, 37°C, i.e. under conditions in which a strong aggregation phenomenon is observed. Since we did not observe any loss of secondary structure with time during aggregation up to 300 minutes, we concluded that the process is not dependent on a partial unfolding, but occurs starting from a native or native-like form of the protein. Furthermore, by exploiting the different behavior of the protein in the apo- and holo-form, we found that aggregation is not reversible. In fact, the addition of 100 μ M PLP (a saturating concentration) to an aggregating mixture of 10 μ M apoAGT-Ma at pH 5.5 at 0.05 M ionic strength was able to stop but not to revert the self-association process. Finally, considering that AGT shows three cysteine

residues per subunit exposed to the solvent (48), we compared the rate constants of aggregation in presence and absence of 0.01 M β -mercaptoethanol. The absence of any effect of the reducing agent on the aggregation rate revealed that the process does not depend on the formation of disulphide bonds.

Altogether, these data allow us to conclude that AGT-Ma aggregation is not an isoelectric precipitation phenomenon, because it is not influenced by the net charge of the protein, and is not due to the formation of disulphide bonds. Rather, it depends on the electrostatic interaction between patches of opposite charge present on the native dimeric species as a consequence of the charge anisotropy of the protein surface. A similar aggregation mechanism has been already reported for β -Lactoglobulin at low ionic strength, which shows a strong aggregation phenomenon at pHs below the *pI* (99). In addition, the comparison between the aggregation rates of the holo- and apo-form of AGT-Ma suggests that PLP binding has a stabilizing effect on the protein. Although the crystal structure of apoAGT has not been solved, biochemical analyses indicate that it could have a tertiary structure slightly different from that of holoAGT, as suggested by the dichroic features in the near-UV region (10, 33), as well as an higher flexibility of the polypeptide chain making it more susceptible to unfolding and proteolytic degradation (31, 92). We can suggest that PLP binding could increase the rigidity of dimeric form of AGT and reduce the exposure of charged residues possibly involved in the aggregation process. Thus, besides its role in promoting AGT dimerization (this thesis) the coenzyme seems to have a wider chaperone role by counteracting the self-association of the protein in the dimeric form.

In order to provide a possible structural explanation to the behavior of AGT-Ma, we evaluated the changes in the electrostatic map of the protein as function of pH, with particular attention on the identification of residues forming oppositely charged patches and to their predicted pK_a value (Fig. 33). At pH 5.5, it can be observed a strongly asymmetric charge distribution and the presence of several negative and positive areas on the AGT surface (Fig. 33, panel A). The negative patches are mainly formed by exposed glutamate and aspartate residues, while the positive ones are mainly formed by exposed histidine, arginine and lysine

residues. Upon increasing the pH from 5.5 to 8, the surface area and the potential of the negative patches remain almost unchanged, while those of the positive patches decrease (Fig. 33, panel B).

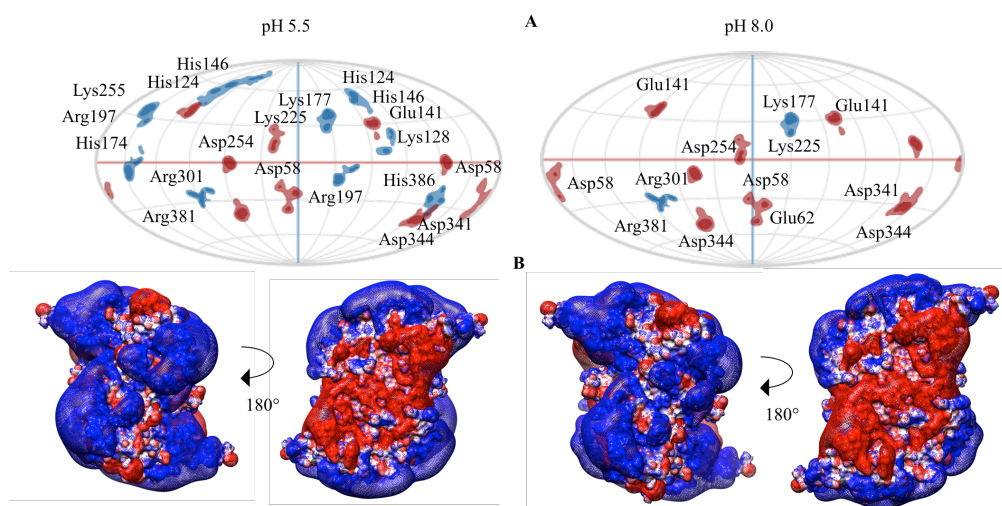


Fig. 33. Comparison between 2D maps (Panel A) and electrostatic potential map (Panel B) of AGT-Ma at the indicated pH values, at 37°C. Panel A: 2D maps calculated using the Patch Analyzer tool of *MOE 2016.08*. The positive and negative patches are colored blue and red, respectively. The residues mainly involved in the formation of each patch are shown. Panel B: electrostatic potential contours (-1.5 (red) and +1.5 (blue) kT/e) around AGT at different pH values.

This effect is mainly due to the side chains of five exposed histidine residues (124, 146, 174, 342 and 386), which pass from the protonated to the neutral form between pH 6.0 and 7.0. This is confirmed by their predicted pK_a values, calculated with the tool “Residue pK_a ” of *MOE 2016.08*, that are in good agreement with the pK_{spec} obtained from the plot of the aggregation rate constants vs pH (Fig. 30). Thus, it can be speculated that patches formed by histidine residues could be the main actors in determining the electrostatically-driven aggregation of AGT, although site-directed mutagenesis experiments would be necessary to confirm this interpretation. Nevertheless, as already mentioned, the attractive forces between positive and negative domain of associating proteins are strongly influenced by the ionic strength of the solution, which in turn influences the charge states of exposed amino acids (99). Accordingly, we found that AGT aggregation is prevented by the presence of salts, which can cover and screen the

charged patches on the surface (Fig. 32). The electrostatic maps of the protein obtained at various ionic strengths between 0.05 M and 1 M reported in Fig. 34, predict strong screening effects of the buffer ions above 0.2 M. This is in line with the data obtained in solution indicating that the aggregation of AGT-Ma is completely prevented at ionic strength ≥ 0.2 M. It can be observed that under conditions mimicking a physiological ionic strength, the surface charge of AGT-Ma should be significantly screened. This explains why no aggregates of AGT have been reported in liver biopsies of healthy subjects (103) and only a small portion of the protein is in the insoluble fraction when overexpressed in cellular systems (32, 55). However, even small changes of either the intracellular chemical/physical conditions or the protein surface as a consequence of inherited mutations could promote aggregation.

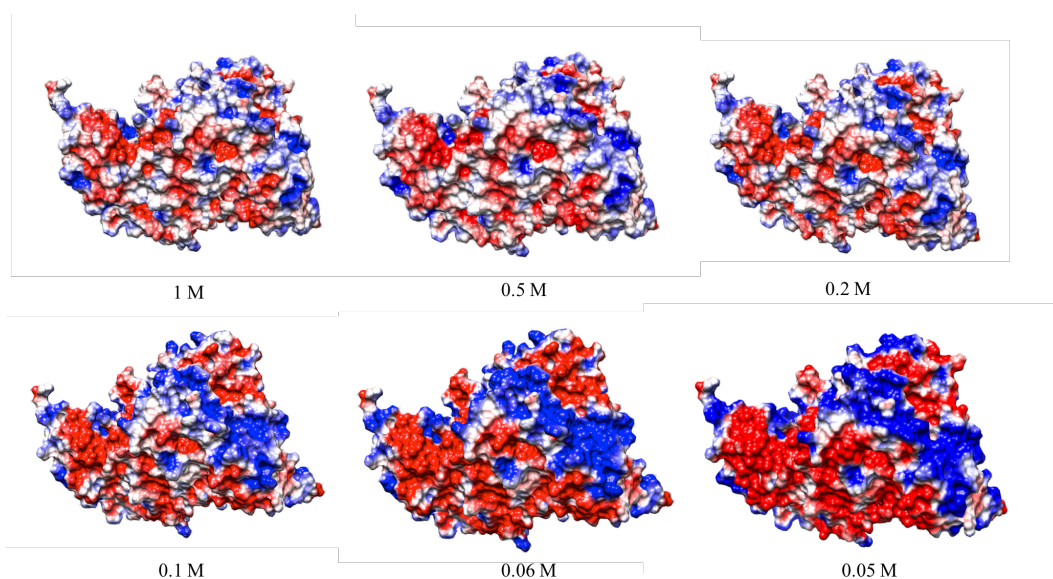


Fig. 34. Potential contours (-1.0 (red) and +1.0 (blue) kT/e) around AGT-Ma at pH 7.4, at 37°C, at the indicated ionic strength.

6.3 Effects of the P11L and I340M polymorphic mutations on the aggregation process of AGT

AGT-Mi displays an increased tendency to aggregation both in the purified form and in cellular systems with respect to AGT-Ma (30, 32). This effect has been attributed to a reduced stability of the dimeric structure, mainly caused by the P11L mutation that could weaken the interaction between the N-terminal arm of one subunit and the large domain of the neighboring subunit thus promoting the population of monomeric forms of the protein prone to aggregate (32). However, it cannot be excluded that either the P11L and/or the I340M mutation typical of the minor allele could also influence the electrostatically-driven aggregation of the protein. Moreover, it has been reported that several pathogenic mutations that lead to PH1 associated with the minor allele, play their effects by increasing the AGT aggregation propensity (32, 35).

We analyzed the aggregation process of apo- and holoAGT-Mi as a function of pH by DLS under the same experimental conditions used for AGT-Ma. We found that the aggregation rate increased at decreasing ionic strength, thus indicating that the process is mediated by electrostatic forces (data not shown). The trends of the k_1 and k_2 as a function of pH of holo- and apoAGT-Mi, reported in Fig. 35, reveal that (i) both species show an increased aggregation propensity at acidic pH with estimated values of pK_{spec} of 5.8 ± 0.3 and 5.7 ± 0.1 for k_1 and 6.4 ± 0.1 and 6.2 ± 0.3 for k_2 of apo and holoAGT-Mi, respectively; (ii) at the same pH, the k_1 values of apoAGT-Mi are 7-, 10- and 15-fold higher than the corresponding of holoAGT-Mi from pH 5.5 to 7.0, while the k_2 values are of the same order of magnitude, thus suggesting that PLP binding to AGT-Mi could mainly affect the nucleation step of the aggregation process. By comparing the aggregation rate of holo- and apoAGT-Mi with the corresponding forms of AGT-Ma we noticed that the minor allelic form shows an increased aggregation propensity. In fact, a visible aggregation event was present at pHs lower or equal to 7 in holoAGT-Mi, while holoAGT-Ma only aggregates at pH 5.5. At the latter pH value, holoAGT-

Mi showed k_1 and k_2 values about 2- and 10-fold higher, respectively, as compared with those of holoAGT-Ma. As for the apo-form, the values of k_1 and k_2 were from 1- to 2.5-fold and from 2- to 4-fold higher than those of apoAGT-Ma, respectively. The species populating during AGT-Mi aggregation were similar to those formed by AGT-Ma although aggregates of higher molecular weight are formed (~1000 nm). Overall, these data allow to conclude that AGT-Mi is prone to an electrostatically-driven process of self-association similar to that already observed for AGT-Ma, but characterized by an higher aggregation tendency. This suggest that one or both of the two polymorphic mutations typical of the minor allele, P11L and I340M, could directly or indirectly change the surface of the protein and somehow influence the interaction between oppositely-charged patches.

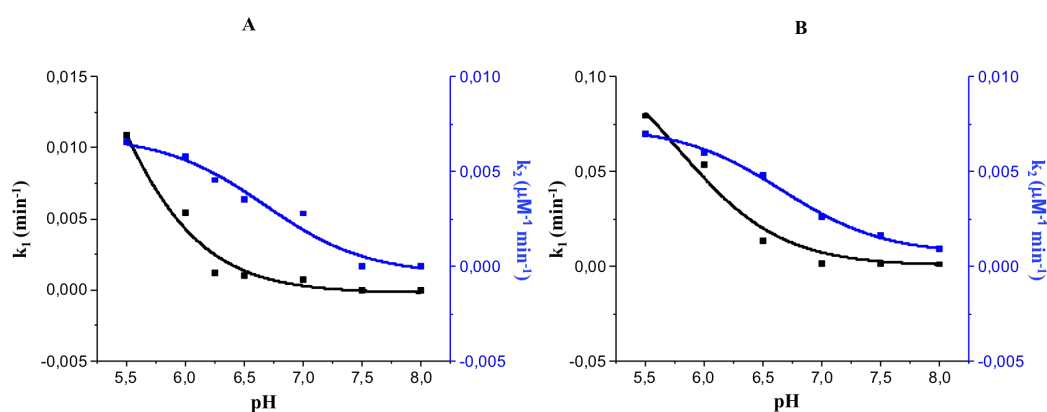


Fig. 35. Plots of k_1 and k_2 values vs pH of holo and apoAGT-Mi. Plot of the k_1 (black dots) and k_2 (blue dots) rate constants (obtained using Eq. 7) as a function of pH. The lines represent the fitting of each set of data to Eq. 8. Holo- (A) or apoAGT-Mi (B) were incubated in 0.1 M potassium phosphate buffer at different pHs and the mean count rate in DLS has been monitored.

In order to understand the structural determinants responsible for the increased aggregation propensity of AGT-Mi, we expressed, purified and characterized the two single mutants P11L and I340M. Their absorbance and CD spectra in the visible region were similar to the corresponding of AGT-Ma and AGT-Mi (data not shown). The P11L and I340M mutations did not alter the $K_{D(\text{PLP})}$ value of AGT as well as the kinetic parameters of the overall transamination reaction, except for a 30% reduction in k_{cat} of the P11L variant (data not shown). Moreover,

the two mutations did not alter the quaternary structure of the protein up to 0.3 μM (the detection limit of SEC experiments). Interestingly, we found that the I340M mutation increased the thermal stability of AGT, as shown by the thermal denaturation curves of apo and holoI340M which showed a single transition at 70.1 ± 0.3 $^{\circ}\text{C}$ and 83.3 ± 0.3 $^{\circ}\text{C}$, respectively. The latter values are higher than those of AGT-Ma, which displays apparent mid-denaturations at 61.1 ± 0.3 $^{\circ}\text{C}$ and 66.4 ± 0.3 $^{\circ}\text{C}$ in the apo-form and 77.5 ± 0.3 $^{\circ}\text{C}$ in the holo-form (33). On the other hand, previous data have shown that the P11L mutation decreases by 3 $^{\circ}\text{C}$ and 1 $^{\circ}\text{C}$ and 4 $^{\circ}\text{C}$ the thermal denaturation mid-point of apo- and holoAGT, respectively.

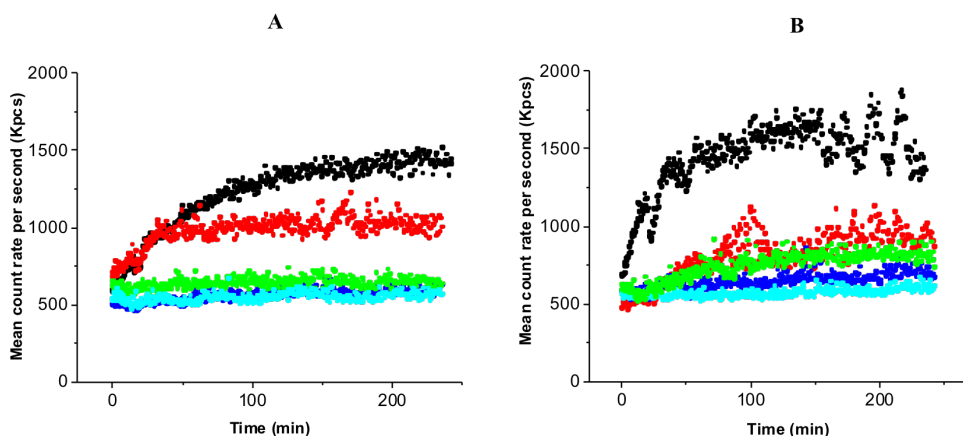


Fig. 36. Time dependence of total count rate of holo (panel A) and apoI340M (panel B) as function of pH, $I = 0.1$ M, at 37°C . Panel A: time dependence of total count rate (measured as kilo counts per second) of holoI340M. Panel B: time dependence of total count rate (measured as kilo counts per second) of apoI340M. Measurements were performed at 10 μM enzyme concentration, 0.1 M ionic strength in potassium phosphate buffer, at 37°C . The color code is the following: black, pH 5.5; red, pH 6.0; green, pH 6.5; blue, pH 7.5 and cyan pH 8.0.

We thus investigated the aggregation behavior of I340M and P11L single variants. The data reported in Fig. 36 panel A, show that holoI340M displayed a visible increase in count rate only at pH 5.5 and 6. At pH 5.5 the values of k_1 and k_2 equal to $1.5 \cdot 10^{-2} \pm 4.0 \cdot 10^{-3} \text{ min}^{-1}$ and $6.0 \cdot 10^{-5} \pm 1.0 \cdot 10^{-6} \text{ min}^{-1} \mu\text{M}^{-1}$, respectively. The value of k_1 was similar to those of holoAGT-Ma but the k_2 is 12-fold lower than the corresponding of holoAGT-Ma. Similarly, apoI340M (Fig. 36,

panel B) only aggregated at pH 5.5, with a k_1 value similar to that of apoAGT-Ma but a k_2 value 14-fold lower than the corresponding one of apoAGT-Ma ($k_1 = 3.2 \cdot 10^{-2} \pm 1.5 \cdot 10^{-3} \text{ min}^{-1}$, $k_2 = 1.9 \cdot 10^{-4} \pm 1.0 \cdot 10^{-5} \text{ min}^{-1} \mu\text{M}^{-1}$). Hence, the I340M mutation has a stabilizing effect on the AGT structure, in terms of both reduced sensitivity to thermal stress and lower aggregation propensity.

A completely different effect is exerted by the P11L mutation, as shows by the pH-dependence of the k_1 and k_2 values of aggregation of the apo and holo variant, respectively (Fig. 37). An increase in count rate was detectable for both forms in the whole pH range, although the k_1 values of apoP11L are from 5- (pH 5.5) to 1.3-fold (pH 8.0) higher than those of holoP11L, in analogy with the data obtained on AGT-Ma and AGT-Mi. The aggregation increased at acidic pH with pK_{spec} for k_1 and k_2 of 6.1 ± 0.2 and 6.4 ± 0.2 respectively, for oloP11L, and 6.1 ± 0.4 and 6.9 ± 0.2 , respectively, for apoP11L.

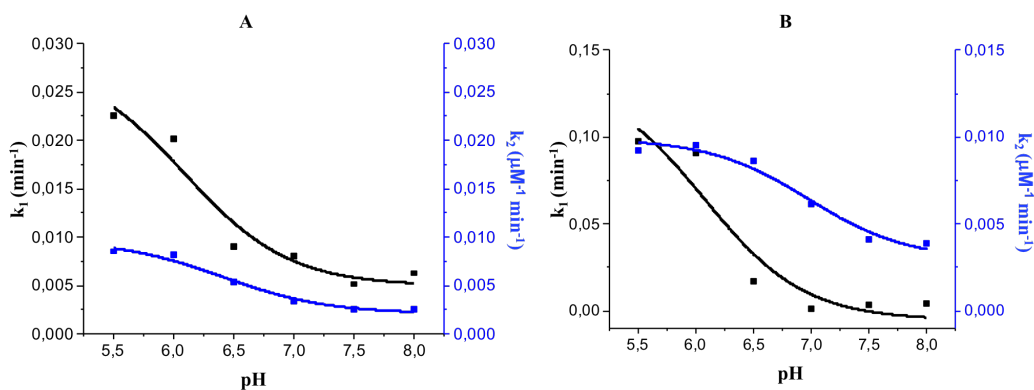


Fig. 37. Plots of k_1 and k_2 values vs pH of holo and apoAGT-P11L. Plot of the k_1 (black dots) and k_2 (blue dots) rate constants (obtained using Eq. 7) as a function of pH. The lines represent the fitting of each set of data to Eq. 8. Holo- (A) or apoP11L (B) were incubated in 0.1 M potassium phosphate buffer at different pHs and the mean count rate in DLS has been monitored.

These values agree quite well with those previously found for AGT-Ma and AGT-Mi (taking into consideration the noise of the count rate signal and the consequent experimental error), thus suggesting that aggregation could be governed by a molecular mechanism similar to that already proposed for AGT-Ma and AGT-Mi

(). Nevertheless, P11L displays a significantly higher aggregation extent with respect to AGT-Ma. In fact, the signal of the dimer disappeared after ~20 minutes during the aggregation process, as reported in the experiment shown in Fig. 38. This indicates that a significant portion of the variant is present as aggregated species in agreement with the fact that the mixture displays a visible turbidity at the end of the analysis.

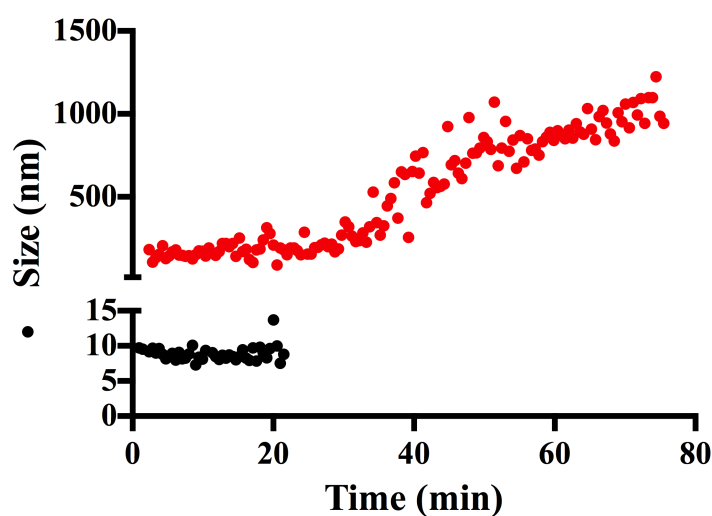


Fig. 38. Time dependent changes of the apparent particle size of 10 μ M apoP11L in KP 0.1 M at pH 5.5, 37°C. Black and red dots indicate dimer and aggregates, respectively.

To investigate the consequences of the aggregation process for AGT functionality, as well as the effect of the two polymorphic mutations, we measured the residual catalytic activity of AGT-Ma, AGT-Mi, P11L and I340M upon 3 h incubation in KP 0.1 M pH 5.5, at a protein concentration of 10 μ M, 37°C. These experimental conditions were chosen to favour the aggregation process as revealed by DLS. The assays were then performed in KP 0.1 M pH 7.4 at 25°C in presence of saturating PLP at saturating substrates concentrations, to stop the aggregation process. Holo and apoAGT-Ma, holo and apoI340M and holoAGT-Mi showed a residual catalytic activity >90%. On the other hand, apoAGT-Mi, holo P11L and apoP11L displayed a residual activity of 64%, 48%, and 26%, respectively. These data indicate that although AGT undergoes a native-like aggregation, the process is associated with loss of protein functionality. Moreover, they confirm the

destabilizing effect of the P11L mutation as well as the protective role of the PLP coenzyme.

By comparing the data obtained on AGT-Mi, the P11L, and the I340M variant, with those of AGT-Ma, we can conclude that while the I340M mutation exerts a stabilizing effect, the P11L mutation significantly increases the aggregation propensity of AGT. The hypothesis that the two polymorphic mutations could have opposite effects on AGT has been previously advanced. Mesa-Torres *N et al* (104) have reported the mutation of Ile340 as one of the consensus amino acids substitutions that contribute to create a form of AGT endowed with a higher stability in solution and in cellular systems. On the other hand, the P11L mutation has been claimed as the responsible for the increased sensitivity of AGT-Mi to chemical and thermal stress (23, 45). However, all these data have been interpreted by looking to the possible effects of the two substitutions on dimer stability (32). Our data indicate that they also play a role on the propensity of the protein to electrostatic aggregation.

From a structural point of view, Pro11 is located at the monomer-monomer interface. The visual inspection of the structure reveal that its substitution with a leucine residue could increase the flexibility of the N-terminal arm of AGT, possibly promoting its dissociation from the neighboring subunit. *In silico* results are also confirmed by biochemical studies revealing an increased susceptibility of AGT variants bearing the P11L mutation to proteolytic cleavage at the N-terminus (92). Based on these data and considerations, we compared the electrostatic map of AGT-Ma with that of a truncated form of the protein deleted by the first 21 residues mimicking the possible detachment of the N-terminal arm (Fig. 39).

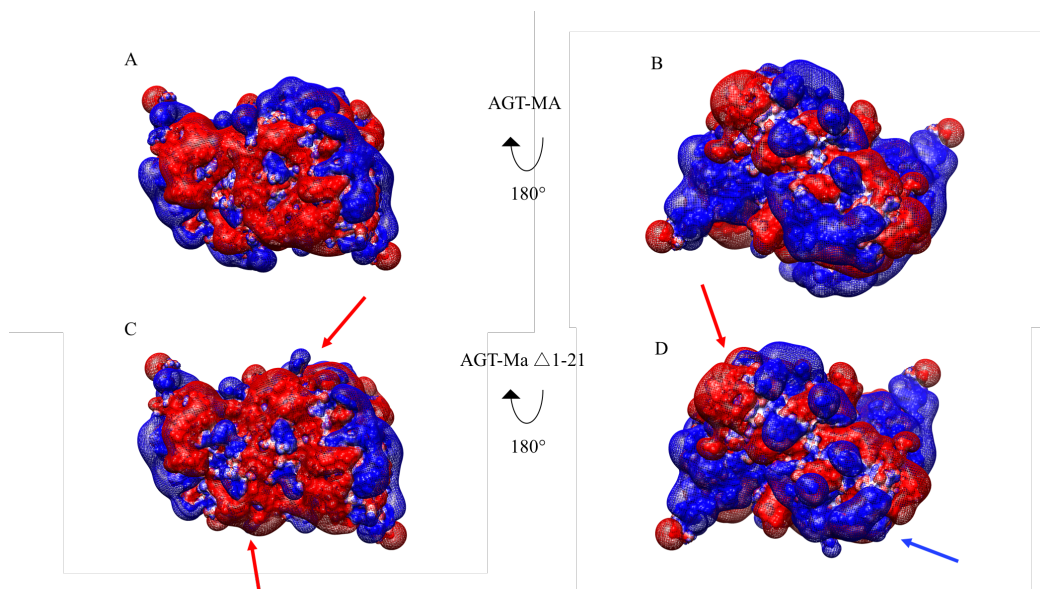


Fig. 39. Electrostatic potential contours (-0.5 (red) and +0.5 (blue) kT/e) of full length AGT-Ma (panels A and B) and that of AGT-Ma truncated of the residues 1-21 (panels C and D) at pH 7.4, ionic strength 0.06 M, 37°C. Blue and red arrows indicate the differences between the electrostatic potential map of AGT-Ma and its truncated form.

In analogy with previous reports, we found that several negatively charged residues are present under the N-terminal arm of AGT, including Asp52, Glu59, Asp196, Glu274 and Glu281. It can be hypothesized that the increased flexibility of the N-terminal arm due to the P11L mutation could promote its transient dissociation from the neighboring subunit, thus causing the exposure of negatively charged residues. This in turn would increase the anisotropy of charge distribution on the AGT surface, thus creating more favorable conditions for the electrostatic interactions between dimers. This hypothesis could also explain the lower aggregation propensity of holoP11L in comparison with the apo-form. PLP binding could increase the overall rigidity of the structure in particular through an indirect effect on the loop 24-32 that is connected to the N-terminal arm on one side, and to the active site on the other side (10). A rigid positioning of the loop reduces the flexibility of the AGT N-terminus. As for the I340M mutation, it is not easy to envisage how the substitution of Ile340 with a Met residue could alter the electrostatic potential of the AGT surface. Ile340 is located in the α -helix 16 at the monomer-monomer interface and it interacts mainly with Gln23 of the other subunit. *In silico* analyses reveal that the contact remains present also after

Ile340-to-Met substitution. However, the predicted binding energy increase from -1.401 kcal/mol of the Ile-Gln interaction to -2.039 kcal/mol of the Met-Gln interaction. The consequent predicted stabilizing effect of Met340 on the position of Gln23 could in turn stabilize interchain hydrogen bonds between Gln23 and Gly47 of the other subunit, thus increasing the overall rigidity of the N-terminal region of AGT.

6.4 Predicted effect of pathogenic mutations on the electrostatic potential of the AGT surface

The peculiar asymmetric distribution of charge on the AGT surface allows to hypothesize that point amino acid substitutions can make the protein more prone to aggregate under physiological condition of pH, temperature and ionic strength. Based on these considerations, we mapped all the missense mutations associated with PH1 known to date on the crystal structure of AGT and we observed that some of them involve residues located on the protein surface (Fig. 40). In particular, we focused our attention on the mutations D129H, E141D, and R289H associated with the major allele, and on the mutations E95K, R197Q and R289C associated with the minor allele. We investigated if and how each amino acid substitution could impact the surface charge distribution and hence the aggregation propensity of the protein.

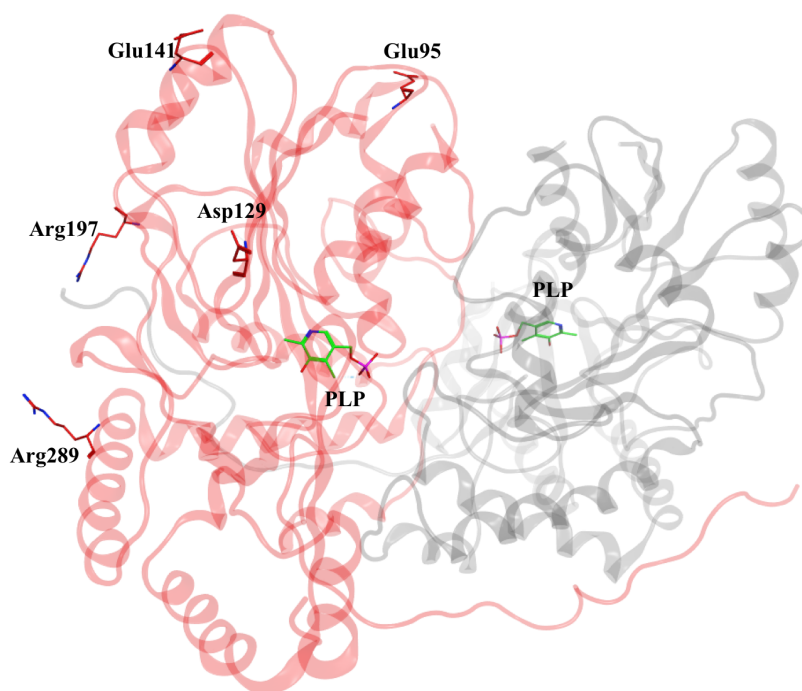


Fig. 40. Representation of surface residues of AGT involved in pathogenic mutations associated with PH1. PLP is represented as green sticks. Glu95, Asp129, Glu141, Arg197 and Arg289 are represented as red sticks in the red monomer. Oxygen, phosphate and nitrogen atoms are colored red, purple and blue, respectively. The figure was rendered using *MOE 2016.08*, by the available AGT structure (PDB 3R9A).

Asp129 is a residue located on the connection loop between the α -helix 5 and 6 and it is highly exposed to the solvent. The estimated exposure is 76%, expressed as computed by *MOE.2016.08* using as reference a Gly_X_Gly triplet. The residue is far away from the active site and has a predicted pK_a of 3.80. Molecular modelling analyses and *in silico* mutagenesis do not reveal any relevant alteration of orientation of residues located near Asp129 upon replacement by a His residue. In line with these predictions, it has been reported that the D129H-Ma mutation causes only a 10% reduction of activity and stability in a heterologous yeast assay (105). By analyzing the electrostatic potential map of the D129H variant (Fig. 41) we observed that the mutation determines an increased exposure to the solvent of Lys128 and Lys357, which in turn increases the potential of the positive patches 7 and 8 (Fig. 29, chapter 6.1). Based on our data indicating that AGT aggregation is promoted by a high charge anisotropy, the increased positive potential could enhance the aggregation propensity of the variant under physiological conditions.

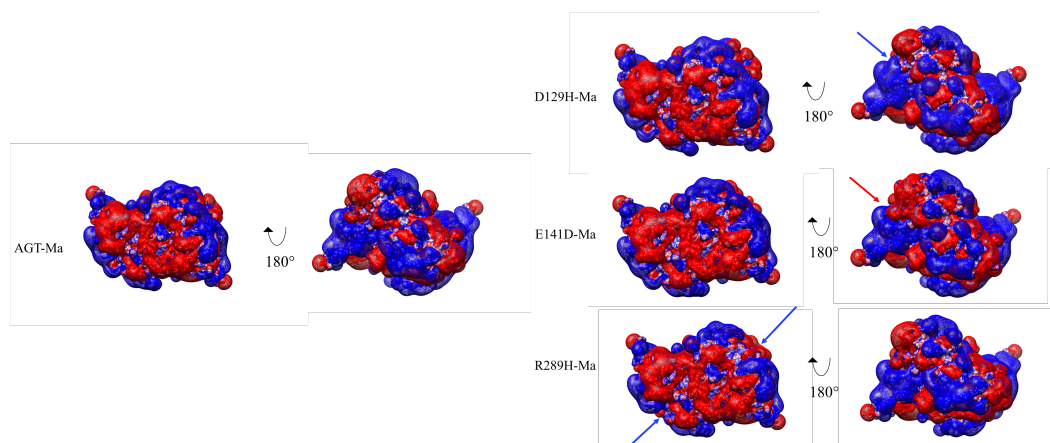


Fig. 41. Distribution of electrostatic potential (-0.5 (red) and +0.5 (blue) kT/e) of AGT-Ma and pathogenic variants D129H-Ma, R289H-Ma and E141D-Ma under physiological conditions (pH 7.4., $I = 0.06$ M, 37°C). Blue and red arrows indicate regions with differences between the electrostatic potential map of AGT-Ma and the variants.

Glu141 is located on the α -helix 6 and it shows a predicted solvent exposure of 59.67% and a predicted pK_a of 4.64. Its main chain is involved in a hydrogen bond with Gln137 of the same helix, which should be maintained upon substitution by an Asp residue, as revealed by molecular modeling studies (data not shown). Although the E141D mutation does not eliminate or change a surface charge, the electrostatic potential map shows that it (i) increases the size and modifies the shape of the negative patches 3 and 4 (red arrows of Fig. 41) and (ii) decreases the exposure to the solvent of Lys234 (from 90.7 to 42.6%) thus changing the shape and slightly reducing the potential of the positive patch 5 and 6 (blue arrows of Fig. 41). While this modest reduction of positive potential could not be enough to prevent AGT aggregation, the increased size of negative patches could promote the electrostatic interactions with positive regions on the surface.

Arg289 is located at the C-terminus of α -helix 11. Having a predicted pK_a of 12.29, it contributes to the AGT surface charge, although it only shows a 41.9% predicted exposure to the solvent. Interestingly, the mutation of Arg289 to His or Cys is pathogenic on the background of the major or the minor allele, respectively. The electrostatic map of the R289H/C variants (identical results were obtained with both mutations) does not shows remarkable differences with

respect to AGT-Ma or AGT-Mi, except for a slight reduction of the size and potential of the positive patches 4 and 5 (blue arrow in Fig. 41), which is expected to reduce the aggregation propensity of AGT under physiological conditions by disfavoring the interaction with the negative patches. Nevertheless, the visual inspection of the AGT structure reveals that Arg289 interacts with Glu293 through an ionic bridge that stabilizes the conformation of α -helix 11. By *in silico* mutagenesis analyses we found that the replacement of Arg289 by a His or a Cys residue could prevent the formation of the ionic bridge with Glu293, thus probably destabilizing the architecture of the region (Fig 42). On these bases, it can be hypothesized that the most probable defect of the R289H-Ma and R289C-Mi variants is a structural alteration of the overall folding, rather than a change of the electrostatic surface promoting aggregation.

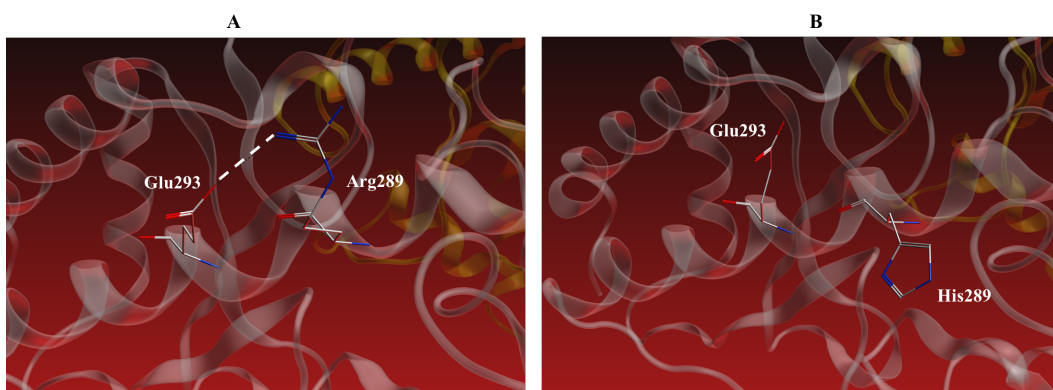


Fig. 42. Ionic bridge between Arg289 and Glu293 (A) and molecular modeling of the mutation R289H (B). The position of Arg289 (A), Glu293 (A and B) and His289 (B) are indicated as sticks. The monomers of AGT are colored yellow and grey. The image was constructed by means of *MOE 2016.08*.

The electrostatic potential map of the pathogenic variant E95K-Mi shows significant alterations of charges distribution in comparison with that of AGT-Mi (Fig. 43). Glu95 is located on a connection loop between α -helix 4 and 5 and it is involved in a hydrogen bond with the main chain of Lys234, which in turn interacts through a hydrogen bond with Thr235 of the same subunit. This residue shows a predicted solvent exposure and pK_a of 12.17% and 3.01, respectively. The Glu-to-Lys substitution remarkably increases the potential and the size of positive patches 5 and 6 as shown by the blue arrows in Fig. 43, due to the presence of Lys95 that is more exposed to the solvent with respect the native Glu95 (28.35% instead of 12.17%).

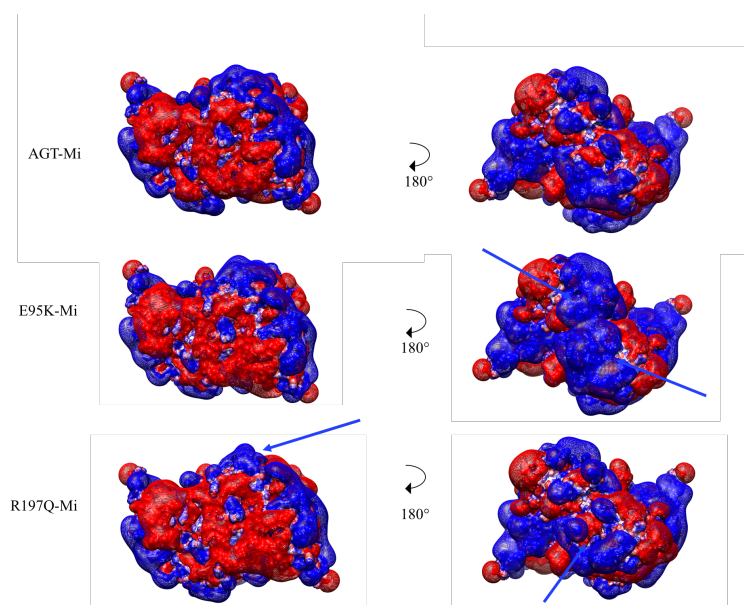


Fig. 43. Distribution of electrostatic potential (-0.5 (red) and +0.5 (blue) kT/e) of AGT-Mi and the pathogenic variants E95K-Mi and R197Q-Mi under physiological conditions (pH 7.4, $I = 0.06$ M, 37°C). The blue arrows indicate regions with differences between the electrostatic potential map of AGT-Mi and the variants.

Thus, the presence of Lys at position 95 not only prevents the formation of the hydrogen bond with Lys234 (Fig. 44), thus probably causing a conformational change, but also generates a wide positive patch on the AGT surface under physiological conditions, which would promote protein aggregation. In agreement

with these considerations, it has been reported that E95K-Mi shows a very low growth and activity in yeast assay (105).

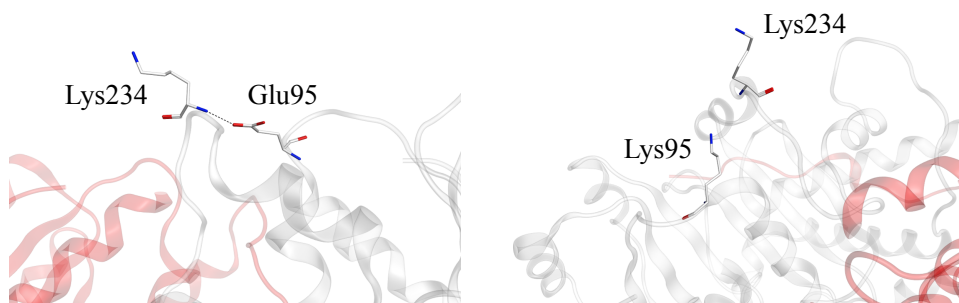


Fig. 44. Hydrogen bond between Glu95 and Lys234 (A) and molecular modeling of the mutation E95K (B). The position of Glu95 (A), Lys236 (A and B) and Lis95 (B) are indicated as sticks. The monomers of AGT are colored red and grey. The image was constructed by means of *MOE 2016.08*.

Arg197, located in the loop between β -strands 7 and 8, shows a 65.17% solvent exposure and it contributes to the formation of the positive patch 7 (Fig. 29). The side chain of Arg197 forms a hydrogen bond with the main chain of Lys5 of the neighboring subunit, which is expected to stabilize the dimeric structure of AGT by forcing the positioning and orientation of the N-terminal arm (106). The presence of a Gln residue at position 197 should interrupt this interaction (Fig. 45). In the R197Q-Mi variant, the consequent increased flexibility of the N-terminal arm could worsen the effects of the P11L mutation and strongly increase the aggregation propensity of AGT. The electrostatic map of the variant only reveals a slight alteration of the charge distribution consisting in a local reduction of the positive potential (blue arrows of Fig. 43), which is not expected to influence the aggregation propensity of AGT *per se*.

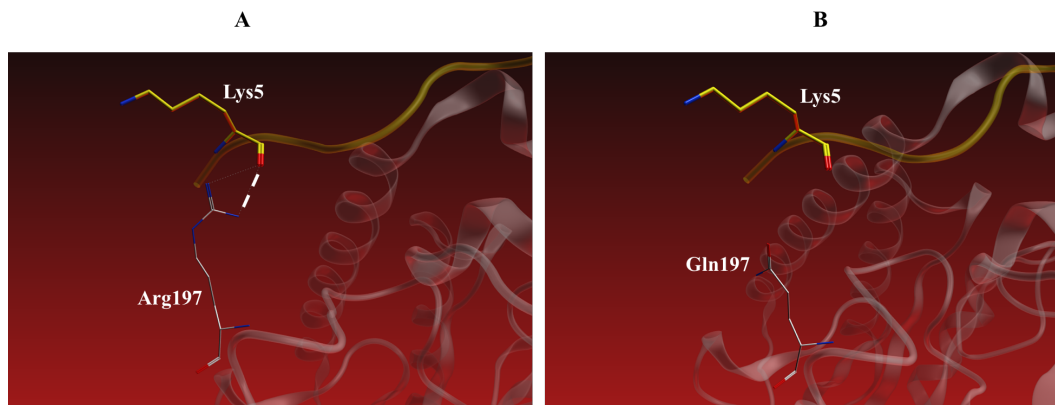


Fig. 45. Hydrogen bond between Arg197 and lys5 (A) and molecular modeling of the mutation R197Q (B). The position of Arg197 (A), Lys5 (A and B) and Gln197 (B) are indicated as sticks. The monomers of AGT are colored yellow and grey. The image was constructed by means of *MOE 2016.08*.

Overall, the *in silico* analyses reported above allow to formulate hypotheses on the possible molecular effects of pathogenic mutations of AGT involving residues exposed to the solvent, taking into account not only the local conformational change caused by each mutation, but also the possible alterations of the electrostatic surface, which could change the aggregation propensity of the protein (Table 9).

Table 1. Predicted effects of pathogenic missense mutations of AGT involving surface residues

Mutation	Allelic background	Surface charge alteration	Folding defect
D129H	Major	Yes	No
E141D	Major	Yes	No
R289H	Major	No	Yes
E95K	Minor	Yes	Yes
R197Q	Minor	Yes	Yes
R289C	Minor	No	Yes

However, site-directed mutagenesis experiments followed by studies at molecular and cellular level will be necessary to better clarify the defect of each variant.

CONCLUSION

We combined *in silico* and *in vitro* study to analyse the aggregative behaviour of AGT and to shed light on the possible influence of polymorphic and pathogenic mutations. The results obtained indicate that: (i) the major allelic form of AGT shows a high surface charge anisotropy that makes it susceptible to an aggregation mediated by electrostatic forces; (ii) PLP binding strongly reduces the aggregation of the protein, thus suggesting that the coenzyme could have a more wide chaperone role than previously known (54); (iii) the P11L mutation enhances the aggregation propensity of AGT, while the I340M mutation has a stabilizing effect; (iv) missense mutations associated with PH1 could play their effects by promoting electrostatic aggregation. These findings, by increasing the knowledge of the biochemical properties of AGT and of the consequences of polymorphic and pathogenic mutations, constitute the base to design new strategies able to improve the stability of the protein as a possible premise for the development of innovative therapeutic strategies for PH1.

7

CONCLUSIONS

The molecular pathogenesis of PH1 is extremely heterogeneous, as diverse enzymatic phenotypes can result in AGT deficiency. A destabilization of the dimeric structure or an increased propensity to aggregation are two of the most frequent defects that characterize disease-causing variants. During my PhD, I analyzed at molecular level both the dimerization and the aggregation processes of AGT. Moreover, I investigated how these phenomena are affected by polymorphic and pathogenic mutations leading to PH1. Altogether, the data obtained allow to:

- 1) identify the interfacial residues Arg118, Phe238, and Phe240, as dimerization hot-spot and engineer a mutated form of AGT stable in solution as a folded monomer;
- 2) demonstrate that the acquisition of the quaternary structure is essential for catalytic activity, study the kinetics of the dimerization process, and provide evidence that monomeric AGT is able to bind PLP and that the coenzyme promotes dimer formation;
- 3) unravel the possible structural basis of the functional synergism between the mutations I244T or F152I and the mutation P11L responsible for the aberrant targeting to mitochondria of the variants I244T-Mi and F152I-Mi associated with PH1;
- 4) elucidate the molecular and cellular consequences of pathogenic mutations involving residues located at the dimer interface and suggest a possible inverse correlation between the degree of structural alteration of a variant and its *in vitro* responsiveness to the treatment with Vitamin B6;
- 5) provide some insights into the AGT folding mechanism, by suggesting that PLP binding and dimerization should be late events of the pathway;
- 6) define that AGT is prone to an electrostatically-driven aggregation process and show that the polymorphic mutations P11L and I340M have opposite effects on the aggregation propensity of the protein.

Overall, these results will contribute to better understand PH1 pathogenesis, by unravelling the molecular defect of several AGT variants, to predict the major determinants of the response of the patients to the available therapy with Vitamin B6, as well as to pave the way for the development of new therapeutic strategies.

8

ADDENDUM

During my PhD course I have been involved in other projects related to 1) the pathogenesis of *AADC* deficiency, a neurometabolic disorder due to the deficit of human Dopa decarboxylase, and 2) the analysis of the pathogenesis of Primary Hyperoxaluria Type I and the development of a new therapeutic strategy based on the use of substrate analogs acting as pharmacological chaperones. A brief summary of the results obtained is reported below.

MOLECULAR PATHOGENESIS OF *AADC* DEFICIENCY

Aromatic amino acid decarboxylase (*AADC*) deficiency is a rare neurometabolic disorder caused by the absence of functional Dopa decarboxylase (*DDC*). More than 50 patients with *DDC* deficiency have been tabulated on the BIOMDB database (http://www.biopku.org/biomdb/biomdb_start.asp), and 23 missense pathogenic mutations have been identified, half of which in homozygous patients. *DDC* is a PLP-dependent enzyme responsible for the production of the neurotransmitters dopamine and serotonin. Although the clinical phenotype associated with the disease has been widely investigated, the molecular effect(s) that each mutation induces on *DDC* are almost unknown. Nonsense and frameshifts mutations lead to the complete loss of the gene product, while missense point mutations cause the synthesis of an aberrant gene product which can be characterized by defects of enzymatic activity, PLP binding, protein stability and/or folding, protein half-life, etc. Current treatments for *AADC* deficiency include the administration of pyridoxine or PLP to increase the residual *DDC* activity, monoamine oxidase inhibitors to minimize dopamine degradation, or dopamine agonists to mime the action of the neurotransmitter. The response to these therapies is variable, but the overall outcome is poor, probably reflecting the allelic heterogeneity. Moreover, since drugs are almost always given in combination, response is hardly ascribable to a single drug. In diseases related to protein malfunction it is diagnostically and therapeutically essential to understand the multiple mechanisms that relate the specific mutants with the pathology. Therefore, the knowledge of the structural and/or functional effect(s) that each amino acid substitution produces on *DDC* would be highly desirable.

1. A comprehensive picture of the mutations associated with aromatic amino acid decarboxylase deficiency: from molecular mechanism to therapy implications.

During my PhD, I contributed to explore the molecular basis of the pathogenesis of *AADC* deficiency. We studied the structural and functional effects caused by 18 pathogenic mutations present in homozygous patients by applying an integrated strategy which uses bioinformatic, spectroscopic and kinetic analyses. These measurements constitute the first comprehensive functional view of *AADC* deficiency mutants. The first point deriving from our study is that all variants either concerning residues located at/near the active site or far from the active site are characterized by a reduced catalytic activity and a different microenvironment of the external aldimines with respect to the wild-type enzyme. Moreover, for all but one (R347Q) we observed a perturbation of the topography of the active site (see below). The second finding is that the majority of the variants show (i) an alteration of the tertiary structure of holoDDC that linearly correlates with an enhanced exposure of hydrophobic sites, (ii) an impairment of the proper apo-holo transition, known to be a conversion from an open to a closed active conformation, and (iii) a decrease of decarboxylase activity. This structure–function relationship allows us to identify the residues which play the most relevant role in the apo-holo conversion (i.e. His70, His72, Tyr79, Phe80 and Pro81 mapping to loop 1 as well as Arg462 and Arg447 directly interacting with loop 1) and suggest that the absence of a proper apo-holo conversion might be sufficient to induce pathogenicity. A different mechanism must be envisaged to explain DDC malfunction for other mutations. R347Q is a catalytic mutation since, albeit no conformational alteration was observed for this variant, it is characterized by a severe loss of decarboxylase activity. On the other hand, replacement of Ala by Gln at position 110 or of Leu by Pro at position 38 appears to have an impact on decarboxylase activity more pronounced than that on the structural integrity of the enzyme. On the basis of the comparative MD study of the putative structure of wild-type, A110Q and L38P, it can be speculated that the

decrease in catalytic activity could be due to the rearrangements occurring around the mutated residue transmitted to the active site, in particular to Phe103 and Ile101 mapping to loop 2. Finally, the finding that, among all the mutations, several of them affect the expression level and solubility of DDC in the *E. coli* expression system suggests folding defects of the variants harboring these mutations. Altogether, our results indicate for the first time that a large percentage of the variants associated with *AADC* deficiency arising from point mutations show conformational changes that, at various degrees, do not allow a proper apoholo transition and a full catalytic activity. This suggests that mutations occurring in distinct regions of a molecule can cause similar conformational changes with similar biological consequences. These events could not be predicted simply based on gene sequences. On the other hand, L38P, A110Q and R347Q result to be mainly or only catalytic mutations, for which additional kinetic features must be identified and understood to explain the kinetic reason(s) underlying their pathogenicity. Overall, these data allow us to acquire a complete knowledge of the enzymatic phenotype associated with each pathogenic mutation and to group patients with AADC deficiency into different therapeutic categories. This general picture of structural and/or functional effects of each mutation linked to AADC deficiency mutations will be a help to guide therapeutic decision and prevent inappropriate use of treatment regimens.

2. The novel R347G pathogenic mutation of aromatic amino acid decarboxylase provides additional molecular insights into enzyme catalysis and deficiency.

This study started from a clinical case of a patient bearing a novel mutation in DDC, R347G, associated with severe enzyme activity deficit. We found that the R347G mutant appears to be affected by a catalytic rather than a folding defect. Thus, we investigated the reason(s) underlying the dramatic loss of decarboxylase activity caused by the substitution of Arg347 with either Gly (~ 475-fold) or Gln (~ 87-fold). The *in silico* modelling of the missing loop 328–339 on the DDC structure predicted interactions of Arg347 with Asp345 and Leu333. Structural and functional features of the new designed mutants, D345A and R347K in

recombinant DDC strongly suggested that residues Arg347, Asp345, and Leu333, as well as their mutual interaction, are structural elements relevant for a proper location/orientation of the substrate and/or of the catalytic groups at or near the active site. Altogether, our data highlight the molecular defects caused by the mutations of Arg347, and allow us to propose a therapeutic approach suitable for patients bearing the mutation R347G. In particular, the low k_{cat} value of the purified recombinant R347G strongly suggests that a dopamine agonist together with folinate could be the best way of assessing a good clinical response of patients bearing the R347G mutation. In fact, while the therapy with dopamine agonists could mime the dopamine effects, the one with folinic acid could not allow its depletion due to the conversion of accumulated l-Dopa into 3-*O*-methylDopa. The same therapy strategy could be applied to patients harbouring the R347Q variant. However, in the case of mutation R347G, which, unlike R347Q, has a 4-fold $K_{D(PLP)}$ value higher than that of the wild-type, the supplementation of pyridoxine could also be useful.

ANALYSIS OF THE PATHOGENESIS OF PRIMARY HYPEROXALURIA TYPE I AND DEVELOPMENT OF A NEW THERAPEUTIC STRATEGY BASED ON THE USE OF PHARMACOLOGICAL CHAPERONES

1. Misfolding caused by the pathogenic mutation G47R on the minor allele of alanine:glyoxylate aminotransferase and chaperoning activity of pyridoxine

Gly47 is a highly conserved residue whose mutation to Arg is associated to PH1. We studied the molecular bases of the AGT deficit caused by Gly47 mutation by expression studies in a mammalian cellular system paired with biochemical analyses on the purified recombinant protein evaluating its responsiveness upon PN treatment.

Recombinant purified G47R-Mi variant exhibits only a 2.5-fold reduction of its k_{cat} , and its apo-form displays a remarkably decreased PLP binding affinity, increased dimer–monomer equilibrium dissociation constant value, susceptibility to thermal denaturation and to N-terminal region proteolytic cleavage, and aggregation propensity. When stably expressed in a mammalian cell line, we found ~ 95% of the intact form of the variant in the insoluble fraction, and proteolyzed (within the N-terminal region) and aggregated forms both in the soluble and insoluble fractions. Moreover, the intact and nicked forms have a peroxisomal and a mitochondrial localization, respectively. Unlike what already seen for G41R-Mi, exposure of G47R-Mi expressing cells to pyridoxine (PN) remarkably increases the expression level and the specific activity in a dose-dependent manner, reroutes all the protein to peroxisomes, and rescues its functionality. Although the mechanism of the different effect of PN on the variants G47R-Mi and G41R-Mi remains elusive, the chaperoning activity of PN may be of value in the therapy of patients bearing the G47R mutation.

2. The Chaperoning Activity of Amino-oxyacetic Acid on Folding-Defective Variants of Human Alanine:Glyoxylate Aminotransferase Causing primary Hyperoxaluria Type I

Pharmacological chaperone (PC) therapy is a newly developed approach for misfolding diseases based on the use of small molecule ligands able to promote the correct folding of a mutant enzyme. We described the interaction of amino-oxyacetic acid (AOA) with the recombinant purified form of the two polymorphic species of AGT, AGT-Ma and AGT-Mi, and with three pathogenic variants bearing previously identified folding defects: G41R-Ma, G170R-Mi and I244T-Mi. We found that for all these enzymes AOA (i) forms an oxime at the active site, (ii) behaves as a slow, tight-binding inhibitor with K_I values in the nanomolar range, and (iii) increases the thermal stability. Furthermore, experiments performed in mammalian cells revealed that AOA act as PC by partly preventing the intracellular aggregation of G41R-Ma and by promoting the correct peroxisomal import of G170R-Mi and I244T-Mi. Based on these data, we carried

out a small-scale screening campaign. We identified four AOA analogues acting as AGT inhibitor, even if only one was found to act as PC. The possible relationship between the structure and the PC activity of these compounds is discussed. Altogether, these results provide the proof-of-principle for the feasibility of a therapy with PCs for PH1-causing variants bearing folding defects and provide the scaffold for the identification of more specific ligands.

9

BIBLIOGRAPHY

1. Danpure CJ (2004) Molecular aetiology of primary hyperoxaluria type 1. (Translated from eng) *Nephron Exp Nephrol* 98(2):e39-44 (in eng).
2. Salido E, Pey AL, Rodriguez R, & Lorenzo V (2012) Primary hyperoxalurias: disorders of glyoxylate detoxification. (Translated from eng) *Biochim Biophys Acta* 1822(9):1453-1464 (in eng).
3. Williams EL, *et al.* (2009) Primary hyperoxaluria type 1: update and additional mutation analysis of the AGXT gene. (Translated from eng) *Hum Mutat* 30(6):910-917 (in eng).
4. Coulter-Mackie MB, Tung A, Henderson HE, Toone JR, & Applegarth DA (2003) The AGT gene in Africa: a distinctive minor allele haplotype, a polymorphism (V326I), and a novel PH1 mutation (A112D) in Black Africans. (Translated from eng) *Mol Genet Metab* 78(1):44-50 (in eng).
5. Danpure CJ (1986) Peroxisomal alanine:glyoxylate aminotransferase and prenatal diagnosis of primary hyperoxaluria type 1. (Translated from eng) *Lancet* 2(8516):1168 (in eng).
6. Osswald H.; Hautmann T (1979) Renal elimination kinetics and plasma half-life of oxalate in man. *Urol Int* 34(6):440-450.
7. Morgan SH, Danpure CJ, Bending MR, & Eisinger AJ (1990) Exclusion of primary hyperoxaluria type I (PHI) in end-stage renal failure by enzymatic analysis of a percutaneous hepatic biopsy. (Translated from eng) *Nephron* 55(3):336-337 (in eng).
8. Zhang X, *et al.* (2003) Crystal structure of alanine:glyoxylate aminotransferase and the relationship between genotype and enzymatic phenotype in primary hyperoxaluria type 1. (Translated from eng) *J Mol Biol* 331(3):643-652 (in eng).
9. Dindo M, *et al.* (2016) Effects of interface mutations on the dimerization of alanine glyoxylate aminotransferase and implications in the mistargeting of the pathogenic variants F152I and I244T. (Translated from eng) *Biochimie* 131:137-148 (in eng).
10. Cellini B, Bertoldi M, Montioli R, Paiardini A, & Borri Voltattorni C (2007) Human wild-type alanine:glyoxylate aminotransferase and its naturally occurring G82E variant: functional properties and physiological implications. (Translated from eng) *Biochem J* 408(1):39-50 (in eng).
11. Ichiyama Aea, . (2000) Oxalate synthesis in mammals: properties and subcellular distributions of serine:pyruvate/alanine:glyoxylate aminotransferase in the liver. *Mol. Ur.* 4:333-340.
12. Danpure CJ, *et al.* (1994) Evolution of alanine:glyoxylate aminotransferase 1 peroxisomal and mitochondrial targeting. A survey of its subcellular distribution in the livers of various representatives of the classes Mammalia, Aves and Amphibia. (Translated from eng) *Eur J Cell Biol* 64(2):295-313 (in eng).
13. Knott TG, *et al.* (2000) The peroxisomal targeting sequence type 1 receptor, Pex5p, and the peroxisomal import efficiency of alanine:glyoxylate aminotransferase. (Translated from eng) *Biochem J* 352 Pt 2:409-418 (in eng).
14. Motley A, *et al.* (1995) Mammalian alanine:glyoxylate aminotransferase 1 is imported into peroxisomes via the PTS1 translocation pathway.

- Increased degeneracy and context specificity of the mammalian PTS1 motif and implications for the peroxisome-to-mitochondrion mistargeting of AGT in primary hyperoxaluria type 1. (Translated from eng) *J Cell Biol* 131(1):95-109 (in eng).
15. Fodor K, Wolf J, Erdmann R, Schliebs W, & Wilmanns M (2012) Molecular requirements for peroxisomal targeting of alanine-glyoxylate aminotransferase as an essential determinant in primary hyperoxaluria type 1. (Translated from eng) *PLoS Biol* 10(4):e1001309 (in eng).
 16. Mesa-Torres N, Tomic N, Albert A, Salido E, & Pey AL (2015) Molecular recognition of PTS-1 cargo proteins by Pex5p: implications for protein mistargeting in primary hyperoxaluria. (Translated from eng) *Biomolecules* 5(1):121-141 (in eng).
 17. Purdue PE, *et al.* (1991) Characterization and chromosomal mapping of a genomic clone encoding human alanine:glyoxylate aminotransferase. (Translated from eng) *Genomics* 10(1):34-42 (in eng).
 18. Purdue PE, Takada Y, & Danpure CJ (1990) Identification of mutations associated with peroxisome-to-mitochondrion mistargeting of alanine:glyoxylate aminotransferase in primary hyperoxaluria type 1. (Translated from eng) *J Cell Biol* 111(6 Pt 1):2341-2351 (in eng).
 19. Purdue PE, Lumb MJ, Allsop J, & Danpure CJ (1991) An intronic duplication in the alanine: glyoxylate aminotransferase gene facilitates identification of mutations in compound heterozygote patients with primary hyperoxaluria type 1. (Translated from eng) *Hum Genet* 87(4):394-396 (in eng).
 20. Purdue PE, Allsop J, Isaya G, Rosenberg LE, & Danpure CJ (1991) Mistargeting of peroxisomal L-alanine:glyoxylate aminotransferase to mitochondria in primary hyperoxaluria patients depends upon activation of a cryptic mitochondrial targeting sequence by a point mutation. (Translated from eng) *Proc Natl Acad Sci U S A* 88(23):10900-10904 (in eng).
 21. Lumb MJ & Danpure CJ (2000) Functional synergism between the most common polymorphism in human alanine:glyoxylate aminotransferase and four of the most common disease-causing mutations. (Translated from eng) *J Biol Chem* 275(46):36415-36422 (in eng).
 22. Lumb MJ, Drake AF, & Danpure CJ (1999) Effect of N-terminal alpha-helix formation on the dimerization and intracellular targeting of alanine:glyoxylate aminotransferase. (Translated from eng) *J Biol Chem* 274(29):20587-20596 (in eng).
 23. Cellini B, Lorenzetto A, Montioli R, Oppici E, & Voltattorni CB (2010) Human liver peroxisomal alanine:glyoxylate aminotransferase: Different stability under chemical stress of the major allele, the minor allele, and its pathogenic G170R variant. (Translated from eng) *Biochimie* 92(12):1801-1811 (in eng).
 24. Hopper ED, Pittman AM, Fitzgerald MC, & Tucker CL (2008) In vivo and in vitro examination of stability of primary hyperoxaluria-associated human alanine:glyoxylate aminotransferase. (Translated from eng) *J Biol Chem* 283(45):30493-30502 (in eng).

25. Coulter-Mackie MB & Lian Q (2006) Consequences of missense mutations for dimerization and turnover of alanine:glyoxylate aminotransferase: study of a spectrum of mutations. (Translated from eng) *Mol Genet Metab* 89(4):349-359 (in eng).
26. Cellini B, Oppici E, Paiardini A, & Montioli R (2012) Molecular insights into primary hyperoxaluria type 1 pathogenesis. (Translated from eng) *Front Biosci (Landmark Ed)* 17:621-634 (in eng).
27. Williams E & Rumsby G (2007) Selected exonic sequencing of the AGXT gene provides a genetic diagnosis in 50% of patients with primary hyperoxaluria type 1. (Translated from eng) *Clin Chem* 53(7):1216-1221 (in eng).
28. Williams EL, Kemper MJ, & Rumsby G (2006) A de novo mutation in the AGXT gene causing primary hyperoxaluria type 1. (Translated from eng) *Am J Kidney Dis* 48(3):481-483 (in eng).
29. Danpure CJ & Rumsby G (2004) Molecular aetiology of primary hyperoxaluria and its implications for clinical management. (Translated from eng) *Expert Rev Mol Med* 6(1):1-16 (in eng).
30. Cellini B, Montioli R, & Voltattorni CB (2011) Human liver peroxisomal alanine:glyoxylate aminotransferase: characterization of the two allelic forms and their pathogenic variants. (Translated from eng) *Biochim Biophys Acta* 1814(11):1577-1584 (in eng).
31. Cellini B, *et al.* (2010) Molecular defects of the glycine 41 variants of alanine glyoxylate aminotransferase associated with primary hyperoxaluria type I. (Translated from eng) *Proc Natl Acad Sci U S A* 107(7):2896-2901 (in eng).
32. Oppici EM, R. Cellini B. (2015) Liver peroxisomal alanine:glyoxylate aminotransferase and the effects of mutations associated with Primary Hyperoxaluria Type I: An overview. *Biochim biophys Acta* 1854(9):1212-1219.
33. Oppici E, *et al.* (2012) Biochemical analyses are instrumental in identifying the impact of mutations on holo and/or apo-forms and on the region(s) of alanine:glyoxylate aminotransferase variants associated with primary hyperoxaluria type I. (Translated from eng) *Mol Genet Metab* 105(1):132-140 (in eng).
34. Oppici E, *et al.* (2013) Crystal structure of the S187F variant of human liver alanine: glyoxylate [corrected] aminotransferase associated with primary hyperoxaluria type I and its functional implications. (Translated from eng) *Proteins* 81(8):1457-1465 (in eng).
35. Oppici E, Roncador A, Montioli R, Bianconi S, & Cellini B (2013) Gly161 mutations associated with Primary Hyperoxaluria Type I induce the cytosolic aggregation and the intracellular degradation of the apo-form of alanine:glyoxylate aminotransferase. (Translated from eng) *Biochim Biophys Acta* 1832(12):2277-2288 (in eng).
36. Cellini B, Montioli R, Paiardini A, Lorenzetto A, & Voltattorni CB (2009) Molecular Insight into the Synergism between the Minor Allele of Human Liver Peroxisomal Alanine:Glyoxylate Aminotransferase and the F152I Mutation. (Translated from eng) *J Biol Chem* 284(13):8349-8358 (in eng).

37. Fargue S, Lewin J, Rumsby G, & Danpure CJ (2013) Four of the most common mutations in primary hyperoxaluria type 1 unmask the cryptic mitochondrial targeting sequence of alanine:glyoxylate aminotransferase encoded by the polymorphic minor allele. (Translated from eng) *J Biol Chem* 288(4):2475-2484 (in eng).
38. Santana A, Salido E, Torres A, & Shapiro LJ (2003) Primary hyperoxaluria type 1 in the Canary Islands: a conformational disease due to I244T mutation in the P11L-containing alanine:glyoxylate aminotransferase. (Translated from eng) *Proc Natl Acad Sci U S A* 100(12):7277-7282 (in eng).
39. Pey AL, Albert A, & Salido E (2013) Protein homeostasis defects of alanine-glyoxylate aminotransferase: new therapeutic strategies in primary hyperoxaluria type I. (Translated from eng) *Biomed Res Int* 2013:687658 (in eng).
40. Mesa-Torres N, *et al.* (2013) The role of protein denaturation energetics and molecular chaperones in the aggregation and mistargeting of mutants causing primary hyperoxaluria type I. (Translated from eng) *PLoS One* 8(8):e71963 (in eng).
41. Danpure CJ (2005) Molecular etiology of primary hyperoxaluria type 1: new directions for treatment. (Translated from eng) *Am J Nephrol* 25(3):303-310 (in eng).
42. Merrill AH & JR & Henderson JM (1990) Vitamin B6 metabolism in human liver. *Ann. N. Y. Acad. Sci.* 585:110-117.
43. Monico CG, Olson JB, & Milliner DS (2005) Implications of genotype and enzyme phenotype in pyridoxine response of patients with type I primary hyperoxaluria. (Translated from eng) *Am J Nephrol* 25(2):183-188 (in eng).
44. Cochat P, *et al.* (2012) Primary hyperoxaluria Type 1: indications for screening and guidance for diagnosis and treatment. (Translated from eng) *Nephrol Dial Transplant* 27(5):1729-1736 (in eng).
45. Pey AL, Salido E, & Sanchez-Ruiz JM (2011) Role of low native state kinetic stability and interaction of partially unfolded states with molecular chaperones in the mitochondrial protein mistargeting associated with primary hyperoxaluria. (Translated from eng) *Amino Acids* 41(5):1233-1245 (in eng).
46. Danpure CJ (2006) Primary hyperoxaluria type 1: AGT mistargeting highlights the fundamental differences between the peroxisomal and mitochondrial protein import pathways. (Translated from eng) *Biochim Biophys Acta* 1763(12):1776-1784 (in eng).
47. Oppici E, *et al.* (2015) The chaperoning activity of Amino-oxyacetic Acid on Folding-Defective Variants of Human:Glyoxylate Aminotransferase Causing Primary Hyperoxaluria Type I. *ACS Chem Biol* 10(10):2227-2236.
48. Roncador A, *et al.* (2016) Use of polymer conjugates for the intraperoxisomal delivery of engineered human alanine:glyoxylate aminotransferase as a protein therapy for primary hyperoxaluria type I. *Nanomedicine*.

49. Hatch M FR (2013) A human strain of Oxalobacter (HC-1) promotes enteric oxalate secretion in the small intestine of mice and reduces urinary oxalate secretion. *Urolithiasis* 41(5):379-384.
50. Hatch M FR, Gyjymishka A, Salido EC, Allison MJ, & RW. F (2011) Reduction of plasma oxalate levels by oral applications of Oxalobacter formigenes in 2 patients with infantile oxalosis. *American Journal of kidney disease: the official journal of the National Kidney Foundation* 58(3):453-455.
51. Castello R bR, D'aria S, Annunziata P, Piccolo P, Brunetti-Pierri N. (2016) Helper-dependent adenoviral vectors for liver-directed gene therapy of primary hyperoxaluria type I. *Gene Therapy* 23(2):129-134.
52. Hoyer-Kuhn H, *et al.* (2014) Vitamin b6 in primary hyperoxaluria I: first prospective trial after 40 years of practice. (Translated from eng) *Clin J Am Soc Nephrol* 9(3):468-477 (in eng).
53. Hoppe B (2012) An update on primary hyperoxaluria. *Nature reviews Nephrology* 8(8):467-475.
54. Cellini B, Montioli R, Oppici E, Astegno A, & Voltattorni CB (2013) The chaperone role of the pyridoxal 5'-phosphate and its implications for rare diseases involving B6-dependent enzymes. (Translated from Eng) *Clin Biochem* (in Eng).
55. Oppici E, *et al.* (2015) Pyridoxamine and pyridoxal are more effective than pyridoxine in rescuing folding-defective variants of human alanine:glyoxylate aminotransferase causing hyperoxaluria type I. *Human Molecular genetics* 24(19):5500-5511.
56. CCG CCGI (Molecular Operating Environment (MOE)1010 Sherbooke St. West, Suite #910, Montreal, QC, Canada, H3A 2R7).
57. Labute P (2010) LowModeMD—implicit low-mode velocity filtering applied to conformational search of macrocycles and protein loops. *J Chem Inf Model* 50:92–800.
58. Anonymous (The Pymol Molecular Graphics System, version 1.8 Schrodinger, LLC).
59. Chen R, LI L, & Z. W (2003) ZDOCK: An initial-stage Protein Docking Algorithm. *Proteins* 52(1):80-87.
60. Dell'orco D, De Benedetti PG, & F F (2007) In silico screening of mutational effects on enzyme-protein inhibitor affinity: a docking based approach. *BMC Struct Biol.* 7(37).
61. Dell'orco D (2009) Fast predictions of thermodynamics and kinetics of protein-protein recognition from structures: from molecular design to system biology. *Mol. Biosystem* 5(4):323-334.
62. Baker NA, Sept D, Joseph S, Holst MJ, & McCammon JA (2001) Electrostatics of nanosystems: application to microtubules and the ribosome. (Translated from eng) *Proc Natl Acad Sci U S A* 98(18):10037-10041 (in eng).
63. The Resource for Biocomputing V, and Informatics (Molecular graphics and analyses performed with UCSF Chimera package University of California, San Francisco).

64. Pettersen EF, *et al.* (2004) UCSF Chimera--a visualization system for exploratory research and analysis. (Translated from eng) *J Comput Chem* 25(13):1605-1612 (in eng).
65. Ren Jingyuan, Williams Nadja, Clementi Luca, Krishnan Sriram, & Wilfred. LW (2010) Opal web service for biomedical applications. *Nucleic Acids Res.*:724-731.
66. Dolinsky TJ, Niesen JE, McCammon JA, & NA. B (2004) PDB2PQR: an automated pipeline for the setup, execution, and analysis of Poisson-Boltzmann electrostatics calculations. *Nucleic Acids Res* 1(32):665-667.
67. Mats H. M. Olsson, Chresten R. Sondergaard, Michal Rostkowski, & Jensen JH (2011) PROPKA3: Consistent Treatment of Internal and Surface Residues in Empirical pKa Predictions. *J. Chem. Theory Comput.* 7(2):525-537.
68. Pronk S, *et al.* (2013) GROMACS 4.5: a high-throughput and highly parallel open source molecular simulation toolkit. (Translated from eng) *Bioinformatics* 29(7):845-854 (in eng).
69. Oostenbrink C, Villa A, Mark AE, & van Gunsteren WF (2004) A biomolecular force field based on the free enthalpy of hydration and solvation: the GROMOS force-field parameter sets 53A5 and 53A6. (Translated from eng) *J Comput Chem* 25(13):1656-1676 (in eng).
70. Berendsen HJ, Postma, J.P., van Gunsteren, W.F. and Hermans, J., (1981) *Interaction models for water in relation to protein hydration. In Intermolecular forces.*
71. Webb BaS, A., (2014) Comparative protein structure modeling using Modeller. *Current protocols in bioinformatics*:5-6.
72. Malde AK, *et al.* (2011) An Automated Force Field Topology Builder (ATB) and Repository: Version 1.0. (Translated from eng) *J Chem Theory Comput* 7(12):4026-4037 (in eng).
73. Berendsen HJ, Postma, J.V., van Gunsteren, W.F., DiNola, A.R.H.J. and Haak, J.R., (1984) Molecular dynamics with coupling to an external bath. . *The Journal of chemical physics* 81(8):3684-3690.
74. Hess B, Bekker, H., Berendsen, H.J. and Fraaije, J.G., (1997) LINCS: a linear constraint solver for molecular simulations. *Journal of computational chemistry* 18(12):1463-1472.
75. York DM, Wlodawer A, Pedersen LG, & Darden TA (1994) Atomic-level accuracy in simulations of large protein crystals. (Translated from eng) *Proc Natl Acad Sci U S A* 91(18):8715-8718 (in eng).
76. Hoover WG (1985) Canonical dynamics: Equilibrium phase-space distributions. (Translated from Eng) *Phys Rev A Gen Phys* 31(3):1695-1697 (in Eng).
77. Parrinello MaR, A., (1981) Polymorphic transitions in single crystals: A new molecular dynamics method. *Journal of Applied physics* 52(12):7182-7190.
78. Donald JE, Kulp DW, & DeGrado WF (2011) Salt bridges: geometrically specific, designable interactions. (Translated from eng) *Proteins* 79(3):898-915 (in eng).
79. Kumar A, Rajendran V, Sethumadhavan R, & Purohit R (2013) Molecular dynamic simulation reveals damaging impact of RAC1 F28L mutation in

- the switch I region. (Translated from eng) *PLoS One* 8(10):e77453 (in eng).
80. Pace CN, Vajdos F, Fee L, Grimsley G, & Gray T (1995) How to measure and predict the molar absorption coefficient of a protein. (Translated from eng) *Protein Sci* 4(11):2411-2423 (in eng).
 81. Manning LR, Dumoulin A, Jenkins WT, Winslow RM, & Manning JM (1999) Determining subunit dissociation constants in natural and recombinant proteins. (Translated from eng) *Methods Enzymol* 306:113-129 (in eng).
 82. Watzky MA & RG. F (1997) Transition metal nanocluster formation kinetic and mechanistic studies. A new mechanism when hydrogen is the reductant:slow, continuous nucleation and fast autocatalytic surface growth. *J. Am. Chem* 119:10382-10400.
 83. Morris AM, Watzky Am, Ahgar JN, & GF. F (2008) Fitting neurological Protein Aggregation Kinetic Data via a 2-Step, Minimal/"Ockham's Razor" Model: The Finke-Watzky Mechanism of Nucleation Followed by Autocatalytic growth. *Biochemistry* 47:2413-2427.
 84. Montioli R, Cellini B, Dindo M, Oppici E, & Voltattorni CB (2013) Interaction of human Dopa decarboxylase with L-Dopa: spectroscopic and kinetic studies as a function of pH. (Translated from eng) *Biomed Res Int* 2013:161456 (in eng).
 85. Bolte S & Cordelieres FP (2006) A guided tour into subcellular colocalization analysis in light microscopy. (Translated from eng) *J Microsc* 224(Pt 3):213-232 (in eng).
 86. Danpure CJ (1998) The molecular basis of alanine: glyoxylate aminotransferase mistargeting: the most common single cause of primary hyperoxaluria type 1. (Translated from eng) *J Nephrol* 11 Suppl 1:8-12 (in eng).
 87. Chien-Yun Lee, Yi-Liang Liu, Chih-Li lin, Gung-Yaw liu, & hung H-C (2014) Functional roles of he Dimer-Interface Residues in human Ornithine Decarboxylase. *Plos One*.
 88. Peverelli MG, Soares da Costa TP, Kirby N, & Perugini MA (2016) Dimerization of Bacterial Diaminopimelate Decarboxylase Is Essential for Catalysis. (Translated from eng) *J Biol Chem* 291(18):9785-9795 (in eng).
 89. Montioli R, Cellini B, Bertoldi M, Paiardini A, & Voltattorni CB (2009) An engineered folded PLP-bound monomer of *Treponema denticola* cystalysin reveals the effect of the dimeric structure on the catalytic properties of the enzyme. (Translated from eng) *Proteins* 74(2):304-317 (in eng).
 90. Alessia David & Sternberg MJE (2015) The contribution of missense mutations in Core and Rim Residues of Protein-Protein UInterface to Human Disease. *J Mol Biol.* 427(17):2886-2898.
 91. Montioli R, *et al.* (2012) The N-terminal extension is essential for the formation of the active dimeric structure of liver peroxisomal alanine:glyoxylate aminotransferase. (Translated from eng) *Int J Biochem Cell Biol* 44(3):536-546 (in eng).

92. Montioli R, *et al.* (2015) Misfolding caused by the pathogenic mutation G47R on the minor allele of alanine:glyoxylate aminotransferase and chaperoning activity of pyridoxine. *Biochim Biophys Acta*.
93. Trunzo R, *et al.* (2016) In vitro residual activity of phenylalanine hydroxylase variants and correlation with metabolic phenotypes in PKU. *Gene*.
94. Oliva A, Llabrès M, & JB F (2015) Fitting bevacizumab aggregation kinetic data with the Finke-Watzky two-step model: Effect of thermal and mechanical stress. *Eur J Pharm Sci.* 18(77):170-179.
95. Philo JS & T A (2009) Mechanism of protein aggregation. *Curr Pharm Biotechnol* 10(4):348-351.
96. Morris AM, Watzky MA, & RG F (2009) Protein aggregation kinetics, mechanism, and curve-fitting: A review of the literature. *Biochimica et Biophysica acta (BBA)* 1794(3):275-397.
97. Fink AL (1998) Protein aggregation: folding aggregates, inclusion bodies and amyloid. *Folding and design* 3(1):R9-R23.
98. Neves-Petersen MT & SB P (2003) Protein electrostatics: a review of the equations and methods used to model electrostatic equations in biomolecules--applications in biotechnology. *Biotechnol Annu Rev.* 9:315-395.
99. Majhi PR, *et al.* (2006) Electrostatically driven protein aggregation: beta-lactoglobulin at low ionic strength. *Langmuir* 24(22):9150-9159.
100. Lee LP & B T (2001) Barstar is electrostatically optimized for tight binding to barnase. *Nature structural biology* 8:73-76.
101. Shen BW, Hennig M, Hohenester E, Jansonius JN, & T. S (1998) Crystal structure of human recombinant ornithine aminotransferase. *J.Mol. Biol* 277:81-102.
102. Lorber B, Fischer F, Bailly M, Roy H, & Kern D (2012) Protein analysis by dynamic light scattering: methods and techniques for students. *Biochem Mol Bio Educ* 40(6):372-382.
103. Danpure CJ, *et al.* (1990) Subcellular distribution of hepatic alanine:glyoxylate aminotransferase in various mammalian species. (Translated from eng) *J Cell Sci* 97 (Pt 4):669-678 (in eng).
104. Mesa-Torres N, *et al.* (2014) The consensus-based approach for gene/enzyme replacement therapies and crystallization strategies: the case of human alanine-glyoxylate aminotransferase. (Translated from eng) *Biochem J* 462(3):453-463 (in eng).
105. Lage MD, Pittman AM, Roncador A, Cellini B, & Tucker CL (2014) Allele-specific characterization of alanine: glyoxylate aminotransferase variants associated with primary hyperoxaluria. (Translated from eng) *PLoS One* 9(4):e94338 (in eng).
106. Djordjevic S, *et al.* (2010) Structural implications of a G170R mutation of alanine:glyoxylate aminotransferase that is associated with peroxisome-to-mitochondrion mistargeting. (Translated from eng) *Acta Crystallogr Sect F Struct Biol Cryst Commun* 66(Pt 3):233-236 (in eng).

10

PUBLICATIONS

A comprehensive picture of the mutations associated with aromatic amino acid decarboxylase deficiency: from molecular mechanisms to therapy implications

Riccardo Montioli^{1,†}, Mirco Dindo¹, Alejandro Giorgetti², Stefano Piccoli², Barbara Cellini¹ and Carla Borri Voltattorni^{1,†,*}

¹Department of Life Sciences and Reproduction (Section of Biological Chemistry) and ²Department of Biotechnology, University of Verona, Verona, Italy

Received April 14, 2014; Revised May 21, 2014; Accepted May 22, 2014

Dopa decarboxylase (DDC), or aromatic amino acid decarboxylase (AADC), is a pyridoxal 5'-phosphate enzyme responsible for the production of the neurotransmitters dopamine and serotonin. Deficit of this enzyme causes AADC deficiency, an inherited neurometabolic disorder. To date, 18 missense homozygous mutations have been identified through genetic screening in ~80 patients. However, little is known about the mechanism(s) by which mutations cause disease. Here we investigated the impact of these pathogenic mutations and of an artificial one on the conformation and the activity of wild-type DDC by a combined approach of bioinformatic, spectroscopic and kinetic analyses. All mutations reduce the k_{cat} value, and, except the mutation R347Q, alter the tertiary structure, as revealed by an increased hydrophobic surface and a decreased near-UV circular dichroism signal. The integrated analysis of the structural and functional consequences of each mutation strongly suggests that the reason underlying the pathogenicity of the majority of disease-causing mutations is the incorrect apo-holo conversion. In fact, the most remarkable effects are seen upon mutation of residues His70, His72, Tyr79, Phe80, Pro81, Arg462 and Arg447 mapping to or directly interacting with loop1, a structural key element involved in the apo-holo switch. Instead, different mechanisms are responsible for the pathogenicity of R347Q, a mere catalytic mutation, and of L38P and A110Q mutations causing structural-functional defects. These are due to local perturbation transmitted to the active site, as predicted by molecular dynamic analyses. Overall, the results not only give comprehensive molecular insights into AADC deficiency, but also provide an experimental framework to suggest appropriate therapeutic treatments.

INTRODUCTION

Dopa decarboxylase (DDC) (EC 4.1.1.28) is a homodimeric stereospecific α -decarboxylase that utilizes pyridoxal 5'-phosphate (PLP) as coenzyme. The enzyme is found in neural and peripheral tissues, notably liver and kidney. DDC is responsible for the conversion of L-Dopa and L-5-hydroxytryptophan (L-5HTP) to dopamine and serotonin, respectively, which are two of the major neurotransmitters of the mammalian nervous system. However, since the enzyme, at least *in vitro*, displays a much broader substrate specificity, it is also named aromatic amino acid decarboxylase (AADC). Naturally occurring and recombinant pig kidney and rat liver enzymes as well as human DDC in the

recombinant form have been purified and characterized (1–3). Many structural and functional data were obtained from pig kidney, and, recently, from human DDC enzymes (4). They consist in the definition of the steady-state kinetic parameters for L-Dopa and L-5-HTP (5,6), the absorbance and dichroic features of the enzyme in the internal and external aldimine forms (5,6), and in the identification of structural elements functionally relevant for catalysis, like a loop susceptible to proteases and some residues at or near the active site (7–10).

Burkhard *et al.* (11) obtained the crystal structure of ligand-free pig kidney DDC and its complex with the anti-Parkinson drug carbidopa. Several features of DDC were evident in these

*To whom correspondence should be addressed at: Department of Life Sciences and Reproduction (section of Biological Chemistry), University of Verona, Strada Le Grazie, 8, Verona, Italy. Tel: +39 0458027175; Fax: +039 0458027179; Email: carla.borrivoltattorni@univr.it

[†]R.M. and C.B.V. are both senior authors of the paper.

structures. The overall structure of the protein is a tightly associated dimer in which each monomer consists of a large domain containing the PLP-binding site, a C-terminal small domain, and a N-terminal domain packing on the top of the large domain. In both these structures a short stretch of 11 amino acids (residues 328–339), invisible in the electron density map, represents a mobile loop important for the catalytic mechanism (7,10). The resolved structures also revealed the way in which PLP is anchored to the enzyme, which amino acid residues might be involved in the catalytic activity of the enzyme, and, importantly, how carbidopa, a substrate analog, binds DDC. The inhibitor forms a hydrazone linkage with PLP, its carboxylate moiety is nearly orthogonal to the PLP ring and its 3' and 4' catechol hydroxyl groups are hydrogen bonded to the hydroxyl group of the phosphate of the coenzyme and to Thr82, respectively. The resolution of the crystal structure of the apo form of human DDC is a recent achievement (12). Unexpectedly, this structure is an open conformation in which the active site becomes solvent exposed and the dimer interface is reduced to only the N-domains. The comparison of this structure with that of the holoenzyme from pig kidney allowed us to establish that a remarkable change of loop 1 (residues 66–84) transmitted to loops 2 (residues 100–110) and 3 (residues 323–357) of the adjacent subunit occurs in the transition from the apo to the holo form of DDC.

The enzyme is of medical interest because it is the target of drugs used in the therapy of Parkinson's disease (13,14) and because its deficit leads to AADC deficiency (OMIM#608643), a human autosomal recessive disorder. This inherited disease is caused by mutations in the *AADC* gene on chromosome 12p123-p12.1 leading to the loss of function of DDC. The clinical phenotype of the pathology varies extensively among patients, but common manifestations include vegetative symptoms, oculogyric crises, dystonia and severe neurologic dysfunction, usually beginning in infancy or childhood (15). A mild form of the disease has also been reported (16). Diagnosis of AADC deficiency may be made by a finding of reduced levels of 5-hydroxyindolacetic acid and homovanillic acid in cerebrospinal fluid in conjunction with elevated levels of 3-O-methyldopa, L-Dopa and L-5HTP in cerebrospinal fluid, plasma and urine (17–19). Definitive diagnosis may be obtained by the measurement of DDC activity in plasma. Genotyping of >80 AADC deficiency homozygous and compound heterozygous patients identified 28 missense mutations, 18 of which in homozygous patients. The distribution of mutants among patients is quite homogeneous (with a mean value of two patients per mutation except for S250F that is present in about five cases). Clinical data for AADC deficiency-causing mutations are limited to a small number of individuals, and, thus the genotype-phenotype correlation is almost completely unknown. The chemical management of AADC deficiency, usually involving vitamin B6, dopamine agonists and monoamine oxidase (MAO) inhibitors, is aimed at correcting the neurotransmitters abnormalities. Moreover, gene therapy appears to be a better prospect for the future treatment of AADC deficiency (20–22). However, up to date treatment options are limited, and in many cases response to the current treatments is disappointing.

Since an inherited mutation can alter protein function in many different ways (change in the kinetic parameters and/or in the coenzyme binding, reduced protein expression level, protein misfolding or instability), it is essential to understand the molecular

mechanism(s) of the effects of each disease-causing mutation. Characterization of some variants linked to AADC deficiency has begun to provide invaluable insights into their molecular defects, thus allowing to foresee the proper therapeutic treatments for patients bearing the examined mutations (3,23). However, a thorough study of the pathogenic effects of a significant number of missense pathogenic mutations is still lacking.

In the present study we have employed bioinformatic, kinetic and spectroscopic analyses to characterize all the AADC deficiency associated point mutations identified in homozygous patients. The already studied pathogenic variants (G102S, F309L and S250F) were included in this study for a more in-depth and complete molecular insights into the pathogenesis of AADC deficiency. In addition, the artificial variant F80A was also taken in consideration since Phe80, a key residue of loop 1, is involved in the switch between the apo and holo forms of the enzyme (12). All variants in the recombinant purified form were analyzed to determine their PLP binding mode and affinity, secondary and tertiary structure, surface hydrophobicity, and kinetic parameters. The results allowed us to highlight a linear correlation between the structural and functional effects of a large number of mutations, and to suggest that the affected residues are involved, even if at a different degree, into the conversion from the open apo conformation to the closed active holo form. This set of mutations does not include the catalytic mutation R347Q or the mutations L38P and A110Q, for which a catalytic effect predominant over a structural one has been observed. Bioinformatic and molecular dynamic (MD) analyses help to envisage the possible role of the residues Arg347, Leu38 and Ala110 affected by pathogenic mutations on the structure–function relationship of DDC.

RESULTS AND DISCUSSION

Location of pathogenic mutations in the crystal structure of human DDC

In the past few decades, a number of rare inborn errors due to the loss of function of enzymes requiring PLP to function were identified (24,25). The genetic defects are most frequently due to missense mutations. Among these inherited diseases, we focused our attention on homocystinuria, gyrate atrophy, primary hyperoxaluria type 1 and AADC deficiency. These are caused, respectively, by deficit of cystathionine- β -synthase (CBS), ornithine aminotransferase (OAT), alanine glyoxylate aminotransferase (AGT) and DDC. The reasons for such focusing are the following. First, a remarkable number (ranging from 8 to 150) of pathogenic mutations have been identified for these disorders. Second, the crystal structure of human CBS (26), OAT (27) and AGT (28) as well as that of pig kidney DDC (11) (~90% sequence identity with human DDC) has been solved. The inspection of these structures reveals that while the pathogenic mutations of CBS, OAT, and AGT are spread out over the entire structure (Supplementary Material, Fig. S1), those of DDC are essentially grouped in a central region of each enzyme monomer. This region comprises a large portion of the large domain, two β -strands and an α -helix of the C-terminal domain as well as a limited portion of the N-terminal domain. The majority of the residues affected by mutations map to highly or moderately conserved residues among α -decarboxylases of distantly related species.

This indicates that they are essential for enzyme structure and function (Fig. 1).

Eight mutations are located at loop 1 (T69M, H70T, H72Y, Y79C, P81L), 2 (G102S, A110Q) and 3 (R347Q), which have a leading role in the conversion from the apo to the holo form of DDC. Even if not affected by a pathogenic mutation, the residue Phe80 mapping to loop 1 deserves note since, together with Tyr79, it represents a key residue in the loop 1 rearrangement (12). The other mutations that affect residues not directly involved in the apo-holo transition comprise two mutations (L38P and P47H) of residues belonging to the N-terminus, four mutations (L408I, R412W, R447H and R462P) of residues lying on the C-terminal domain and four mutations (G123R, S250F, R285W, F309L) of residues mapping to the large domain, but outside the loops (Fig. 2A).

Functional and conformational impact of amino acid replacement on 3D networks of side-chain interactions in human DDC

The position and the possible structural effects of each mutation were analyzed by the inspection of the crystal structures of pig kidney holoDDC (pdb file 1js6) and human apoDDC (pdb file 3rbf), and by *in silico* mutational analysis. On the basis of the position of the mutated residue, the examined mutations can be grouped in four clusters. The first cluster comprises mutations of residues belonging to loops 1, 2 or 3 of DDC (Fig. 2B). The side chain of Thr69 and His70 points far from the active site, whereas His72 side chain faces the active site and contributes to generate the hydrophobic cleft that accommodates the substrate. Mutational analysis predicted that while the T69M substitution does not produce significant steric clashes with the neighboring residues, H70T and H72Y substitution could affect both the loop 1 conformation and the active site microenvironment, and might alter the position of Trp71, a residue involved in the substrate binding (13). Tyr79 and Phe80 are located in the center of loop 1 and, as already reported, upon PLP binding both residues undergo an inversion of position with

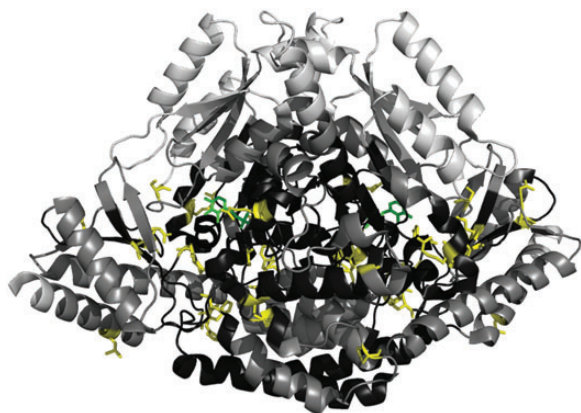


Figure 1. Amino acids conservation and pathogenic mutation sites map of DDC. Ribbon representation of the dimeric structure of pig kidney holoDDC (pdb file 1js6) colored on the basis of the conservation degree as light gray, dark gray and black for low (up to 25%), medium (from 25 to 75%) and high (from 75 to 100%) conservation level, respectively, in the selected subset of DDC homologous sequence (see Material and Methods). The pathogenic mutation sites and the PLP molecules are represented as yellow and green sticks, respectively.

respect to the loop 1 backbone (12). In fact, in the holoDDC structure Tyr79 interacts with the N ϵ 1 of Arg447 and the side chain of Phe103 by, respectively, a hydrogen bond and a σ - π hydrophobic interaction. The phenyl ring of Phe80 engages Arg447 and Tyr274 with a cation- π and a π - π interaction, respectively, while in the apoDDC structure the hydroxyl group of Tyr79 is hydrogen bonded to the N δ 1 of His302, and Phe80 phenyl ring interacts with the Trp71 side chain. Moreover, Tyr79 is involved in the binding of the substrate (13). On this basis, it is reasonable to say that the Y79C and F80A substitutions could cause the loss of important anchoring points that stabilize the loop 1 conformation both in the holo and in the apo form. Pro81 is located in the center of loop 1 and does not interact with any of the neighboring residues neither in the holo- nor in the apoDDC form. Its presence reduces the flexibility of the backbone, thus possibly affecting the torsion movement of loop 1 during the apo-holo transition. It is reasonable to infer that the Pro-to-Leu substitution could alter either the conformation and/or the movement of loop 1. Gly102 and Ala110 are located in proximity of the N- and C-terminal ends of loop 2, respectively. *In silico* analyses, together with previously reported molecular modeling studies (3), indicate that the G102S substitution could introduce a minimal steric hindrance in the cleft between loop 2 and loop 3 and indirectly alter the position of Phe103, a residue that plays a role in substrate binding (11). The A110Q substitution generates a remarkable steric hindrance between the α -helix 8 and the N-terminal α -helix 4 (55–65) that could induce a repositioning of the two helices and a local alteration of loop 2 conformation. Arg347 adopts a central position in loop 3 at the entrance of the active site cavity. It is noteworthy that Arg347 is close to the loop 328–339, a mobile segment invisible in the electron density map that is essential for the decarboxylase activity (7,10,11). Nevertheless, *in silico* analyses predict that R347Q substitution does not generate substantial local structural alterations.

The second cluster comprises the L408I, R412W, R462P and R447H mutations that affect residues belonging to the C-terminal domain of the protein (Fig. 2C). Arg447 and Arg462 are directly interacting with loop 1. In fact, in the holoDDC structure, the side chain of Arg447 interacts with the phenyl ring of the Phe80 through an hydrophobic σ - π linkage and, in the apoDDC structure, the N ϵ 1 of the side chain of Arg462 is hydrogen bonded with the side chain hydroxyl group of Tyr75. Thus, it is reasonable that R447H and R462P substitutions could perturb the correct position of loop 1 and/or the conformational change of the loop during the apo-holo transition. Leu408 is located in the N-terminal end of the β -strand 9 in proximity of Arg447 and contributes in generating the hydrophobic compartment that hosts Phe80 in the holoDDC. The L408I substitution does not change the polarity of the region but could determine a moderate steric hindrance that possibly disturbs the correct position of the side chain of Phe80. Arg412 is a surface residue located far from the active site at the C-terminal end of the β -strand 9 and does not interact with loops 1, 2 and 3. The drastic substitution R412W is predicted to generate a remarkable steric hindrance between β -strand 9 and the α -helix 25, which could impair the correct folding of the overall C-terminal domain conformation.

The third cluster comprises the N-terminal domain mutations L38P and P47H (Fig. 2D). Leu38 belongs to the 3/10 helix 3 and faces the Ala110 side chain, while Pro47 is positioned in the

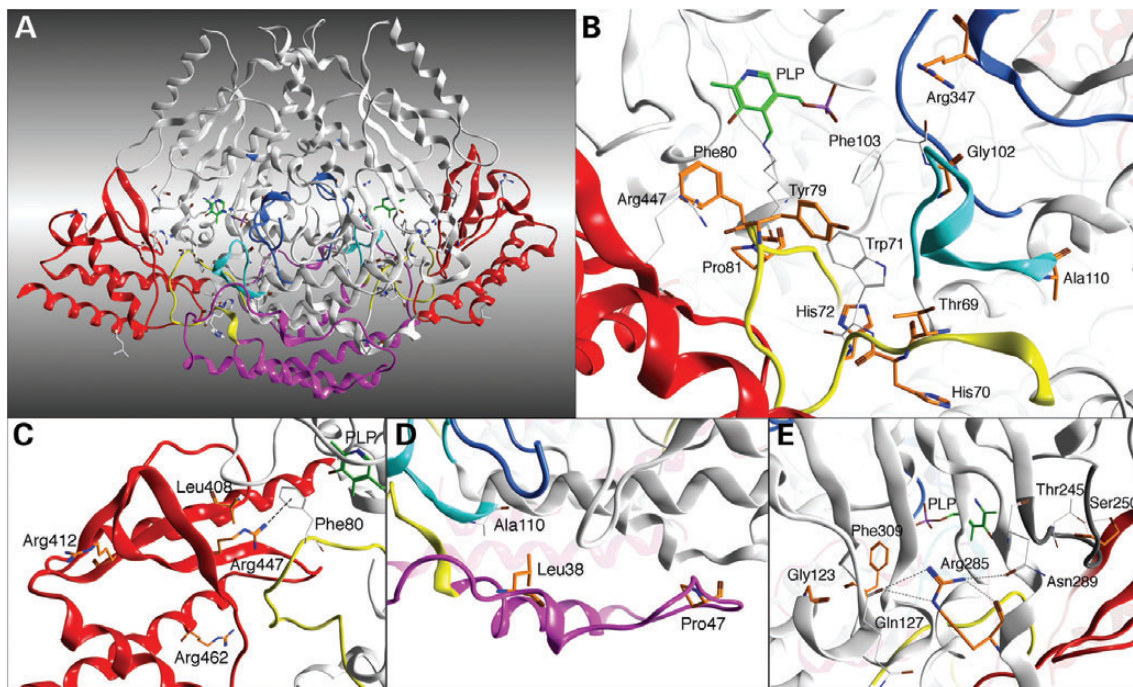


Figure 2. Tridimensional representation of the mutation sites. Ribbons representation of the crystal structure of pig kidney holoDDC. The large domains of both monomers are colored white except for loops 1, 2 and 3 that are colored yellow, cyan and blue, respectively. The C-terminal and the N-terminal domains are colored in red and magenta, respectively. The described color code has been used for all the panels. (A) The overall dimeric structure of holoDDC with all the mutation sites represented as white sticks. (B, C, D and E) The residues subjected to pathogenic mutations (orange stick) and their main contact residues (white sticks) belonging to loops 1, 2 and 3 (B), the C-terminal domain (C), the N-terminal domain (D), and the remaining portion of large domain (E). The PLP molecules are represented as green sticks.

middle of the unstructured loop 42–52. The Leu38→Pro substitution alters the backbone flexibility of the short helix 3 and could impair the hydrophobic contact with Ala110, while the Pro47→His substitution could affect the conformation of loop 42–52. Considering the distance of the mutation sites from the active site, the possible functional effects of both substitutions are expected to be only indirect and hard to predict.

The fourth cluster comprises the G123R, S250F, R285W and F309L mutations that affect residues belonging to the large domain of DDC that do not directly interact with loops 1, 2 and 3 (Fig 2E). Gly123 and Arg285 are located far from the active site on the α -helix 8 and 16, respectively. The bulky arginine side chain introduced by the G123R substitution generates a considerable hindrance between the surface helix 8 and the β -barrel structure that wraps up the active site on the *re* face of PLP. Moreover the R285W substitution impairs the Arg285 side chain interactions with the Gln127 and Asn289, and introduces a bulky hydrophobic side chain in a surface region. Ser250 is located on loop 243–252. As already reported (23), the S250F substitution impairs the H-bond between the Ser250 and Thr245 side chains, and could locally change the surface hydrophobicity and destabilize the conformation of loop 243–252. Considering the distance from the active site and the chemical changes introduced by the G123R, S250F and R285W substitutions, it is reasonable to suggest that these mutations probably cause structural and/or folding alterations with only indirect functional effects. Differently from the other residues belonging to the third cluster that are located far from the coenzyme, Phe309 is placed in proximity of the PLP phosphate group in loop 304–311. As previously reported (3), the reduced

hindrance of Leu309 in the F309L mutant might be less efficient in delimiting the apolar cavity of the substrate binding cleft.

Expression and purification of the variants

All mutations under study were inserted in the DDC cDNA by site-directed mutagenesis, and the variants were expressed in *Escherichia coli* and purified. The purified variants were homogeneous as indicated by a single band on SDS–PAGE electrophoresis with a mobility identical to that of the wild-type. Yields of the mutant enzymes after standard purification were quite variable, ranging from 5 to 90% with respect to that of wild-type. In comparison with wild-type DDC, the total expression level of each variant in *E. coli* was (i) equal, within experimental error, for the L38P, T69M, R347Q and L408I variants, (ii) $\geq 75\%$ for the H70T, H72Y, Y79C, F80A, G102S, A110Q, G123R and F309L variants (iii) between 50 and 75% for the P47H, P81L, S250F, R285W, R412W, R447H and R462P variants. Moreover, the soluble fraction of the lysate contained $\sim 50\%$ of the total protein for all the enzymatic species except the P47H, R285W, R412W and R447H variants, for which this percentage dropped to $\sim 20\%$. The effects of each amino acid substitution were analyzed by means of bioinformatic, spectroscopic and kinetic analyses of the variants.

PLP binding of variants: mode and affinity

Titration analysis of the apomutants with PLP fitted to the appropriate equation yielded the equilibrium dissociation constant for PLP ($K_{D(PLP)}$) values reported in the first column of Table 1. All

Table 1. Equilibrium dissociation constants for PLP ($K_{D(PLP)}$) and steady-state kinetic parameters for L-dopa of wild-type DDC and variants

Enzyme	Location of mutated residue	$K_{D(PLP)}$ (nM)	k_{cat} (s^{-1})	K_m (mM)	k_{cat}/K_m ($mM s^{-1}$)
Wild type		43 ± 12	7.6 ± 0.1	0.11 ± 0.01	70.6 ± 8.4
T69M	LOOP 1	100 ± 13	3.5 ± 0.2	0.46 ± 0.07	7.6 ± 1.2
H70T		510 ± 90	0.34 ± 0.02	0.69 ± 0.09	0.49 ± 0.07
H72Y		2145 ± 409	0.20 ± 0.01	1.38 ± 0.23	0.14 ± 0.02
Y79C		487 ± 110	0.32 ± 0.01	3.98 ± 0.37	0.080 ± 0.007
F80A		1520 ± 280	0.24 ± 0.01	1.03 ± 0.06	0.23 ± 0.04
P81L		390 ± 63	0.50 ± 0.01	0.19 ± 0.02	2.6 ± 0.5
G102S ^a	LOOP 2	61.7 ± 9.2	1.2 ± 0.1	1.2 ± 0.1	1.0 ± 0.1
A110Q		829 ± 60	0.015 ± 0.01	3.6 ± 0.4	0.004 ± 0.002
R347Q	LOOP 3	54 ± 10	0.087 ± 0.005	0.49 ± 0.08	0.16 ± 0.06
L38P	N-Terminal domain	460 ± 58	n.d.	n.d.	n.d.
P47H		100 ± 24	1.70 ± 0.06	0.60 ± 0.05	2.8 ± 0.2
L408I	C-Terminal domain	105 ± 33	0.78 ± 0.06	1.78 ± 0.26	0.44 ± 0.07
R412W		84 ± 23	1.45 ± 0.05	0.27 ± 0.03	5.37 ± 0.61
R447H		1010 ± 160	0.38 ± 0.02	0.79 ± 0.13	0.41 ± 0.07
R462P		544 ± 50	0.40 ± 0.01	0.25 ± 0.03	1.60 ± 0.19
G123R	Large domain (outside loops)	101 ± 13	3.30 ± 0.14	0.74 ± 0.07	4.46 ± 0.45
S250F ^b		62 ± 24	2.1 ± 0.1	0.22 ± 0.04	9.3 ± 1.7
R285W		335 ± 39	2.08 ± 0.08	0.16 ± 0.03	13.0 ± 2.5
F309L ^a		225 ± 26	0.47 ± 0.03	4.8 ± 0.6	0.097 ± 0.013

n.d., not determined.

^aFrom reference (3).^bFrom reference (23).

variants examined, except P47H, T69M, G102S, G123R, R347Q, R412W, L408I and S250F, showed, even if to a different extent, an increased value of the $K_{D(PLP)}$, ranging from 2- to at least 43-fold that of wild-type DDC (Table 1). In most cases, these data are in line with the *in silico* analyses. For the variants L38P and A110Q we could not explain the effect of the mutation on the coenzyme binding affinity by *in silico* mutagenesis, but we referred to MD analyses (see below). Human DDC displays absorbance maxima at 420 and 335 nm (ratio $A_{335nm}/A_{420nm} \approx 2$) associated with positive dichroic bands centered at the same wavelengths, and emits fluorescence at 384 and 504 nm upon excitation at 335 nm and at 504 nm when excited at 420 nm. On the basis of these spectral features and of their dependence on pH, the absorbance bands at 420 and 335 nm have been attributed to the ketoenamine and the enolimine tautomers of the internal aldimine (5). The absorbance and dichroic properties of all variants examined were generally similar to those of the wild-type. However, with respect to the wild-type, the following differences were observed: (i) the absorbance maxima at 420 nm is 1–14 nm blue shifted for all variants but F309L and R347Q (Supplementary Material, Fig. S2), (ii) the ratio between the absorbance and dichroic bands of the enolimine and the corresponding ones of the ketoenamine is lower for all variants but R347Q and (iii) the optical activity (mdeg/absorbance unit) measured at the maximum absorbance of the ketoenamine changes for all variants, with the exception of T69M, G102S, G123R, S250F, R347Q and L408I. Altogether, these data indicate that the chiral environment of the PLP-binding site of the majority of the examined variants is altered, at varying degree.

Structural features of the variants

We first investigated whether the examined mutations affect the secondary structure composition of DDC. We measured the circular dichroism (CD) signal of each variant in the far-UV region

and compared it to that of the wild-type. The overall shape of the CD spectrum of the variants in the region 190–260 nm was essentially identical to that of the wild-type indicating that the mutations do not affect the secondary structure of the protein. To examine whether the mutations previously investigated and under study here affect the tertiary structure of holoDDC, the near-UV CD spectra and the 1-anilino naphthalene sulfonic acid (ANS) emission spectra were acquired for all variants in the holo form and compared with the corresponding ones of the wild-type. As previously reported (3,12), the holo DDC displays a positive dichroic band in the 280 nm region, and binding of ANS to the holoenzyme results in an ~4-fold increase in its fluorescence emission intensity accompanied by a 27-nm blue shift consistent with ANS binding to hydrophobic sites of the enzyme. In fact, it is well known that binding of ANS to the exposed hydrophobic clusters of a protein results in both an increased intensity of the emission of the dye and a blue shift in its maximum emission fluorescence. For all variants but one (R347Q) we observed a reduction, at varying degree, of the magnitude of the CD signal in comparison with that of the wild-type (Supplementary Material, Fig. S3). Moreover, upon addition of ANS to each of the holo variants we saw in comparison with the wild-type (i) no significant changes in the ANS emission spectrum of R347Q and (ii) an enhanced emission fluorescence intensity, even if at a different extent (from 7- to 35-fold) and a blue shift (in the range 14–34 nm) for all other variants (Fig. 3). When we plotted the magnitude of the near-UV CD signal versus the ANS emission intensity, we noticed for all the variants, except L38P and P47H (both bearing mutations of residues located on the N-terminal domain), a linear relation between the variables whose values span over a wide range with R347Q having equivalent values to those of wild-type (Fig. 4A). From this plot it can be derived that (i) the mutation of Arg347 does not significantly affect the tertiary structure of holoDDC and (ii) the H70T, H72Y, Y79C, F80A, P81L,

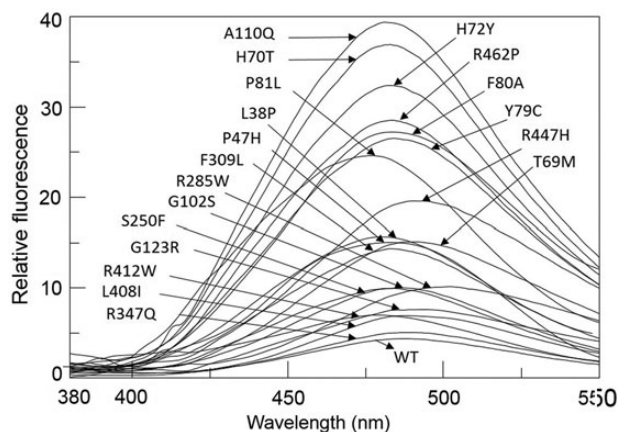


Figure 3. ANS emission fluorescence spectra of wild-type DDC and variants in the holo form. Fluorescence emission spectra of 1 μM wild-type and the indicated variants in the presence of 20 μM PLP incubated with 1 μM ANS at 25°C for 1 h and registered upon excitation at 365 nm. All measurements were made in 100 mM potassium phosphate buffer, pH 7.4.

A110Q, R447H and R462P mutations cause a structural alteration more pronounced than that due to the T69M, G102S, G123R, F309L, S250F, R285W, L408I and R412W mutations.

In order to verify if the alteration of the structural integrity is only limited to the holoforms, the near-UV CD spectra of the variants in the apo form were acquired. The data obtained indicate that (i) the variants T69M, H70T, H72Y, P81L and R447H display a positive dichroic signal whose magnitude is remarkably reduced ($\leq 50\%$) in comparison with that of the wild-type, (ii) the variants L38P and R412W show a slightly negative band and (iii) the remaining variants do not exhibit significant changes in their dichroic spectra, or, as is the case for R347Q, any change at all (Supplementary Material, Fig. S3). The finding that the positive dichroic band of the apo wild-type is ~ 2.8 -fold lower than that of the holo is consistent with the conformational change accompanying the transition from the apo-open form to the holo-closed one of DDC (12). Thus, the extent of the difference between the dichroic bands of the holo and the apo forms could represent an indication of the impact of a mutation on the apo-holo conversion. When we plotted the difference of the near-UV CD signal between the holo and the apo form against the ANS emission intensity of each variant (Fig. 4B), a linear relation similar to that of Figure 4A could be observed. Thus, it seems reasonable to suggest that in the apo-holo transition (i) the mutations H70T, H72Y, Y79C, F80A, P81L, A110Q, R447H and R462P have more marked impact than the mutations T69M, G102S, G123R, F309L, S250F, R285W, L408I and R412W, (ii) the R347Q mutation does not have any effect, and the mutations L38P and P47H appear not to be involved. This could imply that 16 residues affected by mutations are, yet at varying degree, structural elements involved in the achievement of the correct conformation of holoDDC.

Catalytic features of the variants

In order to understand if all mutations taken in consideration in this study affect the decarboxylase activity, the steady-state kinetic parameters of the variants were measured (Table 1).

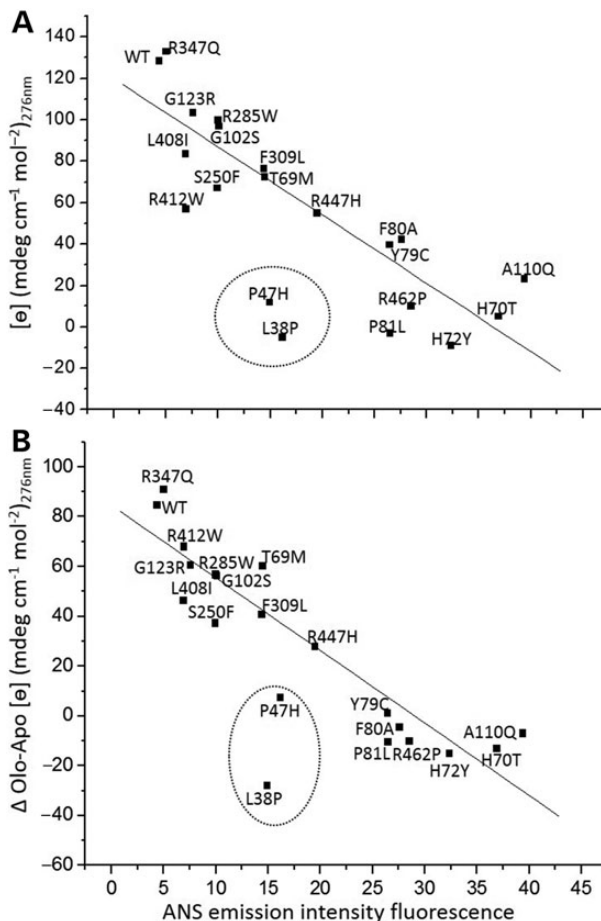


Figure 4. Correlation between the ANS emission fluorescence intensity and the magnitude of the near-UV of wild-type and 19 variants. The ANS emission fluorescence intensity of the holoforms is plotted (A) versus the magnitude of their near-UV CD signal or (B) versus the difference between the magnitude of the near-UV CD signal of the holoenzyme and the corresponding apoenzyme. The diagonal lines correspond to a linear fit, with R^2 values of 0.86 and 0.76, for (A) and (B), respectively.

All variants exhibited a decrease in the k_{cat}/K_m value spanning from ~ 6 -fold to $\sim 17\,000$ -fold. Reduced k_{cat} values were found for variants T69M (46%), G123R (43%), S250F and R285W (27%), P47H (22%), and G102S (16%). The remaining variants showed a more remarkable reduction in k_{cat} value (0.2–10%). For most variants, the K_m value was slightly increased (from 1.5- to 16-fold). Only Y79C, A110Q and F309L show a remarkably decreased L-Dopa affinity with an ~ 35 -fold increase in K_m in comparison with that of the wild-type. The *in silico* analysis predicted a decrease of the substrate binding affinity for the substitution of Tyr79 and Phe309 by Cys and Leu, respectively, but did not explain the high K_m value of A110Q. The kinetic parameters of the L38P variant for L-Dopa were difficult to obtain because of the very slow reaction rate. In fact, when 10 μM variant was allowed to react with 2 mM L-Dopa in the presence of 50 μM PLP, we found that dopamine was linearly produced with time, reaching after 40 min a value of 13 nmol, which corresponds to an initial rate of $2.1 \times 10^{-3} \text{ s}^{-1}$. Assuming that this value is close to the k_{cat} value of decarboxylation, the rate of this reaction in L38P is ~ 3800 -fold lower than the

corresponding reaction in wild-type. Taken together, these results indicate that none of the examined mutations involves residues essential for the catalytic activity of DDC. However, they open the question if the loss of decarboxylase activity is related or not to the incorrect apo-holo transition. In attempting to clarify this point, we plotted the ratio $k_{\text{cat}}(\text{wild-type})/k_{\text{cat}}(\text{variant})$ value as a function of the ratio $\text{ANS}_{\text{emission fluorescence intensity}}(\text{variant})/\text{ANS}_{\text{emission fluorescence intensity}}(\text{wild-type})$ (or the difference of the near-UV CD dichroic signal between the holo and apo form) of the enzymatic species, which fit the linear correlation shown in Figure 4A and B. With the exception of A110Q and R347H, a linear relation statistically significant could be observed for 15 variants (Fig. 5). This implies that for these variants the following relationship holds: high extent of conformational change \rightarrow increase of the exposure of hydrophobic clusters \rightarrow decrease of decarboxylase activity. Thus, on the basis of all our data, the mutations can be arranged in two categories with a different degree of structural and functional effects within each category. One group comprises the holo forms of the variants H70T, H72Y, Y79C, F80A, P81L concerning residues mapping to loop 1, and those of R462P and R447H relative to residues mapping to the C-terminal domain. These variants showed a near-UV CD signal similar or close to that of the corresponding apo form, the highest increase in the additional hydrophobic regions, a relevant change in the PLP binding mode and affinity, and a remarkably decreased catalytic activity (from 15- to 38-fold) in comparison with the wild-type. This is in line with the *in silico* prediction showing that except T69M, all mutations of residues belonging to loop 1 or residues (Arg462 and Arg447) directly interacting with loop 1 could have a remarkable impact on the architecture of the active site. The other group includes the holo forms of T69M, G102S, G123R, S250F, R285W, F309L, L408I and R412W which are characterized by a near-UV-CD signal higher than that of the corresponding apo forms, a mild increase in the accessible hydrophobic surface areas, a modest change in the PLP binding mode and affinity, and a slightly decreased catalytic activity (from 2- to 9-fold) with respect to the wild-type. Consistent with these data, mutations of residues Thr69 and Gly102 located on the N-terminal end of loops 1 and 2, respectively, are predicted to induce a mild local perturbation at the active site microenvironment. Moreover, mutations of residues Gly123, Ser250, Arg285 and Phe309 located on the large domain as well as mutations of residues Leu408 and Arg412 located on the C-terminal domain are predicted not to directly affect both the active site and loops residues.

Besides the variants of these two groups, two variants (A110Q and R347Q) have different characteristics. In fact, the R347Q variant mapping to loop 3 exhibited a severely reduced catalytic activity despite its conformation being comparable to that of wild-type, while the A110Q variant mapping to loop 2 disclosed signs of loss of catalytic activity more pronounced than signs of impairment of structural integrity of its holo form. While the catalytic effect of the R347Q mutation should be related to the proximity of Arg347 to the flexible catalytic loop 328–339, that of A110Q is hard to explain. A more deep kinetic characterization should be required to identify the step(s) along the catalytic pathway of decarboxylation altered in each of these variants. Finally, it was surprising to find a different impact of the mutations L38P and P47H of residues located on the

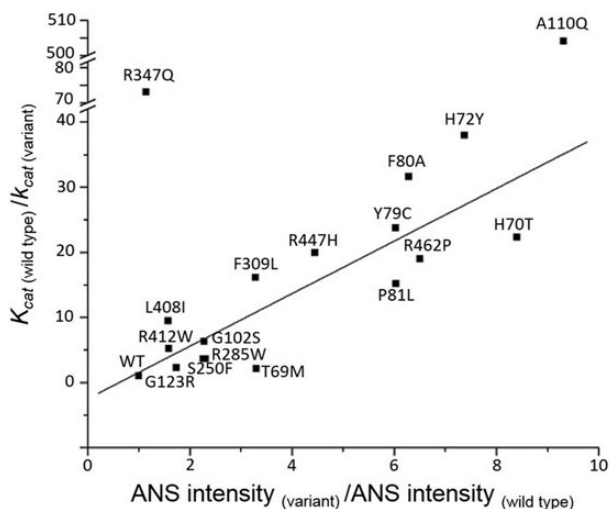


Figure 5. Correlation between the decrease of the k_{cat} and the increase of the ANS emission fluorescence intensity of 17 variants with respect to wild-type. The decrease in the k_{cat} value with respect to wild-type was plotted versus the increase in the ANS emission fluorescence intensity. The diagonal line corresponds to a linear fit with a R^2 value of 0.72.

N-terminal domain and far from the active site. Indeed, both the variants showed similar extents of alteration of their tertiary structure (Fig. 4A). However, while the P47H variant displayed a modestly reduced catalytic activity, the L38P variant unexpectedly exhibited an extremely low decarboxylase activity such that the kinetic parameters values could not be determined.

MD

To gain insights into the functional effect of L38P and A110Q pathogenic mutations, MD simulations were run on DDC for wild-type, L38P and A110Q mutants. A structural analysis of the wild-type protein reveals that Leu38 and Ala110, located on two opposite alpha helices that run parallel to each other, form a hydrophobic interaction (Fig. 2D).

Three MD simulations of 50 ns were performed, totaling 150 ns of total simulation time. We have first calculated the root mean square deviation (RMSD) on the backbone atoms of the three simulations in order to assess the stability of the three systems. Indeed, it can be appreciated (Supplementary Material, Fig. S4) that all systems became equilibrated after the first 10 ns of MD simulations. The simulated time span was long enough to relax and equilibrate the molecules, as indicated by the leveling of the RMSD from the initial conformations to values of ~ 0.3 nm (Supplementary Material, Fig. S4). Moreover, since no significant differences could be observed between the mutants and the wild-type forms, we can assume that the mutations do not destabilize the folding of the enzyme in an extensive manner, in agreement with results obtained with purified proteins (see above).

We then calculated the root mean square fluctuations (RMSF) on the C-alpha atoms of the three systems in order to characterize the flexibility of the three simulated systems and to assess putative differences at the backbone level due to the mutations. Indeed, RMSF represents the standard deviation of atomic positions in the trajectory after fitting to a reference frame. Important

differences on the backbone flexibility only localized in the neighborhoods of the mutated residues could be appreciated (Supplementary Material, Fig. S5). We thus concentrated in analyzing differences in the active site. With this aim, we have analyzed the ψ/Φ angle variation of residues involved in PLP-carbidopa binding during the MD simulation. In particular, we considered residues located on the three loops near the active sites, i.e. loops 1, 2 and 3. While in loops 1 and 3 there were not clear differences in the distribution of the angle values between the three simulations (data not shown), a significant difference could be appreciated for residues belonging to loop 2. Indeed, it can be clearly seen that Ile101 (Fig. 6A) and Phe103 (Fig. 6B) explore different regions of the Ramachandran plot upon mutations compared with the wild-type. In this regard, it can be observed that (i) the L38P mutant showed the most relevant variation with respect to the wild-type, and (ii) the A110Q mutant showed disperse values that localize in the middle between the values obtained for the wild-type and for the L38P mutant. It is interesting to note that Ile101 and Phe103 were already identified as involved in substrate binding (11,13).

In summary, the MD simulations revealed that, although the L38P and the A110Q mutations do not change the conformation of DDC structure in a macroscopic way, they create local perturbations at the backbone level extending, through loop 2, towards the active site. Moreover, differences in the dynamic properties of the A110Q mutant compared with the wild-type were less evident than those of the L38P mutant. Although these predictions are of course not an experimental evidence of the structural effects caused by these mutations, they are consistent with the finding that L38P mutation has an impact on the catalysis higher than that of A110Q.

Catalytic intermediates of variants

In order to ascribe the catalytic consequence of the amino acid substitutions under study to a particular reaction step, the effects of each mutation on the formation of the external aldimine were investigated by means of CD analyses. The CD features of the external aldimine of DDC wild-type with L-Dopa cannot be monitored because the k_{cat} value is 7.6 s^{-1} . This implies that, at $6 \mu\text{M}$ enzyme concentration, the DDC wild-type-L-Dopa complex remains close to saturation for only $\sim 45 \text{ s}$, a time too short to register a CD spectrum. Since the k_{cat} value of the wild-type for L-5HTP is $1.0 \pm 0.1 \text{ s}^{-1}$ ($K_{\text{m}} = 0.05 \pm 0.01 \text{ mM}$), we used this substrate to perform these measurements. As reported previously for wild-type human DDC (3), the binding of L-5HTP to the enzyme leads to the inversion of the 420 nm CD signal, i.e. the disappearance of the original positive CD band and its replacement by a negative CD band shifted to 440 nm and the increase of the positive 335 nm dichroic band. In contrast, when L-5HTP was added to each of the variants examined, the CD spectrum immediately registered was characterized by positive dichroic bands at 420 and 335 nm, the latter with a magnitude unaltered with respect to that of the corresponding holoenzyme. The only exceptions were relative to the R285W and R412W variants, for which the addition of L-5HTP caused a slightly negative dichroic band at $\sim 420 \text{ nm}$ and did not change the 335-nm positive dichroic band (Fig. 7). Taken together, these data indicate that the binding of L-5HTP to each of the variants causes changes in the orientation of the coenzyme, with respect to the neighboring residues,

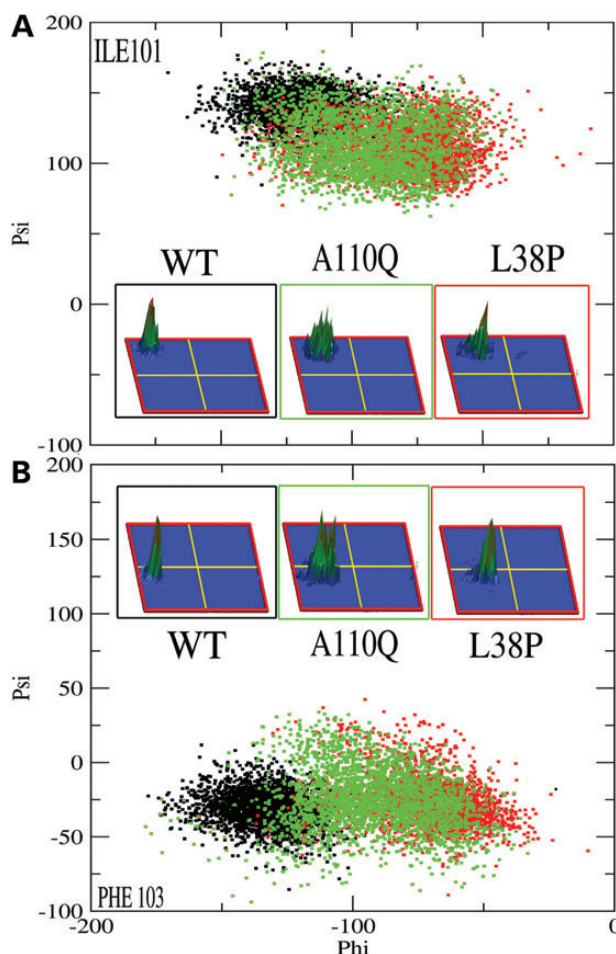


Figure 6. Distribution of the ψ/Φ dihedral angles values along the molecular dynamic trajectories. Dihedrals angle distributions for residues Ile101 (A) and Phe103 (B) in the wild-type form (black squares), the A110Q mutant (green squares) and the L38P mutant (red squares). The corresponding 3D graphic representations are squared in black for the wild-type, in green for the A110Q mutant and in red for the L38P mutant.

different from that of the wild-type. It is of interest to note that this occurs in the case of mutated residues at the active site or interacting with the active site as well as in the case of residues located away from the active site. This suggests that the effect of each of these mutations is possibly communicated throughout the protein by disruption of functionally crucial network of amino acid interactions.

Therapeutic implications

The current clinical management of AADC deficiency is aimed at potentiating monoaminergic transmission, and usually includes the administration of: (i) L-Dopa and pyridoxine to increase the DDC activity; (ii) MAO inhibitors to slow down the dopamine degradation; and (iii) dopamine agonists to mimic the dopamine effect (29,30). Because of the scarcity of information about the molecular defects associated to each pathogenic mutation causing the AADC deficiency, the aforementioned drugs are almost always administered in combination, and in the

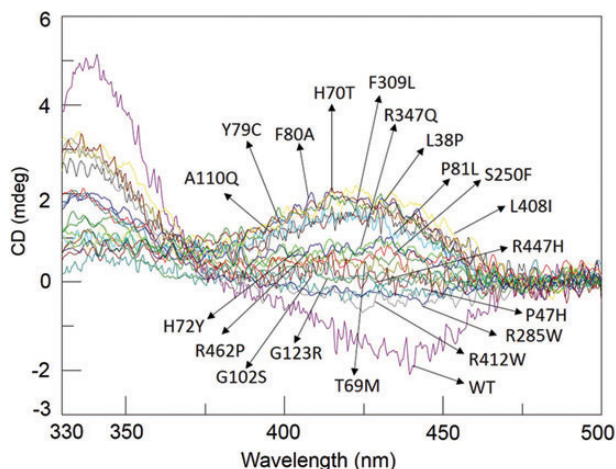


Figure 7. CD spectra of wild-type DDC and variants in the presence of L-5HTP. CD spectra of wild-type DDC and the indicated variants at a concentration of $9 \mu\text{M}$ in 100 mM potassium phosphate buffer, pH 7.4, in the presence of saturating concentration of PLP, registered immediately after the addition of L-5HTP to a final concentration of 5 mM.

absence of specific treatment guidelines. The presented results correlate each patient genotype with a specific enzymatic phenotype and allow us to group the DDC mutations on the basis of the possible responsiveness to the available pharmacological therapies. All mutants display at least one of the following functional defects: (i) high $K_{D(\text{PLP})}$, (ii) high K_m and (iii) low k_{cat} . In particular, among the variants with a modest reduction of k_{cat} (≤ 10 -fold) the P47H, T69M, G102S, G123R, S250F, L408I and R412W mutations only cause a decrease of the substrate binding affinity, while the F309L and R285W mutations induce an increase in both the $K_{D(\text{PLP})}$ and the K_m values. The patients carrying the former group of mutations could be responsive to therapy with L-Dopa, whereas the patients harboring the second group of mutations could be responsive to the combined administration of pyridoxine and L-Dopa. Anyway, MAO inhibitors could be a useful treatment for patients bearing each of these eight mutations. It could be also envisaged, on the basis of our data on the expression level in *E. coli*, that pyridoxine administration to patients with R285W and R412W mutations could result in a chaperoning effect, as already demonstrated for S250F (23).

The mutations L38P, P47H, H70T, H72Y, Y79C, P81L, A110Q, R347Q, R447H and R462P cause a consistent reduction of the k_{cat} value (from 15 to ~ 3600 -fold) with respect to the wild-type DDC. Therefore, although some of them have a remarkable impact on the $K_{D(\text{PLP})}$ and/or the K_m values, the administration of L-Dopa and pyridoxine to patients carrying these mutations may be useless. On the other hand, the administration of dopamine agonists and/or MAO inhibitors could be the most reasonable therapy, except for the patients carrying the mutations L38P and A110Q that cause an extreme reduction of the DDC catalytic activity (500- and 3600-fold). For these patients the only suitable therapeutic management appears to be the administration of dopamine agonists since MAO inhibitors may be ineffective. Unfortunately, considering the limited number of patients with AADC deficiency and the low frequency of each pathogenic mutation, the available data concerning clinical symptoms, disease course and family history are, at present, not sufficient

to propose a correlation between the mutational impact on DDC functionality and the clinical severity of the disease, i.e. an enzymatic-clinical phenotype relationship.

CONCLUSIONS

To explore the molecular basis of the pathogenesis of AADC deficiency we studied the structural and functional effects caused by all the mutations linked to AADC deficiency applying an integrated strategy which uses bioinformatic, spectroscopic and kinetic analyses. To our knowledge, these measurements constitute the first comprehensive functional view of AADC deficiency mutants. The first point deriving from our study is that all variants either concerning residues located at/near the active site or far from the active site are characterized by a reduced catalytic activity, even if at a different degree, and a different microenvironment of the external aldimines with respect to the wild-type. Moreover, for all but one (R347Q) we observed a perturbation of the topography of the active site. The second finding is that the majority of the variants show, to varying extents, an alteration of the tertiary structure of the holoDDC linearly related to an enhanced exposure of hydrophobic sites, to an impairment of the proper apo-holo transition, known to be a conversion from an open to a closed active conformation (12), and to a decrease of the decarboxylase activity. This structure–function relationship allows us to identify the residues which play the most relevant role in the apo-holo conversion, i.e. His70, His72, Tyr79, Phe80 and Pro81 mapping to loop 1 as well as Arg462 and Arg447 directly interacting with loop 1. The data on F80A, an artificial variant, substantiate the essential role of loop1 in this process. Following this view, it can be suggested that residues Pro47, Thr69, Gly102, Gly123, Ser250, Arg285, Phe309, Leu408 and Arg412 are involved, even if to a less extent, in the achievement of the catalytic active holoform of DDC. Thus, the hindrance of a proper apo-holo conversion might be sufficient to induce pathogenicity. A different mechanism must be envisaged to explain the DDC malfunction for mutations that do not fit in this set of mutations. R347Q is a catalytic mutation since, albeit no conformational alteration was observed for this variant, it is characterized by a severe loss of decarboxylase activity. On the other hand, replacement of Ala by Gln at position 110 or of Leu by Pro at position 38 appears to have an impact on decarboxylase activity more pronounced than that on the structural integrity of the enzyme. On the basis of the comparative MD study of the putative structure of wild-type, A110Q and L38P, it can be speculated that the decrease in catalytic activity could be due to the rearrangements occurring around the mutated residue transmitted to the active site, in particular to Phe103 and Ile101 mapping to loop 2.

Finally, the finding that, among all the mutations, several of them affect the expression level and solubility of DDC in the *E. coli* expression system suggests folding defects of the variants harboring these mutations. However, the elucidation of possible folding defects (aggregation and/or cellular degradation) requires, as already done for S250F (23), more detailed and laborious expression studies using mammalian cellular systems, which more closely reflect the true situation.

In conclusion, our results for the first time indicate that a large percentage of the variants associated with AADC deficiency

arising from point mutations shares, irrespective of their location, conformational changes that, at various degrees, do not allow a proper apo-holo transition and a full catalytic activity. This suggests that mutations occurring in distinct regions of a molecule can cause similar conformational changes with similar biological consequences. These events could not be predicted simply based on gene sequences. On the other hand, L38P, A110Q and R347Q result to be mainly or only catalytic mutations, for which additional kinetic features must be identified and understood to explain the kinetic reason(s) underlying their pathogenicity. Overall, these data allow us to acquire a complete knowledge of the enzymatic phenotype associated with each pathogenic mutation and to group patients with AADC deficiency into different therapeutic categories. This general picture of structural and/or functional effects of each mutation linked to AADC deficiency mutations will be a help to guide therapeutic decision and prevent inappropriate use of treatment regimens, thus improving the clinical outcome of this disease.

assay described by Sherald *et al.* (31), and modified by Charteris and John (32). Measurements were performed in the presence of 50 μM PLP in 100 mM potassium phosphate buffer, pH 7.4. Data of enzymatic activity as a function of substrate concentration were fitted to the Michaelis–Menten equation.

Apoenzyme preparation and determination of $K_{D(\text{PLP})}$

For the apoenzyme preparation, each variant was incubated with 10 mM hydroxylamine in 0.5 M potassium phosphate buffer, pH 6.9 at 25°C for 3 h and the mixture was loaded on a desalting 26/10 column (GE Healthcare) pre-equilibrated with the same buffer without hydroxylamine (33).

The $K_{D(\text{PLP})}$ value from the variants was determined by measuring the quenching of the intrinsic fluorescence of the apoenzyme (0.15 μM) in the presence of PLP at a concentration range of 0.01–10 μM in 100 mM potassium phosphate buffer, pH 7.4 and by fitting the data to the following equation:

$$Y = Y_{\text{MAX}} \frac{[E]_t + [\text{PLP}]_t + K_{D(\text{PLP})} - \sqrt{([E]_t + [\text{PLP}]_t + K_{D(\text{PLP})})^2 - 4[E]_t[\text{PLP}]_t}}{2[E]_t}$$

MATERIALS AND METHODS

Materials

PLP, L-Dopa, L-5HTP, 2,4,6-trinitrobenzene-1-sulfonic acid, isopropyl- β -D-thiogalactopyranoside, protease inhibitor cocktail were purchased from Sigma. ANS was purchased from Molecular Probes. All other chemicals were of the highest purity available.

Site-directed mutagenesis

The pDDChis plasmid, expressing the wild-type human DDC equipped with a C-terminal hexahistidine tag, and the expression vectors of the G102S, F309L and S250F DDC variants have been previously obtained (3,23). The expression vectors of the 16 DDC variants listed in Supplementary Material, Table S1 have been constructed using the Quick-Change II site-directed mutagenesis kit (Agilent Technologies) using the pDDChis plasmid as template and the oligonucleotides reported in Supplementary Material, Table S1. Successful mutagenesis was verified by DNA sequencing of the entire open reading frame.

Enzyme purification and assay

Purification of his-tagged wild-type DDC and of the variants was performed following the procedure previously described (3). Protein concentration was determined using the $\epsilon_M = 142\,000\text{ M}^{-1}\text{ cm}^{-1}$ at 280 nm. The PLP content of the variants was determined by releasing the coenzyme in 0.1 M NaOH and by using $\epsilon_M = 6600\text{ M}^{-1}\text{ cm}^{-1}$ at 388 nm. The decarboxylase activity toward L-Dopa of wild-type DDC and the variants in the purified form was measured by the spectrophotometric

where $[E]_t$ and $[\text{PLP}]_t$ represent the total concentrations of the enzyme and PLP, respectively, Y refers to the intrinsic quenching changes at a PLP concentration, $[\text{PLP}]$, and Y_{max} refers to the aforementioned changes when all enzyme molecules are complexed with coenzyme.

Molecular modeling and conservation analysis

Starting from the available structure of pig kidney holoDDC (pdb file 1JS6) (11) and human apoDDC (pdb file 3RBF) (12), the inspection of the 3D structures and the prediction of the possible steric clashes, loosing of interactions and local structural rearrangements caused by the analyzed mutations have been performed using the Molecular Operating Environment (MOE) software by Chemical Computing Group (34). The evolutionary conservation score of each amino acid of DDC has been calculated using the ConSurf server (35,36). The closed homologous sequences of DDC (150) have been collected from UNIREF90 using PSI-BLAST algorithm and the multiple sequence alignment was constructed using T-COFFEE.

MD simulations

The MD simulations were performed using the Gromacs program (37), and the structure of DDC enzyme carrying carbidopa inhibitor [pdb file 1JS3 (11)]. Since in this homodimeric structure the crystallographic coordinates between residues 328–339 are missing, a loop modeling script of the Modeller 9.8 software (38) was constructed. The mutations in the DDC enzyme were prepared using VMD software (39). The carbidopa ligand was parameterized with ProdrG software (40). Proteins were simulated in explicit aqueous solution inserted into a tetrahedral box of water

molecules, ensuring that the solvent shell would extend for at least 1.0 nm around them. Gromos96 43a1 fields (41), in combination with the explicit simple point charge (spc/e) force field, were used for the simulation. Long-range electrostatic interactions were treated with the particle mesh Ewald (PME) method using a grid with a spacing of 0.12 nm (42). The time step was set to 2 fs. The cut-off radius for the Lennard–Jones interactions, as well as for the real part of the PME calculations, was set to 1 nm. The LINCS algorithm was used to constrain all bond lengths involving hydrogen atoms, and the time step used was 2 fs. The three systems were energy-minimized imposing harmonic position restraints of 1000 kJ mol⁻¹ nm⁻² on solute atoms, allowing the equilibration of the solvent without distorting the solution structure. After an energy minimization of the solvent and the solute without harmonic restraints, the systems were equilibrated and temperature was gradually increased from 0 to 300 K in 2 ns of simulation. The system was finally simulated for 50 ns for the analysis shown in this report. The RMSD/RMSF analysis and the Ramachandran plot analysis were performed through Gromacs tools. The 3D Ramachandran plots were obtained using VMD analysis tools.

Spectral measurements

All the spectral measurements were carried out using 100 mM potassium phosphate, pH 7.4, at 25°C. Absorption spectra were recorded with a Jasco V-550 spectrophotometer. CD measurements were made with a Jasco J-710 spectropolarimeter at a protein concentration of 6 μM. CD spectra were recorded at a scan speed of 50 nm/min with a band width of 2 nm and averaged automatically except where indicated. The ANS fluorescence measurements were taken with a FP750 Jasco spectrofluorimeter using 5 nm excitation and emission bandwidths at 1 μM protein and 15 μM ANS concentration.

Statistical analysis

Data analysis was performed by linear and non-linear regression curve fitting using Origin[®] 7.03 (Origin Lab) and the errors indicated result from fitting to the appropriate equation.

SUPPLEMENTARY MATERIAL

Supplementary Material is available at *HMG* online.

ACKNOWLEDGEMENT

We thank the AADC research Trust (UK) for its interest in our research.

Conflicts of Interest statement. None declared.

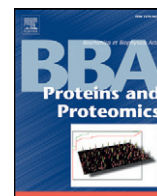
FUNDING

This work was supported by grants from M.I.U.R and the Consorzio Interuniversitario per le Biotecnologie CIB (IT).

REFERENCES

- Moore, P.S., Dominici, P. and Borri Voltattorni, C. (1996) Cloning and expression of pig kidney dopa decarboxylase: comparison of the naturally occurring and recombinant enzymes. *Biochem. J.*, **315**(Pt 1), 249–256.
- Dominici, P., Tancini, B., Barra, D. and Voltattorni, C.B. (1987) Purification and characterization of rat-liver 3,4-dihydroxyphenylalanine decarboxylase. *Eur. J. Biochem.*, **169**, 209–213.
- Montioli, R., Cellini, B. and Borri Voltattorni, C. (2011) Molecular insights into the pathogenicity of variants associated with the aromatic amino acid decarboxylase deficiency. *J. Inherit. Metab. Dis.*, **34**, 1213–1224.
- Bertoldi, M. (2014) Mammalian dopa decarboxylase: structure, catalytic activity and inhibition. *Arch. Biochem. Biophys.*, **546**, 1–7.
- Montioli, R., Cellini, B., Dindo, M., Oppici, E. and Voltattorni, C.B. (2013) Interaction of human Dopa decarboxylase with L-Dopa: spectroscopic and kinetic studies as a function of pH. *Biomed. Res. Int.*, **2013**, 161456.
- Voltattorni, C.B., Minelli, A. and Dominici, P. (1983) Interaction of aromatic amino acids in D and L forms with 3,4-dihydroxyphenylalanine decarboxylase from pig kidney. *Biochemistry*, **22**, 2249–2254.
- Bertoldi, M., Frigeri, P., Paci, M. and Voltattorni, C.B. (1999) Reaction specificity of native and nicked 3,4-dihydroxyphenylalanine decarboxylase. *J. Biol. Chem.*, **274**, 5514–5521.
- Bertoldi, M. and Voltattorni, C.B. (2009) Multiple roles of the active site lysine of Dopa decarboxylase. *Arch. Biochem. Biophys.*, **488**, 130–139.
- Dominici, P., Moore, P.S., Castellani, S., Bertoldi, M. and Voltattorni, C.B. (1997) Mutation of cysteine 111 in Dopa decarboxylase leads to active site perturbation. *Protein Sci.*, **6**, 2007–2015.
- Bertoldi, M., Gonsalvi, M., Contestabile, R. and Voltattorni, C.B. (2002) Mutation of tyrosine 332 to phenylalanine converts dopa decarboxylase into a decarboxylation-dependent oxidative deaminase. *J. Biol. Chem.*, **277**, 36357–36362.
- Burkhard, P., Dominici, P., Borri-Voltattorni, C., Jansonius, J.N. and Malashkevich, V.N. (2001) Structural insight into Parkinson's disease treatment from drug-inhibited DOPA decarboxylase. *Nat. Struct. Biol.*, **8**, 963–967.
- Giardina, G., Montioli, R., Gianni, S., Cellini, B., Paiardini, A., Voltattorni, C.B. and Cutruzzola, F. (2011) Open conformation of human DOPA decarboxylase reveals the mechanism of PLP addition to Group II decarboxylases. *Proc. Natl Acad. Sci. USA*, **108**, 20514–20519.
- Daidone, F., Montioli, R., Paiardini, A., Cellini, B., Macchiarulo, A., Giardina, G., Bossa, F. and Borri Voltattorni, C. (2012) Identification by virtual screening and *in vitro* testing of human DOPA decarboxylase inhibitors. *PLoS One*, **7**, e31610.
- Ren, J., Zhang, Y., Jin, H., Yu, J., Zhou, Y., Wu, F. and Zhang, W. (2014) Novel inhibitors of human DOPA decarboxylase extracted from euonymus glabra Roxb. *ACS Chem. Biol.*, **9**, 897–903.
- Brun, L., Ngu, L.H., Keng, W.T., Ch'ng, G.S., Choy, Y.S., Hwu, W.L., Lee, W.T., Willemsen, M.A., Verbeek, M.M., Wassenberg, T. *et al.* (2010) Clinical and biochemical features of aromatic L-amino acid decarboxylase deficiency. *Neurology*, **75**, 64–71.
- Tay, S.K., Poh, K.S., Hyland, K., Pang, Y.W., Ong, H.T., Low, P.S. and Goh, D.L. (2007) Unusually mild phenotype of AADC deficiency in 2 sibs. *Mol. Genet. Metab.*, **91**, 374–378.
- Hyland, K. and Clayton, P.T. (1990) Aromatic amino acid decarboxylase deficiency in twins. *J. Inherit. Metab. Dis.*, **13**, 301–304.
- Maller, A., Hyland, K., Milstien, S., Biaggioni, I. and Butler, I.J. (1997) Aromatic L-amino acid decarboxylase deficiency: clinical features, diagnosis, and treatment of a second family. *J. Child Neurol.*, **12**, 349–354.
- Swoboda, K.J., Hyland, K., Goldstein, D.S., Kuban, K.C., Arnold, L.A., Holmes, C.S. and Levy, H.L. (1999) Clinical and therapeutic observations in aromatic L-amino acid decarboxylase deficiency. *Neurology*, **53**, 1205–1211.
- Lee, N.C., Chien, Y.H., Hu, M.H., Liu, W.S., Chen, P.W., Wang, W.H., Tzen, K.Y., Byrne, B.J. and Hwu, W.L. (2014) Treatment of congenital neurotransmitter deficiencies by intracerebral ventricular injection of an adeno-associated virus serotype 9 vector. *Hum. Gene Ther.*, **25**, 189–198.
- Chtarto, A., Bockstael, O., Tshibangu, T., Dewitte, O., Levivier, M. and Tenenbaum, L. (2013) A next step in adeno-associated virus-mediated gene therapy for neurological diseases: regulation and targeting. *Br. J. Clin. Pharmacol.*, **76**, 217–232.
- Hwu, W.L., Muramatsu, S., Tseng, S.H., Tzen, K.Y., Lee, N.C., Chien, Y.H., Snyder, R.O., Byrne, B.J., Tai, C.H. and Wu, R.M. (2012) Gene therapy

- for aromatic L-amino acid decarboxylase deficiency. *Sci. Transl. Med.*, **4**, 134ra161.
23. Montioli, R., Oppici, E., Cellini, B., Roncador, A., Dindo, M. and Voltattorni, C.B. (2013) S250F variant associated with aromatic amino acid decarboxylase deficiency: molecular defects and intracellular rescue by pyridoxine. *Hum. Mol. Genet.*, **22**, 1615–1624.
 24. Cellini, B., Montioli, R., Oppici, E., Astegno, A. and Voltattorni, C.B. (2013) The chaperone role of the pyridoxal 5'-phosphate and its implications for rare diseases involving B6-dependent enzymes. *Clin. Biochem.*, **47**, 158–165.
 25. Clayton, P.T. (2006) B6-responsive disorders: a model of vitamin dependency. *J. Inherit. Metab. Dis.*, **29**, 317–326.
 26. Meier, M., Janosik, M., Kery, V., Kraus, J.P. and Burkhard, P. (2001) Structure of human cystathionine beta-synthase: a unique pyridoxal 5'-phosphate-dependent heme protein. *EMBO J.*, **20**, 3910–3916.
 27. Shen, B.W., Hennig, M., Hohenester, E., Jansonius, J.N. and Schirmer, T. (1998) Crystal structure of human recombinant ornithine aminotransferase. *J. Mol. Biol.*, **277**, 81–102.
 28. Zhang, X., Roe, S.M., Hou, Y., Bartlam, M., Rao, Z., Pearl, L.H. and Danpure, C.J. (2003) Crystal structure of alanine:glyoxylate aminotransferase and the relationship between genotype and enzymatic phenotype in primary hyperoxaluria type 1. *J. Mol. Biol.*, **331**, 643–652.
 29. Manegold, C., Hoffmann, G.F., Degen, I., Ikonomidou, H., Knust, A., Laass, M.W., Pritsch, M., Wilichowski, E. and Horster, F. (2009) Aromatic L-amino acid decarboxylase deficiency: clinical features, drug therapy and follow-up. *J. Inherit. Metab. Dis.*, **32**, 371–380.
 30. Pons, R., Ford, B., Chiriboga, C.A., Clayton, P.T., Hinton, V., Hyland, K., Sharma, R. and De Vivo, D.C. (2004) Aromatic L-amino acid decarboxylase deficiency: clinical features, treatment, and prognosis. *Neurology*, **62**, 1058–1065.
 31. Sherald, A.F., Sparrow, J.C. and Wright, T.R. (1973) A spectrophotometric assay for *Drosophila* dopa decarboxylase. *Anal. Biochem.*, **56**, 300–305.
 32. Minelli, A., Charteris, A.T., Voltattorni, C.B. and John, R.A. (1979) Reactions of DOPA (3,4-dihydroxyphenylalanine) decarboxylase with DOPA. *Biochem. J.*, **183**, 361–368.
 33. Voltattorni, C.B., Minelli, A., Vecchini, P., Fiori, A. and Turano, C. (1979) Purification and characterization of 3,4-dihydroxyphenylalanine decarboxylase from pig kidney. *Eur. J. Biochem.*, **93**, 181–188.
 34. Molecular Operating Environment (MOE), Chemical Computing Group Inc. (2013), 1010 Sherbooke St. West, Suite #910, Montreal, QC, Canada, H3A 2R7.
 35. Ashkenazy, H., Erez, E., Martz, E., Pupko, T. and Ben-Tal, N. (2010) ConSurf 2010: calculating evolutionary conservation in sequence and structure of proteins and nucleic acids. *Nucleic Acids Res.*, **38**, W529–W533.
 36. Celniker, G. (2013) ConSurf: using evolutionary data to rise testable hypotheses about protein function. *Isr. J. Chem.*, **53**, 199–206.
 37. Van Der Spoel, D., Lindahl, E., Hess, B., Groenhof, G., Mark, A.E. and Berendsen, H.J. (2005) GROMACS: fast, flexible, and free. *J. Comput. Chem.*, **26**, 1701–1718.
 38. Eswar, N., Webb, B., Marti-Renom, M.A., Madhusudhan, M.S., Eramian, D., Shen, M.Y., Pieper, U. and Sali, A. (2006) Comparative protein structure modeling using Modeller. *Curr. Protoc. Bioinformatics*, Chapter 5, Unit 5.6.
 39. Humphrey, W., Dalke, A. and Schulten, K. (1996) VMD: visual molecular dynamics. *J. Mol. Graph.*, **14**, 33–38, 27–38.
 40. Schuttelkopf, A.W. and van Aalten, D.M. (2004) PRODRG: a tool for high-throughput crystallography of protein-ligand complexes. *Acta Crystallogr. D Biol. Crystallogr.*, **60**, 1355–1363.
 41. Van Gunsteren, W.F.B. (1996) *Biomolecular Simulation: the GROMOS96 Manual and User Guide*. Zurich/Groningen.
 42. Ulrich, E. (1995) A smooth particle mesh Ewald method. *J. Chem. Phys.*, **103**, 8577–8593.



Misfolding caused by the pathogenic mutation G47R on the minor allele of alanine:glyoxylate aminotransferase and chaperoning activity of pyridoxine



Riccardo Montioli¹, Elisa Oppici¹, Mirco Dindo, Alessandro Roncador², Giovanni Gotte, Barbara Cellini, Carla Borri Voltattorni^{*}

Department of Life and Reproduction Sciences, University of Verona, Verona, Italy

ARTICLE INFO

Article history:

Received 3 June 2015

Accepted 3 July 2015

Available online 3 July 2015

Keywords:

Alanine:glyoxylate aminotransferase

Primary Hyperoxaluria Type 1

Pyridoxal 5'-phosphate

Pathogenic variant

Pyridoxine treatment

ABSTRACT

Liver peroxisomal alanine:glyoxylate aminotransferase (AGT), a pyridoxal 5'-phosphate (PLP) enzyme, exists as two polymorphic forms, the major (AGT-Ma) and the minor (AGT-Mi) haplotype. Deficit of AGT causes Primary Hyperoxaluria Type 1 (PH1), an autosomal recessive rare disease. Although ~one-third of the 79 disease-causing missense mutations segregates on AGT-Mi, only few of them are well characterized. Here for the first time the molecular and cellular defects of G47R-Mi are reported. When expressed in *Escherichia coli*, the recombinant purified G47R-Mi variant exhibits only a 2.5-fold reduction of its k_{cat} , and its apo form displays a remarkably decreased PLP binding affinity, increased dimer–monomer equilibrium dissociation constant value, susceptibility to thermal denaturation and to N-terminal region proteolytic cleavage, and aggregation propensity. When stably expressed in a mammalian cell line, we found ~95% of the intact form of the variant in the insoluble fraction, and proteolyzed (within the N-terminal region) and aggregated forms both in the soluble and insoluble fractions. Moreover, the intact and nicked forms have a peroxisomal and a mitochondrial localization, respectively. Unlike what already seen for G41R-Mi, exposure of G47R-Mi expressing cells to pyridoxine (PN) remarkably increases the expression level and the specific activity in a dose-dependent manner, reroutes all the protein to peroxisomes, and rescues its functionality. Although the mechanism of the different effect of PN on the variants G47R-Mi and G41R-Mi remains elusive, the chaperoning activity of PN may be of value in the therapy of patients bearing the G47R mutation.

© 2015 Published by Elsevier B.V.

1. Introduction

The human inborn error of metabolism Primary Hyperoxaluria Type 1 (PH1; OMIM 259900) is caused by a disfunction of liver peroxisomal alanine:glyoxylate aminotransferase (AGT; EC 2.6.1.4.4), and is inherited in an autosomal recessive fashion [1]. AGT is a pyridoxal 5'-phosphate (PLP) enzyme, which catalyzes the conversion of alanine and glyoxylate into pyruvate and glycine [2]. Human AGT is present as two polymorphic

forms, the most frequent called the major allele (AGT-Ma) and a less common polymorphic variant called the minor allele (AGT-Mi). The minor allele shows two point mutations leading to single amino acid substitutions (P11L and I340M) among other genomic changes [3]. Even though AGT-Mi is not pathogenic, it exhibits a 30% reduction of transaminase activity with respect to AGT-Ma and 5% of mistargeting to mitochondria [4,5]. The solved crystal structure of AGT reveals that the enzyme belongs to the Fold Type I family of PLP-enzymes and is a compact homodimer, each subunit of which contains one PLP-binding site [6]. Each protomer folds into a large N-terminal domain (residues 22–282) and a smaller C-terminal domain (283–392). Most of the contacts within the dimer involve the large domain. Besides them, a long unstructured N-terminal tail (residues 1–21) grabs the subunits within the dimer. In the latter structural element, not typical of the family to which AGT belongs, is located Pro11 whose replacement by Leu is an important structural element since it generates a functionally ineffective mitochondrial targeting sequence (MTS), which represents an anchoring point for binding to the mitochondrial import receptor TOM20 [7,8]. Among the 79 disease-associated missense mutations identified up to date in the human *AGXT* gene, 36 and 26 are on the

Abbreviations: PH1, Primary Hyperoxaluria Type I; AGT, alanine:glyoxylate aminotransferase; PLP, pyridoxal 5'-phosphate; MTS, mitochondrial targeting sequence; CHO, Chinese hamster ovary; GO, glycolate oxidase; PBS, phosphate buffered saline; $K_{D(PLP)}$, PLP equilibrium dissociation constant; KP, phosphate buffer; PN, pyridoxine; IFM, immunofluorescence microscopy.

^{*} Corresponding author at: Department of Life and Reproduction Sciences (Section of Biological Chemistry) Strada Le Grazie, 8 37134 Verona, Italy.

E-mail address: carla.borrivoltattorni@univr.it (C. Borri Voltattorni).

¹ R.M. and E.O. contribute equally to this work.

² Present address: Center for Integrative Biology (CIBIO), University of Trento, Trento, Italy.

background of the major and the minor allele, respectively, while only 5 are on the background of either the major or the minor allele [9]. For the remaining mutations the allele in which are present has not yet been identified. Expression analyses in *E. coli*, yeast and/or mammalian cellular systems of ~60 PH1-related variants have allowed to establish differences in their kinetic behavior and/or coenzyme binding mode and affinity, degradation and/or aggregation propensity, expression level, thermodynamic and/or kinetic stability and subcellular localization [2, 5,10–25]. Among the variants on the background of the minor allele, only G170R, F152I, G161S, G161C, G41R and I244T have been in depth characterized [13–16,18,22]. The subcellular localization of these variants is different. G170R, F152I and I244T mutations cause a partial or complete mistargeting into mitochondria in patients and/or mammalian cells [13], Gly161 variants give rise to aggregates in the cytosol of Chinese hamster ovary (CHO) cells [18], G41R leads to a partial mistargeting and intraperoxisomal aggregates [13]. Moreover, multiple mechanisms of action of pyridoxine (PN) on these variants have been observed [18,26]. In order to have a wider picture of the defects generated by mutations on the background of the minor allele, we decided to focus our attention on the pathogenic variant G47R-Mi. Biochemical and cellular biology experiments allowed us to establish that several defects, similar to those of G41R [15], characterize the variant G47R-Mi. In particular, the mutation generates a misfolded apoprotein with a low PLP binding affinity, an increased dimer–monomer equilibrium dissociation constant value, prone to aggregation inside peroxisomes and to proteolytic degradation inside mitochondria. However, unlike what already observed for G41R-Mi [26], PN is found to rescue the functionality of the variant by partially preventing aggregation and degradation, and by redirecting all the protein to the peroxisome.

2. Materials and methods

2.1. Materials

PLP, L-alanine, sodium glyoxylate, rabbit muscle L-lactic dehydrogenase, PN, betaine, 4-phenylbutyric acid (4-PBA), tauroursodeoxycholic acid (TUDCA), phenylmethylsulfonyl fluoride (PMSF), dithiothreitol (DTT), and glycolate were purchased from Sigma. Aniline-1-naphthalenesulphonic acid (ANS) was purchased from Molecular Probes. Ham's F12 Glutamax medium, zeocin, geneticin and Alexa Fluor antibodies were purchased from Life-technologies. All other chemicals were of the highest purity available. Chinese hamster ovary (CHO)-glycolate oxidase (GO) cells, CHO-GO cells expressing AGT-Mi (CHO-GO-AGT-Mi), the rabbit polyclonal antihuman AGT, the rabbit polyclonal anti-AGTLeu11 and the guinea-pig anti-peroxisomal protein antibodies were kindly provided by Prof. C.J. Danpure of the University College London (UK). The anti-rabbit HRP antibody was purchased from GE Healthcare. Oligonucleotides for site directed mutagenesis were purchased from MWG Biotech AG (Anzingen, Germany).

2.2. Site directed mutagenesis

Site-directed mutagenesis was performed by the QuikChange II site-directed mutagenesis kit (Stratagene) using pAGThis-Mi [16] and pcDNA3.1AGT-Mi [18], as templates. On each vector, the pathogenic G47R mutation was introduced by using the primer 5'-GCTGCAGATG ATCCGGTCCATGAGCAAGG-3' and its complement (the mutated codon is underlined). The mutation was confirmed by entire DNA sequence analysis.

2.3. Enzyme expression and purification

AGT-Mi and G47R-Mi in their His-tagged form were expressed and purified as already described [2]. The apo forms of both variants were prepared as previously reported [2]. The protein concentration in

the AGT samples was determined by absorbance spectroscopy using an extinction coefficient of $9.4 \times 10^4 \text{ M}^{-1} \text{ cm}^{-1}$ at 280 nm.

2.4. Spectroscopic measurements

Absorption measurements were made with a Jasco V-550 spectrophotometer with 1 cm path length quartz cuvettes at a protein concentration of 1–10 μM . Circular dichroism (CD) spectra were made with a Jasco-J710 spectropolarimeter by using 0.1 or 1 cm path-length cuvettes for the near UV and far UV measurements, respectively, at 1–5 μM enzyme concentration.

ANS fluorescence measurements were taken with a FP750 Jasco spectrofluorimeter using 5 nm excitation and emission bandwidths at 1 μM protein and 15 μM ANS concentration. All the absorbance, CD and fluorescence measurements were performed at 25 °C in 100 mM potassium phosphate (KP) buffer, pH 7.4. Dynamic light scattering (DLS) measurements were performed on a Zetasizer Nano S device (Malvern Instruments) equipped with a Peltier temperature controller by using disposable 12.5 × 45-mm cells with stopper. The aggregation kinetics were studied by incubating the enzymes in KP buffer, pH 7.4 at different ionic strengths at 37 °C. The buffer was filtered immediately before use to eliminate any impurities.

2.5. Binding affinity for PLP

The equilibrium dissociation constant for PLP ($K_{D(\text{PLP})}$) of G47R-Mi was determined by CD spectrophotometric titration at 420 nm of the apo form (5 μM) in the presence of PLP at concentrations ranging from 1 to 100 μM . The experiment was carried out in 100 mM KP buffer, pH 7.4. The $K_{D(\text{PLP})}$ value was obtained using the following equation:

$$Y = Y_{\text{MAX}} \frac{[E]_t + [\text{PLP}]_t + K_{D(\text{PLP})} - \sqrt{([E]_t + [\text{PLP}]_t + K_{D(\text{PLP})})^2 - 4[E]_t [\text{PLP}]_t}}{2[E]_t}$$

where $[E]_t$ and $[\text{PLP}]_t$ represent the total concentrations of the G47R-Mi and PLP, respectively, Y refers to the 420 nm dichroic signal changes at a PLP concentration $[\text{PLP}]_t$, and Y_{MAX} refers to the maximum intensity of the 420 nm dichroic signal when all enzyme molecules are complexed with coenzyme.

2.6. Thermostability

The thermostability studies on purified G47R-Mi in the holo- (in the presence of saturating PLP) or the apo-form were performed at 10 μM enzyme concentration in 100 mM KP buffer, pH 7.4, by monitoring the CD signal at 222 nm from 25 to 90 °C at a heating rate of 1.5 °C/min [17]. Calculation of the melting temperatures (T_m) was carried out by fitting the data using the Origin Pro7 software according to the method of Pace [27].

2.7. Limited proteolysis

Holo and apoG47R-Mi at 10 μM enzyme concentration were treated with proteinase K at a protease/enzyme ratio of 1/10 (w/w) in 100 mM KP buffer, pH 7.4, at 25 °C. At various times, 15 μl -aliquots were removed for electrophoresis or western-blot analysis. The protease reaction was stopped by the addition of 2 mM PMSF. After staining with Coomassie blue the band intensities were visualized and analyzed using the ImageJ software (Rasband, WS).

2.8. Cell culture and selection

CHO-GO cells were cultured at 37 °C under O₂/CO₂ (19:1) in Ham's F12 Glutamax medium, containing 0.3 μM PN hydrochloride (Invitrogen), supplemented with fetal bovine serum (10% v/v),

penicillin (100 units/ml), streptomycin (100 µg/ml) and zeocin (0.4 mg/ml). Cells were transfected with the pcDNA3.1G47R-Mi construct by using the Turbofect™ Transfection Reagent (Thermo-Fisher) according to manufacturer instructions. After 24 h, G-418 (1.25 mg/ml) was added as selective agent and cells were left to grow for 48 h. To generate a monoclonal stably transformed cell line (CHO-GO-G47R-Mi), the antibiotic-resistant cells were seeded at limiting dilution of 10 cells/ml in 96-well plates in selective medium and incubated until single colonies started growing. Clones (at least 12) were then grown and screened for exogenous gene expression by western-blot and immunofluorescence analysis.

Where indicated, CHO-GO-G47R-Mi cells were treated with PN (0.3, 1, 3, 10, 30, 100 and 300 µM), betaine (15 mM), β-alanine (5 mM), 4-PBA (1 mM) and TUDCA (0.5 mM) for three days. Preliminary experiments demonstrated that three days is a time sufficient to allow that all the protein is synthesized in the presence of the selected compound.

2.9. Cell lysis and western-blot analyses

Cells were harvested after 24 h and lysed in phosphate saline buffer (PBS), pH 7.2, plus protease inhibitor cocktail (Complete Mini, Roche), by five freeze/thaw cycles followed by addition of DNase (100 units/ml) at room temperature for 45 min. The whole cell extract was separated by centrifugation (29,200 g, 10 min, 4 °C) to obtain the soluble fraction. Pellets were then resuspended in an equal volume of denaturing gel loading buffer to obtain the insoluble fraction. The protein concentration in the soluble fraction was measured using the Bradford protein assay, as previously described [18].

Two micrograms of AGT-Mi cell lysate and 10 µg of G47R-Mi cell lysate were loaded per lane on a Mini Protean TGX™ pre-cast gel (10%, Biorad) along with the Precision plus protein Kaleidoscope™ (Bio-Rad) molecular mass markers. Following transfer on a nitrocellulose membrane by the iBlot device (Invitrogen) the membrane was blocked with 5% milk in TBST (50 mM Tris-HCl pH 7.5, 150 mM NaCl, 0.1% Tween 20) for 1 h at 37 °C. For AGT detection the membrane was incubated with polyclonal rabbit anti-AGT serum (dilution 1:6000) or with polyclonal rabbit anti-AGT Leu11 serum (1:2000), washed three times in TBST and then incubated with peroxidase-conjugated anti rabbit IgG (dilution 1:1000). Blotted proteins were detected with ECL® (Millipore), using the ChemiDoc XRS Imaging System (Bio-Rad, Hercules, CA). For densitometry analysis of western-blot, the band volume (intensity × mm²) was quantified using the software Quantity One 4.6.3. Results were expressed relative to the densitometry of AGT-Mi.

2.10. Enzymatic assays

90 µg of cell lysate were incubated with 0.5 M L-alanine and 10 mM glyoxylate at 25 °C in 100 mM KP buffer, pH 7.4 in the presence or in the absence of 200 µM PLP. In order to obtain a detectable signal of pyruvate in the linear phase of the kinetics, the reaction time was set to 20 min for cells expressing AGT-Mi, and to 120 min for cells expressing G47R-Mi. The kinetic parameters for the overall transamination of the pair L-alanine/glyoxylate of G47R-Mi were determined by incubating the purified protein (0.1 µM) in the presence of 200 µM PLP in 100 mM KP buffer at 25 °C and by varying the substrate concentration at a fixed cosubstrate concentration. Data were fitted to the Michaelis–Menten equation. For the activity assay on both the purified protein and the cell lysate the reactions were stopped by adding TCA 10% (v/v) and pyruvate production was measured using a spectrophotometric assay coupled with lactate dehydrogenase as previously described [2].

2.11. Glycolate toxicity assay

CHO-GO cells expressing AGT-Mi and G47R-Mi were grown for three days in the absence or in the presence of 3 µM PN. After treatment

cells were seeded at 8000 cells/well in a 96-well plate and incubated 24 h before inducing glyoxylate production by adding Hepes buffered glycolate pH 7.0 at a final concentration of 500 µM. Cell viability was evaluated after further 24 h incubation using the crystal violet staining (Sigma Aldrich) as previously described [19]. Eight replicates were performed for each assay condition. Statistical analysis was done with GraphPad Prism Version 5.0 (GraphPad software, San Diego, CA, USA).

2.12. Size exclusion chromatography (SEC)

SEC analyses were performed on an Akta FPLC system (GE Healthcare) using the Unicorn 5.01 (GE Healthcare) software and a Sephacryl S-300 10/600 column at 25 °C. The injection volume was 100 µl with detection at 280 nm, and the flow rate was 0.4 ml/min. To determine the dimer–monomer equilibrium dissociation constant, $K_{\text{dim-mon}}$, the AGT-Mi or G47R-Mi either in the apo or holo forms was incubated at different enzyme concentrations (from 3 to 12 µM) in 100 mM KP buffer, pH 7.4, for 1 h at 25 °C (a sufficient time to reach the equilibrium between monomer and dimer), and then subjected to SEC. The elution volume and the peak areas were measured using the software Unicorn 5.01 (Amersham Biosciences). The rapid equilibrium dissociation process observed for the G47R-Mi variant in the apo form was analyzed according to the method of Manning et al. [28]. If the maximum amount of AGT dimer is [E] and the concentrations of monomeric and dimeric species are [M] and [D], respectively, so that %D = 100 [D] / [E], it follows that

$$K_{\text{dim-mon}} = \frac{[M]^2/[D]}{4([E]-[D])^2/[D]} = \frac{[(100-\%D)^2[E]/(25\%D)]}{0.04(100-\%D)[E]/\%D}$$

hence,

$$\text{Log}(K_{\text{dim-mon}}) = \text{log}[E] - \text{log}\left(\frac{\%D}{0.04(100-\%D)^2}\right).$$

Thus, a plot of $\text{log}[\%D / (0.04(100 - \%D)^2)]$ to $\text{log}[E]$ results in a straight line of slope 1. When $(\%D / (0.04(100 - \%D)^2)) = 1$, $K_{\text{dim-mon}} = [E]$.

SEC analyses of lysates of CHO-GO cells were performed according to the method of Siekierska A. et al. [29]. Four 10 cm diameter dishes of confluent CHO-GO-G47R-Mi cells were grown in the absence or in the presence of PN (3 µM), harvested and lysed in 500 µl of PBS as previously described. Total lysates were then loaded into a Superdex 200 H10/30 column (GE Healthcare), equilibrated in PBS plus 1 mM EDTA, 1 mM EGTA and 1 mM DTT, using an AKTA FPLC system (Amersham Biosciences). The absorbance signal of the eluate at 280 nm, representing the total protein content, was registered. TCA 20% (v/v) was added to each eluted fraction and the samples were incubated overnight at 4 °C. After centrifugation at 16,000 g for 30 min, the precipitated protein was washed twice in PBS and resuspended in 40 µl of denaturing gel loading buffer. 15 µl of each sample were separated by SDS-PAGE and immunoblotted against anti-AGT or anti-Leu11 as previously described [18].

2.13. Immunofluorescence microscopy (IFM)

CHO-GO cells expressing AGT-Mi and G47R-Mi were grown for three days in the absence or in the presence of 3 µM PN. Approximately 3×10^5 cells were seeded into each well of a 24-well plate, containing a 13-mm glass coverslip, and grown for 24 h in complete Ham's F12 medium at 37 °C under O₂/CO₂ (19:1). Mitochondria were vitally stained prior to fixation by incubating the cells for 30 min with MitoTracker (Red CMXRos version; Molecular Probes, Life technologies) in complete Ham's F12 medium following the manufacturer's instructions. Cells were fixed in 4% (w/v) paraformaldehyde permeabilized with 0.3% Triton X-100 in PBS and then blocked in 3% bovine serum albumin

(BSA) in PBS. For the immunolabeling, rabbit polyclonal anti-human AGT rabbit polyclonal anti-human Leu11, and anti-peroxisomal protein from guinea-pig were used as primary antibodies, and Alexa Fluor conjugated antibodies (AF488 and AF555, Life technologies) were used as secondary antibodies. Nuclei were stained with DAPI and the coverslips were mounted over slides in AF1 medium (Dako). Images were captured using a confocal laser-scanning fluorescence microscope Leica SP5 (Leica Microsystem, Mannheim, Germany) at 63 \times magnification. For figure preparation images were processed using Adobe Photoshop.

3. Results

3.1. Impact of the G47R mutation on the specific activity and the expression level of AGT-Mi in *E. coli* and in CHO cells stably expressing GO

As a first assessment of structural and/or functional consequence(s) of the G47R mutation segregating on the minor allele of AGT, we expressed the variant in *E. coli* and in CHO-GO cells [30]. The catalytic activity, expressed as specific activity, and the expression level in the soluble crude cellular extracts of cells expressing G47R-Mi were measured and compared with the corresponding ones of cells expressing AGT-Mi. In *E. coli* the specific activity and the immunoreactivity of the G47R-Mi variant were both about 30% of the corresponding ones of AGT-Mi. On the other hand, in CHO-GO cells the specific activity was not measurable since no transaminase activity could be detected and the intensity of the specific band of immunoreactive AGT was about 0.6% that of AGT-Mi. Furthermore, when we compared the soluble and insoluble fractions of lysates of CHO-GO cells expressing AGT-Mi and G47R-Mi by means of western-blot, we observed that, while about 80% of AGT-Mi was present in the soluble fraction, more than 95% of G47R-Mi in its intact form was present in the insoluble fraction. Moreover, a proteolyzed form of G47R-Mi was found in definitely higher amount with respect to the intact one in the soluble fraction. In contrast, the undigested form highly prevailed in the insoluble fraction. Nonetheless, aggregated forms of the variant were detected in either the soluble and the insoluble fractions (Fig. 1). All together, these data provide a first evidence that the loss of catalytic activity and the reduction of the expression level, possibly due to proteolytic degradation and formation of aggregates, underlie the pathogenicity of G47R-Mi. Thus, we decided to explore in detail the structural and functional properties of the variant by combining biochemical analyses on the purified recombinant protein with expression studies in mammalian cells, and to compare them with the corresponding ones of AGT-Mi.

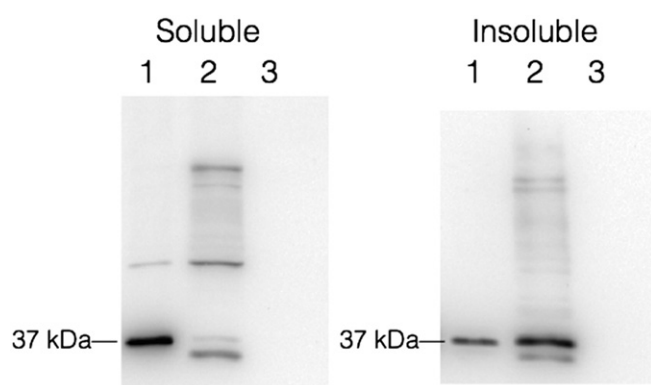


Fig. 1. Analyses of the AGT expression in CHO-GO cells expressing AGT-Mi and G47R-Mi variant. The soluble and insoluble fractions of CHO-GO (10 μ g), CHO-GO-AGT-Mi (2 μ g) and CHO-GO-G47R-Mi (10 μ g) cellular lysates were subjected to SDS-PAGE and immunoblotted with anti-AGT (1:6000). Immunoblot lanes are coded as follows: (1) CHO-GO-AGT-Mi, (2) CHO-GO-G47R-Mi and (3) CHO-GO.

3.2. Impact of the G47R mutation on the spectroscopic and kinetic features of AGT-Mi

The equilibrium dissociation constant value for PLP, $K_{D(PLP)}$, of the G47R-Mi variant was equal to 10 μ M, i.e. 38-fold higher than that of AGT-Mi (Table 1). The visible CD spectrum of the variant in the presence of a saturating PLP concentration showed a positive dichroic band at 420 nm whose magnitude was slightly lower than that of AGT-Mi. Furthermore, the substitution of Gly by Arg at position 47 mainly alters the tertiary structure of the apo form, as indicated by a consistent change in the magnitude of the dichroic bands in the near-UV region with respect to those of AGT-Mi (Fig. 2A). This is consistent with the finding that the apo form of the variant showed a \sim 1.5-fold reduction of the intrinsic fluorescence emission intensity and a maximum intensity 2 nm red-shifted with respect to apo AGT-Mi (Fig. 2B). On the other hand, as compared with AGT-Mi, both the holo and the apo forms of the variant exhibited a \sim 5-fold increase in ANS fluorescence emission intensity as well as 6-nm blue shift of the emission maximum (inset of Fig. 2B). Taken together, these data reveal that, although the G47R mutation causes a similar increase in the surface hydrophobicity of both the holo and the apo forms of the variant, it generates an altered asymmetry of certain aromatic amino acid residues, most probably those associated with the active site, more pronounced for the apo than for the holo. However, the mutation does not affect the overall secondary structure of the enzyme since the CD spectra in the range 190–240 nm of the mutant and AGT-Mi enzymes appear to be almost indistinguishable (data not shown).

To understand if the structural changes caused by the G47R mutation have consequences on the catalysis of AGT, the steady-state kinetic parameters for the pair alanine-glyoxylate for AGT-Mi and G47R-Mi were compared (Table 1). The k_{cat}/K_m value of the variant is reduced only about 5-fold as compared with that of AGT-Mi. This reduction is due to approximately equal magnitude changes in the k_{cat} and K_m values. Considering that the k_{cat} value of the variant is \sim 2.5-fold lower than that of AGT-Mi, it can be established that the not measurable specific activity of the G47R-Mi variant in CHO-GO cells is mainly due to a low expression level of the intact protein.

3.3. Impact of the G47R mutation on the dimer–monomer dissociation, thermal stability and propensity to aggregation and degradation of AGT-Mi

The conformational changes induced by the replacement of Gly47 by arginine lead to further consequences on the dimeric structure of the enzyme. The first concerns the $K_{dim-mon}$ value of the enzyme. SEC experiments performed on holo and apo AGT-Mi from 5 to 0.1 μ M enzyme concentrations (the latter value being the detection limit) previously demonstrated that the enzyme eluted as a single peak with a retention volume corresponding to a dimer [15]. Since an identical behavior was observed for the variant G47R-Mi in the holo form, we can claim that the $K_{dim-mon}$ value of these species is \ll 0.1 μ M. Therefore, the possible effect of the mutation G47R-Mi on the $K_{dim-mon}$ of the holoenzyme is not measurable. On the other hand, we observed that the apo form of the variant under study eluted as a single peak whose position shifts from that of the dimeric to that of the monomeric form as the enzyme concentration decreased from 1 to 0.17 μ M. This indicates a rapid equilibrium process. A plot of the percent dimer as a function of apoG47R-Mi concentration gives a hyperbolic curve, whose linear transformation yields a $K_{dim-mon}$ value of $0.73 \pm 0.3 \mu$ M (Supplementary Fig. 1). These data clearly indicate that the G47R mutation causes an at least \sim 7-fold increase of the $K_{dim-mon}$ value of apoAGT-Mi.

A second aspect taken in consideration is the effect of the mutation G47R on the thermal stability of AGT-Mi. Thermal protein denaturation was studied by monitoring the decrease of the dichroic signal at 222 nm, indicative of the loss of the protein secondary structure. Like holoAGT-Mi, the holo form of G47R-Mi displayed a single thermal transition, but the transition from the native to the unfolded state occurred at a

Table 1
Kinetic parameters, $K_{D(PLP)}$ and T_m values of AGT-Mi and G47R-Mi.

Enzyme	$K_{D(PLP)}$ (μM)	$K_m(\text{L-Ala})$ (mM)	k_{cat} (s^{-1})	k_{cat}/K_m ($\text{M}^{-1}\text{s}^{-1}$)	T_m holo ($^{\circ}\text{C}$)	T_m apo ($^{\circ}\text{C}$)
AGT-Mi	0.26 ± 0.02^a	28 ± 2^a	37 ± 5^a	1.32 ± 0.2^a	73.6 ± 0.3^b	53.1 ± 0.3^b 66.0 ± 0.3^b
G47R-Mi	10.1 ± 0.7	61 ± 3	14 ± 1	0.23 ± 0.02	61.4 ± 0.1	48.6 ± 0.1

^a Ref. [16].

^b Ref. [17].

temperature 12°C lower than that of holoAGT-Mi. On the other hand, unlike apoAGT-Mi showing two unfolding phases with mid-denaturations at 53°C and 66°C [17], apoG47R-Mi exhibited a single thermal denaturation transition with a mid-point at about 48°C (Table 1). Thus, the G47R mutation leads to a reduction in the thermal stability of both the holo and the apo forms of AGT-Mi.

Then, we decided to establish if other effects, like protein degradation and/or aggregation, could be induced by the mutation on both the apo and holo forms of the variant G47R-Mi.

Limited proteolysis is used for probing protein conformation. It can provide important information on local unfolding and the equilibrium between the native state of an oligomeric protein and its folding intermediates, since misfolded proteins are more susceptible to degradation by proteases [31]. Therefore, the variant G47R-Mi was probed with

proteinase K, because its proteolysis is not limited to sequence specificity but is also linked to stereochemistry and flexibility of the protein substrate. Unlike AGT-Mi [15], when the holo or the apo forms of G47R-Mi were subjected to limited proteolysis by proteinase K under experimental conditions identical to those of AGT-Mi (protease:substrate ratio = 1:500 at 25°C), the gradual disappearance of the 37 kDa band (corresponding to the undigested enzyme) and the concomitant appearance of a 35 kDa band (corresponding to the major proteolytic fragment) could be seen. The proteolytic cleavage proceeded for the apo at a rate higher than for the holo form of the variant. In particular, apo and holo showed a half-life of 12 min and higher than 60 min, respectively, with residual protein amounts of 10 and 60% after 60 min of reaction (Fig. 3A). Moreover, the finding that only the 37 kDa band of the apo variant stained with an antibody raised against AGTLeu11, as revealed by western blot analysis, indicates that the cleavage occurs within the N-terminal region (Fig. 3B). This is consistent with the finding that when the soluble fraction of CHO-GO cells stably expressing AGT-Ma, AGT-Mi or G47R-Mi was incubated with antibody against AGTLeu11 an immunoreactive band appeared only for AGT-Mi (Fig. 3C). Thus,

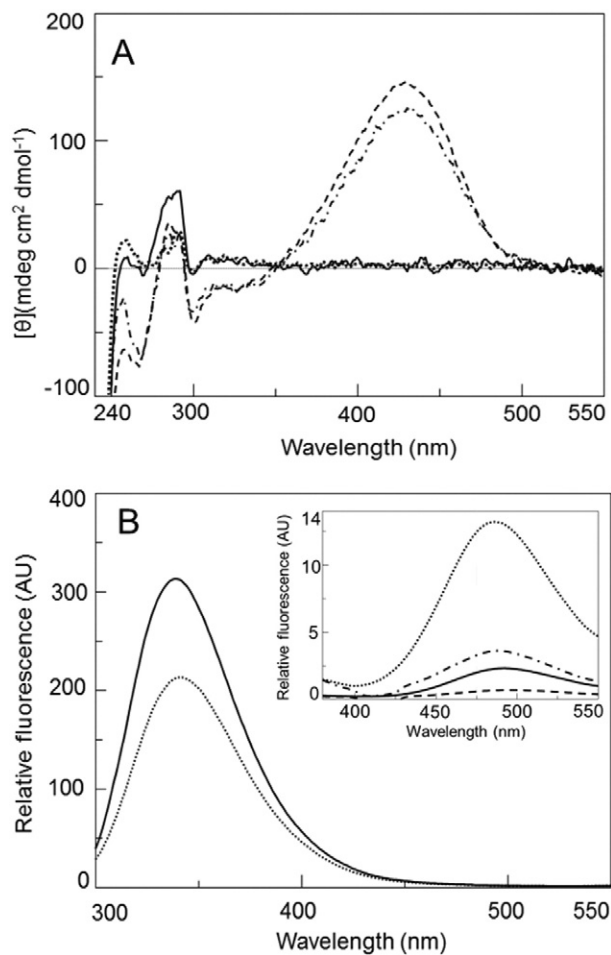


Fig. 2. Comparative spectroscopic analysis of AGT-Mi and G47R-Mi. (A) Dichroic spectra of apo AGT-Mi (—), holo AGT-Mi (---), apo G47R-Mi (— · —) and holo G47R-Mi (— · — · —) at $5 \mu\text{M}$ enzyme concentration; (B) intrinsic fluorescence emission spectra of apo AGT-Mi and apo G47R-Mi at $1 \mu\text{M}$ enzyme concentration; inset in panel B: ANS fluorescence emission spectra of AGT-Mi and G47R-Mi in both apo and holo forms at $1 \mu\text{M}$ enzyme concentration after the incubation with $15 \mu\text{M}$ ANS. Symbols are the same in each panel. All the spectra were registered in 100 mM KP buffer, pH 7.4.

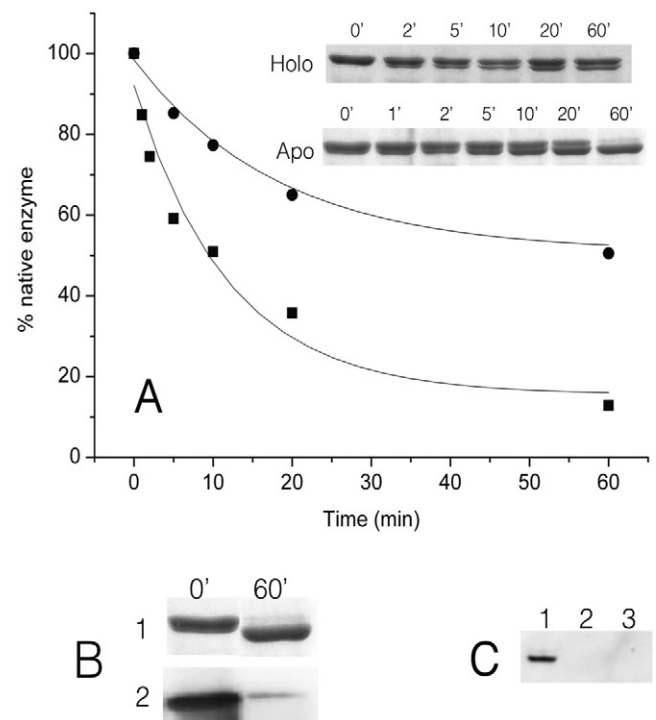


Fig. 3. Proteolytic cleavage of the G47R-Mi variant. (A) Kinetics of proteolysis of apo and holo G47R-Mi $10 \mu\text{M}$ incubated at 25°C in 100 mM KP buffer, pH 7.4, at a 500:1 (w/w) mutant:proteinase K ratio. At times indicated, aliquots were removed, treated with 2 mM PMSF and subjected to 12% SDS-PAGE. The band intensities were analyzed using the ImageJ software (Rasband, WS) and the rate of proteolysis was determined by plotting the percentage of native apo (■) and holo (●) enzyme vs time and fitting to a first-order equation (B) SDS-PAGE (1) and western blot (2) analysis of the native (0') and digested (60') apoG47R-Mi with proteinase K. (C) The soluble fraction of CHO-GO-AGT-Ma ($2 \mu\text{g}$), CHO-GO-AGT-Mi ($2 \mu\text{g}$) and CHO-GO-G47R-Mi ($10 \mu\text{g}$) cellular lysates was subjected to SDS-PAGE and immunoblotted with anti-AGTLeu11 (1:6000). Immunoblot lanes are coded as follows: (1) CHO-GO-AGT-Mi, (2) CHO-GO-AGT-Ma and (3) CHO-GO-G47R-Mi.

increased susceptibility to proteases occurs within the N-terminal region as a consequence of structural changes due to mutation G47R. It could have been of interest to measure the extent of the susceptibility of the variant to proteasomal degradation in CHO-GO cells. Unfortunately, considering the low amount of the immunoreactive band corresponding to the intact protein, it was not possible to measure the half-life of the pathogenic variant.

As mentioned above, about 95% of the variant G47R-Mi stably expressed in CHO-GO cells is present in the insoluble fraction. This observation strongly suggests the propensity of the variant to aggregation. Indeed, when the crude extract of CHO-GO cells stably expressing the G47R-Mi variant was fractionated by SEC, the immunoreactive protein was detected both in fractions with an elution volume corresponding to proteic species with apparent molecular weight ranging from ~350 to more than 1000 kDa, and in fractions with an elution volume corresponding to that of the active dimeric form of AGT. While the intact form was more populated in the aggregated fraction, the contrary was true in the second peak, which indeed mainly contained the nicked form. Thus, the aggregates are primarily formed by the intact form of the variant (Fig. 4).

To further examine the self-association process, DLS experiments of the recombinant purified variant both in the holo and apo forms were performed under physiological conditions (37°C, 150 mM ionic strength, pH 7.4) and the results were compared with those of AGT-Mi. As already known [15], the count rate as a function of time increases in a slow manner for apo and holo AGT-Mi, and their dimer signal is always present over the incubation time examined, even if small aggregates appear at about 10 min. Since in DLS experiments the effective weight of the oligomers on the photon correlation signal is modest due to the $1/d^6$ scaling of scattered light intensity, we concluded that the dimer is the species most relevant in solution. On the contrary, following the incubation of the holo or apo forms of G47R-Mi under the same experimental conditions, the total count rate plotted as a function of time shows typical aggregation curves more fast for the apo than for the holo form, and leveling off after about 50 and 100 min for apo and holo, respectively (Fig. 5A). Moreover, the time dependence of the apparent particle size of both the holo and apo forms of the variant indicates (i) the disappearance of the dimeric species of the holo and apo variant at about 84 min and 20 min, respectively, (ii) the presence

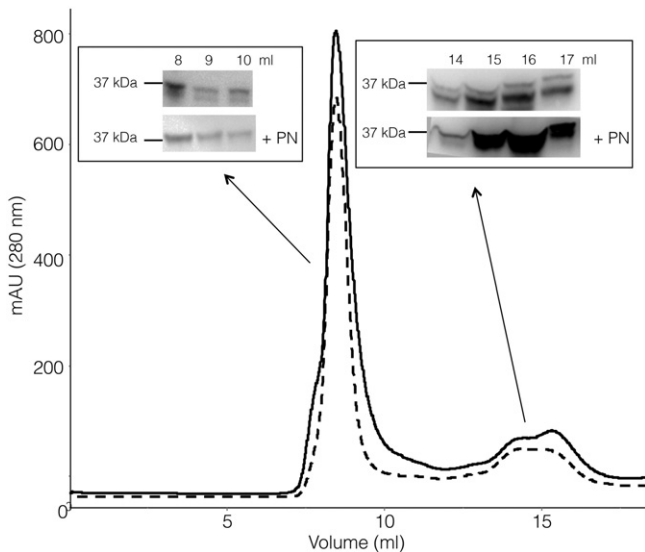


Fig. 4. Gel filtration analyses of CHO-GO cells expressing the G47R-Mi variant. CHO-GO-G47R-Mi cells grown in the absence or in the presence of 3 μ M PN were harvested, lysed and the total lysate was loaded on a Superdex 200 H10/30 SEC column run in PBS containing 1 mM EDTA, 1 mM EGTA and 1 mM DTT. The picture shows the elution profile of the total lysate of CHO-GO-G47R-Mi grown in the absence (solid line) or in the presence (dashed line) of PN. Insets show the western blot analyses of the selected SEC fractions.

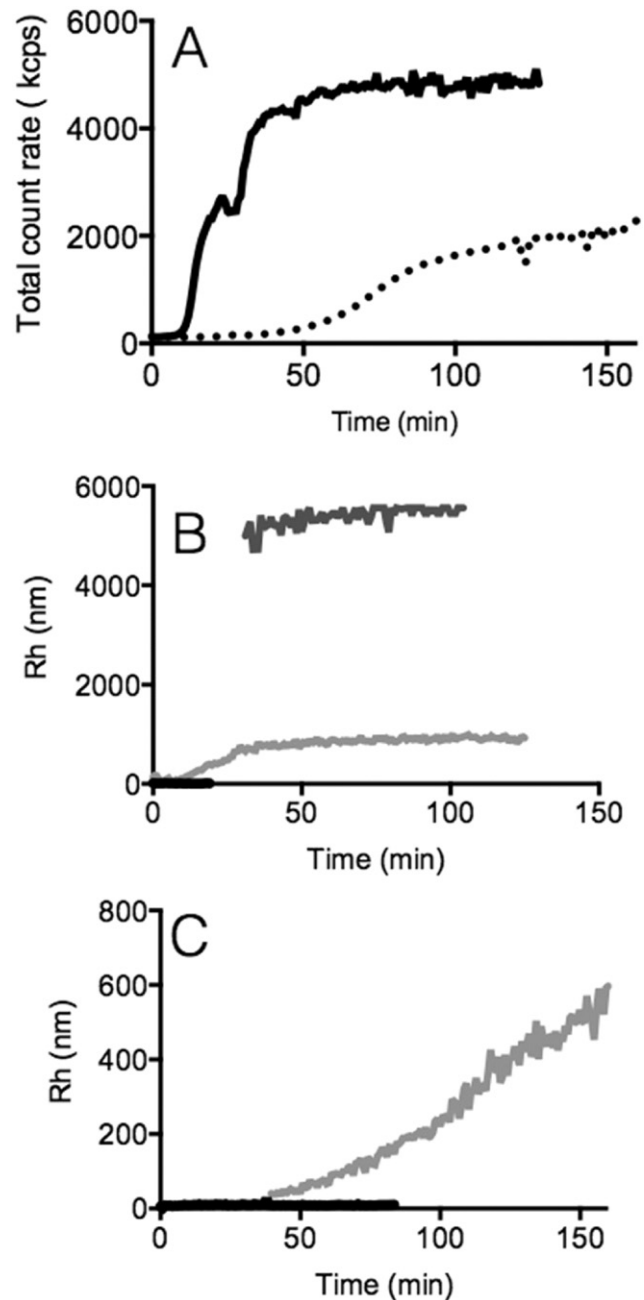


Fig. 5. Time dependent aggregation of G47R-Mi variant. (A) The total count rate (measured as kilo counts per second) of apoG47R-Mi (solid line) and holoG47R-Mi (dotted line) variants is plotted as a function of time. The diameter of the species present in solution is reported as function of time for (B) holoG47R-Mi and (C) apoG47R-Mi. Color code: black, dimer; light gray, aggregates; dark gray, high-molecular weight aggregates. All measurements have been performed at 1 μ M enzyme concentration, 37 °C, in 60 mM KP buffer, pH 7.4.

of two populations, a dimeric form with a hydrodynamic diameter of 10 nm, and high order oligomers of both apo and holo forms with a hydrodynamic diameter of 200–600 nm appearing after about 40 min, and (iii) the appearance of an additional and distinct population of higher order oligomers of apovariant (~5000 nm) at about 25 min (Fig. 5B and C). This aggregation phenomenon was also analyzed under different ionic strengths (from 0.15 to 1.5 mM) or enzyme concentrations (from 1 to 20 μ M). The results indicate that the aggregation extent increases as the ionic strength decreases and as the protein concentration increases, thus suggesting the involvement of dimer–dimer electrostatic interactions in the formation of aggregates of the variant

G47R-Mi. Taken together, all these data provide evidence that the mutation causes an altered folding equilibrium shifted towards folding intermediates and destabilization due to local protein unfolding leading to protein degradation and aggregation. These effects appear in the recombinant purified variant more pronounced for the apo than for the holo one. Considering that the apo variant displays a ~38-fold increase in $K_{D(PLP)}$ value as well as an increase of the $K_{dim-mon}$ value with respect to AGT-Mi, it can be inferred that the apo form of the G47R-Mi variant could be the form mainly present in CHO-GO cells where it undergoes dimer–monomer dissociation, aggregation and/or degradation.

3.4. Impact of the G47R mutation on the subcellular localization of AGT-Mi

As shown in Fig. 6A, IFM experiments indicated that the variant G47R-Mi exhibits a double subcellular localization: peroxisomal and mitochondrial. To investigate the subcellular localization of the intact and the nicked form of G47R-Mi we stained CHO-GO-AGT-Ma, CHO-GO-AGT-Mi and CHO-GO-G47R-Mi cells with an anti-AGTLeu11, an antibody that specifically recognized Leu11. As expected, while no immunoreactive AGT signal is visible in cells expressing AGT-Ma, a signal that co-localized with peroxisomes is visible in cells expressing AGT-Mi (Supplementary Fig. 2). Interestingly, in cells expressing G47R-Mi the staining with anti-AGTLeu11 gives a signal that completely co-localizes with that of peroxisomes, but does not show any co-localization with mitochondria (Fig. 6B). These data indicate that the intact species of G47R-Mi is exclusively peroxisomal whereas the nicked one, or at least the majority of it, is mitochondrial. On the basis of the $K_{dim-mon}$ value of the recombinant variant (higher than that of AGT-Mi) and on the observed subcellular localization of G47R-Mi, it is reasonable to suggest that a fraction of the monomeric apo form (unfolded or partly unfolded) of the variant, once imported into mitochondria is subjected to proteolysis giving rise to species lacking the N-terminal region, and that another fraction of the unproteolyzed

apodimer is imported into peroxisomes, where in large amounts possibly undergoes self-association. However, it cannot be excluded that events of degradation and aggregation could occur, at least in part, in the cytosol.

3.5. Effects of PN on the specific activity, the expression level, the susceptibility to protease, the propensity to aggregation and the subcellular localization of the G47R-Mi variant

Following all the above data on the impact of the G47R mutation, we investigated the effect of compounds, known to act as chaperones, on the expression level of the G47R-Mi variant in the soluble fraction of lysates of CHO cells. No one of the tested compounds, except 4-PBA and PN, affects the expression level of the variant. 4-PBA increases the expression level of only about 2-fold (Supplementary Fig. 3). Thus, considered its small effect, the compound was not further explored in subsequent experiments. Instead, the remarkable effect of PN along with its current use in clinical cases to treat PH1 patients [32], urged us to investigate in detail its action. In the presence of PN (from 0.3 to 300 μ M) in the culture medium the expression level of the G47R-Mi variant in the soluble fraction raises. At 3 μ M PN the improvement is about 30-fold with respect to the untreated cells (Fig. 7A and B). Indeed the protein level of the variant reaches ~26% that of AGT-Mi. Moreover, at this PN concentration the amount of the immunoreactive band corresponding to the proteolyzed variant appears to be remarkably reduced in comparison with that detected in the soluble fraction of the variant grown in the basal medium. On the other hand, the analysis of the insoluble fraction of CHO-GO cells expressing G47R-Mi provides a rough evidence for the different amounts of insoluble G47R-Mi in the absence or presence of 3 μ M PN. However, if the total amount of the expressed AGT-Mi and G47R-Mi is normalized to 100%, it can be observed that upon addition of 3 μ M PN to the culture medium the relative amounts of soluble and insoluble fractions of AGT-Mi remain unchanged, while

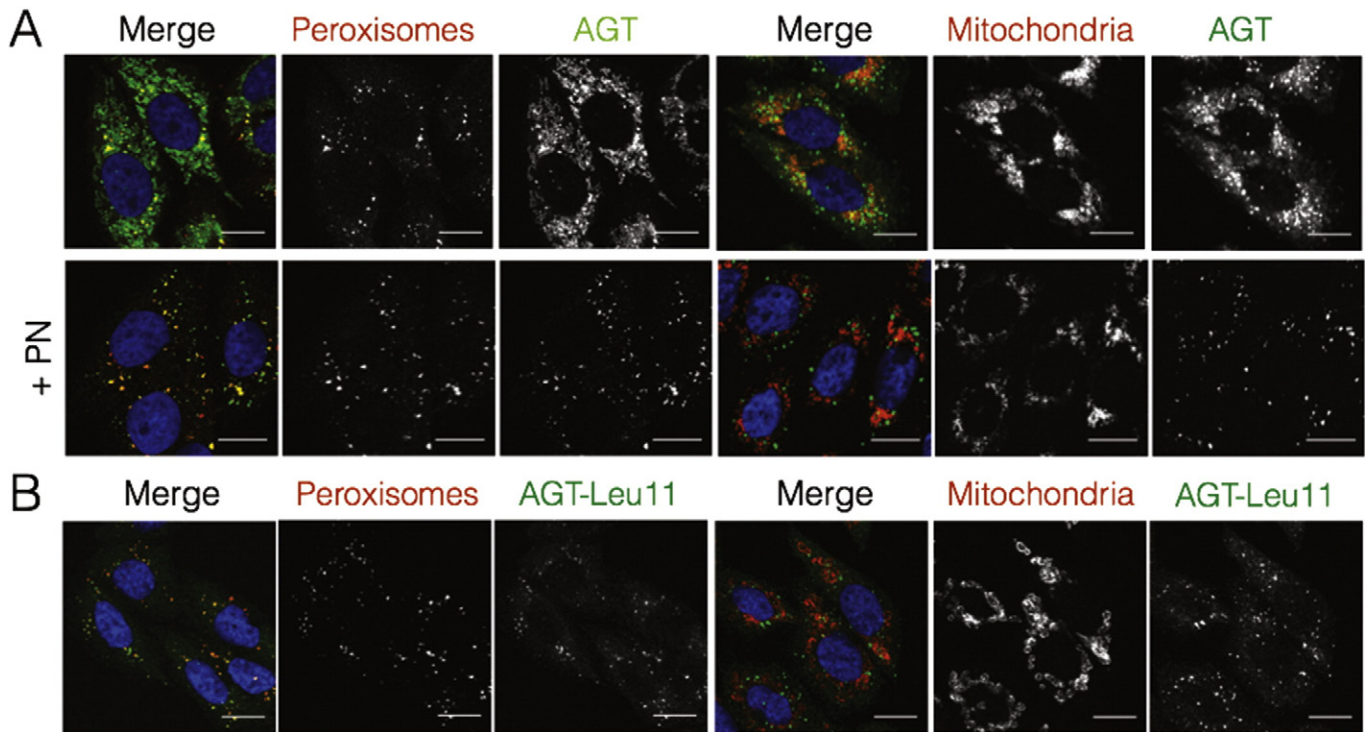


Fig. 6. Subcellular localization of AGT in CHO-GO cells expressing the G47R-Mi variants. Cells grown in the absence or in the presence of 3 μ M PN have been fixed and stained as follows: (A) anti-AGT (green), anti-peroxisomal protein (red), MitoTracker® (red); (B) anti-AGTLeu11 (green), anti-peroxisomal protein (red), MitoTracker® (red). Nuclei were stained with Dapi (blue). Merge and single channel images come from a single z-plane. Scale bar: 10 μ m.

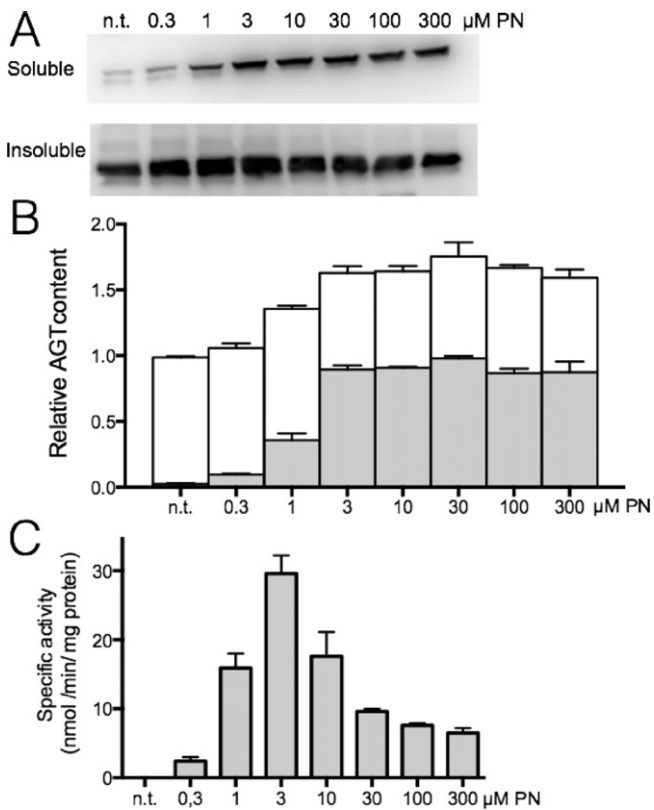


Fig. 7. Effect of PN treatment on AGT expression level and specific activity in CHO-GO cells expressing G47R-Mi variant. CHO-GO-G47R-Mi cells were grown at the reported PN concentrations. After three days cells were harvested lysed and assayed for the AGT immunoreactivity and transaminase activity. (A) The soluble and insoluble fractions of lysate (10 μg) of CHO-GO-G47R-Mi grown at different PN concentration were subjected to SDS-PAGE and immunoblotted with anti-AGT (1:6000). (B) Immunoblot band quantification performed by the software Quantity One 4.6.3. Histogram bars are colored as follows: white, insoluble fraction; gray, soluble fraction. (C) Histogram representative of the AGT specific activity. In all cases 100 μg of soluble lysate were incubated with 0.5 M L-alanine, 10 mM glyoxylate and 200 μM PLP at 25 °C in 100 mM KP buffer, pH 7.4 for 120'. Bar graphs represent the mean ± SEM. Data come from the mean of three different experiments.

the amount of the insoluble fraction decreases of about 3-fold, reaching a value about 2-fold that of AGT-Mi (Fig. 8). The dose–response for the specific activity of the soluble fraction is similar to that observed for the expression level, even if, as already seen [18,26], it decreases at PN concentrations higher than 3 μM (Fig. 7C). It was previously suggested

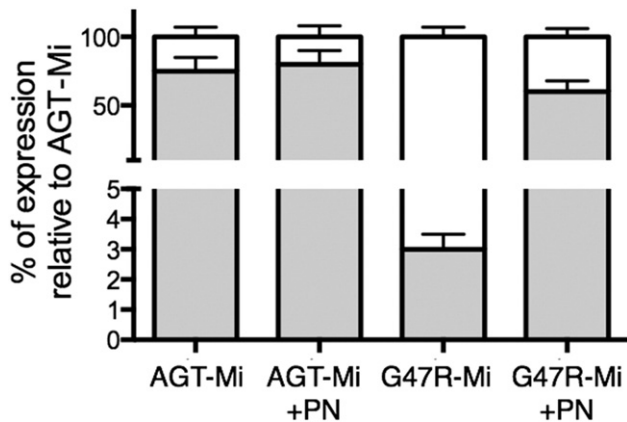


Fig. 8. Effect of PN on the soluble/insoluble protein ratios of AGT-Mi and G47R-Mi expressed in CHO-GO cells. Histogram bars represent the percentage of soluble (gray) and insoluble (white) amount of AGT for the analyzed enzymatic species in the reported conditions. Bar graphs represent the mean ± SEM. Data come from the mean of three different experiments.

that PN at high concentrations could exert an inhibitory action against PLP binding to the apoenzyme, possibly due to the formation of an inactive complex at the active site of the enzyme [26]. We also found that when the lysate of cells expressing G47R-Mi in the presence of 3 μM PN was subjected to SEC, the immunoreactive protein was found both in fractions corresponding to aggregates and in fractions corresponding to the dimer, as already seen in the absence of PN. However, in this case, both fractions mainly contain undigested protein (Fig. 4), thus suggesting that PN limits the proteolytic cleavage without completely preventing its aggregation. In order to establish if PN rescues the intracellular level of the apo and/or holo form of the variant, we measured the catalytic activity of the soluble fraction of lysates of CHO-GO cells expressing G47R-Mi in the presence of 3 μM PN. The measurements, performed in the presence or absence of added PLP in the assay mixture, allowed us to distinguish between the total amount of active AGT, i.e. holo plus apo, and the active holoAGT. Although we are aware that a comparison with our data on the variant grown in the basal medium is not possible since the amount of the holo and apo forms is not detectable, it is of interest to point out that when 3 μM PN was present in the culture medium, the amount of holo and apo forms of the variant represents the 80 and 20%, respectively, of the total amount of the enzyme. A less relevant effect was seen for AGT-Mi under the same experimental conditions, i.e. an increase from 75 to 95% for the holo and a decrease from 25 to 5% for the apo. Thus, PN mainly increases the intracellular level of the active holo form of the variant. The impact of PN on the subcellular localization of G47R-Mi was also investigated. IFM analyses revealed that upon addition of PN to the culture medium of the G47R-Mi variant the protein is only present in the peroxisomes in its intact form (as revealed by staining with the anti-AGTLeu11 antibody). Accordingly, assays aimed at measuring the ability of the variant to detoxify glyoxylate by using CHO-GO cells treated with glycolate showed that PN causes a 4-fold increase in the functionality reaching a value of relative viability of the cells equal to about 40% that of untreated AGT-Mi (data not shown). Altogether, the results indicate that PN acts as a chaperone on the G47R-Mi variant. In particular, it was demonstrated that the action of PN consists in increasing the proper folding, in partly rescuing the catalytic activity, and in preventing proteolytic degradation and aggregation of the variant. Moreover, PN is able to redirect all the protein to peroxisomes, thus restoring the ability to detoxify glyoxylate. A partial reroute to peroxisomes was previously reported for the variants G170R-Mi and F152I-Mi upon PN supplementation to the culture medium [26].

4. Discussion

This paper reports biochemical studies on the purified recombinant G47R-Mi in combination with expression experiments in CHO-GO cells aimed at identifying the consequences of the mutation G47R on the structural and/or functional features of AGT-Mi. The role of PN in rescuing the intracellular functionality of this variant was also investigated.

The variant G47R-Mi was first expressed in *E. coli*, purified, and the spectroscopic and kinetic properties analyzed. Our results show that the mutation causes only a 5.7-fold reduction of the catalytic efficiency. This result, consistent with the modest change in the visible CD spectrum of the variant with respect to AGT-Mi, indicates that the residue at position 47 does not play a critical role in the catalysis and does not provide any indication for the pathogenicity of the variant. Nevertheless, we noticed that the Gly47 mutation causes consistent changes mainly to the apo form with respect to the apo form of AGT-Mi. They consist in remarkable changes in the dichroic signals in the near-UV region and in the intrinsic emission fluorescence, a significant increase of the $K_D(\text{PLP})$ and $K_{D(\text{dim-mon})}$ values, a considerable propensity to proteolysis occurring within its N-terminal region, and a meaningful propensity to form high order aggregates resulting from dimer–dimer electrostatic interactions. Several relevant observations could be also made by examining CHO-GO cells stably expressing G47R-Mi: (i) while AGT-Mi remains in the supernatant, more than 95% of the variant comes down

in the pellet, (ii) the transaminase activity could not be detected in the soluble fraction neither in the absence nor in the presence of added PLP in the assay mixture, (iii) only a low amount of undigested variant is detected in the soluble fraction where we also noticed the presence of the variant proteolyzed within the N-terminal region as well as of aggregates of high molecular weight, and (iv) the nicked protein was localized into mitochondria, while the intact protein was found in the peroxisomes, where it possibly undergoes aggregation. Taken together, these data indicate that (i) the G47R mutation cannot be considered a catalytic mutation, rather a folding mutation, and (ii) altered subcellular localization, aggregation and proteolytic degradation represent critical issues in the pathogenicity of G47R-Mi (Scheme 1). The aberrant intracellular trafficking is shared with other mutants on the background of the minor allele characterized by a low kinetic stability of their apo forms, like F152I-Mi, I244T-Mi, G170R-Mi and G41R-Mi [14–16], even if is the first time that a nicked form of a pathogenic variant was found localized into mitochondria in a cellular model. It has been already suggested that a distribution between mitochondria and peroxisomes could be due to mutations of residues causing a kinetic interference with the dimerization process of the enzyme [33]. Besides the mistargeting, it should be noted that both variants G47R-Mi and G41R-Mi are characterized by a remarkable propensity to proteolytic degradation and aggregation [15]. This is not unexpected considering that both the residues (i) belong to the N-terminal region and are located at the dimer interface (Supplementary Fig. 4) and (ii) are replaced by a bulky polar side chain lying between the N-terminal regions of two subunits. As already predicted by *in silico* analysis on the G41R-Mi [15], the Gly47 to Arg substitution is expected to weaken the interactions between the two monomers and promote the fluctuation of the N-terminal arm. The latter event could cause the exposure of negatively charged residues leading to the electrostatically-driven aggregation of the protein, and a susceptibility of the N-terminal region to proteolytic attack. On the basis of all these considerations, it can be advanced the view that a different partitioning between protein mitochondrial mistargeting, aggregation and degradation of variants on the background of the minor allele might depend on the location of the mutated residue in the structure of AGT-Mi.

Besides all these data and considerations, the most relevant finding is that PN appears to facilitate appropriate folding of the variant G47R-

Mi, by increasing the intracellular concentration of PLP, which possibly acts as a nucleation site. This is consistent with the following data: (i) a remarkable increase of the expression level and the specific activity of the variant, (ii) a decreased extent of proteolytic degradation and aggregation, (iii) a redirection of all the protein into peroxisomes, and (iv) an increased ability to detoxify glyoxylate. Basing on these data, the fate of the variant in the presence of PN is depicted in Scheme 1. It is of interest to note that, although there is no report of PN responsiveness in patients with G47R or G41R mutations, PN has been found to have little or no effect on specific activity, expression level and subcellular localization of the G41R-Mi variant in the same cellular system we used [26]. Thus, the most striking difference between the variants G47R-Mi and G41R-Mi is the response to PN. These data imply that PN plays a role in the folding and/or dimerization of G47R-Mi, while it has a modest impact, if any, on G41R-Mi. This effect is surprising considering that the two mutated residues are near to each other in the primary structure of AGT even if they have a different location in the crystal structure. Gly41 lies in an α -helix, whereas Gly47 in a mobile loop. It can be speculated that these residues may have a distinct role in the folding and/or dimerization process of AGT. However, since the folding pathway and the possible role of the coenzyme are unknown, no valid conclusions can be drawn on this issue.

5. Conclusions

Overall, the combined molecular and cellular analyses of the effects of the G47R mutation on AGT-Mi allow us to conclude that the G47R-Mi variant exhibits a folding defect resulting in (i) an altered dimerization process of the apo-form, which leads to mitochondrial mistargeting, and (ii) an increased flexibility of the N-terminus, which causes a remarkable propensity to proteolytic cleavage inside mitochondria and aggregation inside peroxisomes. Although G47R-Mi shares many of these features with Gly41 variants, it differs because it responds to PN, whose main effect is to prevent the mitochondrial mistargeting and the proteolytic degradation. Therefore, a confident prediction of PN responsiveness of PH1-causing mutations based only on the structural context of the mutated residues is unfortunately not possible. The same is also true for tetrahydrobiopterin responsive mutations associated with phenylketonuria [34].

Nevertheless, whatever the mechanism of action of PN could be, the significant functional rescue of the variant might be clinically relevant, and, therefore, it might be a great promise for the use of PN in the treatment of PH1 patients bearing the G47R mutation.

Supplementary data to this article can be found online at <http://dx.doi.org/10.1016/j.bbapap.2015.07.002>.

Transparency document

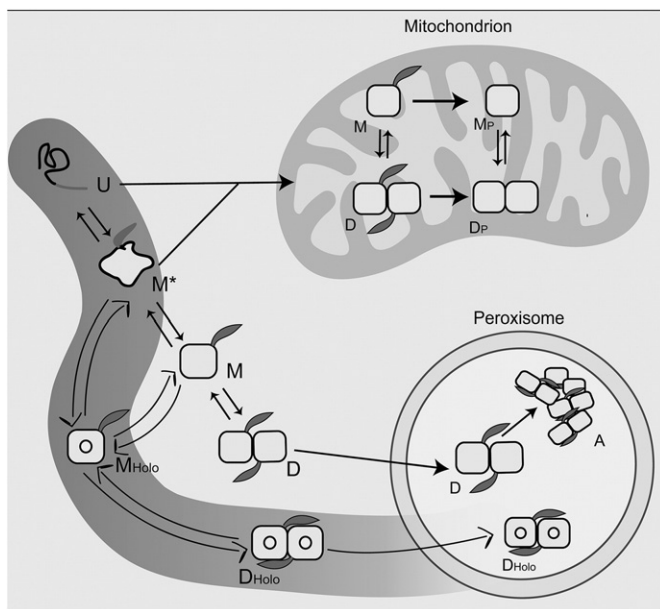
The Transparency document associated with this article can be found, in the online version.

Acknowledgments

This work was supported by grants from Telethon (GGP10092 to C.B.V.) and Oxalosis and Hyperoxaluria Foundation (OHF2012) (to B.C.). This paper is dedicated to the memory of Prof. Donatella Barra.

References

- [1] C.J. Danpure, Peroxisomal alanine:glyoxylate aminotransferase and prenatal diagnosis of Primary Hyperoxaluria Type 1, *Lancet* 2 (1986) 1168.
- [2] B. Cellini, M. Bertoldi, R. Montioli, A. Paiardini, C. Borri Voltattorni, Human wild-type alanine:glyoxylate aminotransferase and its naturally occurring G82E variant: functional properties and physiological implications, *Biochem. J.* 408 (2007) 39–50.
- [3] P.E. Purdue, M.J. Lumb, J. Allsop, C.J. Danpure, An intronic duplication in the alanine:glyoxylate aminotransferase gene facilitates identification of mutations in compound heterozygote patients with Primary Hyperoxaluria Type 1, *Hum. Genet.* 87 (1991) 394–396.



Scheme 1. Schematic representation of the molecular defect of the G47R-Mi variant and of the proposed PN mechanism of action. (U) Unfolded polypeptide chain, (M*) partly folded monomer, (M) folded apo-monomer, (M_{Holo}) folded holo-monomer, (M_P) proteolyzed monomer, (D) apo-dimer, (D_{Holo}) holo-dimer, (D_P) proteolyzed dimer and (A) aggregates.

- [4] P.E. Purdue, Y. Takada, C.J. Danpure, Identification of mutations associated with peroxisome-to-mitochondrion mistargeting of alanine:glyoxylate aminotransferase in Primary Hyperoxaluria Type 1, *J. Cell Biol.* 111 (1990) 2341–2351.
- [5] M.J. Lumb, C.J. Danpure, Functional synergism between the most common polymorphism in human alanine:glyoxylate aminotransferase and four of the most common disease-causing mutations, *J. Biol. Chem.* 275 (2000) 36415–36422.
- [6] X. Zhang, S.M. Roe, Y. Hou, M. Bartlam, Z. Rao, L.H. Pearl, C.J. Danpure, Crystal structure of alanine:glyoxylate aminotransferase and the relationship between genotype and enzymatic phenotype in Primary Hyperoxaluria Type 1, *J. Mol. Biol.* 331 (2003) 643–652.
- [7] M.J. Lumb, A.F. Drake, C.J. Danpure, Effect of N-terminal alpha-helix formation on the dimerization and intracellular targeting of alanine:glyoxylate aminotransferase, *J. Biol. Chem.* 274 (1999) 20587–20596.
- [8] P.E. Purdue, J. Allsop, G. Isaya, L.E. Rosenberg, C.J. Danpure, Mistargeting of peroxisomal L-alanine:glyoxylate aminotransferase to mitochondria in primary hyperoxaluria patients depends upon activation of a cryptic mitochondrial targeting sequence by a point mutation, *Proc. Natl. Acad. Sci. U. S. A.* 88 (1991) 10900–10904.
- [9] E. Oppici, R. Montioli, B. Cellini, Liver peroxisomal alanine:glyoxylate aminotransferase and the effects of mutations associated with Primary Hyperoxaluria Type I: an overview, *Biochim. Biophys. Acta* 1854 (9) (2015) 1212–1219.
- [10] C.J. Danpure, Molecular etiology of Primary Hyperoxaluria Type 1: new directions for treatment, *Am. J. Nephrol.* 25 (2005) 303–310.
- [11] M.B. Coulter-Mackie, Q. Lian, Consequences of missense mutations for dimerization and turnover of alanine:glyoxylate aminotransferase: study of a spectrum of mutations, *Mol. Genet. Metab.* 89 (2006) 349–359.
- [12] M.B. Coulter-Mackie, Q. Lian, Partial trypsin digestion as an indicator of mis-folding of mutant alanine:glyoxylate aminotransferase and chaperone effects of specific ligands. Study of a spectrum of missense mutants, *Mol. Genet. Metab.* 94 (2008) 368–374.
- [13] S. Fargue, J. Lewin, G. Rumsby, C.J. Danpure, Four of the most common mutations in Primary Hyperoxaluria Type 1 unmask the cryptic mitochondrial targeting sequence of alanine:glyoxylate aminotransferase encoded by the polymorphic minor allele, *J. Biol. Chem.* 288 (2013) 2475–2484.
- [14] B. Cellini, A. Lorenzetto, R. Montioli, E. Oppici, C.B. Voltattorni, Human liver peroxisomal alanine:glyoxylate aminotransferase: different stability under chemical stress of the major allele, the minor allele, and its pathogenic G170R variant, *Biochimie* 92 (2010) 1801–1811.
- [15] B. Cellini, R. Montioli, A. Paiardini, A. Lorenzetto, F. Maset, T. Bellini, E. Oppici, C.B. Voltattorni, Molecular defects of the glycine 41 variants of alanine glyoxylate aminotransferase associated with primary hyperoxaluria type I, *Proc. Natl. Acad. Sci. U. S. A.* 107 (2010) 2896–2901.
- [16] B. Cellini, R. Montioli, A. Paiardini, A. Lorenzetto, C.B. Voltattorni, Molecular insight into the synergism between the minor allele of human liver peroxisomal alanine:glyoxylate aminotransferase and the F152I mutation, *J. Biol. Chem.* 284 (2009) 8349–8358.
- [17] E. Oppici, R. Montioli, A. Lorenzetto, S. Bianconi, C. Borri Voltattorni, B. Cellini, Biochemical analyses are instrumental in identifying the impact of mutations on holo and/or apo-forms and on the region(s) of alanine:glyoxylate aminotransferase variants associated with primary hyperoxaluria type I, *Mol. Genet. Metab.* 105 (2012) 132–140.
- [18] E. Oppici, A. Roncador, R. Montioli, S. Bianconi, B. Cellini, Gly161 mutations associated with Primary Hyperoxaluria Type I induce the cytosolic aggregation and the intracellular degradation of the apo-form of alanine:glyoxylate aminotransferase, *Biochim. Biophys. Acta* 1832 (2013) 2277–2288.
- [19] R. Montioli, A. Roncador, E. Oppici, G. Mandrile, D.F. Giachino, B. Cellini, C. Borri Voltattorni, S81L and G170R mutations causing Primary Hyperoxaluria type I in homozygosis and heterozygosis: an example of positive interallelic complementation, *Hum. Mol. Genet.* 23 (2014) 5998–6007.
- [20] E. Oppici, K. Fodor, A. Paiardini, C. Williams, C.B. Voltattorni, M. Wilmanns, B. Cellini, Crystal structure of the S187F variant of human liver alanine:glyoxylate [corrected] aminotransferase associated with primary hyperoxaluria type I and its functional implications, *Proteins* 81 (2013) 1457–1465.
- [21] A.M. Pittman, M.D. Lage, V. Poltoratsky, J.D. Vrana, A. Paiardini, A. Roncador, B. Cellini, R.M. Hughes, C.L. Tucker, Rapid profiling of disease alleles using a tunable reporter of protein misfolding, *Genetics* 192 (2012) 831–842.
- [22] A. Santana, E. Salido, A. Torres, L.J. Shapiro, Primary Hyperoxaluria Type 1 in the Canary Islands: a conformational disease due to I244T mutation in the P11L-containing alanine:glyoxylate aminotransferase, *Proc. Natl. Acad. Sci. U. S. A.* 100 (2003) 7277–7282.
- [23] M.D. Lage, A.M. Pittman, A. Roncador, B. Cellini, C.L. Tucker, Allele-specific characterization of alanine:glyoxylate aminotransferase variants associated with primary hyperoxaluria, *PLoS One* 9 (2014) e94338.
- [24] N. Mesa-Torres, I. Fabelo-Rosa, D. Riverol, C. Yunta, A. Albert, E. Salido, A.L. Pey, The role of protein denaturation energetics and molecular chaperones in the aggregation and mistargeting of mutants causing primary hyperoxaluria type I, *PLoS One* 8 (2013) e71963.
- [25] N. Mesa-Torres, E. Salido, A.L. Pey, The lower limits for protein stability and foldability in primary hyperoxaluria type I, *Biochim. Biophys. Acta* 1844 (2014) 2355–2365.
- [26] S. Fargue, G. Rumsby, C.J. Danpure, Multiple mechanisms of action of pyridoxine in Primary Hyperoxaluria Type 1, *Biochim. Biophys. Acta* 1832 (2013) 1776–1783.
- [27] B.A. Shirley, C.N. Pace, J.T. Thompson, Measuring the conformational stability of a protein, in: T.E. Creighton (Ed.), *Protein Structure, a Practical Approach*, IRL Press, Oxford, England 1989, pp. 311–330.
- [28] L.R. Manning, A. Dumoulin, W.T. Jenkins, R.M. Winslow, J.M. Manning, Determining subunit dissociation constants in natural and recombinant proteins, *Methods Enzymol.* 306 (1999) 113–129.
- [29] A. Siekierska, G. De Baets, J. Reumers, R. Gallardo, S. Rudyak, K. Broersen, J. Couceiro, J. Van Durme, J. Schymkowitz, F. Rousseau, Alpha-galactosidase aggregation is a determinant of pharmacological chaperone efficacy on Fabry disease mutants, *J. Biol. Chem.* 287 (2012) 28386–28397.
- [30] J.T. Behnam, E.L. Williams, S. Brink, G. Rumsby, C.J. Danpure, Reconstruction of human hepatocyte glyoxylate metabolic pathways in stably transformed Chinese-hamster ovary cells, *Biochem. J.* 394 (2006) 409–416.
- [31] A. Fontana, P.P. de Laureto, B. Spolaore, E. Frare, P. Picotti, M. Zamboni, Probing protein structure by limited proteolysis, *Acta Biochim. Pol.* 51 (2004) 299–321.
- [32] H. Hoyer-Kuhn, S. Kohlbrot, R. Volland, J. Franklin, B. Hero, B.B. Beck, B. Hoppe, Vitamin b6 in primary hyperoxaluria I: first prospective trial after 40 years of practice, *Clin. J. Am. Soc. Nephrol.* 9 (2014) 468–477.
- [33] C.J. Danpure, Primary Hyperoxaluria Type 1: AGT mistargeting highlights the fundamental differences between the peroxisomal and mitochondrial protein import pathways, *Biochim. Biophys. Acta* 1763 (2006) 1776–1784.
- [34] C. Heintz, R.G. Cotton, N. Blau, Tetrahydrobiopterin, its mode of action on phenylalanine hydroxylase, and importance of genotypes for pharmacological therapy of phenylketonuria, *Hum. Mutat.* 34 (2013) 927–936.

The Chaperoning Activity of Amino-oxyacetic Acid on Folding-Defective Variants of Human Alanine:Glyoxylate Aminotransferase Causing Primary Hyperoxaluria Type I

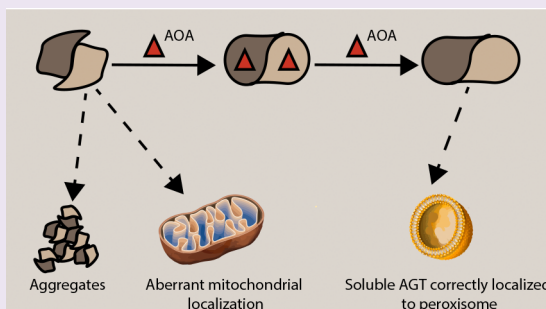
Elisa Oppici,[†] Riccardo Montioli,[†] Mirco Dindo,[†] Laura Maccari,[‡] Valentina Porcari,[‡] Antonio Lorenzetto,[†] Sara Chellini,[‡] Carla Borri Voltattorni,[†] and Barbara Cellini^{*,†}

[†]Department of Life Sciences and Reproduction, Section of Biological Chemistry, University of Verona, Strada Le Grazie 8 37134 Verona, Italy

[‡]Siena Biotech S.p.A., Strada del Petriccio e Belriguardo, 35 53100 Siena, Italy

Supporting Information

ABSTRACT: The rare disease Primary Hyperoxaluria Type I (PH1) results from the deficit of liver peroxisomal alanine:glyoxylate aminotransferase (AGT), as a consequence of inherited mutations on the *AGXT* gene frequently leading to protein misfolding. Pharmacological chaperone (PC) therapy is a newly developed approach for misfolding diseases based on the use of small molecule ligands able to promote the correct folding of a mutant enzyme. In this report, we describe the interaction of amino-oxyacetic acid (AOA) with the recombinant purified form of two polymorphic species of AGT, AGT-Ma and AGT-Mi, and with three pathogenic variants bearing previously identified folding defects: G41R-Ma, G170R-Mi, and I244T-Mi. We found that for all these enzyme AOA (i) forms an oxime at the active site, (ii) behaves as a slow, tight-binding inhibitor with K_i values in the nanomolar range, and (iii) increases the thermal stability. Furthermore, experiments performed in mammalian cells revealed that AOA acts as a PC by partly preventing the intracellular aggregation of G41R-Ma and by promoting the correct peroxisomal import of G170R-Mi and I244T-Mi. Based on these data, we carried out a small-scale screening campaign. We identified four AOA analogues acting as AGT inhibitors, even if only one was found to act as a PC. The possible relationship between the structure and the PC activity of these compounds is discussed. Altogether, these results provide the proof-of-principle for the feasibility of a therapy with PCs for PH1-causing variants bearing folding defects and provide the scaffold for the identification of more specific ligands.



Primary Hyperoxaluria Type I (PH1, OMIM 259900) is a rare metabolic recessive disorder whose principal hallmark is the formation of calcium oxalate stones at first in the kidneys and then in the whole body.¹ Although renal dysfunctions are the first clinical manifestations of the disease, the cause is the functional deficit of liver peroxisomal alanine:glyoxylate aminotransferase (AGT).² AGT is a pyridoxal 5'-phosphate (PLP)-dependent enzyme, which catalyzes the conversion of L-alanine and glyoxylate into pyruvate and glycine. In the absence of functional AGT, glyoxylate accumulates and is oxidized to oxalate, an end product of metabolism that undergoes renal excretion, leading to the formation and deposition of calcium oxalate crystals (CaOx).³

AGT is homodimeric and belongs to the aspartate aminotransferase family of PLP-dependent enzymes.⁴ The protein is highly specific for the glyoxylate-to-glycine conversion, in line with its physiological role in glyoxylate detoxification.⁵ Like in all PLP enzymes, the coenzyme is bound through a Schiff base linkage with a lysine residue that in AGT is Lys209. This complex, called internal aldimine, gives rise to two absorbance

bands at 423 and 330 nm, attributed to the ketoenamine and enolimine tautomer of the internal aldimine, respectively.⁵

The *AGXT* gene encoding AGT is present in humans as two polymorphic forms named "major allele," coding for AGT-Ma, and "minor allele," coding for AGT-Mi. The minor allele has a frequency of 20% in European and North American populations and differs from the major allele by a 74 bp-duplication in intron 1 and by two point mutations leading to the P11L and I340M amino acid substitutions.⁶ Biochemical and cell biology studies performed in the past few years have highlighted that many mutations associated with PH1 (among the 150 identified so far) cause folding defects in AGT that result in (i) an increased aggregation propensity, either in the cell cytosol or in the peroxisomes; (ii) a reduced stability of the dimeric structure of the protein, usually in the apo-form; (iii) an increased susceptibility to proteolytic degradation; and/or

Received: February 26, 2015

Accepted: July 10, 2015

Published: July 10, 2015

(iv) a mislocalization of the protein to mitochondria.⁷ Thus, PH1 can be also referred to as a misfolding disease.

Only two curative treatments are currently available for PH1: the administration of pyridoxine, a precursor of the PLP coenzyme effective only in a minority (25–35%) of the patients,⁸ and liver transplantation, a very invasive procedure often carried out in combination with kidney transplantation.⁹ Thus, the development of new specific and noninvasive treatments would be highly desirable. Among the strategies under investigation to treat misfolding diseases there is the use of pharmacological chaperones (PCs), small molecules that bind a target protein and enable its proper folding and trafficking.¹⁰ In the case of diseases due to enzymatic deficits, molecules acting as PCs are usually competitive inhibitors of the enzyme involved.¹⁰ On these bases, it can be hypothesized that molecules acting as competitive inhibitors of AGT could represent useful PCs for pathogenic variants bearing folding defects. Aminooxyacetic acid (AOA) is a well-known inhibitor that binds the AGT active site by mimicking the position of the substrate *L*-alanine and is supposed to form an oxime with the carbonyl group of PLP, similarly to what happens in other PLP-dependent enzymes.^{11–13} It has been reported that AOA increases the thermal stability of both AGT-Ma and AGT-Mi¹⁴ and decreases the sensitivity to trypsin digestion of some AGT variants.¹⁵ However, neither the interaction of AOA with AGT nor its possible effect as a PC for PH1-causing variants has been extensively investigated.

In this study, we analyzed the interaction of AOA with AGT-Ma, AGT-Mi, and three pathogenic variants known to be affected by folding defects: G41R-Ma, characterized by a less stable dimeric structure in the apo-form and by an increased susceptibility to aggregation and proteolytic degradation; G170R-Mi, which shows an aberrant targeting to mitochondria;¹⁶ and I244T-Mi, which is prone to aggregation and proteolytic degradation and is partly mistargeted to mitochondria.^{16–18} We found that AOA (i) acts as a slow, tight-binding competitive inhibitor of the examined species in the purified recombinant form and (ii) behaves as a PC by reducing the aggregation propensity of G41R-Ma and promoting the correct localization of G170R-Mi and I244T-Mi. Moreover, to look for novel AGT ligands, we carried out a small-scale screening campaign of AOA analogues that were tested both for their ability to inhibit recombinant purified AGT and for their activity as a PC. The possible implications of the results for the pharmacological treatment of PH1 are discussed.

RESULTS AND DISCUSSION

AOA Forms an Oxime at the Active Site of AGT-Ma, AGT-Mi, and Pathogenic Variants. The binding of AOA to recombinant purified AGT-Ma and AGT-Mi was monitored by absorbance and CD spectroscopy. The absorbance spectrum of AGT-Ma and AGT-Mi presents a visible band at 423 nm associated with a positive CD band at 429 nm and a minor shoulder at 330 nm associated with a negative dichroic band at 340 nm. These bands have been already attributed to the ketoenamine and the enolimine tautomer of the internal aldimine, respectively.⁵ The addition of 20 μ M AOA caused the immediate disappearance of the absorbance and dichroic bands at 423 and 330 nm and the concomitant appearance of an absorbance band at 350 nm associated with a positive dichroic signal (Figure 1 and inset). Moreover, AOA binding caused a remarkable change in the near-UV region consisting in an increase of the magnitude of the dichroic bands at 280 and 260

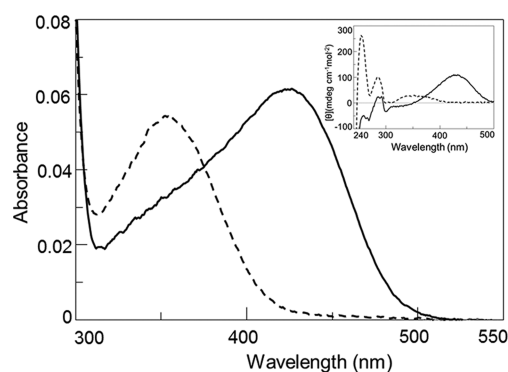


Figure 1. Absorbance and dichroic spectra of AGT-Ma in complex with AOA. Absorbance and CD (inset) spectra of 6 μ M AGT-Ma in the absence (solid line) and in the presence (dotted line) of 20 μ M AOA. Spectra were recorded in 100 mM KP, pH 7.4, at 25 °C. The absorbance and CD spectral properties of AGT-Mi under the same experimental conditions are identical to those of AGT-Ma.

nm (inset of Figure 1). Upon excitation at 350 nm, the AGT-Ma–AOA and the AGT-Mi–AOA complexes showed a fluorescence emission spectrum with a maximum at 450 nm, typical of the oxime PLP–AOA.^{11,12} The spectral features of G170R-Mi, I244T-Mi, and G41R-Ma in complex with AOA appeared to be similar to those of the AGT-Ma–AOA and AGT-Mi–AOA complexes (data not shown). These data indicate that the interaction of AOA with the enzymatic species under study involves the formation of an oxime with PLP at the active site, consistently with what was already observed for other PLP enzymes.¹³ Moreover, CD spectral changes in the near-UV suggest that oxime formation is accompanied by a conformational change of aromatic amino acid residues, possibly located at or near the active site. However, it cannot be excluded that the optically active band at 260 nm is a signal due to the PLP–AOA complex itself. Notably, the crystal structure of the AGT–AOA complex does not reveal the presence of a Schiff base linkage between the inhibitor and PLP. In fact, although the carboxyl moiety of AOA is hydrogen-bonded to Arg360, thus mimicking the position of the amino donor *L*-alanine, the PLP cofactor appears to be in the internal aldimine form.⁴ It can be speculated that the rigid conformation of the protein in the crystalline state does not allow the displacement of Lys209 by the amino group of AOA.

AOA Is a Slow, Tight-Binding Inhibitor of AGT-Ma, AGT-Mi, and Pathogenic Variants. The preincubation of 5 μ M AGT-Ma or AGT-Mi with 10 μ M AOA for 30' at 25 °C caused a complete loss of enzymatic activity, in line with what was previously found by Horvath et al., who reported that AOA at 50 μ M concentration is able to completely inhibit AGT-Ma activity in liver homogenates.¹⁹ The recovery of the transaminase activity was not observed even after extensive dialysis of the mixture against 100 mM potassium phosphate (KP) buffer at pH 7.4. However, when the AGT-Ma–AOA or the AGT-Mi–AOA complex was incubated at 25 °C in the presence of 500 mM *L*-alanine, a slow recovery of up to 75% of the enzymatic activity was observed in 24 h. These data strongly suggest that AOA acts as a slow, tight-binding inhibitor. A similar behavior has been also reported for aspartate aminotransferase from pig heart, whose reaction with AOA can only be reversed in the presence of the substrate analogue cysteine sulphinic acid.¹³

Further evidence for slow, tight-binding inhibition was obtained by measuring pyruvate production at different times after the addition of AGT-Ma or AGT-Mi in the presence of saturating PLP to assay mixtures containing L-alanine (250 mM), glyoxylate (10 mM), and AOA at concentrations ranging from 100 to 700 nM. The resulting progression curves (Figure 2A and B) revealed that the initial velocities (v_0) were

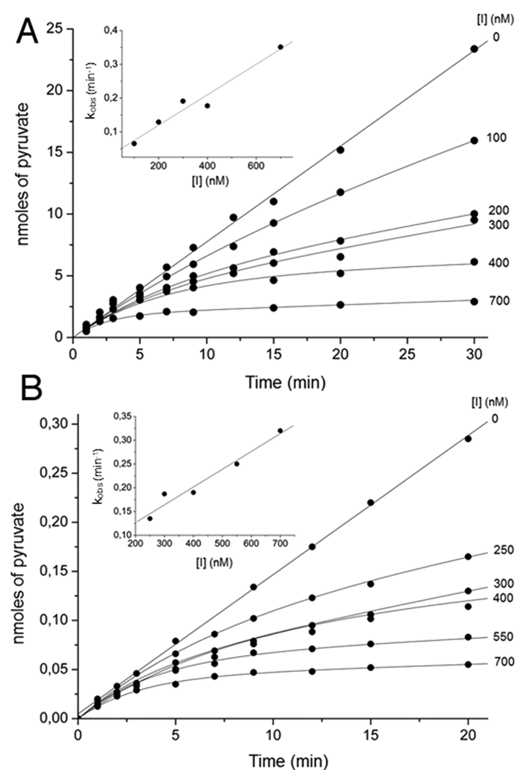


Figure 2. Kinetic analysis of the slow, tight-binding inhibition of AGT-Ma and AGT-Mi by AOA. Progression curves of pyruvate production during the reaction of 50 nM AGT-Ma (A) or AGT-Mi (B) in the presence of 10 mM glyoxylate, 250 mM L-alanine, and AOA at the indicated concentrations. The reactions were performed in 100 mM KP, pH 7.4, at 25 °C. Kinetic data were fitted to eq 1. Insets show the linear fits of the obtained k_{obs} values as a function of the inhibitor concentration.

independent of inhibitor concentration, and that the reaction rate gradually decreased with time reaching a steady-state value (v_s). Similar progression curves were obtained for G41R-Ma, G170R-Mi, and I244T-Mi. Data for AGT-Ma, AGT-Mi, and the pathogenic variants were fitted to eq 1, using the estimated v_0 and v_s values to determine the k_{obs} for each AOA concentration. The k_{obs} were then plotted against AOA concentration, and a linear relationship was observed (inset of Figure 2). Both features indicate that AOA is a slow, tight-

binding inhibitor for all the examined enzymatic species according to a mechanism reflecting the direct formation of a slowly dissociating E-AOA complex without the initial formation of a rapidly reversible E-AOA complex. The data were fitted to eqs 2 and 3, and k_{-1} , k_1 , and K_I were determined. As reported in Table 1, the K_I value for AOA of G41R-Ma is ~ 17 fold higher than that of AGT-Ma, while the K_I values of G170R-Mi and I244T-Mi are ~ 2 - and ~ 5 -fold higher, respectively, than that of AGT-Mi. These increases are due to approximately equal magnitude changes in k_1 and k_{-1} . The decrease in the AOA binding affinity of the pathogenic variants could be a consequence of the subtle active site alterations induced by each mutation, as revealed by the slight differences observed in the spectral and kinetic properties of the variants with respect to AGT-Ma and AGT-Mi^{20–22} (Supporting Information Figure 1 and Supporting Information Table 1).

AOA Increases the Thermal Stability of AGT-Ma, AGT-Mi, and Pathogenic Variants. It is well-known that the binding of low-molecular weight ligands can increase the thermal stability of proteins, an effect that has many important implications for the evaluation of the inhibitor potency and efficacy in a cellular environment.²³ Thus, we investigated if AOA binding could affect the thermal stability of AGT-Ma, AGT-Mi, G41R-Ma, G170R-Mi, and I244T-Mi by determining the melting curve in the absence and in the presence of the inhibitor at a saturating concentration (Table 1). As previously shown by both circular dichroism and calorimetry studies,^{22,24} all the species display a two-state unfolding pathway. AGT-Mi has a lower thermal stability with respect to AGT-Ma. In agreement with previous data,^{20,22} the G170R and I244T mutations do not significantly affect the T_m of AGT-Mi in the holo-form, while the G41R mutation significantly reduces the thermal stability of AGT-Ma.²¹ The binding of AOA has a global stabilizing effect, as indicated by the shift of 5–10 °C of the melting temperature. The lowest effect observed for G41R-Ma and I244T-Mi could be understood considering the reduced affinity of these variants for AOA and the correlation existing between the thermal stabilization exerted by a ligand on a protein and its binding affinity.²⁵ Since the ability of a ligand to prevent the heat-induced unfolding of an enzyme could indicate a possible stabilizing effect of the ligand,²⁶ these data suggest that AOA could behave as a PC for AGT.

AOA Variably Affects the Specific Activity and the Expression Level of AGT-Ma, AGT-Mi, and Pathogenic Variants. We wonder if AOA could be able to partly counteract three pathogenic mutations that do not significantly affect the AGT catalytic activity but cause a folding defect, by forcing the variants to assume the proper conformation. To this aim, we studied the interaction between AOA and AGT in a well-known cellular model of PH1 made of Chinese Hamster Ovary (CHO) cells stably expressing glycolate oxidase (GO).²⁷ In particular, we used the previously characterized clones of

Table 1. AOA: Kinetic Constants of Inhibition and Effect on Thermal Stability

Enzymatic species	k_1 ($\text{nM}^{-1} \text{min}^{-1}$)	k_{-1} (min^{-1})	K_I (k_{-1}/k_1) (nM)	$T_{\text{m-holo}}$ (°C)	$T_{\text{m-holo+AOA}}$ (°C)
AGT-Ma	$44 \cdot 10^{-4} \pm 2 \cdot 10^{-4}$	0.038 ± 0.012	9 ± 3	81.91 ± 0.04	>90 °C
AGT-Mi	$36 \cdot 10^{-4} \pm 3 \cdot 10^{-4}$	0.056 ± 0.015	15.5 ± 4.4	73.73 ± 0.06	83.91 ± 0.03
G41R-Ma	$8.3 \cdot 10^{-4} \pm 1.7 \cdot 10^{-4}$	0.125 ± 0.009	149.7 ± 29.9	60.03 ± 0.02	65.09 ± 0.03
G170R-Mi	$25 \cdot 10^{-4} \pm 3 \cdot 10^{-4}$	0.093 ± 0.008	37.2 ± 5.6	73.83 ± 0.09	84.40 ± 0.04
I244T-Mi	$32 \cdot 10^{-4} \pm 7 \cdot 10^{-4}$	0.269 ± 0.041	83.5 ± 19	73.42 ± 0.02	80.80 ± 0.03

CHO-GO cells stably expressing AGT-Ma (CHO-GO-AGT-Ma), AGT-Mi (CHO-GO-AGT-Mi), G170R-Mi (CHO-GO-G170R-Mi), and I244T-Mi (CHO-GO-I244T-Mi),¹⁶ and we selected a clone of CHO-GO cells expressing the G41R-Ma variant (CHO-GO-G41R-Ma). We first measured the AGT specific activity (Figure 3) and the expression level (Figure 4A

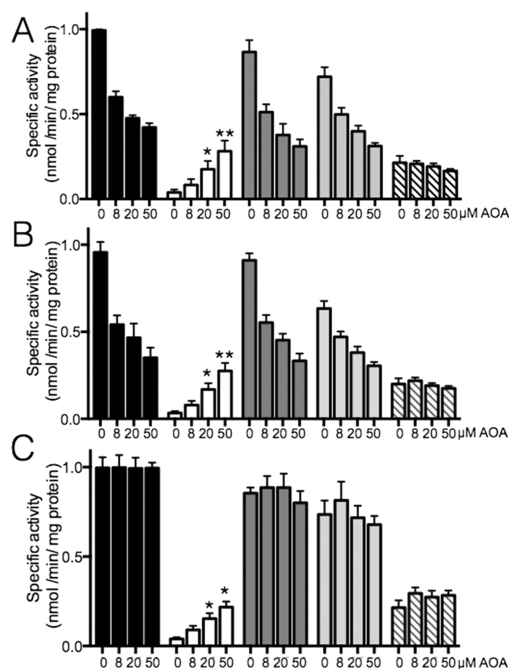


Figure 3. Effect of AOA treatment on AGT specific activity. The AGT specific activity in the cellular lysate was determined under three different conditions: (A) immediately after lysis, (B) after 24 h incubation at 4 °C and (C) after 24 h incubation at 4 °C with 0.5 M L-alanine. In all cases 100 μ g of lysate were incubated with 0.5 M L-alanine, 10 mM glyoxylate and 200 μ M PLP at 25 °C in 100 mM KP, pH 7.4. Bars are colored as follow: CHO-GO-AGT-Ma (black), CHO-GO-G41R-Ma (white), CHO-GO-AGT-Mi (dark gray), CHO-GO-G170R-Mi (light gray) and CHO-GO-I244T-Mi (stripe). Data are representative of three independent experiments. Bar graphs represent the mean \pm SEM. The statistical significance of the increment in specific activity in the presence of different AOA concentrations with respect to the value in absence of AOA is shown: * $P < 0.05$, ** $P < 0.005$.

and B) in the soluble fraction of the lysates of each clone. In line with previous data,¹⁶ the specific activity of G170R-Mi and I244T-Mi in CHO-GO cells was about 80% and 25%, respectively, and their expression level was about 83% and 70%, respectively, as compared with the corresponding values of AGT-Mi. Moreover, here we found that the specific activity and expression level of CHO-GO-G41R-Ma cells were 4% and 18%, respectively, as compared with those of CHO-GO-AGT-Ma. Since, under our experimental conditions, both I244T and G41R mutations slightly reduce the enzymatic activity of AGT-Mi and AGT-Ma, respectively (Supporting Information Table 1), the decreased specific activity of the I244T-Mi and G41R-Ma variants in CHO-GO cells can be ascribed partly to the reduced activity and partly to the reduced expression level.

To investigate whether AOA could act as a PC, CHO-GO-AGT-Ma, CHO-GO-AGT-Mi, CHO-GO-G41R-Ma, CHO-GO-G170R-Mi, and CHO-GO-I244T-Mi cells were grown in the presence of AOA in the culture medium. AGT-Ma and

AGT-Mi have a half-life of 29 and 27 h, respectively;²⁸ thus we chose an incubation time of 7 days to allow the majority of AGT to be synthesized in the presence of AOA. Moreover, considering that the predicted partition coefficient of AOA (LogP) is equal to -0.978 ,²⁹ which indicates a very low membrane passive permeability, we treated the cells with ligand concentrations (8 μ M, 20 μ M, and 50 μ M) much higher than the K_i of the analyzed species (Table 1). We checked that, under our experimental conditions, the presence of AOA in the culture medium up to 50 μ M does not interfere with cell growth and does not adversely affect the cellular fine structure (data not shown). Upon incubation, we determined the AGT specific activity (Figure 3) and expression level (Figure 4) in the soluble fraction of the cellular lysates. Since AOA is a slow, tight-binding inhibitor of each species in the recombinant purified form, thus implying that the dissociation from the enzyme occurs only in the presence of the substrate, we measured the specific activity under three different conditions: (i) immediately after cell lysis (Figure 3A), (ii) after incubation of the lysate for 24 h at 4 °C (Figure 3B), and (iii) after incubation of the lysate for 24 h at 4 °C in the presence of excess substrate (0.5 M L-alanine; Figure 3C). From the data obtained at increasing AOA concentrations, we could make the following observations. First, the expression level of cells expressing AGT-Ma, AGT-Mi, and G170R-Mi did not change, but their specific activity decreased, reaching a value equal to 42%, 36%, and 43%, respectively, of untreated cells. Similar results were observed upon incubation at 4 °C in the absence of the substrate, while the specific activity was completely restored after prolonged incubation of the lysate with saturating amounts of substrate. These data indicate that, in the stable clones of CHO-GO cells, AOA behaves as a tight-binding inhibitor of AGT-Ma, AGT-Mi, and G170R-Mi. It should be noted that although we treated cells with AOA concentrations much higher than the K_i of the analyzed species, we did not observe a 100% inhibition of the enzymatic activity, as expected if AOA was totally internalized. We speculate that this could be due to (i) the low permeability of AOA, leading to an intracellular concentration of the inhibitor much lower than the extracellular one, and (ii) the highly reactive aminic group of AOA, able to interact with many molecules endowed with reactive carbonyl groups, thus lowering the effective amount of inhibitor available for AGT. Second, the specific activity of CHO-GO-I244T-Mi cells does not change under the three different assay conditions (Figure 3), and the expression level remains unaltered (Figure 4A and B), in agreement with previous results.¹⁷ These data appear to indicate that AOA does not act as a tight-binding inhibitor of I244T-Mi. However, we cannot exclude that under our experimental conditions AOA could dissociate from I244T-Mi considering that this variant has values of K_i and k_{-1} higher than those of AGT-Ma, AGT-Mi, and G170R-Mi. Third, the specific activity of CHO-GO-G41R-Ma cells increased, reaching a value \sim 7-fold higher than that of untreated cells under the three assay conditions, and their expression level increased by 1.7 fold, reaching a value of 33% as compared to CHO-GO-AGT-Ma cells. These data suggest that at the actual intracellular concentration AOA does not exert a detectable inhibitory effect on G41R-Ma for reasons similar to what was already proposed for I244T-Mi (see above). Notably, AOA is able to partly rescue for the effect of the G41R mutation by possibly acting as a PC. Since the purified G41R-Ma variant has a strong propensity to aggregate under physiological conditions,²¹ we determined the amount of

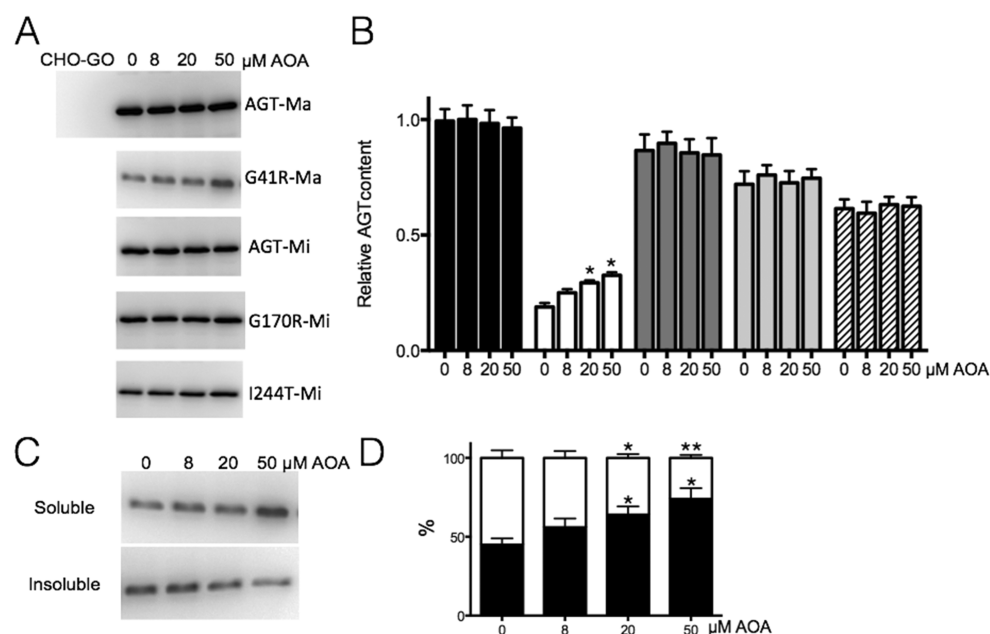


Figure 4. Effect of AOA treatment on AGT expression. (A) 2 μ g of lysate of CHO-GO cells expressing the analyzed species grown in the absence or in the presence of AOA at different concentrations were subjected to SDS/PAGE, immunoblotted with anti-AGT from rabbit (1:6000), and then detected by chemiluminescence. (B) Histogram showing the band volume of the immunoblot in A. Bars are colored as follows: CHO-GO-AGT-Ma (black), CHO-GO-G41R-Ma (white), CHO-GO-AGT-Mi (dark gray), CHO-GO-G170R-Mi (light gray), and CHO-GO-I244T-Mi (stripe). (C) 2 μ g of the soluble and insoluble fractions of lysate of CHO-GO-G41R-Ma cells grown in the absence or in the presence of AOA at different concentrations were subjected to SDS/PAGE, immunoblotted with anti-AGT from rabbit (1:6000), and then detected by a chemiluminescent substrate. (D) Histograms representative of the percentage of protein in the soluble (black) and insoluble (white) fractions of the lysate. Data are representative of three independent experiments. Bar graphs represent the mean + SEM. The statistical significance of the increment in protein expression level in the presence of different AOA concentrations with respect to the value in the absence of AOA is shown: * $P < 0.05$.

protein present in the soluble and insoluble fraction of the lysate of CHO-GO-G41R-Ma cells grown for 7 days in the absence and in the presence of AOA at 8 μ M, 20 μ M, and 50 μ M concentrations. We did not see any change of the total expression level of the variant, but we noticed a progressive decrease of the protein present in the insoluble fraction and a concomitant increase of the protein present in the soluble fraction of the lysate. These data reinforce the view that G41R-Ma has a significant aggregation propensity inside the cell and led us to conclude that the treatment with AOA could partially counteract this effect. It has been demonstrated that the aggregation of G41R-Ma is a consequence of the increased flexibility of the N-terminal arms of the variant in the dimeric form leading to the exposure of negatively charged residues, which interact with the positively charged surface of neighboring protein dimers.²¹ It can be hypothesized that the formation of the oxime AOA-PLP could counteract the perturbation caused by Gly41 mutation by promoting the correct positioning of the loop 24–32. This in turn would decrease the flexibility of the N-terminal arm thus reducing the aggregation extent.

In order to have a solid confirmation of the PC role of AOA, we also investigated its effects on the specific activity and the expression level of each species transiently expressed in CHO-GO or COS7 cells in the absence or in the presence of 50 μ M AOA (Supporting Information Figure 2). The results are consistent with those obtained in stable clones of CHO-GO cells. However, in transient transfection experiments, AOA was found to behave as a tight-binding inhibitor for both G41R-Ma and I244T-Mi, as shown by the increase in the specific activity observed upon incubation with excess L-alanine. This could be due to the higher intracellular concentration of the variants in

transiently transfected cells as compared with stable clones, which would possibly favor the formation of the enzyme–AOA complexes.

AOA Promotes the Peroxisomal Localization of G170R-Mi and I244T-Mi. Investigations performed in stably transformed CHO-GO cells have demonstrated that both G170R-Mi and I244T-Mi, the two most common variants associated with PH1 present in European patients, are mistargeted to mitochondria.^{16,30,31} Thus, we investigated if AOA could affect the subcellular localization of the variants by determining the AGT intracellular compartmentalization in CHO-GO-AGT-Mi, CHO-GO-G170R-Mi, and CHO-GO-I244T-Mi cells before and after a 7-day treatment with 50 μ M AOA. We performed both a qualitative inspection of the images and a quantitative analysis, by determining the Pearson's coefficient for the colocalization of the AGT/peroxisomes and the AGT/mitochondria signals. As expected, the distribution of AGT-Mi was entirely peroxisomal (Figure 5A), and no colocalization with the mitochondrial marker was detected (Supporting Information Figure 3A). In agreement with previous results,¹⁶ G170R-Mi was entirely mitochondrial while I244T-Mi was equally distributed between peroxisomes and mitochondria (Figure 5A and Supporting Information Figure 3A). No change of AGT-Mi localization was seen upon treatment with AOA, while an increased amount of peroxisomal AGT (and a decreased amount of mitochondrial AGT) was observed in cells expressing G170R-Mi and I244T-Mi (Figure 5B and Supporting Information Figure 3B). In fact, upon AOA treatment, the Pearson's coefficient for the colocalization AGT/peroxisomes increased from 0.15 to 0.51 and from 0.53 to 0.76, respectively, while the Pearson's coefficient for the colocalization AGT/mitochondria decreased from 0.81 to 0.68 and from

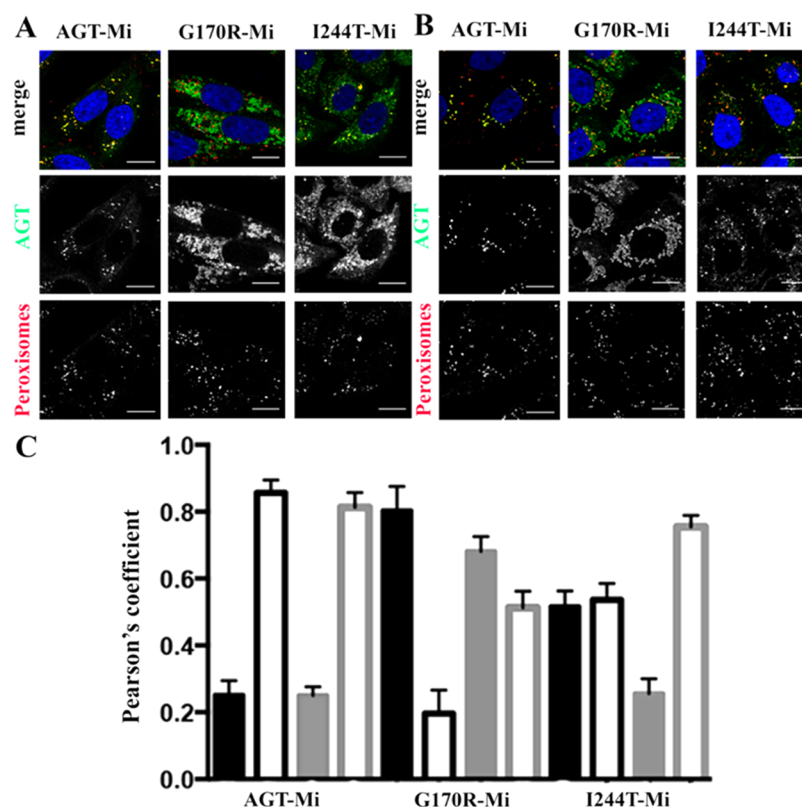


Figure 5. Effect of AOA treatment on the subcellular localization of AGT-Mi, G170R-Mi, and I244T-Mi. After 7 days of culture in the absence (A) or in the presence (B) of 50 μM AOA, cells were fixed and colored as follows: anti-AGT (green) and antiperoxisomal proteins (red). Nuclei were stained with Dapi (blue). Merge and single-channel images come from a single z-plane. Scale bar: 10 μm . (C) Pearson's coefficients for the subcellular distribution of the analyzed clones grown for 7 days in the absence (black) or in the presence (gray) of 50 μM AOA. Full and empty bars represent the Pearson's coefficient calculated for the colocalization of AGT and mitochondria or AGT and peroxisomes, respectively. The results are given as means (+SEM) of several images; at least 30 individual cells were analyzed for each sample.

0.51 to 0.26 for G170R-Mi and I244T-Mi, respectively. These data indicate that the treatment with AOA significantly favors the peroxisomal import of the two variants. In particular, for I244T-Mi, this effect is so strong that its colocalization with the mitochondrial marker becomes nonsignificant. An analogous trend can be also observed in CHO-GO or COS7 cells transiently expressing G170R-Mi or I244T-Mi. As shown in Supporting Information Figure 2C and F, upon treatment with 50 μM AOA, both variants display an increased peroxisomal localization. It should be noted that, as previously found,¹⁷ the I244T-Mi variant transiently expressed in COS7 cells does not show a mitochondrial localization, but it is almost equally distributed between peroxisomes and cytosol, probably as a consequence of the different expression of cellular components involved in protein folding and trafficking in the two cell types.

Both Gly170 and Ile244 are located at the AGT subunit interface.⁴ It has been widely claimed that the erroneous localization of G170R-Mi and I244T-Mi is due to the occurrence of two necessary conditions: (i) a putative mitochondrial targeting sequence (MTS) produced by the P11L polymorphic mutation^{16,32,33} and (ii) a folding defect caused by the pathogenic mutation, allowing the population of partly folded monomeric intermediates able to interact with the mitochondrial import machinery.^{16,20,34} On these bases, the most plausible explanation for the peroxisomal import induced by AOA is that its binding to the AGT active site could promote the attainment or the maintenance of the dimeric structure, thus preventing the mitochondrial import and

allowing the interaction with the peroxisomal import machinery that acts on fully folded dimeric proteins.³⁵ Since residues of both subunits form the AGT active site, the presence of a ligand mimicking the substrate such as AOA is expected to force the positioning of the active site residues in the conformation typical of the native enzyme and shift the equilibrium toward a dimeric structure. A similar effect has been already documented for a monomeric variant of *T. denticola* cystalysin.³⁶

AOA Increases the Glyoxylate Detoxification Ability of G41R-Ma, G170R-Mi, and I244T-Mi. When CHO-GO cells are treated with glycolate, they produce glyoxylate inside peroxisomes through GO. Since glyoxylate induces cell death, the viability of the cells in the presence of glycolate represents a measure of the amount of functional AGT.²⁷ After 7 days of culture either in the presence or in the absence of 50 μM AOA, CHO-GO cells stably expressing all the analyzed species were treated with 1 mM glycolate for 24 h to allow the formation of peroxisomal glyoxylate. As shown in Figure 6, the viability of cells treated with glycolate with respect to untreated cells was around 13% for CHO-GO cells, while it increased up to 60–70% for cells expressing AGT-Ma and AGT-Mi and drastically dropped to 17%, 20%, and 21% for cells expressing G41R-Ma, G170R-Mi, and I244T-Mi, respectively. The growth in the presence of AOA did not affect the viability of cells expressing AGT-Ma and AGT-Mi, while it increased 1.6-, 1.5-, and 1.9-fold the viability of cells expressing G41R-Ma, G170R-Mi, and I244T-Mi, respectively. Thus, the treatment with AOA is able to significantly increase the amount of functional AGT in cells

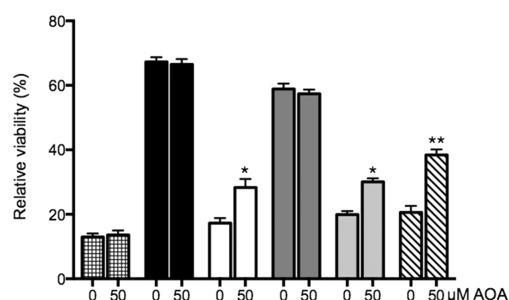


Figure 6. Effect of AOA treatment on AGT functionality. Glycolate-toxicity assay of CHO-GO cells expressing the analyzed AGT variants after growing in the absence or presence of 50 μM AOA. The histogram represents cell viability expressed as a percentage of the untreated control. Bars are colored as follows: CHO-GO (square), CHO-GO-AGT-Ma (black), CHO-GO-G41R-Ma (white), CHO-GO-AGT-Mi (dark gray), CHO-GO-G170R-Mi (light gray), and CHO-GO-I244T-Mi (stripe). Bar graphs represent the mean + SEM. The statistical significance of the increment in relative cellular viability in the presence of different AOA concentrations with respect to the value in the absence of AOA is shown: * $P < 0.05$, ** $P < 0.005$.

expressing the G41R-Ma, G170R-Mi, and I244T-Mi variants reaching values of about 50% with respect to those of AGT-Ma or AGT-Mi. The increased glyoxylate detoxification ability of cells treated with AOA probably derives from the increased amount of active soluble AGT, in the case of CHO-GO-G41R-Ma cells, and from the increased peroxisomal localization of AGT, in the case of CHO-GO-G170R-Mi and CHO-GO-I244T-Mi cells.

Small-Size Screening Campaign. To select AOA analogues, a substructure search was carried out along with a virtual screening of the available “drug-like” chemical space. We tested the 426 compounds retrieved for their ability to inhibit AGT-Ma by automated enzymatic assays, and we identified eight primary hits. We then performed hit confirmation by concentration–response curves, to obtain a preliminary SAR. Under the experimental conditions used, an IC_{50} of 0.15 μM was found for AOA. This value agrees well with that predicted from the K_i value of the inhibitor that is equal to 0.118 μM .³⁷ We identified four inhibitors with IC_{50} ranging from 0.3 to 16.7 μM (Table 2). Interestingly, replacement of the carboxylic moiety by an aromatic moiety such as a phenyl ring is tolerated, as demonstrated by compound 3. On the contrary, replacement by a hydroxyl group (compound 2) exerts a detrimental effect on the inhibitory activity. The elongation of the carbon chain length by two and three methylene units allows maintaining activity (compounds 4 and 5), while a complete loss of activity is recorded in the absence of the oxygen atom of the amino-oxy group (compounds 6, 7, and 8). The ramification of the carbon chain seems to be permitted, as shown by compound 9 where a benzyl substituent on the methylene unit of AOA still gives a moderate activity. All the identified molecules are able to bind the AGT active site, as indicated by the conversion of the 423 nm absorbance band into a band at 365–375 nm (data not shown). This corroborates the hypothesis that their binding mode is similar to that of AOA.

We then performed preliminary experiments to investigate if the AOA analogues active as AGT inhibitors could also play a PC role. We grew CHO-GO-AGT-Ma, CHO-GO-AGT-Mi, CHO-GO-G41R-Ma, CHO-GO-G170R-Mi, and CHO-GO-I244T-Mi cells for 7 days in the absence or in the presence of compound 3, 4, 5, or 9 at 50 μM concentration. None of the

Table 2. *In Vitro* Activity Data of AOA Analogues

Compound Name	Structure	IC_{50} (μM)
1, AOA		0.15
2		inactive
3		3
4		0.3
5		1.4
6		inactive
7		inactive
8		inactive
9		16.7

compounds was found to affect cell viability or morphology. Compounds 3, 4, and 5 do not significantly affect the specific activity, the expression level, and the subcellular localization of all the analyzed enzymatic species (data not shown). On the other hand, compound 9 (i) does not change the expression level of AGT-Ma but causes a $\sim 30\%$ reduction of its specific activity (Supporting Information Figure 4A–C), which is recovered upon incubation of the lysate with excess L-alanine (Supporting Information Figure 4D), thus suggesting a tight-binding behavior; (ii) causes a ~ 2 -fold increase of the G41R-Ma expression level and a similar increase in specific activity only evident upon incubation of the lysate with excess L-alanine (Supporting Information Figure 4A–D), thus suggesting a partial inhibition; (iii) does not affect the specific activity and the expression level of G170R-Mi and I244T-Mi but promotes their peroxisomal import (Supporting Information Figure 4E). Overall, these data indicate that only compound 9 appears to behave as a PC for the three folding-defective AGT variants stably expressed in CHO-GO cells. The different behavior of the tested compounds can be interpreted considering that, while compounds 4 and 5 have a negative $\log P$ (-0.89 and -0.44 , respectively), compound 9 has a positive $\log P$ value (0.50) that suggests a higher membrane permeability with respect to AOA and thus an increased intracellular concentration. More difficult is to understand the behavior of compound 3, which has a positive $\log P$ value (1.13) and a lower IC_{50} with respect to compound 9, but does not appear to play any PC role. It can only be speculated that the presence of

the carboxyl moiety could be important for the chaperone activity. However, no solid conclusions can be drawn about the relationship between the structure and the PC activity in the absence of detailed analyses of the actual membrane permeability of each compound and of the kinetic parameters of their interaction with all enzymatic species. Studies to this aim are in progress.

Conclusions. In PH1, the majority of disease-causing missense mutations result in the biosynthesis of AGT variants that are catalytically competent but display folding defects making them more susceptible to aggregation, intracellular degradation, or mistargeting.⁷ Each of these effects reduces the amount of functional AGT present inside peroxisomes and, therefore, generates the enzymatic deficit found in PH1 patients. Small molecules acting as PCs on misfolded but catalytically active variants offer a convenient and cost-effective therapeutic strategy for loss-of-function diseases. They have been developed for a number of rare diseases, and some are already in the market.³⁸

Although the possibility of a new therapy for PH1 addressing the homeostasis defects of AGT has been widely claimed, no investigations on molecules acting as PCs have been reported until now. In PH1, it has been already documented that the coenzyme PLP enhances the thermodynamic and kinetic stability of pathogenic variants of AGT and, in some cases, improves their folding efficiency in the cytosolic milieu.^{7,39,40} These results prompted the designation of PLP as a natural PC in PH1 and explained the responsiveness of some patients bearing folding mutations to pyridoxine, a PLP precursor.⁴¹ However, only about 30% of PH1 patients are pyridoxine-responsive, even if they do not show complete remission of the disease symptoms.⁴¹ Here, we provide the first evidence that AOA (i) is a slow, tight-binding competitive inhibitor of the analyzed species in the purified form and (ii) is able to act as a PC for three pathogenic variants showing folding defects, including the two most common. Thus, we provided the proof-of-principle that a therapy with PCs is feasible for conformationally defective pathogenic variants associated with PH1. In this regard, a weak effect of AOA has been also documented for pathogenic forms of human cystathionine- β -synthase.⁴² Notably, some missense mutations associated with PH1 affect the stability and/or the folding of AGT in the apo-form. We can speculate that in the latter cases a useful therapeutic strategy could be a combination of pyridoxine and AOA, which could act as PCs for the apoenzymatic and the holoenzymatic form of each variant, respectively, thus possibly producing a synergic effect.

We are aware that although AOA is effective as a PC, it lacks of specificity because it interacts with many PLP enzymes and free PLP, thanks to the highly reactive aminic group.¹³ Therefore, alongside the characterization of AOA activity as AGT inhibitor and PC, we carried out a small screening campaign. We identified four compounds structurally related to AOA endowed with inhibitory activity against AGT-Ma in the micromolar range. Moreover, we found that one of these compounds is effective as a PC. These data allowed (i) the identification of the molecular structural moieties that are thought to contribute to AOA activity and (ii) the establishment of a framework that, by increasing the number of compounds screened, should lead to the identification of more specific AGT ligands possibly lacking the tight-binding behavior and endowed with an increased PC activity, thus representing a valuable starting point for drug discovery.

MATERIALS AND METHODS

Materials. PLP, L-alanine, sodium glyoxylate, rabbit muscle L-lactic dehydrogenase, isopropyl- β -D-thiogalactoside, EDTA, AOA, glycolate, and imidazole were purchased from Sigma. Ham's F12 Glutamax medium was purchased from Invitrogen. CHO-GO, CHO-GO-AGT-Ma, CHO-GO-AGT-Mi, CHO-GO-G170R-Mi, CHO-GO-I244T-Mi, the rabbit polyclonal anti-AGT human, and the guinea-pig antiperoxisomal protein antibodies were kindly provided by Prof. C.J. Danpure (University College London). The antirabbit HRP antibody was purchased from GE Healthcare. Oligonucleotides for site directed mutagenesis were purchased from MWG Biotech AG (Anzinger, Germany). All other chemicals were of the highest purity available.

Site-directed Mutagenesis. The G41R mutation on the cDNA of AGT cloned into a pcDNA3.1/V5-His-TOPO vector and the I244T mutation on the pAGThis-Mi vector were introduced using the QuikChange II kit (Agilent Technologies). We used the oligonucleotides GCAGCCCGCGGGCTGCAGATGATCGG and its complement and the oligonucleotide CCTTCTACCTGGACACCA-AGTGGCTGGCC and its complement for the G41R and the I244T mutation, respectively. The mutations were confirmed by sequencing.

Protein Expression and Purification. Wild type and mutant enzymes in their histidine-tagged form were expressed in *E. coli* and purified by the procedure already described.⁵ The apoform of the I244T-Mi variant was prepared as previously described.⁵ The protein concentration of AGT-Ma, AGT-Mi, and the variants was determined by absorbance spectroscopy using an extinction coefficient of $9.54 \times 10^4 \text{ M}^{-1} \text{ cm}^{-1}$ at 280 nm.⁵

Cell Culture and Lysis. CHO-GO cells and COS7 cells were cultured as described in the SI. To study the effect of AOA on protein expression and activity, stable clones of CHO-GO cells were seeded at a density of 7.2×10^5 cell/10 cm dish and grown for 7 days in the absence or in the presence of different AOA concentrations (8 μM , 20 μM , and 50 μM) in the culture medium. Transient transfection experiments were performed as described in the SI. Cells were harvested and lysed in PBS, pH 7.2, plus protease inhibitor cocktail (Complete Mini, Roche), by five freeze/thaw cycles followed by treatment with DNase (10 units) at RT for 45 min. The whole cell extract was separated by centrifugation (29 200g, 10 min, 4 °C) to obtain the soluble fraction. The pellets were then resuspended in an equal volume of denaturing gel loading buffer to obtain the insoluble fraction. The protein concentration in the soluble fraction was measured using the Bradford protein assay.

Enzymatic Activity Assays. The transaminase activity of the purified enzymes and of the cellular lysates was assayed as previously described.⁵

Slow, Tight-binding Kinetic Determination. Slow, tight binding kinetics of AOA with AGT-Ma, AGT-Mi, and pathogenic variants were evaluated by the progression curve approach described by Chou *et al.*⁴³ A series of inhibition progression curves for each enzymatic species at different concentrations of AOA were generated. A total of 0.05 μM of each enzyme in the presence of saturating PLP was added to separate reaction mixtures containing AOA (up to 700–900 nM), L-alanine (250 mM), and glyoxylate (10 mM). Data for each progression curve were fitted to the integrated rate equation for slow-binding inhibitors:

$$[P] = v_s t + (v_0 + v_s)(1 - \exp(-k_{\text{obs}})/k_{\text{obs}}) \quad (1)$$

where $[P]$ is the concentration of pyruvate produced at the time t , v_0 and v_s are the initial and steady state rates of transamination, respectively, and k_{obs} is the apparent first order kinetic constant obtained by the best fit to the data. The individual rate (k_{-1} and k_1) and inhibition constants (K_1) were determined from plots of k_{obs} against the inhibitors' concentration by fitting the data to the following equations:

$$k_{\text{obs}} = k_{-1} + k_1[I]/(1 + [S]/K_m) \quad (2)$$

$$K_1 = k_{-1}/k_1 \quad (3)$$

Spectrophotometric Measurements. Spectroscopic measurements and thermal stability studies were performed as described in the SI.

Western-blot Analysis. A total of 2 μg of cell lysate was loaded per lane on a Mini Protean TGX precast gel (Biorad) along with the Precision plus protein Kaleidoscope (Bio-Rad) molecular mass markers. Following transfer on a nitrocellulose membrane by the iBlot device (Invitrogen), the membrane was blocked in 5% milk solution in TBST (50 mM Tris-HCl pH 7.5, 150 mM NaCl, 0.1% Tween 20) for 1 h at 37 °C. For AGT detection, the membrane was incubated with polyclonal rabbit anti-AGT serum (dilution 1:6000), washed three times in TBST and then incubated with peroxidase-conjugated anti-rabbit IgG (dilution 1:10 000). Blotted proteins were detected and quantified with ECL (Millipore), using the ChemiDoc XRS Imaging System (Bio-Rad, Hercules, CA).

Immunofluorescence Microscopy (IFM). Cell fixation and staining were performed as described in ref 44. Details are given in the SI.

Glycolate Toxicity Assay. Cells cultured 7 days in the absence or in the presence of 50 μM AOA were harvested and plated at a density of 8000 cells/well in a 96-well plate. After 24 h, glyoxylate production was induced by the addition of Hepes buffered glycolate at pH 7.0 at a final concentration of 1 mM. Cell viability was evaluated after 24 h of incubation by crystal violet staining as previously reported.⁴⁵

Virtual Screening. A virtual screening approach was applied aimed at selecting a library of molecules to be tested as potential AGT inhibitors. Details are given in the SI.

Screening of AGT Ligands. The AGT transaminase activity assay was initially adapted for a screening at higher throughput and used to analyze the inhibitory activity of the compounds selected by virtual screening. Compounds active as AGT inhibitors were then tested in stable clones of CHO-GO cells. Details are given in the SI.

Statistical Analysis. Experiments were performed at least in triplicate. Statistic analysis was performed with Origin 7.03 (Origin Lab) or GraphPad Prism version 5.0 (GraphPad software, San Diego, CA, USA).

■ ASSOCIATED CONTENT

■ Supporting Information

We provided as Supporting Information: (i) a detailed description of the methods, (ii) the steady-state kinetic parameters and the spectroscopic properties of all the analyzed species, (iii) the results of transient transfection experiments, (iv) the IFM experiments with mitochondrial staining, and (v) the results on the effects of compound 9 treatment on expression level, specific activity, and subcellular localization of all the analyzed species. The Supporting Information is available free of charge on the ACS Publications website at DOI: 10.1021/acscchembio.5b00480.

■ AUTHOR INFORMATION

■ Corresponding Author

*Tel.: +39 0458027293. Fax: +39 0458027170. E-mail: barbara.cellini@univr.it.

■ Notes

The authors declare no competing financial interest.

■ ACKNOWLEDGMENTS

This work was supported by funding from the University of Verona (Joint Projects 2010, to B.C.) and from the Telethon foundation (GGP10092, to C.B.V.). We thank S. Bianconi for her skilful technical assistance. We are grateful to G. Gaviraghi for his advice and his interest in our research.

■ ABBREVIATIONS

AGT, alanine:glyoxylate aminotransferase; PH1, Primary Hyperoxaluria Type I; PLP, pyridoxal 5'-phosphate; PBS, phosphate-buffered saline; KP, potassium phosphate buffer; IFM, immunofluorescence microscopy; PC, pharmacological chaperone; AOA, aminooxyacetic acid; BSA, bovine serum albumine; CHO, chinese hamster ovary; GO, glycolate oxidase; CD, circular dichroism; SAR, structure–activity relationship

■ REFERENCES

- (1) Danpure, C. J., and Rumsby, G. (2004) Molecular aetiology of primary hyperoxaluria and its implications for clinical management. *Expert Rev. Mol. Med.* 6, 1–16.
- (2) Danpure, C. J., and Jennings, P. R. (1986) Peroxisomal alanine:glyoxylate aminotransferase deficiency in primary hyperoxaluria type I. *FEBS Lett.* 201, 20–24.
- (3) Morgan, S. H., Purkiss, P., Watts, R. W., and Mansell, M. A. (1987) Oxalate dynamics in chronic renal failure. Comparison with normal subjects and patients with primary hyperoxaluria. *Nephron* 46, 253–257.
- (4) Zhang, X., Roe, S. M., Hou, Y., Bartlam, M., Rao, Z., Pearl, L. H., and Danpure, C. J. (2003) Crystal structure of alanine:glyoxylate aminotransferase and the relationship between genotype and enzymatic phenotype in primary hyperoxaluria type 1. *J. Mol. Biol.* 331, 643–652.
- (5) Cellini, B., Bertoldi, M., Montioli, R., Paiardini, A., and Borri Voltattorni, C. (2007) Human wild-type alanine:glyoxylate aminotransferase and its naturally occurring G82E variant: functional properties and physiological implications. *Biochem. J.* 408, 39–50.
- (6) Purdue, P. E., Lumb, M. J., Allsop, J., and Danpure, C. J. (1991) An intronic duplication in the alanine: glyoxylate aminotransferase gene facilitates identification of mutations in compound heterozygote patients with primary hyperoxaluria type 1. *Hum. Genet.* 87, 394–396.
- (7) Oppici, E., Montioli, R., and Cellini, B. (2015) Liver peroxisomal alanine:glyoxylate aminotransferase and the effects of mutations associated with Primary Hyperoxaluria Type I: An overview. *Biochim. Biophys. Acta, Proteins Proteomics*, DOI: 10.1016/j.bbapap.2014.12.029.
- (8) Monico, C. G., Olson, J. B., and Milliner, D. S. (2005) Implications of genotype and enzyme phenotype in pyridoxal response of patients with type I primary hyperoxaluria. *Am. J. Nephrol.* 25, 183–188.
- (9) Cochat, P., Hulton, S. A., Acquaviva, C., Danpure, C. J., Daudon, M., De Marchi, M., Fargue, S., Groothoff, J., Harambat, J., Hoppe, B., Jamieson, N. V., Kemper, M. J., Mandrile, G., Marangella, M., Picca, S., Rumsby, G., Salido, E., Straub, M., and van Woerden, C. S. (2012) Primary hyperoxaluria Type I: indications for screening and guidance for diagnosis and treatment. *Nephrol., Dial., Transplant.* 27, 1729–1736.
- (10) Ringe D, P. G. (2009) What are pharmacological chaperones and why are they interesting? *J. Biol.* 13, 1.
- (11) Beeler, T., and Churchich, J. E. (1976) Reactivity of the phosphopyridoxal groups of cystathionase. *J. Biol. Chem.* 251, 5267–5271.
- (12) Clausen, T., Huber, R., Messerschmidt, A., Pohlenz, H. D., and Laber, B. (1997) Slow-binding inhibition of Escherichia coli cystathionine beta-lyase by L-aminoethoxyvinylglycine: a kinetic and X-ray study. *Biochemistry* 36, 12633–12643.
- (13) John, R. A., and Charteris, A. (1978) The reaction of amino-oxyacetate with pyridoxal phosphate-dependent enzymes. *Biochem. J.* 171, 771–779.
- (14) Hopper, E. D., Pittman, A. M., Fitzgerald, M. C., and Tucker, C. L. (2008) In vivo and in vitro examination of stability of primary hyperoxaluria-associated human alanine:glyoxylate aminotransferase. *J. Biol. Chem.* 283, 30493–30502.
- (15) Coulter-Mackie, M. B., and Lian, Q. (2008) Partial trypsin digestion as an indicator of mis-folding of mutant alanine:glyoxylate aminotransferase and chaperone effects of specific ligands. Study of a spectrum of missense mutants. *Mol. Genet. Metab.* 94, 368–374.

- (16) Fargue, S., Lewin, J., Rumsby, G., and Danpure, C. J. (2013) Four of the most common mutations in primary hyperoxaluria type 1 unmask the cryptic mitochondrial targeting sequence of alanine:glyoxylate aminotransferase encoded by the polymorphic minor allele. *J. Biol. Chem.* 288, 2475–2484.
- (17) Santana, A., Salido, E., Torres, A., and Shapiro, L. J. (2003) Primary hyperoxaluria type 1 in the Canary Islands: a conformational disease due to I244T mutation in the P11L-containing alanine:glyoxylate aminotransferase. *Proc. Natl. Acad. Sci. U. S. A.* 100, 7277–7282.
- (18) Fargue, S., Rumsby, G., and Danpure, C. J. (2013) Multiple mechanisms of action of pyridoxine in primary hyperoxaluria type 1. *Biochim. Biophys. Acta, Mol. Basis Dis.* 1832, 1776–1783.
- (19) Horvath, V. A. P., and Wanders, R. J. A. (1995) Aminooxyacetic acid: a selective inhibitor of alanine:glyoxylate aminotransferase and its use in diagnosis of primary hyperoxaluria type I. *Clin. Chim. Acta* 243, 105–115.
- (20) Cellini, B., Lorenzetto, A., Montioli, R., Oppici, E., and Voltattorni, C. B. (2010) Human liver peroxisomal alanine:glyoxylate aminotransferase: Different stability under chemical stress of the major allele, the minor allele, and its pathogenic G170R variant. *Biochimie* 92, 1801–1811.
- (21) Cellini, B., Montioli, R., Paiardini, A., Lorenzetto, A., Maset, F., Bellini, T., Oppici, E., and Voltattorni, C. B. (2010) Molecular defects of the glycine 41 variants of alanine glyoxylate aminotransferase associated with primary hyperoxaluria type I. *Proc. Natl. Acad. Sci. U. S. A.* 107, 2896–2901.
- (22) Mesa-Torres, N., Fabelo-Rosa, I., Riverol, D., Yunta, C., Albert, A., Salido, E., and Pey, A. L. (2013) The role of protein denaturation energetics and molecular chaperones in the aggregation and mistargeting of mutants causing primary hyperoxaluria type I. *PLoS One* 8, e71963.
- (23) Underhaug, J., Aubi, O., and Martinez, A. (2012) Phenylalanine hydroxylase misfolding and pharmacological chaperones. *Curr. Top Med. Chem.* 12, 2534–2545.
- (24) Oppici, E., Montioli, R., Lorenzetto, A., Bianconi, S., Borri Voltattorni, C., and Cellini, B. (2012) Biochemical analyses are instrumental in identifying the impact of mutations on holo and/or apo-forms and on the region(s) of alanine:glyoxylate aminotransferase variants associated with primary hyperoxaluria type I. *Mol. Genet. Metab.* 105, 132–140.
- (25) Johnson, C. M. (2013) Differential scanning calorimetry as a tool for protein folding and stability. *Arch. Biochem. Biophys.* 531, 100–109.
- (26) Pey, A. L., Ying, M., Cremades, N., Velazquez-Campoy, A., Scherer, T., Thony, B., Sancho, J., and Martinez, A. (2008) Identification of pharmacological chaperones as potential therapeutic agents to treat phenylketonuria. *J. Clin. Invest.* 118, 2858–2867.
- (27) Behnam, J. T., Williams, E. L., Brink, S., Rumsby, G., and Danpure, C. J. (2006) Reconstruction of human hepatocyte glyoxylate metabolic pathways in stably transformed Chinese-hamster ovary cells. *Biochem. J.* 394, 409–416.
- (28) Oppici, E., Roncador, A., Montioli, R., Bianconi, S., and Cellini, B. (2013) Gly161 mutations associated with Primary Hyperoxaluria Type I induce the cytosolic aggregation and the intracellular degradation of the apo-form of alanine:glyoxylate aminotransferase. *Biochim. Biophys. Acta, Mol. Basis Dis.* 1832, 2277–2288.
- (29) Tetko, I. V., Gasteiger, J., Todeschini, R., Mauri, A., Livingstone, D., Ertl, P., Palyulin, V. A., Radchenko, E. V., Zefirov, N. S., Makarenko, A. S., Tanchuk, V. Y., and Prokopenko, V. V. (2005) Virtual computational chemistry laboratory—design and description. *J. Comput.-Aided Mol. Des.* 19, 453–463.
- (30) Danpure, C. J., Purdue, P. E., Fryer, P., Griffiths, S., Allsop, J., Lumb, M. J., Guttridge, K. M., Jennings, P. R., Scheinman, J. I., Mauer, S. M., et al. (1993) Enzymological and mutational analysis of a complex primary hyperoxaluria type I phenotype involving alanine:glyoxylate aminotransferase peroxisome-to-mitochondrion mistargeting and intraperoxisomal aggregation. *Am. J. Hum. Genet.* 53, 417–432.
- (31) Danpure, C. J. (2006) Primary hyperoxaluria type 1: AGT mistargeting highlights the fundamental differences between the peroxisomal and mitochondrial protein import pathways. *Biochim. Biophys. Acta, Mol. Cell Res.* 1763, 1776–1784.
- (32) Lumb, M. J., Drake, A. F., and Danpure, C. J. (1999) Effect of N-terminal alpha-helix formation on the dimerization and intracellular targeting of alanine:glyoxylate aminotransferase. *J. Biol. Chem.* 274, 20587–20596.
- (33) Purdue, P. E., Allsop, J., Isaya, G., Rosenberg, L. E., and Danpure, C. J. (1991) Mistargeting of peroxisomal L-alanine:glyoxylate aminotransferase to mitochondria in primary hyperoxaluria patients depends upon activation of a cryptic mitochondrial targeting sequence by a point mutation. *Proc. Natl. Acad. Sci. U. S. A.* 88, 10900–10904.
- (34) Cellini, B., Montioli, R., Paiardini, A., Lorenzetto, A., and Voltattorni, C. B. (2009) Molecular Insight into the Synergism between the Minor Allele of Human Liver Peroxisomal Alanine:Glyoxylate Aminotransferase and the F152I Mutation. *J. Biol. Chem.* 284, 8349–8358.
- (35) Wolf, J., Schliebs, W., and Erdmann, R. (2010) Peroxisomes as dynamic organelles: peroxisomal matrix protein import. *FEBS J.* 277, 3268–3278.
- (36) Montioli, R., Cellini, B., Bertoldi, M., Paiardini, A., and Voltattorni, C. B. (2009) An engineered folded PLP-bound monomer of *Treponema denticola* cystalysin reveals the effect of the dimeric structure on the catalytic properties of the enzyme. *Proteins: Struct., Funct., Genet.* 74, 304–317.
- (37) Cha, S. (1975) Tight-binding inhibitors-I. Kinetic behavior. *Biochem. Pharmacol.* 24, 2177–2185.
- (38) Muntau, A. C., Leandro, J., Staudigl, M., Mayer, F., and Gersting, S. W. (2014) Innovative strategies to treat protein misfolding in inborn errors of metabolism: pharmacological chaperones and proteostasis regulators. *J. Inherited Metab. Dis.* 37, 505–523.
- (39) Cellini, B., Montioli, R., Oppici, E., Astegno, A., and Voltattorni, C. B. (2014) The chaperone role of the pyridoxal 5'-phosphate and its implications for rare diseases involving B6-dependent enzymes. *Clin. Biochem.* 47, 158–165.
- (40) Pey, A. L., Albert, A., and Salido, E. (2013) Protein homeostasis defects of alanine-glyoxylate aminotransferase: new therapeutic strategies in primary hyperoxaluria type I. *BioMed Res. Int.* 2013, 687658.
- (41) Hoyer-Kuhn, H., Kohbrok, S., Volland, R., Franklin, J., Hero, B., Beck, B. B., and Hoppe, B. (2014) Vitamin B6 in primary hyperoxaluria I: first prospective trial after 40 years of practice. *Clin. J. Am. Soc. Nephrol.* 9, 468–477.
- (42) Melenovska, P., Kopecka, J., Krijt, J., Hnizda, A., Rakova, K., Janosik, M., Wilcken, B., and Kozich, V. (2015) Chaperone therapy for homocystinuria: the rescue of CBS mutations by heme arginate. *J. Inherited Metab. Dis.* 38, 287.
- (43) Chou, C. J., Herman, D., and Gottesfeld, J. M. (2008) Pimelic diphenylamide 106 is a slow, tight-binding inhibitor of class I histone deacetylases. *J. Biol. Chem.* 283, 35402–35409.
- (44) Montioli, R., Roncador, A., Oppici, E., Mandrile, G., Giachino, D. F., Cellini, B., and Borri Voltattorni, C. (2014) S81L and G170R mutations causing Primary Hyperoxaluria type I in homozygosis and heterozygosis: an example of positive interallelic complementation. *Hum. Mol. Genet.* 23, 5998–6007.
- (45) Roncador, A., Oppici, E., Montioli, R., Maset, F., and Cellini, B. (2013) TAT-Mediated Delivery of Human Alanine:Glyoxylate Aminotransferase in a Cellular Model of Primary Hyperoxaluria Type I. *Int. J. Pept. Res. Ther.* 19, 175.

Natural and Unnatural Compounds Rescue Folding Defects of Human Alanine: Glyoxylate Aminotransferase Leading to Primary Hyperoxaluria Type I

Elisa Oppici^{1,#}, Riccardo Montioli^{1,#}, Mirco Dindo¹ and Barbara Cellini^{1,*}

¹Department of Neurological, Biomedical and Movement Sciences, Section of Biological Chemistry, University of Verona, Strada le Grazie 8, 37134 Verona (VR), Italy

Abstract: The functional deficit of alanine:glyoxylate aminotransferase (AGT) in human hepatocytes leads to a rare recessive disorder named primary hyperoxaluria type I (PH1). PH1 is characterized by the progressive accumulation and deposition of calcium oxalate stones in the kidneys and urinary tract, leading to a life-threatening and potentially fatal condition. In the last decades, substantial progress in the clarification of the molecular pathogenesis of the disease have been made. They resulted in the understanding that many mutations cause AGT deficiency by affecting the folding pathway of the protein leading to a reduced expression level, an increased aggregation propensity, and/or an aberrant mitochondrial localization. Thus, PH1 can be considered a misfolding disease and possibly treated by approaches aimed at counteracting the conformational defects of the variants. In this review, we summarize recent advances in the development of new strategies to identify molecules able to rescue AGT folding and trafficking either by acting as pharmacological chaperones or by preventing the mistargeting of the protein.

Keywords: Primary hyperoxaluria type I, alanine: glyoxylate aminotransferase, misfolding disease, pyridoxal 5'-phosphate, pathogenic variants, pharmacological chaperones.

1. INTRODUCTION

Since the first introduction of the concept of “molecular disease” in 1949 [1], the field of molecular medicine has greatly expanded and many efforts have been devoted to the identification of the molecular mechanisms underlying genetic diseases as well as to develop effective treatment strategies. In the field of diseases caused by enzymatic deficits, it is becoming increasingly clear that the inability of the mutated protein to acquire its functional conformation is one of the main pathogenetic mechanisms. In fact, most mutations do not interfere with the enzyme catalytic activity, but reduce the efficiency of the folding pathway by stabilizing folding intermediates prone to aggregation, degradation, or aberrant interactions with other cellular components such as protein targeting systems [2]. This has pointed the attention of the scientific community to the identification of molecules that could rescue for the conformational defects of disease-causing variants, thus paving the way for the development of new treatment strategies. In this scenario, the present review focuses on recent advances made on the understanding of the pathogenetic mechanisms underlying primary hyperoxaluria type I (PH1) and on the development of new treatment approaches.

*Address correspondence to this author at the Department of Neurological, Biomedical and Movement Sciences, Section of Biological Chemistry, University of Verona, Strada le Grazie 8, 37134 Verona (VR), Italy; Tel: +39 0458027293; Fax: +39 0458027170; E-mail: barbara.cellini@univr.it

These authors contributed equally to this work.

2. PRIMARY HYPEROXALURIA TYPE I

Primary hyperoxaluria (PH) refers to diseases of genetic origin characterized by an abnormal production of endogenous oxalate in the liver. Since oxalate is an end-product of human metabolism that is excreted by urine, this condition results into an excessive urinary oxalate concentration, which in turn causes the deposition of insoluble calcium oxalate (CaOx) crystals in the urinary tract manifesting as urolithiasis and/or nephrocalcinosis [3, 4]. In the most severe forms renal failure occurs at early stages. The consequent increased plasmatic oxalate concentration leads to systemic oxalosis with CaOx deposition in various organs, including mainly bones and vessels, but also skin and retina [5, 6]. The clinical spectrum of PH is heterogeneous and varies from infantile nephrocalcinosis and renal failure to less aggressive forms manifesting as recurrent kidney stones formation in adulthood. The genetic background of the patient is one of the factors that contribute to the clinical heterogeneity of the disease, along with environmental factors (*i.e.* the daily fluid intake) and modifier genes [7].

Three forms of PH are known that are transmitted as autosomal recessive disorders. PH1 (OMIM 256600) is the most common, accounting for approximately 80% of PH patients. It has an estimated prevalence of 1-3 per million population and an incidence around 1:120000 live births per year in Europe [8, 9]. However, the incidence is higher in countries with a high level of consanguinity and in historically isolated populations such as in the Canary Islands [10]. PH1 is caused by the deficit of alanine:glyoxylate aminotransferase (AGT), an enzyme specifically present in

Please provide
corresponding author(s)
photograph
size should be 4" x 4" inches

liver peroxisomes that converts L-alanine and glyoxylate to pyruvate and glycine, respectively [11]. This reaction represents a glyoxylate detoxification reaction. In fact, in the absence of AGT glyoxylate builds up and is converted to oxalate by L-lactate dehydrogenase in the hepatocyte cytosol (Fig. 1) [12]. The resulting increased urinary oxalate concentration is the primary cause of CaOx stones formation in PH1 patients.

From a clinical point of view, an increased concentration of urinary oxalate and recurrent urolithiasis with rapid progression to renal failure are signs indicative of PH1. Although the first symptoms usually appear during the first decade of life, the diagnosis is often delayed and many patients are recognized only upon recurrent CaOx stones formation after kidney transplantation. The definitive diagnosis of the disease is made by genetic tests indicating the presence of mutations on the *AGXT* gene on chromosome 2q37.3 that encodes AGT [13].

The currently available treatment strategies for PH1 comprise both conservative and curative measures. A high fluid intake, the administration of crystallization inhibitors and a low-oxalate diet are the most used conservative treatments along with dialysis under selected clinical conditions [13]. These approaches can efficiently slow down the disease progression and in some patients they can prevent kidney failure. The administration of vitamin B6 in form of pyridoxine (PN), a precursor of the AGT coenzyme, is helpful in a minority of PH1 patients (25-35%) but the biochemical mechanisms underlying responsiveness have not been completely clarified [14, 15]. The only curative treatment available to date is liver transplantation. It replaces the organ responsible for excessive oxalate production, but it is a very invasive and risky procedure that comes with important side-effects and long-term complications. Indeed, combined liver-kidney transplantation is the present choice only for PH1 patients presenting end-stage renal disease [10, 16-18].

3. AGT FUNCTIONAL AND STRUCTURAL PROPERTIES

AGT is a pyridoxal 5'-phosphate (PLP)-dependent peroxisomal enzyme specifically expressed in human liver and it is involved in the metabolism of glyoxylate. The physiological reaction catalyzed by AGT, the conversion of L-alanine and glyoxylate to pyruvate and glycine, occurs by a ping-pong mechanism typical of PLP-dependent aminotransferases [11]. In the first half-reaction, L-alanine reacts with the PLP form of the enzyme (AGT-PLP) producing pyruvate and the pyridoxamine 5'-phosphate form of the enzyme (AGT-PMP). In the second half-reaction, glyoxylate reacts with AGT-PMP to form AGT-PLP and glycine. The equilibrium constant of the overall transamination is ~ 9500 and the k_{cat} of the direct reaction (L-alanine + glyoxylate \rightarrow pyruvate + glycine) is about 100-fold higher than that of the reverse reaction, thus providing the experimental evidence that the physiological function of the enzyme is glyoxylate detoxification [11]. Besides the transaminase activity, AGT also shows an eliminase activity toward β -chloro-L-alanine and an eliminase activity accompanied by a half-transaminase activity toward L-cysteine, whose physiological significance has not been demonstrated yet [19].

Structural studies reveal that AGT is a compact homodimer and belongs the Fold Type I class of the PLP-enzymes family [20]. Each monomer contains a PLP-binding site and consists of an N-terminal domain (residues 1-21) that grasps the surface of the other monomer, a large domain (residues 22-282) that includes the dimerization interface and the active site, and a smaller C-terminal domain (residues 283-392) comprising an atypical KKL peroxisomal targeting sequence (PTS1) (Fig. 2A). The PLP cofactor is covalently bound to the protein by a Schiff base linkage with Lys209, a base stacking hydrophobic π interaction involving Trp108 and the pyridine ring, a salt bridge between the side chain of Asp183 and the N1 nitrogen of PLP, a hydrogen bond between the side chain of Ser158 and the 3'-hydroxyl group of PLP, and

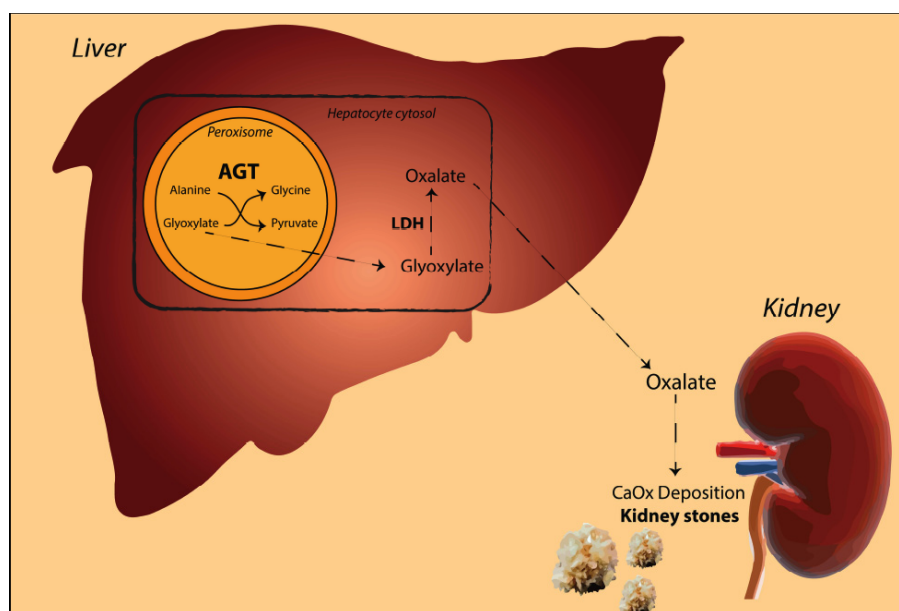


Fig. (1). Metabolic consequences of AGT deficiency. Sites and mechanisms of oxalate formation are shown. LDH, lactic dehydrogenase.

hydrogen bonds between residues belonging to both subunits (Ser81, Gly82, His83, Tyr260* and Thr263*) and the phosphate group of the cofactor [20]. The enzyme in the AGT-PLP form shows an absorption maximum at 423 nm associated with a positive dichroic band at 429 nm, attributed to the ketoenamine tautomer of the internal aldimine, and a shoulder at 340 nm associated with a negative dichroic signal at the same wavelength, attributed to the enolimine tautomer [11].

The *AGXT* gene is present in humans as two polymorphic forms: the most common major allele encoding AGT-Ma, and the less common minor allele encoding AGT-Mi. The latter, which has a frequency around 20% in Caucasian population, differs from the major allele for the presence of a 74-bp duplication in intron 1 and of two polymorphisms leading to the Pro11-to-Leu and Ile340-to-Met amino acid substitutions (Fig. 2A) [21-23]. It has been demonstrated that the P11L polymorphism causes an ~30% reduction of the AGT catalytic activity, destabilizes the dimeric structure, and promotes the aggregation and the degradation of the protein [24]. Moreover, while AGT-Ma is 100% peroxisomal, AGT-Mi is about 95% peroxisomal and 5% mitochondrial [21]. Evidence has been provided that the P11L polymorphism generates a weak putative mitochondrial targeting sequence (MTS), an important structural element acting as anchoring point for the mitochondrial import receptor TOM20. However, the rapid dimerization of AGT-Mi in the cell cytosol makes it incompatible with the mitochondrial import machinery that only operates on partly-folded or unfolded monomeric species. This explains why the vast majority of AGT is correctly located into peroxisomes even in the presence of the polymorphism and why the minor allele is not pathogenic *per se* [25].

Like most peroxisomal proteins bearing a PTS1 targeting sequence, AGT is imported into the peroxisomal matrix upon interaction with the Pex5p carrier [26]. This interaction is quite weak, being mediated by a non-canonical PTS1 sequence (KKL) at the C-terminus and by an “extended PTS1” formed by residues 381–388 and 327–330 [27] (Fig. 2B). The knowledge of the import mechanisms is still scarce, but it has been clarified that peroxisomes import their matrix proteins in a folded and even oligomerized manner, probably through the formation of a transient translocation pore in the membrane [28]. Thus, Pex5p is proposed to bind the folded AGT dimer and the complex then translocates into the peroxisomal matrix. This implies that AGT should achieve its final dimeric structure in the cell cytosol before the import and that the efficiency of the enzyme folding and dimerization pathway dictates how much of the newly synthesized AGT molecules reach their active conformation and final subcellular localization. Many groups have investigated the AGT folding and dimerization pathways *in vitro*, as a prerequisite to dissect the molecular effect(s) of pathogenic mutations leading to structural rather than functional defects. Studies performed by means of either chemical and/or thermal denaturation methods [24, 29-33] have revealed that (i) AGT-Ma is an extremely stable protein, whose denaturation follows a two-state process in the holo-form and a two- or three-state process in the apo-form; (ii) the coenzyme PLP exerts a remarkable stabilizing effect, by either maintaining the integrity of the dimeric structure and/or by increasing the

denaturation free energy of each subunit (see below); (ii) the unfolding pathway of both holo- and apoAGT involves the formation of aggregation-prone intermediates able to interact with molecular chaperones [30]. This has been also demonstrated by the resolution of the structure of a folding intermediate of a pathogenic AGT variant in complex with GroEL by cryoelectron microscopy [34]; (iii) AGT-Mi displays a lower stability with respect to AGT-Ma, mainly as a consequence of the P11L polymorphism, which increases the flexibility of the N-terminal arm [35, 36] and reduces the stability of the dimeric structure. Unfortunately, the very low refolding efficiency of AGT upon denaturation did not allow researchers to draw thermodynamic conclusions about the equilibrium refolding pathway. Nevertheless, the data obtained have provided a solid base to rationalize the effects of several PH1-associated mutations, as well as to design and test therapeutic approaches able to overcome folding-defective variants [37, 38].

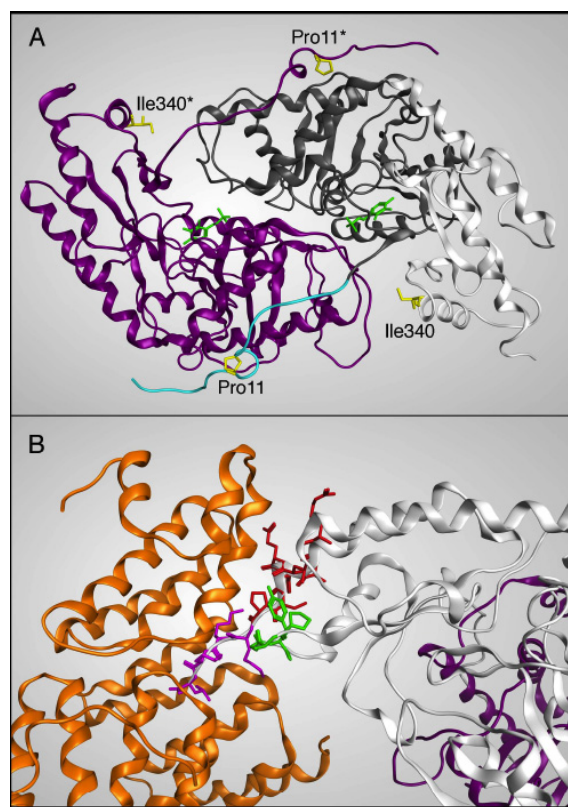


Fig. (2). Structural representation of AGT and of the AGT-Pex5p complex. (A) Ribbons representation of the AGT dimeric structure. The N-terminal domain, the large domain and the C-terminal domain of one monomer are coloured cyan, dark, grey, and white, respectively. The neighbouring monomer is coloured purple. Pro11 and Ile340 residues are represented as yellow sticks and the PLP molecules are shown as green sticks. (B) Ribbons representation of the C-terminal domain of AGT (white) interacting with the Pex5p carrier (orange). Residues forming the PTS1 are represented as magenta sticks, while residues 381-388 and 327-330, originating the “extended PST1”, are coloured green and red, respectively. Structures were generated starting from the coordinate files of AGT (pdb file 1H0C) and of the AGT-Pex5p complex (pdb file 3R9A). The images were rendered using the MOE 2013 software (CCG group).

4. FOLDING DEFECTS LEADING TO AGT DEFICIENCY IN PH1

Over 150 mutations on the *AGXT* gene have been identified until now as being associated with PH1. About half of these are point mutations leading to single amino acid substitutions on the enzyme sequence. Missense mutations identified so far are spread over the protein structure, thus suggesting that different enzymatic phenotypes could lead to AGT deficiency, and many of them co-segregate and functionally synergize with the minor allele [25].

It is well known that the substitution of just one residue of a protein can have a dramatic effect on the macromolecular structure itself, the binding of ligands, the ability to interact with protein partners, and the cellular localization. Studies on both purified proteins and cellular model systems have been used to determine the impact of missense mutations on AGT, in order to shed light on the pathogenetic mechanisms underlying PH1 [4, 37, 38]. The results obtained have indicated that all mutations cause a remarkable reduction of the amounts of active peroxisomal AGT. In many cases this is not due to a reduced catalytic efficiency of the enzyme itself, as a consequence for example of the mutation of residues involved in catalysis or in PLP binding. Rather, most mutations mainly affect the structural properties and decrease the amount of correctly folded AGT present inside peroxisomes. In all these conditions PH1 is caused by a proteostasis impairment, as a result of alterations of the AGT folding/misfolding thermodynamics or kinetics, and/or of the inability of the polypeptide chain to interact with the proteostasis network components that facilitate protein folding [24, 30, 32, 33, 39-47]. Moreover, a mutation can impact the behaviour of AGT in the cellular microenvironment in a much more complex way than predicted by the simple description of the effects at a structural level. Three main effects can be outlined (Fig. 3) with more than one effect possibly co-existing in a variant:

1) *The mutation strongly reduces the AGT expression level and specific activity.* When expressed in a cellular system

many AGT variants are characterized by a very low or even undetectable specific activity and expression level [48], thus indicating that they are affected by a structural defect that reduces the amount of protein reaching the folded and active conformation. This condition can be produced by mutations that strongly reduce the AGT folding efficiency, as revealed by the enhanced interaction with molecular chaperones, thus suggesting the trapping in partly-folded states [30]. The latter effect has been observed for the G170R, A295T and P319L mutations [30, 32]. Alternatively, the pathogenic mutation can reduce the half-life of AGT by making the protein prone to degradation in the cell cytosol, as demonstrated for the Gly161 mutation. In fact, pulse-chase experiments performed in a cellular disease model have shown that the half-life of the G161R-Ma, G161S-Mi and G161C-Mi variants is reduced from 2- to more than 7-fold as compared with that of AGT-Ma or AGT-Mi [43]. Analogous results have been obtained for the G41R-Mi, W108R-Mi, G156R-Ma, C173Y-Ma, S187F-Ma and S205P-Ma variants expressed in cell-free systems [46]. A reduced intracellular stability has been also postulated as the defect of some variants on the basis of limited proteolysis experiments [46], starting from the idea that an increased sensitivity to proteolytic cleavage indicates an increased local flexibility of the polypeptide chain, which in turn suggests the population of high-energy folding intermediates prone to degradation. Interestingly, a decreased resistance to thermal or chemical stress often accompanies the reduced expression level of pathogenic variants of AGT in the recombinant purified form. Studies performed by means of spectroscopy and calorimetry techniques [24, 29, 30, 32, 33, 39, 47] have revealed that PH1-causing mutations affect the thermodynamic and/or the kinetic stability of AGT. In many cases the structural defect is only or mainly evident on the apo-form of the variants and is rescued by the binding of the coenzyme PLP, which probably exerts a chaperone role (see section 5). Moreover, the effect of many mutations is enhanced by the presence of the P11L amino acid substitution, in agreement with the finding that they are pathogenic only when inherited on the background of the minor allele [24, 25, 31, 39].

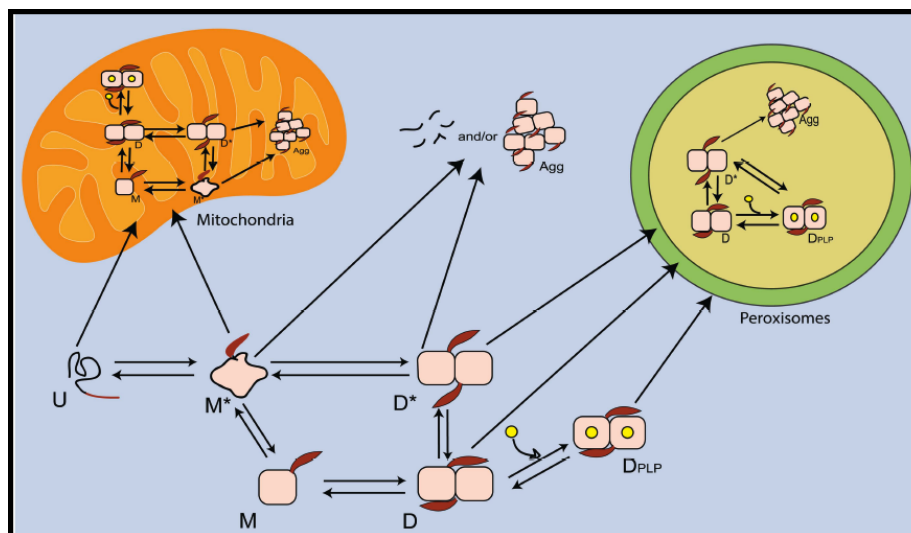


Fig. (3). Folding defects of AGT variants leading to PH1. U: unfolded monomer, M*: partially folded monomer, M: folded monomer, D*: partly folded apodimer, D: apodimer, D_{PLP}: PLP-bound dimer, Agg: aggregates.

2) *The mutation increases the aggregation propensity of AGT.* The formation of protein aggregates, with either an ordered (*i.e.* in form of amyloid fibrils) or a disordered structure, is common to most misfolding diseases [49]. In the case of PH1, the presence of a large amount of AGT in form of high-molecular weight aggregates has been initially observed in cells expressing the I244T-Mi variant, which is mainly present in the insoluble fraction of the lysate [45]. More recently, the mutation of residues Gly41, Gly47 or Gly161 was also found to make AGT prone to aggregation both inside the cell and in the purified form [42-44, 47]. Investigations on the molecular and cellular properties of the aggregates have revealed that they are stabilized by electrostatic interactions, do not show any ordered conformation, and are not toxic for the cell, in agreement with PH1 having a loss-of-function pathogenesis [37]. While aggregates of Gly41 and Gly47 variants are deposited inside peroxisomes, those formed by Gly161 variants accumulate in the cell cytosol. This is probably linked to the relationship between the two kinetics of aggregation and peroxisomal import of each variant.

3) *The mutation causes the aberrant targeting of AGT to mitochondria.* When inherited on the background of the minor allele, pathogenic mutations that interfere with the folding pathway of AGT can make the population of monomeric intermediates susceptible to import by the mitochondrial import machinery, thanks to the presence of the putative MTS generated by the P11L polymorphism [22]. Mitochondrial AGT is still catalytically active, but is metabolically ineffective because it is not able to convert peroxisomal glyoxylate to glycine. This is the case of the G170R-Mi variant, the most common in PH1. The G170R mutation does not affect neither the spectroscopic nor the kinetic properties of AGT, but favours the mitochondrial import of the protein, as shown both in patient tissues and in cellular models [44, 50, 51]. On purified AGT, the substitution of Gly170 by an Arg residue reduces the resistance to chemical denaturation and the kinetic stability of the protein in the apo-form [24, 30], thus promoting the formation of monomeric partly-folded intermediates that can be imported into mitochondria. Moreover, the G170R-Mi variant displays an enhanced interaction with the molecular chaperones Hsp70, Hsp90 and Hsp60, which can present the protein to mitochondrial receptors [30]. A similar behaviour has been found in other variants such as F152I-Mi, I244T-Mi, G41R-Mi and G47R-Mi [42, 44, 52] and it has been speculated that the mitochondrial mistargeting could be a common effect of all mutations that are pathogenic on the background of the minor allele [44].

Recently, a comprehensive analysis of the effect of several naturally-occurring and consensus-based mutations on the energetics of the AGT stability has been carried out [33]. These studies support the view that while AGT-Ma represents the state endowed with the optimal conformational stability to fold and be targeted efficiently in a cell, AGT-Mi represents the lower limit of AGT foldability leading to a minimum glyoxylate detoxification ability. Following this view, a model has been proposed in which most mutations favour AGT misfolding by reducing the thermodynamic stability below the threshold of AGT-Mi and natural or unnatural AGT ligands rescue for the effect of the mutations by

increasing the stability of pathogenic variants above the threshold.

5. USE OF B6 VITAMERS FOR THE PHARMACOLOGICAL TREATMENT OF PH1

Almost all inborn errors of metabolism caused by mutations in a gene encoding a PLP-dependent enzyme, including PH1, are treated by the administration of vitamin B6 in form of PN [53]. The first evidence that PN treatment was able to reduce urine oxalate (Uox) levels in PH1 patients was provided in 1961 [54]. However, only after the discovery that mutations on the *AGXT* gene are the cause of the disease [12] PN is used as therapeutic standard. A three month-treatment with 5 to 20 mg/kg/day of PN is recommended to all patients [55], especially to those bearing missense mutations [4, 13]. However, only 25-35% of PH1 patients are reported to be responsive. Although in 2014 a prospective trial with vitamin B6 in form of PN has reported an efficacy of the treatment in about 50% of the patients examined, no complete reduction of the Uox levels to normal values has been observed [56]. In addition, since the number of disease cases is very low and the determination of Uox levels to establish PN responsiveness has some limitations [56, 57], it is not possible to predict the effectiveness of the treatment on the basis of the patient genotype.

Despite the long-time use of PN and the well-known mechanisms of absorption in the intestine and conversion to PLP in the liver [58], the molecular bases of the positive effects on responsive PH1 patients are still under investigation. PLP would be expected to play essentially a prosthetic role for pathogenic variants with a low coenzyme binding affinity or an altered coenzyme binding mode [59]. However, the available clinical data demonstrate that responsive patients bear mutations of residues located far from the active site of the protein (such as F152I, G170R and I244T associated with the minor allele) that lead to the accumulation of folding intermediates causing protein aggregation, degradation and/or mitochondrial mistargeting (Fig. 3) [56, 57, 60]. In order to shed light on the molecular mechanism underlying PN administration, the effects of vitamin B6 have been widely investigated in the last few years. The results obtained have revealed that PLP exerts a stabilizing effect on purified recombinant AGT by: (i) increasing the resistance to chemical and thermal unfolding [24, 29, 31], (ii) enhancing the kinetic stability of 4-5 orders of magnitude [30, 32] and (iii) reducing the aggregation propensity [39, 47] and the proteolytic cleavage susceptibility [39, 47]. Since the responsive F152I-Mi, G170R-Mi and I244T-Mi variants display a reduced stability in the apo-form with respect to AGT-Mi [24, 30, 32, 33, 39], it has been proposed that PLP might influence the folding pathway of the variants by shifting the equilibrium from the unstable apo-form to the more stable holo-form (Fig. 4A). However, it remains to be established if the coenzyme binds partly-folded intermediates or the apoenzyme once folded. Recent studies focused on the behavior of PN-responsive variants in a cellular model of PH1, specifically Chinese Hamster Ovary (CHO) cells stably expressing glycolate oxidase (GO)[61], have revealed that the coenzyme exerts a chaperone role [62, 63]. In fact, the presence of PN in the culture media of CHO-GO cells expressing F152I-Mi, G170R-Mi or I244T-Mi variants not only im-

proves the specific activity, but also increases the total expression level of the variants and promotes their correct sub-cellular localization, thus enhancing the capability to detoxify glyoxylate. These data suggest that PLP increases the productive folding of the proteins and prevents their aggregation and degradation, leading to higher amounts of active dimers imported inside peroxisomes (Fig. 4A) [62, 63]. Interestingly, the increase of PN concentration up to 250 μM reduces by about 50% the specific activity and the glyoxylate detoxification capability of cells expressing AGT-Ma and AGT-Mi [62, 63]. This effect, in the absence of reduced protein expression levels, has been attributed to the finding that the supplementation with PN leads not only to the intracellular accumulation of PLP, but also of pyridoxine 5'-phosphate (PNP) and PN [62, 63]. PNP, but not PN, is able to interact with AGT-Ma, AGT-Mi, F152I-Mi and G170R-Mi variants in the purified form and to compete with PLP for apoenzyme binding giving rise to an inactive AGT-PNP complex (Fig. 4A) [63]. Thus, the global positive effect seen upon PN administration is probably a balance between the chaperone effect exerted by PLP and the inhibitory effect exerted by PNP (Fig. 4A) [63]. Following this idea, the B6-responsiveness measured upon PN administration could be underestimated. Even if no clinical data have been published

that support this thesis, it is worth noting that most patients respond to low PN doses ($< 10 \text{ mg/kg/day}$) [58, 64] and that Uox levels are not correlated with serum B6 levels [56].

Expanding upon the inhibitory effects of PN administration, other B6 vitamers were investigated for their effects [63]. In fact, although only PN has been used for the treatment of PH1, two other un-phosphorylated B6 vitamers are absorbed by the intestine and then converted to PLP by the liver salvage pathway [65]: pyridoxamine (PM) and pyridoxal (PL). In 2005 Chetyrkin *et al.* [66, 67] reported that the administration of PM reduced Uox and kidney crystals in hyperoxaluric untreated animals but the mechanism of action was not investigated. Recently, our group [63] could show that PM and PL are more effective than PN in rescuing the two PN-responsive variants F152I-Mi and G170R-Mi when expressed in a cellular model of PH1. Indeed, PM or PL supplementation causes the intracellular accumulation of PLP and PMP, the two active forms of the coenzyme exerting both a chaperone and a prosthetic role, without any accumulation of PNP (Fig. 4B) [63]. These results support the potential use of PM and PL as a novel coenzyme administration therapy for patients bearing PH1-causing mutations that affect protein folding. In this regard, it is of note that the administration of PM and PL to mice does not result in the sub-

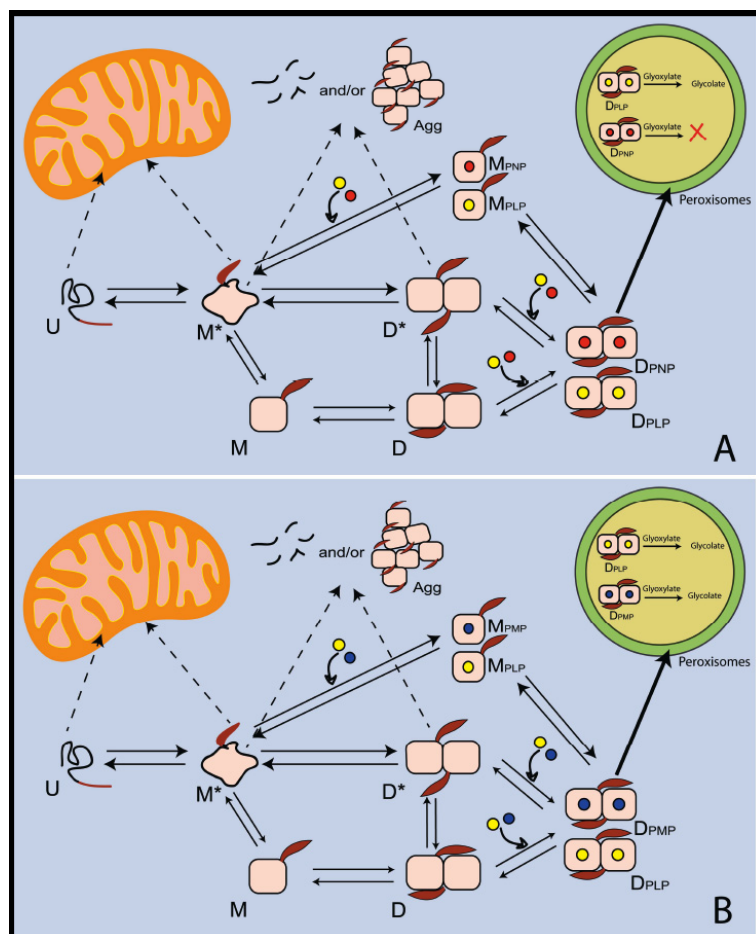


Fig. (4). Proposed molecular effect of PN (A) and of PM or PL (B) treatment on AGT variants bearing folding defects. U: unfolded monomer, M*: partially folded monomer, M: folded monomer, M_{PLP}: PLP-bound monomer, M_{PNP}: PNP-bound monomer, M_{PMP}: PMP-bound monomer D*: partly folded apodimer, D: apodimer, D_{PLP}: PLP-bound dimer, D_{PNP}: PNP-bound dimer, D_{PMP}: PMP-bound dimer, Agg: aggregates. PLP, PNP and PMP are represented as yellow, red or blue circles, respectively. Dashed arrows indicate minor routes.

the neurological effects seen with high PN doses, and that PM is actually under phase II clinical trial for diabetes type I and type II (Pyridorin™) and does not appear to be toxic for humans even at high doses [68, 69].

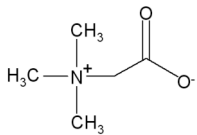
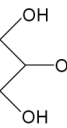
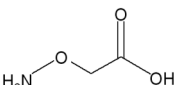
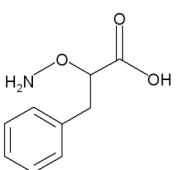
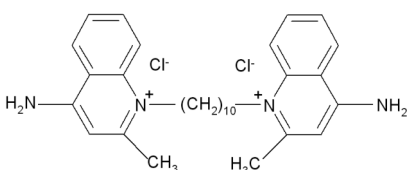
6. INNOVATIVE TREATMENT STRATEGIES BASED ON THE USE OF UNNATURAL COMPOUNDS

Upon the discovery that the majority of PH1-causing missense mutations negatively influence AGT folding, numerous efforts have been dedicated to the identification of small molecules able to promote the achievement of the native structure. In particular, the effect of compounds possibly acting as chemical chaperones (CCs) or pharmacological chaperones (PCs) for AGT has been tested on folding-defective variants in the purified form and/or expressed in cellular models. CCs are usually low molecular weight compounds that nonselectively stabilize proteins and assist the folding process. CCs require high concentrations to rescue *in vivo* misfolded proteins, making them unsuitable for therapy. On the other hand, PCs are site-specific compounds that usually resemble natural ligands of the target protein and facilitate the correct folding by acting on protein thermodynamic and/or kinetic stability, leading to improved folding and trafficking in cells. The higher specificity permits them to be effective at very low concentrations [70]. Glycerol, betaine, phenylbutyric acid (PBA), and trimethylamine N-oxide (TMAO) are potential CCs tested on AGT variants [31, 45, 46, 71] (Table 1). Glycerol has been found to prevent the

mistargeting to mitochondria of the G170R-Mi variant and to redirect the enzyme to peroxisomes in COS7 cells [71]. It has been suggested that glycerol could stabilize the protein, enabling it to adopt a more compact dimeric form that is incompatible with the mitochondrial import machinery. Betaine is able to increase the solubility of the I244T-Mi variant expressed in COS7 cells by reducing the amount of protein present as insoluble aggregates [45]. Moreover, it also exerts a stabilizing effect, by decreasing the sensitivity of the G41R-Ma and G41V-Ma variants to tryptic digestion *in vitro* [46]. None or minimal effects on protein solubility, stability or protease sensitivity have been observed upon treatment of AGT variants with PBA or TMAO [45, 46].

Compounds acting as PCs for diseases caused by an enzymatic deficit are usually competitive inhibitors of the enzyme involved, because they show high binding affinity and specificity [70]. A compound known to act as an AGT inhibitor is aminooxyacetic acid (AOA) (Table 1), which binds the active site mimicking the position of the substrate L-alanine [52]. Although AOA displays a low specificity, because it binds and inhibits many PLP-dependent enzymes [72-74], the possible action of this molecule as PC for folding-defective AGT variants has been tested by various groups and in different experimental conditions [31, 45, 46, 52]. The first evidence of the stabilizing effect of AOA on AGT was provided by a mass spectrometry-based technique and by differential scanning fluorimetry (DSF). These analyses revealed that the binding of AOA increases the thermal

Table 1. Unnatural compounds able to rescue AGT misfolding or mistargeting.

Compound	Structure	Action	References
Betaine		Chemical chaperone	[45, 46]
Glycerol		Chemical chaperone	[71]
Aminooxyacetic acid (AOA)		Pharmacological chaperone	[46, 52]
2-aminooxy 3-phenylpropionic acid		Pharmacological chaperone	[52]
Dequalinium chloride (DECA)		Inhibitor of the mitochondrial protein import	[76]

stability of both AGT-Ma and AGT-Mi [31]. AOA was also reported to reduce the trypsin sensitivity of several AGT pathogenic variants (G41R-Ma, G41R-Mi, G41V-Ma, S218L, G156R, V336D-Mi) by presumably promoting their correct folding and reducing the exposure of flexible loops susceptible to proteolytic cleavage [75]. An in-depth study elucidating the mode of action of AOA as AGT inhibitor and its effectiveness as PC for three pathogenic variants has been recently published [52]. By kinetic analyses on purified proteins, AOA was found to act as a slow, tight-binding competitive inhibitor of AGT with a K_i value in the low nanomolar range. The presence of AOA in the culture medium increases the amount of functional AGT of cells expressing conformational variants. In particular, it improves the folding of G41R-Ma, a variant mainly characterized by an increased susceptibility to aggregation and proteolytic degradation, and promotes the peroxisomal localization of G170R-Mi and I244T-Mi, two variants aberrantly targeted to mitochondria. These findings have confirmed that AOA works as a PC for AGT, even though the slow, tight-binding behaviour and the low specificity make it unsuitable for use in therapy. Nonetheless, based on the idea that AOA could represent the chemical scaffold for the development of more specific ligands, a preliminary screening campaign on several AOA derivatives was carried out [52]. Among the compounds showing AGT inhibitory activity, 2-aminooxy-3-phenylpropionic acid (Table 1) was found to work as PC for folding-defective variants. This finding represents the proof-of-principle that a therapy with PCs for PH1 is feasible and it is a first step toward the identification of more effective compounds.

In the search of a new pharmacological non-invasive therapeutic for the treatment of PH1, a different approach was used by Miyata *et al.* [76], who restored the trafficking of the G170R-Mi variant from mitochondria to peroxisomes by using an inhibitor of the mitochondrial protein import. Since the G170R substitution on the minor allele generates an enzyme that is catalytically active but erroneously localized, any molecule that prevents the aberrant targeting should allow the variant to acquire its correct dimeric structure and be imported into peroxisomes in the active form [25, 44]. A small-scale genetic screening has been applied to identify FDA-approved molecules able to inhibit protein translocation to mitochondria. The most promising inhibitor identified is dequalinium chloride (DECA). Upon treatment of cells expressing G170R-Mi with DECA, the variant is correctly imported into peroxisomes and the glyoxylate detoxification ability of the cells is partly restored. It has been also shown that DECA inhibits the import of the variant to mitochondria. The mechanism of action is independent of uncoupling and maintains the protein in a conformation competent for the import into peroxisomes. This accounts for the low toxicity of the compound with respect to traditional uncouplers that block the import of all mitochondrial proteins by a non-selective mechanism. In addition, the effect of DECA seems to be additive with that of PN treatment, which raises the intracellular PLP concentration and promotes the correct folding of the protein [53]. Since the AGT mitochondrial mistargeting is induced by mutations that affect the folding of the protein it can be suggested that the combination of a treatment able to rescue protein folding with a mito-

chondrial transport blocker could increase the responsiveness of the patients.

Overall, the data obtained provide the base for the use of mitochondrial import inhibitors as models for the study of AGT intracellular trafficking, as well as for the development of new therapeutics. In this regard, it should be noticed however that although DECA has been approved by FDA, with the specific indication of treating vaginal infections by topical application, it has been proved to be toxic upon parenteral administration to murine models [77]. On these bases, safety assessment should be carefully evaluated when designing therapeutic approaches for PH1 based on the use of mitochondrial import inhibitors.

7. CONCLUSIONS

In the last few years, many progresses have been made on the elucidation of the molecular pathogenesis of PH1 by performing analyses on cellular model systems and purified proteins. The picture emerging from these studies depicts PH1 as a disease mainly caused by conformational defects, thus driving the current research activity of many groups in the field towards the development of therapeutic strategies able to rescue misfolded variants. The approaches currently under investigation ranges from the testing of more effective B6 vitamers to the identification of synthetic molecules acting as pharmacological chaperones or mitochondrial import inhibitors. The growing body of evidence will form the basis for future projects aimed at the design of more specific and more effective compounds, with the not-so-distant horizon of a personalized treatment of this life-threatening and potentially fatal disease.

LIST OF ABBREVIATIONS

PLP	=	Pyridoxal 5'-phosphate
AGT	=	Alanine: glyoxylate aminotransferase
PH1	=	Primary hyperoxaluria type I
PTS1	=	Peroxisomal targeting sequence type 1
MTS	=	Mitochondrial targeting sequence
PN	=	Pyridoxine
PNP	=	Pyridoxine 5'-phosphate
PM	=	Pyridoxamine
PL	=	Pyridoxal
PMP	=	Pyridoxamine 5'-phosphate
CHO	=	Chinese hamster ovary
GO	=	Glycolate oxidase
AOA	=	Aminoxyacetic acid
PC	=	Pharmacological chaperone
CC	=	Chemical chaperone

CONFLICT OF INTEREST

The authors confirm that this article content has no conflict of interest.

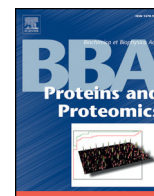
ACKNOWLEDGEMENTS

This work was supported by funding from the Oxalosis and Hyperoxaluria Foundation (OHF2012 to B.C.)

REFERENCES

- [1] Pauling L, Itano HA, *et al.* Sickle cell anemia a molecular disease. *Science* 1949; 110(2865): 543-8.
- [2] Bross P, Corydon TJ, Andresen BS, Jorgensen MM, Bolund L, Gregersen N. Protein misfolding and degradation in genetic diseases. *Hum Mutat* 1999; 14(3): 186-98.
- [3] Cochat P, Rumsby G. Primary hyperoxaluria. *N Engl J Med* 2013; 369(7): 649-58.
- [4] Salido E, Pey AL, Rodriguez R, Lorenzo V. Primary hyperoxalurias: disorders of glyoxylate detoxification. *Biochim Biophys Acta* 2012; 1822(9): 1453-64.
- [5] Morgan SH, Purkiss P, Watts RW, Mansell MA. Oxalate dynamics in chronic renal failure. Comparison with normal subjects and patients with primary hyperoxaluria. *Nephron* 1987; 46(3): 253-7.
- [6] Lorenzo V, Torres A, Salido E. Primary hyperoxaluria. *Nefrologia* 2014; 34(3): 398-412.
- [7] Cochat P, Groothoff J. Primary hyperoxaluria type 1: practical and ethical issues. *Pediatr Nephrol* 2013; 28(12): 2273-81.
- [8] Cochat P, Deloraine A, Rotily M, Olive F, Liponski I, Deries N. Epidemiology of primary hyperoxaluria type 1. Societe de Nephrologie and the Societe de Nephrologie Pediatrique. *Nephrol Dial Transplant*. 1995;10 Suppl 8:3-7.
- [9] van Woerden CS, Groothoff JW, Wanders RJ, Davin JC, Wijburg FA. Primary hyperoxaluria type 1 in The Netherlands: prevalence and outcome. *Nephrol Dial Transplant* 2003; 18(2): 273-9.
- [10] Lorenzo V, Alvarez A, Torres A, Torregrosa V, Hernandez D, Salido E. Presentation and role of transplantation in adult patients with type 1 primary hyperoxaluria and the I244T AGXT mutation: Single-center experience. *Kidney Int* 2006; 70(6): 1115-9.
- [11] Cellini B, Bertoldi M, Montioli R, Paiardini A, Borri Voltattorni C. Human wild-type alanine:glyoxylate aminotransferase and its naturally occurring G82E variant: functional properties and physiological implications. *Biochem J* 2007; 408(1): 39-50.
- [12] Danpure CJ, Jennings PR. Peroxisomal alanine:glyoxylate aminotransferase deficiency in primary hyperoxaluria type I. *FEBS Lett* 1986; 201(1): 20-4.
- [13] Cochat P, Hulton SA, Acquaviva C, *et al.* Primary hyperoxaluria Type 1: indications for screening and guidance for diagnosis and treatment. *Nephrol Dial Transplant* 2012; 27(5): 1729-36.
- [14] Gibbs DA, Watts RW. The action of pyridoxine in primary hyperoxaluria. *Clin Sci* 1970; 38(2): 277-86.
- [15] Watts RW, Veall N, Purkiss P, Mansell MA, Haywood EF. The effect of pyridoxine on oxalate dynamics in three cases of primary hyperoxaluria (with glycolic aciduria). *Clin Sci (Lond)* 1985; 69(1): 87-90.
- [16] Harambat J, van Stralen KJ, Espinosa L, *et al.* Characteristics and outcomes of children with primary oxalosis requiring renal replacement therapy. *Clin J Am Soc Nephrol* 2012; 7(3): 458-65.
- [17] Bergstralh EJ, Monico CG, Lieske JC, *et al.* Transplantation outcomes in primary hyperoxaluria. *Am J Transplant* 2010; 10(11): 2493-501.
- [18] Jamieson NV. The results of combined liver/kidney transplantation for primary hyperoxaluria (PH1) 1984-1997. The European PH1 transplant registry report. *European PH1 Transplantation Study Group. J Nephrol* 1998; 11 Suppl 1: 36-41.
- [19] Bertoldi M, Cellini B, Paiardini A, Montioli R, Borri Voltattorni C. Reactions of human liver peroxisomal alanine:glyoxylate aminotransferase with beta-chloro-L-alanine and L-cysteine: spectroscopic and kinetic analysis. *Biochim Biophys Acta* 2008; 1784(9): 1356-62.
- [20] Zhang X, Roe SM, Hou Y, *et al.* Crystal structure of alanine:glyoxylate aminotransferase and the relationship between genotype and enzymatic phenotype in primary hyperoxaluria type I. *J Mol Biol* 2003; 331(3): 643-52.
- [21] Purdue PE, Takada Y, Danpure CJ. Identification of mutations associated with peroxisome-to-mitochondrion mistargeting of alanine:glyoxylate aminotransferase in primary hyperoxaluria type I. *J Cell Biol* 1990; 111(6 Pt 1): 2341-51.
- [22] Purdue PE, Lumb MJ, Allsop J, Danpure CJ. An intronic duplication in the alanine: glyoxylate aminotransferase gene facilitates identification of mutations in compound heterozygote patients with primary hyperoxaluria type I. *Hum Genet* 1991; 87(4): 394-6.
- [23] Purdue PE, Lumb MJ, Fox M, *et al.* Characterization and chromosomal mapping of a genomic clone encoding human alanine:glyoxylate aminotransferase. *Genomics* 1991; 10(1): 34-42.
- [24] Cellini B, Lorenzetto A, Montioli R, Oppici E, Voltattorni CB. Human liver peroxisomal alanine:glyoxylate aminotransferase: Different stability under chemical stress of the major allele, the minor allele, and its pathogenic G170R variant. *Biochimie* 2010; 92(12): 1801-11.
- [25] Lumb MJ, Danpure CJ. Functional synergism between the most common polymorphism in human alanine:glyoxylate aminotransferase and four of the most common disease-causing mutations. *J Biol Chem* 2000; 275(46): 36415-22.
- [26] Huber PA, Birdsey GM, Lumb MJ, *et al.* Peroxisomal import of human alanine:glyoxylate aminotransferase requires ancillary targeting information remote from its C terminus. *J Biol Chem* 2005; 280(29): 27111-20.
- [27] Fodor K, Wolf J, Erdmann R, Schliebs W, Wilmanns M. Molecular requirements for peroxisomal targeting of alanine-glyoxylate aminotransferase as an essential determinant in primary hyperoxaluria type I. *PLoS Biol* 2012; 10(4): e1001309.
- [28] Platta HW, Erdmann R. The peroxisomal protein import machinery. *FEBS Lett* 2007; 581(15): 2811-9.
- [29] Oppici E, Montioli R, Lorenzetto A, Bianconi S, Borri Voltattorni C, Cellini B. Biochemical analyses are instrumental in identifying the impact of mutations on holo and/or apo-forms and on the region(s) of alanine:glyoxylate aminotransferase variants associated with primary hyperoxaluria type I. *Mol Genet Metab* 2012; 105(1): 132-40.
- [30] Pey AL, Salido E, Sanchez-Ruiz JM. Role of low native state kinetic stability and interaction of partially unfolded states with molecular chaperones in the mitochondrial protein mistargeting associated with primary hyperoxaluria. *Amino Acids* 2011; 41(5): 1233-45.
- [31] Hopper ED, Pittman AM, Fitzgerald MC, Tucker CL. *In vivo* and *in vitro* examination of stability of primary hyperoxaluria-associated human alanine:glyoxylate aminotransferase. *J Biol Chem* 2008; 283(45): 30493-502.
- [32] Mesa-Torres N, Fabelo-Rosa I, Riverol D, *et al.* The role of protein denaturation energetics and molecular chaperones in the aggregation and mistargeting of mutants causing primary hyperoxaluria type I. *PLoS One* 2013; 8(8): e71963.
- [33] Mesa-Torres N, Salido E, Pey AL. The lower limits for protein stability and foldability in primary hyperoxaluria type I. *Biochim Biophys Acta* 2014; 1844(12): 2355-65.
- [34] Albert A, Yunta C, Arranz R, *et al.* Structure of GroEL in complex with an early folding intermediate of alanine glyoxylate aminotransferase. *J Biol Chem* 2010; 285(9): 6371-6.
- [35] Purdue PE, Allsop J, Isaya G, Rosenberg LE, Danpure CJ. Mistargeting of peroxisomal L-alanine:glyoxylate aminotransferase to mitochondria in primary hyperoxaluria patients depends upon activation of a cryptic mitochondrial targeting sequence by a point mutation. *Proc Natl Acad Sci USA* 1991; 88(23): 10900-4.
- [36] Lumb MJ, Drake AF, Danpure CJ. Effect of N-terminal alpha-helix formation on the dimerization and intracellular targeting of alanine:glyoxylate aminotransferase. *J Biol Chem* 1999; 274(29): 20587-96.
- [37] Oppici E, Montioli R, Cellini B. Liver peroxisomal alanine: glyoxylate aminotransferase and the effects of mutations associated with Primary Hyperoxaluria Type I: An overview. *Biochim Biophys Acta* 2015; 1854(9): 1212-9.
- [38] Pey AL. Protein homeostasis disorders of key enzymes of amino acids metabolism: mutation-induced protein kinetic destabilization and new therapeutic strategies. *Amino Acids* 2013; 45(6): 1331-41.
- [39] Cellini B, Montioli R, Paiardini A, Lorenzetto A, Voltattorni CB. Molecular Insight into the Synergism between the Minor Allele of Human Liver Peroxisomal Alanine:Glyoxylate Aminotransferase and the F152I Mutation. *J Biol Chem* 2009; 284(13): 8349-58.
- [40] Pittman AM, Lage MD, Poltoratsky V, *et al.* Rapid profiling of disease alleles using a tunable reporter of protein misfolding. *Genetics* 2012; 192(3): 831-42.
- [41] Lage MD, Pittman AM, Roncador A, Cellini B, Tucker CL. Allele-specific characterization of alanine: glyoxylate aminotransferase variants associated with primary hyperoxaluria. *PLoS One* 2014; 9(4): e94338.
- [42] Montioli R, Oppici E, Dindo M, *et al.* Misfolding caused by the pathogenic mutation G47R on the minor allele of alanine: glyoxy-

- late aminotransferase and chaperoning activity of pyridoxine. *Biochim Biophys Acta* 2015; 1854(10 Pt A): 1280-9.
- [43] Oppici E, Roncador A, Montioli R, Bianconi S, Cellini B. Gly161 mutations associated with Primary Hyperoxaluria Type I induce the cytosolic aggregation and the intracellular degradation of the apoforn of alanine:glyoxylate aminotransferase. *Biochim Biophys Acta* 2013;1832(12):2277-88.
- [44] Fargue S, Lewin J, Rumsby G, Danpure CJ. Four of the most common mutations in primary hyperoxaluria type I unmask the cryptic mitochondrial targeting sequence of alanine:glyoxylate aminotransferase encoded by the polymorphic minor allele. *J Biol Chem*. 2013; 288(4): 2475-84.
- [45] Santana A, Salido E, Torres A, Shapiro LJ. Primary hyperoxaluria type I in the Canary Islands: a conformational disease due to I244T mutation in the P11L-containing alanine:glyoxylate aminotransferase. *Proc Natl Acad Sci USA* 2003; 100(12): 7277-82.
- [46] Coulter-Mackie MB, Lian Q. Partial trypsin digestion as an indicator of mis-folding of mutant alanine:glyoxylate aminotransferase and chaperone effects of specific ligands. Study of a spectrum of missense mutants. *Mol Genet Metab* 2008; 94(3): 368-74.
- [47] Cellini B, Montioli R, Paiardini A, *et al.* Molecular defects of the glycine 41 variants of alanine glyoxylate aminotransferase associated with primary hyperoxaluria type I. *Proc Natl Acad Sci USA* 2010; 107(7): 2896-901.
- [48] Oppici E, Montioli R, Cellini B. Liver peroxisomal alanine: glyoxylate aminotransferase and the effects of mutations associated with Primary Hyperoxaluria Type I: An overview. *Biochim Biophys Acta* 2015.
- [49] Chiti F, Dobson CM. Protein misfolding, functional amyloid, and human disease. *Annu Rev Biochem* 2006; 75: 333-66.
- [50] Danpure CJ, Jennings PR, Leiper JM, Lumb MJ, Oatey PB. Targeting of alanine: glyoxylate aminotransferase in normal individuals and its mistargeting in patients with primary hyperoxaluria type I. *Ann N Y Acad Sci* 1996; 804: 477-90.
- [51] Danpure CJ, Purdue PE, Fryer P, *et al.* Enzymological and mutational analysis of a complex primary hyperoxaluria type I phenotype involving alanine:glyoxylate aminotransferase peroxisome-to-mitochondrion mistargeting and intraperoxisomal aggregation. *Am J Hum Genet* 1993; 53(2): 417-32.
- [52] Oppici E, Montioli R, Dindo M, *et al.* The Chaperoning Activity of Amino-oxyacetic Acid on Folding-Defective Variants of Human Alanine:Glyoxylate Aminotransferase Causing Primary Hyperoxaluria Type I. *ACS Chem Biol* 2015.
- [53] Cellini B, Montioli R, Oppici E, Astegno A, Voltattorni CB. The chaperone role of the pyridoxal 5'-phosphate and its implications for rare diseases involving B6-dependent enzymes. *Clin Biochem* 2014; 47(3): 158-65.
- [54] McLaurin AW, Beisel WR, McCormick GJ, Scalettar R, Herman RH. Primary hyperoxaluria. *Ann Intern Med* 1961; 55: 70-80.
- [55] Hoppe B, Latta K, von Schnakenburg C, Kemper MJ. Primary hyperoxaluria--the German experience. *Am J Nephrol* 2005; 25(3): 276-81.
- [56] Hoyer-Kuhn H, Kohbrok S, Volland R, *et al.* Vitamin b6 in primary hyperoxaluria I: first prospective trial after 40 years of practice. *Clin J Am Soc Nephrol* 2014; 9(3): 468-77.
- [57] Monico CG, Olson JB, Milliner DS. Implications of genotype and enzyme phenotype in pyridoxine response of patients with type I primary hyperoxaluria. *Am J Nephrol* 2005; 25(2): 183-8.
- [58] Clayton PT. B6-responsive disorders: a model of vitamin dependency. *J Inher Metab Dis* 2006; 29(2-3): 317-26.
- [59] Ames BN, Elson-Schwab I, Silver EA. High-dose vitamin therapy stimulates variant enzymes with decreased coenzyme binding affinity (increased K(m)): relevance to genetic disease and polymorphisms. *Am J Clin Nutr* 2002; 75(4): 616-58.
- [60] van der Hoeven SM, van Woerden CS, Groothoff JW. Primary hyperoxaluria type 1, a too often missed diagnosis and potentially treatable cause of end-stage renal disease in adults: results of the Dutch cohort. *Nephrol Dial Transplant* 2012; 27(10): 3855-62.
- [61] Behnam JT, Williams EL, Brink S, Rumsby G, Danpure CJ. Reconstruction of human hepatocyte glyoxylate metabolic pathways in stably transformed Chinese-hamster ovary cells. *Biochem J* 2006; 394(Pt 2): 409-16.
- [62] Fargue S, Rumsby G, Danpure CJ. Multiple mechanisms of action of pyridoxine in primary hyperoxaluria type I. *Biochim Biophys Acta* 2013; 1832(10): 1776-83.
- [63] Oppici E, Fargue S, Reid ES, *et al.* Pyridoxamine and pyridoxal are more effective than pyridoxine in rescuing folding-defective variants of human alanine:glyoxylate aminotransferase causing primary hyperoxaluria type I. *Hum Mol Genet* 2015; 24(19): 5500-11.
- [64] Yendt ER, Cohanin M. Response to a physiologic dose of pyridoxine in type I primary hyperoxaluria. *N Engl J Med* 1985; 312(15): 953-7.
- [65] di Salvo ML, Contestabile R, Safo MK. Vitamin B(6) salvage enzymes: mechanism, structure and regulation. *Biochim Biophys Acta* 2011; 1814(11): 1597-608.
- [66] Chetyrkin SV, Kim D, Belmont JM, Scheinman JI, Hudson BG, Voziyani PA. Pyridoxamine lowers kidney crystals in experimental hyperoxaluria: a potential therapy for primary hyperoxaluria. *Kidney Int* 2005; 67(1): 53-60.
- [67] Scheinman JI, Voziyani PA, Belmont JM, Chetyrkin SV, Kim D, Hudson BG. Pyridoxamine lowers oxalate excretion and kidney crystals in experimental hyperoxaluria: a potential therapy for primary hyperoxaluria. *Urol Res* 2005; 33(5): 368-71.
- [68] Degenhardt TP, Alderson NL, Arrington DD, *et al.* Pyridoxamine inhibits early renal disease and dyslipidemia in the streptozotocin-diabetic rat. *Kidney Int* 2002; 61(3): 939-50.
- [69] Williams ME, Bolton WK, Khalifah RG, Degenhardt TP, Schotzinger RJ, McGill JB. Effects of pyridoxamine in combined phase 2 studies of patients with type 1 and type 2 diabetes and overt nephropathy. *Am J Nephrol* 2007; 27(6): 605-14.
- [70] Ringe D, Petsko GA. What are pharmacological chaperones and why are they interesting? *J Biol* 2009; 8(9): 80.
- [71] Lumb MJ, Birdsey GM, Danpure CJ. Correction of an enzyme trafficking defect in hereditary kidney stone disease *in vitro*. *Biochem J* 2003; 374(Pt 1): 79-87.
- [72] Clausen T, Huber R, Messerschmidt A, Pohlenz HD, Laber B. Slow-binding inhibition of Escherichia coli cystathionine beta-lyase by L-aminoethoxyvinylglycine: a kinetic and X-ray study. *Biochemistry* 1997; 36(41): 12633-43.
- [73] John RA, Charteris A. The reaction of amino-oxyacetate with pyridoxal phosphate-dependent enzymes. *Biochem J* 1978; 171(3): 771-9.
- [74] Beeler T, Churchich JE. Reactivity of the phosphopyridoxal groups of cystathionase. *J Biol Chem* 1976; 251(17): 5267-71.
- [75] Coulter-Mackie MB, Lian Q. Consequences of missense mutations for dimerization and turnover of alanine:glyoxylate aminotransferase: study of a spectrum of mutations. *Mol Genet Metab* 2006; 89(4): 349-59.
- [76] Miyata N, Steffen J, Johnson ME, Fargue S, Danpure CJ, Koehler CM. Pharmacologic rescue of an enzyme-trafficking defect in primary hyperoxaluria I. *Proc Natl Acad Sci USA* 2014; 111(40): 14406-11.
- [77] Gamboa-Vujicic G, Emma DA, Liao SY, Fuchtnner C, Manetta A. Toxicity of the mitochondrial poison dequalinium chloride in a murine model system. *J Pharm Sci* 1993; 82(3): 231-5.



The novel R347g pathogenic mutation of aromatic amino acid decarboxylase provides additional molecular insights into enzyme catalysis and deficiency



Riccardo Montioli ^{a,1}, Alessandro Paiardini ^{b,1}, Manju A. Kurian ^{c,d}, Mirco Dindo ^a, Giada Rossignoli ^a, Simon J.R. Heales ^{e,f}, Simon Pope ^f, Carla Borri Voltattorni ^a, Mariarita Bertoldi ^{a,*}

^a Department of Neurosciences, Biomedicine and Movement, University of Verona, Verona, Italy

^b Department of Biology and Biotechnology "Charles Darwin", La Sapienza University of Roma, Roma, Italy

^c Developmental Neurosciences, UCL-Institute of Child Health, London, UK

^d Department of Neurology, Great Ormond Street Hospital, London, UK

^e Clinical Chemistry, Great Ormond Street Hospital, London, UK

^f Neurometabolic Unit, National Hospital of Neurology and Neurosurgery, UK

ARTICLE INFO

Article history:

Received 9 November 2015

Received in revised form 15 March 2016

Accepted 15 March 2016

Available online 17 March 2016

Keywords:

AADC deficiency

Aromatic amino acid decarboxylase

Pathogenic variant

Pyridoxal 5'-phosphate

ABSTRACT

We report here a clinical case of a patient with a novel mutation (Arg347 → Gly) in the gene encoding aromatic amino acid decarboxylase (AADC) that is associated with AADC deficiency. The variant R347G in the purified recombinant form exhibits, similarly to the pathogenic mutation R347Q previously studied, a 475-fold drop of k_{cat} compared to the wild-type enzyme. In attempting to unravel the reason(s) for this catalytic defect, we have carried out bioinformatics analyses of the crystal structure of AADC-carbidopa complex with the modelled catalytic loop (residues 328–339). Arg347 appears to interact with Phe103, as well as with both Leu333 and Asp345. We have then prepared and characterized the artificial F103L, R347K and D345A mutants. F103L, D345A and R347K exhibit about 13-, 97-, and 345-fold k_{cat} decrease compared to the wild-type AADC, respectively. However, unlike F103L, the R347G, R347K and R347Q mutants as well as the D345A variant appear to be more defective in catalysis than in protein folding. Moreover, the latter mutants, unlike the wild-type protein and the F103L variant, share a peculiar binding mode of dopa methyl ester consisting of formation of a quinonoid intermediate. This finding strongly suggests that their catalytic defects are mainly due to a misplacement of the substrate at the active site. Taken together, our results highlight the importance of the Arg347-Leu333-Asp345 hydrogen-bonds network in the catalysis of AADC and reveal the molecular basis for the pathogenicity of the variants R347. Following the above results, a therapeutic treatment for patients bearing the mutation R347G is proposed.

© 2016 Elsevier B.V. All rights reserved.

1. Introduction

Aromatic amino acid decarboxylase (AADC) deficiency is a rare autosomal recessive disorder (OMIM #608643) caused by the deficit of Dopa or aromatic amino acid decarboxylase (AADC), a pyridoxal 5'-phosphate (PLP) enzyme, which catalyses the conversion of L-Dopa and L-5-hydroxytryptophan to dopamine and serotonin, respectively. The main structural and functional properties of AADC have been recently reviewed

Abbreviations: PLP, pyridoxal 5'-phosphate; AADC, aromatic amino acid decarboxylase; HDC, histidine decarboxylase; DME, dopa methyl ester; ANS, 1,8-anilinonaphthalene sulfonic acid; PMP, pyridoxamine 5'-phosphate; $K_{D(PLP)}$, equilibrium dissociation constant for PLP; TNB, 2,4,6-trinitrobenzene-1-sulfonic acid.

* Corresponding author at: Department of Neurosciences, Biomedicine and Movement, Section of Biological Chemistry, University of Verona, Strada Le Grazie, 8, 37134 Verona, Italy.

E-mail address: mita.bertoldi@univr.it (M. Bertoldi).

¹ RM and AP contribute equally to this work.

[1]. In AADC deficiency, impaired enzyme activity is mainly due to point mutations in the AADC gene that lead to the synthesis of pathogenic variants. The most commonly reported symptoms of AADC deficiency include hypotonia, neurodevelopmental delay, oculogyric crises and complex movement disorder with autonomic features [2,3]. Studies of cerebrospinal fluid are key to diagnosis, showing reduced levels of 5-hydroxyindoleacetic acid and homovanillic acid together with elevated concentrations of L-Dopa, L-5-hydroxytryptophan and 3-O-methylDopa [4–6]. Diagnosis is confirmed by quantification of plasma AADC enzyme activity and AADC gene sequencing. To date, around 100 patients with homozygous or compound heterozygous mutations have been genotyped. Among them, 26 missense mutations have been identified, 18 of which are homozygous in the affected patients (<http://www.biopku.org/home/jake.asp>). Biochemical characterizations of the latter variants in the purified recombinant form of the enzyme, together with bioinformatics analyses, revealed that most of the examined variants displayed k_{cat} values linearly related to the magnitude of the near-UV CD signals and the ANS

emission fluorescence intensities [7]. These variants concern mutations of residues mapping to or interacting with loops 1 (aa 66–84), 2 (aa 100–110) and 3 (aa 323–357). Since the comparison of the crystal structure of the apo and holo forms of AADC highlights the relevance of these structural elements for the transition from the apo open form to the holo closed form [8], it was proposed that the pathogenicity of these mutations is due to incorrect apo-to-holo conversion [7]. The only exception is represented by the mutation R347Q which, although presenting no conformational alteration and maintaining a PLP binding affinity similar to that of the wild-type, exhibits severely decreased k_{cat} value [7]. To date, the reasons(s) for the loss of decarboxylase activity of this variant are unknown. Here we report a clinical case of a patient with a novel homozygous mutation, R347G, associated with AADC deficiency. This finding, together with the fact that the point mutation of Arg347 (to Gln or Gly) represents one of the most frequent pathogenic mutation and is present both in homozygous and in compound heterozygous states, urged us to undertake a detailed investigation on the molecular effects caused by the mutations of Arg347. The biochemical characterization of the variant R347G in the purified recombinant form reveals that it shares many structural and functional features with the variant R347Q. Thereafter we have explored by bioinformatics analyses the possible interactions of Arg347 in the crystal structure of the carbidopa-AADC complex in which the conformation of the mobile loop (residues 328–339), invisible in this structure, is modelled using the homologous region of histidine decarboxylase (HDC) as a template [9]. These studies, together with the biochemical characterization of the artificial mutants F103L, D345A, and R347K, allow us not only to identify the Arg347-Leu333-Asp345 triad as an important hydrogen bonds network for efficient catalysis of human AADC but also to unravel the molecular basis of the pathogenicity of the R347 mutations. Thus, our data provide potentially clinically translatable information for the therapy of patients harbouring pathogenic mutations at Arg347.

2. Materials and methods

2.1. Ascertainment of clinical case

Patient A was referred to a Tertiary Paediatric Neurology Centre with expertise in neurotransmitter disorders. Investigations and treatment strategies were investigated as part of routine clinical care.

2.2. Materials

PLP, L-Dopa, L-Dopa methyl ester (DME), 2,4,6-trinitrobenzene-1-sulfonic acid (TNB) and isopropyl-β-D-thiogalactopyranoside were purchased from Sigma-Aldrich. Protease inhibitor cocktail were purchased from Roche. The 1,8-anilinonaphtalene sulfonic acid (ANS) was purchased from Molecular Probes. The other chemicals were of the highest purity available.

2.3. Construction, expression and purification of the variants R347G, R347K, F103L and D345A

The R347G, R347K, F103L and D345A variants of AADC were constructed starting from the pDDChis construct that contains the complete open reading frame of the human AADC including a C-terminal 6xhistag and cloned into a pTrcHis2A expression vector [10]. Mutations were introduced by the QuikChange site-directed mutagenesis kit (Agilent Technologies) using the oligonucleotides 5'-CTGCATCG GCTTATCTGGGCGGCAAG-3' and its complement, 5'-GCTTATCACTGA CTACGGGCAATTGGCAG-3' and its complement, 5'-GGGCTTATCACTGA CTACAAGCATTGGCAG-3' and its complement, 5'-GGCTTATC ACTGCTACCGCATTGG-3' and its complement for F103L, R347G, R347K and D345A, respectively (the mutated codons are underlined). All the mutations were confirmed by the entire DNA sequence analysis. Expression plasmids of wild-type AADC [10], R347Q [7], F103L, R347G,

R347K and D345A variants were used to transform *Escherichia coli* JM109 cells. Recombinant enzymes were expressed and purified by following the procedure previously described [10], and stored at -20°C . The mutants yield after the standard purification was about 70% that of the wild-type enzyme. Protein concentrations were determined using the $\epsilon_{\text{M}} = 142,000 \text{ M}^{-1} \text{ cm}^{-1}$ at 280 nm and the PLP content of the enzymes was determined by releasing the coenzyme in the presence of 0.1 M NaOH and by using $\epsilon_{\text{M}} 6600 \text{ M}^{-1} \text{ cm}^{-1}$ at 388 nm [11]. The purified variants were homogeneous as indicated by a single band upon migration in SDS-PAGE with mobility identical to that of the wild-type protein.

2.4. Spectroscopic measurements

Absorption measurements of F103L, R347G, R347Q, R347K, and D345A were performed using a Jasco V-550 spectrophotometer at a protein concentration of 10 μM in the absence or in the presence of 300 μM DME. CD measurements were made with a Jasco J-710 spectropolarimeter at a protein concentration of 6 μM . ANS binding spectra were recorded using a FP Jasco spectrofluorimeter setting at 5 nm excitation and emission bandwidths, following excitation at 365 nm of 1 μM enzyme sample that was previously incubated in the presence of 15 μM ANS for 1 h at 25°C (in the dark) and in the presence of 20 μM PLP. All the spectroscopic measurements were carried out in 100 mM potassium phosphate buffer, pH 7.4, at 25°C .

2.5. Apoenzyme preparation and coenzyme binding affinity

Apoenzyme was prepared as described previously [10]. The equilibrium dissociation constant for PLP, $K_{\text{D(PLP)}}$, of the variants R347G, R347K, F103L, and D345A was determined by measuring the quenching of the intrinsic fluorescence of 0.15 μM apoenzyme in the presence of PLP at concentrations ranging from 0.01 to 20 μM in 100 mM potassium phosphate buffer, pH 7.4 and by fitting the data to the following equation

$$Y = Y_{\text{max}} \frac{[E]_t + [\text{PLP}]_t + K_{\text{D(PLP)}} - \sqrt{([E]_t + [\text{PLP}]_t + K_{\text{D(PLP)}})^2 - 4[E]_t[\text{PLP}]_t}}{2[E]_t}$$

where $[E]_t$ and $[\text{PLP}]_t$ represent the total concentrations of the enzyme and PLP, respectively, Y refers to the intrinsic quenching changes at a PLP concentration, $[\text{PLP}]$, and Y_{max} refers to the fluorescence changes when all enzyme molecules are complexed with coenzyme. Curves fitting was performed using Origin® 7.03 (OriginLab).

2.6. Enzyme activity assay

The decarboxylase activity of the AADC variants was measured by a spectrophotometric assay as previously described [12] and modified [13]. Briefly, after an appropriate incubation time (a time within which a linear product formation is observed) of the enzyme in the presence of 2 mM L-Dopa and 10 μM PLP in a final volume of 250 μl , the reaction is stopped by heating at 100°C for 1 min. Toluene (1.5 ml) and TNB (1 ml of a 4.3 mM solution) are then added, and the extraction of trinitrophenyldopamine is carried out at 42°C for 1 h with continuous shaking. The concentration of trinitrophenyldopamine in the toluene layer is measured by using $12,400 \text{ M}^{-1} \text{ cm}^{-1}$ as the molar extinction coefficient for trinitrophenyldopamine at 340 nm [14]. The kinetic parameters were determined by incubating the mutant recombinant proteins in the presence of different L-Dopa concentrations under saturating PLP concentration in 100 mM potassium phosphate buffer, pH 7.4. The concentrations of F103L, D345A, R347G, and R347K were 0.3 μM , 2 μM , 3 μM , and 5 μM , respectively, while the reaction times were 10 min for F103L and D345A, or 20 min for R347G and R347K. Data were fitted to the Michaelis–Menten equation.

2.7. HPLC analyses

Following incubation for 3 h in the presence of 300 μM DME in 100 mM potassium phosphate buffer, pH 7.4, at 25 °C, wild-type or variants AADC 10 μM were denatured by the addition of trichloroacetic acid to a final concentration of 5% (v/v). The quenched solutions were centrifuged to remove protein, and the supernatants were analysed by HPLC, using a Nucleodur 100–5 C18 (250 \times 4.6 mm) (Macherey-Nagel) column connected to a Jasco PU-2080 Plus HPLC control system. The eluent was 50 mM potassium phosphate buffer, pH 2.35, at a flow rate of 1 ml/min. A Jasco UV-2075 Plus detector set at 295 nm was employed. Peaks corresponding to PLP and pyridoxamine 5'-phosphate (PMP) were integrated using the Jasco Borwin software. Standard curves of peak area as a function of PLP or PMP concentration were prepared.

2.8. Atomic coordinates and modelling

Atomic coordinates were taken from the Protein Data Bank (PDB): the ID code 1JS3 was used for AADC complexed with carbidopa and ID code 4E1O for HDC [9,15]. The visualization of structures and contacts analyses were performed using the Molecular Operating Environment (MOE) software. Energy minimization refinement, applying the AMBER99 force field, and the protonation state correction were performed using MOE software. Missing or substituted atoms and loop residues in AADC, either native or mutant, were modelled using MODELLER 9.10 [16] and the solved HDC loop (residues 328–346) [9]. Structural superimpositions were conducted using PyMol [17].

3. Results and discussion

3.1. Identification of a new homozygous mutation of AADC causing AADC deficiency

Patient A, a male infant, was referred for further investigation of neurodevelopmental delay. Routine diagnostic testing revealed a raised prolactin level and a vanillyl lactate peak on urinary organic acids. A low homovanillic acid, low 5-hydroxyindoleacetic acid, raised 3-orthomethyl-dopa and 5-hydroxytryptophan were evident on cerebrospinal fluid neurotransmitter analysis. Plasma AADC enzyme activity was undetectable. Molecular genetic testing of AADC revealed a homozygous mutation, c.1039C > G (R347G) in the proband, with appropriate familial segregation. Pyridoxine and calcium folinate treatment were commenced initially, with some discernible clinical improvement in baseline tone and involuntary movements. Following this, the MAO inhibitor, Selegeline, was added and led to further clinical improvement. A latter addition of the dopamine agonist, Pramipexole, has led to ongoing benefits. Overall there has been reduction of the frequency and severity of the oculogyric crises as well as further neurodevelopmental gains with improvement in axial and peripheral tone.

3.2. Impact of the R347G mutation on the structure and function of AADC

The spectroscopic features of the R347G variant in the purified recombinant form were compared with the corresponding ones of the wild-type AADC. No differences were observed between the far-UV CD spectra of the mutated and the wild-type forms of the enzyme (data not shown), suggesting that the mutation does not affect the overall secondary structure of AADC. As shown in Fig. 1 and inset, the R347G variant exhibited in the visible region absorbance and positive dichroic bands at 420 and 335 nm whose intensities were similar to the corresponding ones of the wild-type AADC. The R347G variant had a $K_{\text{D(PLP)}}$ value ~ 4 -fold higher than that of the wild-type enzyme (Table 1). In order to evaluate the structural features of the mutated protein, near-UV CD spectra and ANS fluorescence spectra of this variant were monitored. When ANS binds to hydrophobic surfaces of proteins, it emits a fluorescence signal whose maximum wavelength (at around 450 nm)

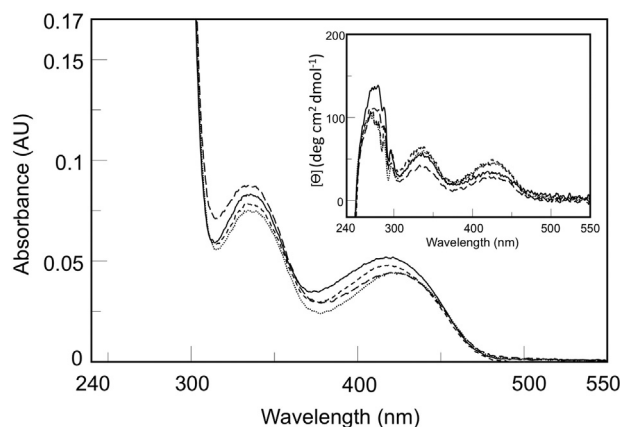


Fig. 1. Absorbance and CD spectra of wild-type AADC and variants. Absorption and CD (inset) spectra of (—) wild-type, (---) R347G, (···) R347K, (-·-) F103L, and (----) D345A at 10 μM enzyme concentration in 100 mM potassium phosphate buffer, pH 7.4.

is red-shifted and the intensity increases. The near-UV CD spectra of the holo and the apo forms of the R347G variant as well as the ANS emission spectra of the holo form revealed a modest decrease in the difference of the dichroic signals between the holo- and the apo- forms as well as a slight increase of the ANS emission intensity of the holo form (data not shown), in comparison to the wild-type enzyme. Thus, these data fit the linear relation depicted in Fig. 2A, suggesting that the R347G mutation has a modest impact on the apo-holo transition. To determine the functional effects of replacing Arg347 by Gly, the steady-state kinetic parameters of the R347G variant were measured and compared to those of the wild-type enzyme (Table 1). The variant exhibits a very large drop in its catalytic efficiency, ~ 2760 -fold, mainly driven by the ~ 475 -fold decrease of its k_{cat} value. Interestingly, the location of the R347G variant on the curve in Fig. 2B is similar to that of the R347Q variant, suggesting that both variants R347Q and R347G behave similarly in sharing a sharp decrease in the k_{cat} value (corresponding to a residual catalytic activity of 1.1% and 0.2%, respectively), despite no or only modest conformational alterations. Based on these results, we have decided to gain further insights into the catalytic relevance of the large and positively charged side chain of Arg347 by using bioinformatics analyses aiming to identify the possible interaction(s) between Arg347 and other AADC residues.

3.3. Bioinformatics analyses

The position and possible interactions of Arg347 were analysed, starting from the coordinate file of the pig kidney AADC in complex with carbidopa (PDB file 1JS3). Arg347 belongs to loop 3 and maps near the active site cavity in proximity of the 328–339 loop. This is a mobile segment, invisible in the electron density maps, that seems to be important for the catalytic mechanism [15,18]. Before inspecting the structure, the protonation state of the molecule was corrected to mimic the physiological condition, and the structure was refined by

Table 1
Kinetic parameters and coenzyme binding affinity.

Enzyme	k_{cat} (s^{-1})	K_{m} (mM)	$k_{\text{cat}}/K_{\text{m}}$ ($\text{s}^{-1} \text{mM}^{-1}$)	$K_{\text{D(PLP)}}$ (nM)
Wild-type ^a	7.6 ± 0.1	0.11 ± 0.01	69 ± 6	43 ± 12
R347Q ^b	0.087 ± 0.005	0.49 ± 0.08	0.18 ± 0.03	54 ± 10
R347G	0.016 ± 0.001	0.64 ± 0.13	0.025 ± 0.05	178 ± 14
R347K	0.022 ± 0.003	0.31 ± 0.01	0.071 ± 0.011	214 ± 12
F103L	0.55 ± 0.09	0.15 ± 0.01	3.67 ± 0.007	98 ± 18
D345A	0.078 ± 0.001	0.60 ± 0.03	0.13 ± 0.65	150 ± 20

^a Ref. [8].

^b Ref. [6].

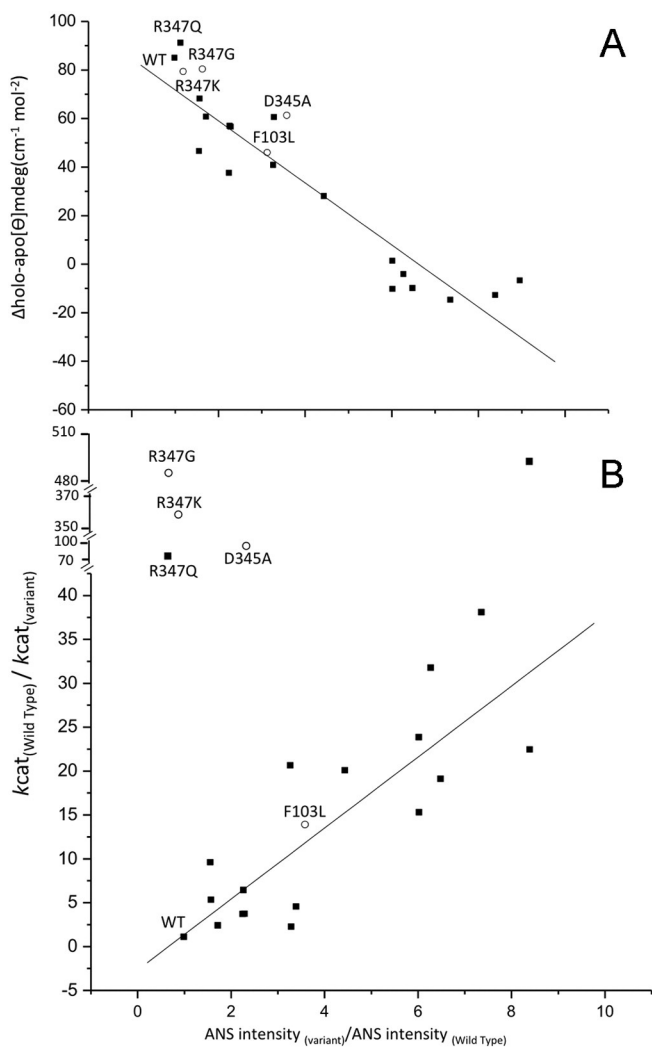


Fig. 2. Relationship between conformational and catalytic features of wild-type and variants. The position of wild-type AADC and variants R347G, R347Q, R347K, D345A and F103L are indicated. The solid symbol (■) represents positions of variants previously studied [7]. (A) Plot of difference of the magnitude of the near-UV dichroic signal of holo and the corresponding apo enzyme as a function of the ratio of ANS intensity of each variant and the wild-type, and (B) plot of the decrease of k_{cat} as a function of the increase of ANS intensity. The diagonal lines correspond to a linear fit, with R^2 values of -0.926 and 0.842 for (A) and (B), respectively.

energy minimization. As shown in Fig. 1 of SM, the side chain of Arg347 is predicted to form a hydrogen bond with the main chain oxygen of Phe103, an active site residue composing the hydrophobic cavity that hosts the substrate. The π system of Phe103 appears to be involved in the binding and orientation of the substrate as well as in stabilizing the position of the Tyr79 side chain [15]. Moreover, the proximity of Arg347 in the primary structure to the C-terminus of the loop (aa 328–339) missing in the structure, urged us to also explore the possible interaction(s) of this residue with those of the loop. Thus, we modelled the latter starting from the structure of AADC complexed with carbidopa, using the homologous region of HDC (PDB: 4E10; residues 328–346) as template [9]. The modelling results obtained are shown in Figs. 3 and Fig. 2 of SM. Two main interactions are engaged by Arg347: 1) the guanidine moiety is placed at hydrogen-bond distance from the main-chain oxygen atom of Leu333 (~ 3.1 Å), the latter residue being adjacent to Tyr332, which is involved in the decarboxylase activity [18]; 2) the second one takes place between Arg347 and Asp345 (~ 2.4 Å), which also interacts also with the imidazole ring of His335 (~ 3.1 Å; Fig. 3). Therefore, it is predicted that there is a network of interactions involving residues Asp345, Arg347, His335 and Leu333, the role

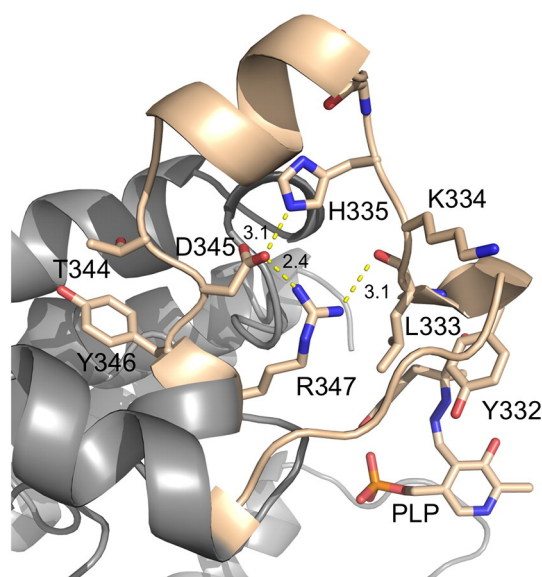


Fig. 3. Modelled mobile loop of human AADC (residues 326–346). The position of the loop (pink ribbons and sticks) is shown in the context of the AADC structure (grey ribbons). The predicted hydrogen bonds network involving Arg347, Asp345 and residues of the mobile loop (Leu333 and His335) is shown in yellow, together the relative distances (Å).

of which is probably to stabilize the closed conformation of the AADC catalytic loop. Similar interactions were also observed in the crystal structure of the close homologous human HDC (e.g., Asp345–His337; Fig. 2 of SM). However, in HDC the stabilization of residue Leu333 reasonably involves a hydrophobic interaction between its side-chain and Met347, which corresponds to Arg347 in human AADC. Since both interactions of Arg347 with Leu333 and Asp345 are missing in the R347G mutant, we have modelled the previously characterized pathogenic variant R347Q in an attempt to analyse the interactions of Gln347 with neighbouring residues. As shown in Fig. 4, the modelling study reveals that (i) the interaction (i.e., a hydrogen-bond) with Asp345 is still conserved, even if the minimum distance between the residues Gln347 and Asp345 (3.5 Å) is greater compared to the distance observed for the residues Arg347 and Asp345, and (ii) the interaction with Leu333 is completely lost, presumably leading to destabilization

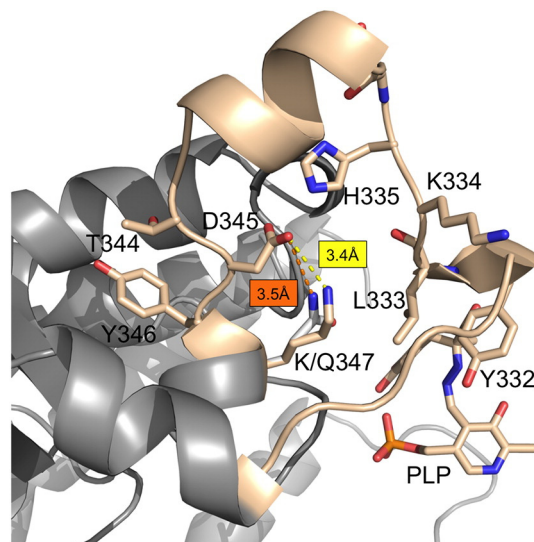


Fig. 4. Modelled R347Q and R347K mutants of human AADC. The position of the loop 326–346 (pink ribbons and sticks) is shown in the context of the dimeric AADC structure. Chain A is represented as grey ribbons. The distance (Å) between residues Gln/Lys347 and Asp345 is shown in yellow and orange, respectively.

of the catalytic loop. Therefore, we could reason that the Arg347–Leu333 interaction is pivotal for the proper positioning of the active site residue Tyr332 and that the lack of such interaction would result in impaired decarboxylase activity. We have also modelled an artificial R347K mutant that, according to our assumptions, was predicted to be engaged in a similar pattern of interactions as observed for the wild-type AADC. Interestingly, as shown in Fig. 4, the ϵ -amino group of Lys347 preserves the electrostatic interaction with Asp345 (3.4 Å), but, as in the case of the R347Q mutant, it loses the hydrogen-bond with the main-chain O atom of Leu333, leading us to suppose that such a mutant would also have exhibited a sharp decrease in catalytic activity similar to that observed for the mutants R347G and R347Q. Therefore, on the basis of all the above observations, we have prepared and characterized the F103L, D345A and R347K mutants.

3.4. Impact of the mutations F103L, D345A and R347K on the structural and functional properties of the wild-type AADC

The variants F103L, D345A, and R347K were expressed in *E. coli* and purified to homogeneity, as described in Methods section. A comparison of their far-UV CD spectra with that of the wild-type protein revealed superimposable features, indicating that substitution of Phe103, Asp345 or Arg347 for leucine, alanine or lysine, respectively, does not alter the secondary structure of the wild-type AADC, significantly (results not shown). The visible absorption and CD spectra of the variants F103L, D345A and R347K were similar to the corresponding spectra of wild-type AADC (Fig. 1 and inset). The $K_{D(PLP)}$ values of the variants F103L, D345A and R347K were ~ 2 -, ~ 3.5 -, and 5-fold, respectively, higher than the corresponding value of the wild-type enzyme (Table 1). Dichroic spectra in the near-UV region of both holo and apo form of the three variants together with the ANS fluorescence emission spectra of their holo forms were acquired and compared with the corresponding spectra of the wild-type protein. As shown in Fig. 2A, the plot of these data indicates that the examined mutations fit the linear correlation of the differences between the dichroic signals of holo and apo form against the ANS emission intensity of each holo mutant. The position of the F103L and D345A mutants on the curve is indicative of the meaningful impact of the mutations F103L and D345A on the apoholo transition, even if less pronounced than that of mutations of residues mapping to loop 1 (H70T, H72Y, Y79C, P81L) [8]. On the other hand, the finding that the position of the R347K in this curve is similar to that of the wild-type AADC, R347Q and R347G variants strongly suggests that the mutation R347K does not alter the tertiary structure of holo-AADC. In order to find out if the mutations under study have an impact on decarboxylase activity, the steady-state kinetic parameters of the variants were measured (Table 1). The k_{cat}/K_m of the variants F103L, D345A, and R347K was decreased by ~ 19 -, 530-, and 970-fold, respectively, in comparison with the wild-type AADC value. The decrease in catalytic efficiency is mainly driven by the decrease in k_{cat} (~ 14 -fold in F103L, ~ 97 -fold in D345A, and ~ 345 -fold in the case of R347K). When Phe103, belonging to the substrate binding pocket, and in van der Waals contact with the catecholic ring of carbidopa (a substrate analogue) [15], is substituted with a residue bearing an aliphatic side chain, there was a little change in the K_m value.

As shown in Fig. 2B, F103L fits the linear relation between the structural and catalytic changes already identified for other AADC variants [7]. This result, in line with the fact that Phe103 maps to loop 2, suggests that mispositioning of the aromatic ring of Phe103 due to the loss of the interaction with R347 could not explain the remarkable loss of catalytic activity of the R347 variants (Table 1). On the other hand, it is evident that D345A and R347K do not fit the linear relation, taking in the plot a location similar to that of the wild-type protein and the other R347 variants (Fig. 2B). In other words, the drop in catalytic activity of the variants R347Q, R347G, R347K and D345A is definitely more consistent than the change in their conformation. These findings are in line with the bioinformatics analyses prediction and strongly suggest that the

hydrogen bonds between Arg347 and both Asp345 and Leu333 are relevant for the catalytic mechanism of AADC. In this regard, it is of interest to note that both Arg347 and Asp345 residues are close to the dynamic catalytic loop (residues 328–339) of AADC, while Leu333 is in the middle of this loop. Previous spectroscopic and kinetic studies indicated that this catalytic loop undergoes a conformational change upon substrate binding, leading to a closure of the active site thereby achieving a conformational state that is productive for decarboxylation [19]. Indeed, site-directed mutagenesis has strongly suggested that Tyr332 performs the protonation of the C α atom of the quinonoid intermediate which is crucial for the decarboxylation pathway [18].

3.5. Binding mode of variants with DME

Based on the above-mentioned results and considerations, we have decided to analyse the effects of the mutations under study on the formation of the external aldimine. This is the first intermediate that forms upon covalent binding of the substrate to the formyl group of the cofactor in PLP-enzymes while exchanging internal with external Schiff base through a gem-diamine intermediate [20]. PLP reactivity has been widely studied for this family of enzymes and the generally accepted hypothesis is based on Dunathan's proposal, published in 1966, suggesting that PLP-enzymes employ stereoelectronic effects to control their reaction specificity [21]. Dunathan's hypothesis assumes that enzymes place the bond to be broken of the external aldimine parallel to the p-system. In this way the developing p orbital is aligned for maximal overlap with the extended p system, lowering the energy of the transition state and increasing the reaction rate. In decarboxylases, the C α -COO $^-$ should be found in the orthogonal position to the p-system and its rupture allows the generation of a carboanionic quinonoid intermediate which is further protonated at the C α leading to amine generation [22].

We have selected DME, a substrate analogue that contains an esterified carboxyl group and, therefore, is not susceptible to decarboxylation. For this reason, the AADC-DME complex appears to be a good model for studying the external aldimine intermediate. The absorption spectra upon addition of DME to the wild-type AADC and the variants under study have been registered up to 3 h, a time after which DME undergoes oxidation. As shown in Fig. 5, a prominent absorbance band centred at 398 nm, already attributed to the formation of the external aldimine, as well as a band at 325 nm characterize the complex of the wild-type enzyme or F103L with DME. This is similar to what was already seen for liver and kidney AADC [23,24]. On the contrary, we have noticed that DME added to R347G, R347Q, R347K, and D345A caused, in addition to the absorbance bands at 398 nm and 325 nm (the latter being more pronounced than for wild-type AADC and F103L), an absorbance band at 500 nm, typical of a quinonoid

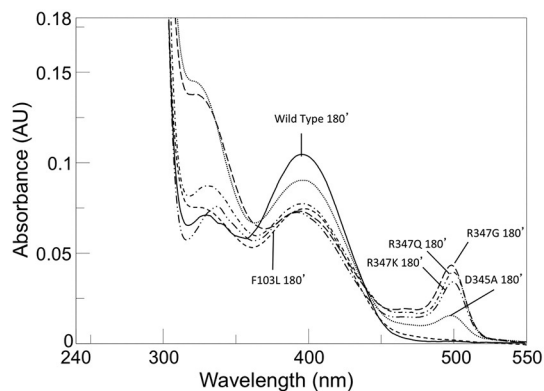


Fig. 5. Absorption spectra of the complex of wild-type and variants with DME. Absorption spectra of wild-type and variants (10 μ M) after 3 h of incubation with 300 μ M DME at 25 $^{\circ}$ C in 100 mM potassium phosphate buffer, pH 7.4.

intermediate. It was also observed that both 325 and 500 nm bands increased with time, concomitantly with the decrease of the 398 nm band. To determine if this reaction converts PLP into PMP or other coenzyme forms, aliquots were withdrawn after 3 h of incubation of the wild-type enzyme and the variants F103L, R347Q, or R347G or R347K or D345A with 300 μ M DME. These samples were then subjected to HPLC analysis after total denaturation. Interestingly, it was found that, while the original PLP content of the wild-type AADC and the mutant F103L remained unchanged, about 10–15% of the PLP of mutants R347Q, R347G, R347K and D345A was converted into PMP.

These results may indicate that the reaction in mutants R347Q, R347G, R347K and D345A does not stop at the step of external aldimine formation. Instead, the appearance of the quinonoid species at 500 nm and the production of PMP are consistent with the suggestion of DME binding at the active site of the variants in a conformation orienting the C α –H bond perpendicular to the plane of the cofactor system. In other words, such an event is indicative of a mispositioning of the external aldimine at the active site of these variants.

3.6. The structural and functional relevance of the Arg347-Leu333-Asp345 triad

Taken together, these results rule out the possibility that the lack of the interaction of Arg347 with the main chain oxygen of Phe103 could be responsible for decreased catalytic activity of the different R347 mutants. Rather, they point to a set of hydrogen bonds engaged by Arg347 with both Asp345 and Leu333 and its effect on the decarboxylase activity of the human AADC. As predicted by bioinformatics analyses, the disruption of both hydrogen bonds occurs upon mutation of Arg347 to Gly, while the disruption of one hydrogen bond takes place upon mutation of Arg347 to Gln or Lys or in mutant D345A. Since remarkable decreases in the k_{cat} (even if to different degree) is shared by all the tested R347 mutants and the D345 mutant, it is reasonable to suggest that the Arg347-Leu333-Asp345 hydrogen bonds network plays an important role in the catalysis of AADC. Moreover, the significant decrease in the k_{cat} values of R347G, R347Q, R347K, and D345A appears to be a consequence of an incorrect location of the external aldimine at their active site. These findings allow us to (i) indicate that Leu333, belonging to dynamic catalytic loop, and the Arg347 and Asp345 residues adjacent to it, are structural elements that impose important constraints on the alignment of the catalytic groups at the active site of the human AADC upon substrate binding, and (ii) offer an explanation for the molecular basis of the pathogenicity of the R347Q and R347G variants.

3.7. Therapeutic suggestions

Up to date, specific treatments guidelines are lacking for patients with AADC deficiency. Thus, a combination of pyridoxine, L-Dopa, MAO inhibitors and dopamine agonists is often administered in order to potentiate dopaminergic transmission. Like other diseases related to protein malfunctioning, an inherited mutation can be a catalytic and/or a folding mutation, thus altering protein function in different ways. For this reason, a detailed analysis into how missense mutations induce AADC deficit may provide a useful guidance for a proper therapeutic choice, and thereby improve clinical outcome. Only in the last three years studies performed using pathogenic AADC variants in the purified recombinant form have allowed identifying, at the protein and/or cellular level, their defects and, on these bases, stratify patients into different therapeutic categories [7,10,25]. Following this view, characterization of the variants R347Q and R347G provides the basis for delineate the most appropriate pharmacological therapy for patients bearing the pathogenic mutations of Arg347. The low k_{cat} value of the purified recombinant R347G strongly suggests that a dopamine agonist together with folinate could be the best way of assessing a good clinical response of patients bearing the R347G mutation. In fact, while the therapy with dopamine agonists could mime the dopamine effects, the one

with folinic acid could not allow its depletion due to the conversion of accumulated L-Dopa into 3-O-methylDopa. The same therapy strategy could be applied to patients harbouring the R347Q variant. However, in the case of mutation R347G, which, unlike R347Q, has a 4-fold $K_{\text{D(PLP)}}$ value higher than that of the wild-type, the supplementation of pyridoxine could also be useful. All these considerations seem to be consistent with the improvement observed following the treatment of patient A.

4. Conclusion

A clinical case of a patient bearing a novel mutation in AADC, R347G, associated with severe enzyme activity deficiency is reported. Similarly to the pathogenic R347Q variant previously studied [7], the R347G mutant appears to be defective in catalysis rather than protein folding. The reason(s) for the dramatic loss of decarboxylase activity caused by the substitution of Arg347 with either Gly (~475-fold) or Gln (~87-fold) were investigated. The *in silico* modelling of the missing loop 328–339 of AADC structure predicted interactions of Arg347 with Asp345 and Leu333. Structural and functional features of the new designed mutants, D345A and R347K in recombinant AADC, strongly suggested that residues Arg347, Asp345, and Leu333, as well as their mutual interaction, are structural elements relevant for a proper location/orientation of the substrate and/or of the catalytic groups at or near the active site. Altogether, our data highlight the molecular defects caused by the mutations of Arg347, and allow us to suggest a therapeutic management of patients bearing the mutation R347G.

Supplementary data to this article can be found online at <http://dx.doi.org/10.1016/j.bbapap.2016.03.011>.

Transparency document

The Transparency document associated with this article can be found, in online version.

Acknowledgments

We are grateful to Prof. Moshe Finel, University of Helsinki, for carefully proof-reading the manuscript and correcting English. We thank the AADC research Trust (UK) for the interest in our research. This work was supported by grants from AADC research Trust (to C.B.V.) and from the University of Verona, FUR2014 (to M.B.).

References

- [1] M. Bertoldi, Mammalian Dopa decarboxylase: structure, catalytic activity and inhibition, *Arch. Biochem. Biophys.* 546 (2014) 1–7.
- [2] L. Brun, L.H. Ngu, W.T. Keng, G.S. Ch'ng, Y.S. Choy, W.L. Hwu, W.T. Lee, M.A. Willemsen, M.M. Verbeek, T. Wassenberg, L. Regal, S. Orcesi, D. Tonducci, P. Accorsi, H. Testard, J.E. Abdenur, S. Tay, G.F. Allen, S. Heales, I. Kern, M. Kato, A. Burlina, C. Manegold, G.F. Hoffmann, N. Blau, Clinical and biochemical features of aromatic L-amino acid decarboxylase deficiency, *Neurology* 75 (2010) 64–71.
- [3] C. Manegold, G.F. Hoffmann, I. Degen, H. Ikonomidou, A. Knust, M.W. Laass, M. Pritsch, E. Wilichowski, F. Horster, Aromatic L-amino acid decarboxylase deficiency: clinical features, drug therapy and follow-up, *J. Inher. Metab. Dis.* 32 (2009) 371–380.
- [4] K. Hyland, P.T. Clayton, Aromatic amino acid decarboxylase deficiency in twins, *J. Inher. Metab. Dis.* 13 (1990) 301–304.
- [5] K.J. Swoboda, K. Hyland, D.S. Goldstein, K.C. Kuban, L.A. Arnold, C.S. Holmes, H.L. Levy, Clinical and therapeutic observations in aromatic L-amino acid decarboxylase deficiency, *Neurology* 53 (1999) 1205–1211.
- [6] G. Haliloglu, E. Vezir, L. Baydar, S. Onol, S. Sivri, T. Coskun, M. Topcu, When do we need to perform a diagnostic lumbar puncture for neurometabolic diseases? Positive yield and retrospective analysis from a tertiary center, *Turk. J. Pediatr.* 54 (2012) 52–58.
- [7] R. Montioli, M. Dindo, A. Giorgetti, S. Piccoli, B. Cellini, C.B. Voltattorni, A comprehensive picture of the mutations associated with aromatic amino acid decarboxylase deficiency: from molecular mechanisms to therapy implications, *Hum. Mol. Genet.* 23 (2014) 5429–5440.
- [8] G. Giardina, R. Montioli, S. Gianni, B. Cellini, A. Paiardini, C.B. Voltattorni, F. Cutruzzola, Open conformation of human DOPA decarboxylase reveals the

- mechanism of PLP addition to Group II decarboxylases, *Proc. Natl. Acad. Sci. U. S. A.* 108 (2011) 20514–20519.
- [9] H. Komori, Y. Nitta, H. Ueno, Y. Higuchi, Structural study reveals that Ser-354 determines substrate specificity on human histidine decarboxylase, *J. Biol. Chem.* 287 (2012) 29175–29183.
- [10] R. Montioli, B. Cellini, C. Borri Voltattorni, Molecular insights into the pathogenicity of variants associated with the aromatic amino acid decarboxylase deficiency, *J. Inher. Metab. Dis.* 34 (2011) 1213–1224.
- [11] E.A. Peterson, H.A. Sober, Preparation of crystalline phosphorylated derivatives of vitamin B6, *J. Am. Chem. Soc.* 76 (1954) 169–175.
- [12] A.F. Sherald, J.C. Sparrow, T.R. Wright, A spectrophotometric assay for *Drosophila* dopa decarboxylase, *Anal. Biochem.* 56 (1973) 300–305.
- [13] A. Charteris, R. John, An investigation of the assay of dopamine using trinitrobenzenesulphonic acid, *Anal. Biochem.* 66 (1975) 365–371.
- [14] C. Streffer, A method for determining aromatic amino acid decarboxylase, *Biochim. Biophys. Acta* 139 (1967) 193–195.
- [15] P. Burkhard, P. Dominici, C. Borri-Voltattorni, J.N. Jansonius, V.N. Malashkevich, Structural insight into Parkinson's disease treatment from drug-inhibited DOPA decarboxylase, *Nat. Struct. Biol.* 8 (2001) 963–967.
- [16] B. Webb, A. Sali, Comparative protein structure modeling using MODELLER, *Curr. Protoc. Bioinformatics* 47 (2014) (5 6 1–5 6 32).
- [17] E. Bramucci, A. Paiardini, F. Bossa, S. Pascarella, PyMod: sequence similarity searches, multiple sequence-structure alignments, and homology modeling within PyMOL, *BMC Bioinf.* 13 (Suppl. 4) (2012) S2.
- [18] M. Bertoldi, M. Gonsalvi, R. Contestabile, C.B. Voltattorni, Mutation of tyrosine 332 to phenylalanine converts dopa decarboxylase into a decarboxylation-dependent oxidative deaminase, *J. Biol. Chem.* 277 (2002) 36357–36362.
- [19] M. Bertoldi, P. Frigeri, M. Paci, C.B. Voltattorni, Reaction specificity of native and nicked 3,4-dihydroxyphenylalanine decarboxylase, *J. Biol. Chem.* 274 (1999) 5514–5521.
- [20] R.A. John, Pyridoxal phosphate-dependent enzymes, *Biochim. Biophys. Acta* 1248 (1995) 81–96.
- [21] H.C. Dunathan, Conformation and reaction specificity in pyridoxal phosphate enzymes, *Proc. Natl. Acad. Sci. U. S. A.* 55 (1966) 712–716.
- [22] M.D. Toney, Controlling reaction specificity in pyridoxal phosphate enzymes, *Biochim. Biophys. Acta* 1814 (2011) 1407–1418.
- [23] P.S. Moore, M. Bertoldi, P. Dominici, C. Borri Voltattorni, Aromatic amino acid methyl ester analogs form quinonoidal species with Dopa decarboxylase, *FEBS Lett.* 412 (1997) 245–248.
- [24] H. Hayashi, H. Mizuguchi, H. Kagamiyama, Rat liver aromatic L-amino acid decarboxylase: spectroscopic and kinetic analysis of the coenzyme and reaction intermediates, *Biochemistry* 32 (1993) 812–818.
- [25] R. Montioli, E. Oppici, B. Cellini, A. Roncador, M. Dindo, C.B. Voltattorni, S250F variant associated with aromatic amino acid decarboxylase deficiency: molecular defects and intracellular rescue by pyridoxine, *Hum. Mol. Genet.* 22 (2013) 1615–1624.



Research paper

Effects of interface mutations on the dimerization of alanine glyoxylate aminotransferase and implications in the mistargeting of the pathogenic variants F152I and I244T



Mirco Dindo ^a, Riccardo Montioli ^a, Mirko Busato ^b, Alejandro Giorgetti ^b, Barbara Cellini ^a, Carla Borri Voltattorni ^{a,*}

^a Department of Neurosciences, Biomedicine and Movement Sciences (Section of Biological Chemistry), University of Verona, Verona, Italy

^b Department of Biotechnology, University of Verona, Verona, Italy

ARTICLE INFO

Article history:

Received 2 August 2016

Received in revised form

2 October 2016

Accepted 2 October 2016

Available online 5 October 2016

Keywords:

Primary hyperoxaluria type 1

Human alanine glyoxylate aminotransferase

Interface hot spots

Protein dimerization

Molecular dynamics

Protein mistargeting

ABSTRACT

In this work the dimerization process of the minor allelic form of human alanine glyoxylate aminotransferase, a pyridoxal 5'-phosphate enzyme, was investigated. Bioinformatic analyses followed by site-directed mutagenesis, size exclusion chromatography and catalytic activity experiments allowed us to identify Arg118, Phe238 and Phe240 as interfacial residues not essential for transaminase activity but important for dimer-monomer dissociation. The apo and the holo forms of the triple mutant R118A-Mi/F238S-Mi/F240S-Mi display a dimer-monomer equilibrium dissociation constant value at least ~260- and 31-fold larger, respectively, than the corresponding ones of AGT-Mi. In the presence of PLP, the apomonomer of the triple mutant undergoes a biphasic process: the fast phase represents the formation of an inactive PLP-bound monomer, while the slow phase depicts the monomer-monomer association that parallels the regain of transaminase activity. The latter events occur with a rate constant of $-0.02 \mu\text{M}^{-1}\text{min}^{-1}$. In the absence of PLP, the apomonomer is also able to dimerize but with a rate constant value ~2700-fold lower. Thereafter, the possible interference with the dimerization process of AGT-Mi exerted by the mutated residues in the I244T-Mi and F152I-Mi variants associated with Primary Hyperoxaluria type 1 was investigated by molecular dynamics simulations. On the basis of the present and previous studies, a model for the dimerization process of AGT-Mi, I244T-Mi and F152I-Mi, which outlines the structural defects responsible for the complete or partial mistargeting of the pathogenic variants, was proposed and discussed.

© 2016 Elsevier B.V. and Société Française de Biochimie et Biologie Moléculaire (SFBBM). All rights reserved.

1. Introduction

Human liver peroxisomal alanine glyoxylate aminotransferase (AGT) (EC 2.6.1.44) catalyses the transamination of L-alanine and

glyoxylate to pyruvate and glycine, respectively, by a classical ping-pong mechanism. In the first half-reaction the enzyme in the pyridoxal 5'-phosphate (PLP) form (AGT-PLP) reacts with L-alanine generating pyruvate and the enzyme in the pyridoxamine 5'-phosphate form (AGT-PMP). Then, in the second half-reaction, AGT-PMP binds glyoxylate and converts it to glycine regenerating AGT-PLP [1]. Human AGT is a dimer and belongs to the Fold Type I class of the PLP-enzyme family [2]. The crystal structure reveals that each subunit is composed of an N-terminal extension (residues 1–21) that wraps over the surface of the other subunit, a large domain (residues 22–282) containing most of the active site residues and of the dimerization interface, and a small domain (residues 283–392) containing a peculiar KKL type 1 peroxisomal targeting sequence (PTS1) at the C-terminus [2]. A deficit of AGT causes Primary Hyperoxaluria Type I (PH1) (OMIM

Abbreviations: AGT-Mi, minor allele of human alanine glyoxylate aminotransferase; PH1, Primary Hyperoxaluria type I; PTS1, type 1 peroxisomal targeting sequence; $K_d(\text{dim-mon})$, dimer-monomer equilibrium dissociation constant; MD, molecular dynamics; ASA, solvent accessible area; $K_d(\text{PLP})$, equilibrium dissociation constant for PLP; SEC, size exclusion chromatography; DLS, dynamic light scattering; ANS, 8-anilino-1-naphthalenesulfonic acid; RMSD, root mean square deviation; RMSF, root mean square fluctuation; ED, essential dynamics.

* Corresponding author. Department of Neurosciences, Biomedicine and Movement Sciences (Section of Biological Chemistry), University of Verona, Strada Le Grazie, 8, Verona, Italy.

E-mail address: carla.borrivoltattorni@univr.it (C. Borri Voltattorni).

259900), a rare metabolic recessive disease due to inborn errors affecting the metabolism of glyoxylate in liver peroxisomes [3]. The AGXT gene encoding AGT is present in humans in two polymorphic forms: the most common major allele encoding AGT-Ma, and the less common minor allele encoding AGT-Mi. The latter differs from the major allele for the presence of a 74-bp duplication in intron 1 and of two mutations leading to the Pro11-to-Leu and Ile340-to-Met amino acid substitutions [4]. The P11L replacement generates a structural motif of binding to the mitochondrial import receptor TOM 20, and this could partly explain why AGT-Ma is 100% peroxisomal, while AGT-Mi is 95% peroxisomal and 5% mitochondrial. Moreover, as compared with AGT-Ma, AGT-Mi has a reduced (~70%) catalytic activity and, importantly, a reduced dimeric stability under chemical stress [5, 6]. Nevertheless, since the true value of the dimer-monomer equilibrium dissociation constant ($K_{d(\text{dim-mon})}$) for both AGT-Ma and AGT-Mi is only assumed to be lower than 0.3 μM [5], it is not possible to establish if the mutations P11L and/or I340M alter the dimer-monomer dissociation under native conditions. The AGT-Mi polymorphism is not pathogenic *per se*, but many mutations are pathogenic only when they functionally synergize with the minor allele. Some of them, like G170R, F152I, I224T, G47R and G41R cause a complete or partial aberrant targeting of AGT to mitochondria, thus resulting in a hampering of the metabolic function. Fargue et al. [7] advanced the possibility that all PH1-causing mutations segregating with the minor allele synergize with the P11L mutation unmasking the cryptic mitochondrial targeting sequence, and, as a consequence, leading to peroxisome-to-mitochondrion mistargeting. However, it should be noted that, when transiently expressed in CHO cells, the G16I variants co-segregating with the minor allele were found as cytosolic aggregates [8]. Again, it was reported that (i) the G41R-Mi shows a complex picture, some mitochondrial labelling and some peroxisomal in the shape of intraperoxisomal aggregates [9], and (ii) G47R-Mi shows a peroxisomal and mitochondrial localization [10]. Moreover, the structural basis of the suggested synergic interaction of P11L with each mutation leading to mistargeting is far from being elucidated. Since AGT in the monomeric form and containing the P11L mutation is a prerequisite for the aberrant targeting of the enzyme, we decided to study the associative/dissociative process of AGT-Mi in the apo and holo forms. Up to date, the self-association of the subunits of AGT including the structural elements which contribute to dimer formation is unknown. It was only demonstrated that the deletion of the N-terminal extension does not prevent AGT dimer formation [11], and it was suggested the involvement of the P11L mutation in the destabilization of the dimeric structure of AGT [5, 11].

In this work, guided by bioinformatic information, a series of single, double, and triple mutants was engineered and analyzed for their catalytic activity, spectroscopic features, and quaternary structure. Taken together, our studies allowed us to identify Arg118 as a hotspot dimer interfacial residue playing a relevant role in the dimerization process of AGT-Mi. Moreover, we noticed that the combination of R118A mutation with F238S and F240S mutations significantly alter the extent of monomerization of both apo and holoAGT-Mi. Starting from the folded apomonomer of the triple mutant the process of dimerization was investigated. We established that in the presence of PLP the formation of a PLP-bound monomer precedes the generation of the holodimer, which parallels the regain of transaminase activity. These events occur with a rate constant of $0.020 \pm 0.002 \mu\text{M}^{-1}\text{min}^{-1}$. The apomonomer, in the absence of exogenous PLP, is also able to dimerize even if with a rate constant 2700-fold lower than that of the PLP-bound monomer. In addition, predictions by means of

molecular dynamics (MD) simulations of the structural effects caused by the mutations F152I and I244T on the minor allele provide a possible interpretation and explanation for their interference with the dimerization process.

2. Materials and methods

2.1. Materials

PLP, L-alanine, NADH, rabbit muscle L-lactic dehydrogenase, and isopropyl- β -D-thiogalactopyranoside (IPTG) were obtained from Sigma. 8-anilino-1-naphthalenesulfonic acid (ANS) was purchased from Molecular Probes. All other chemicals were of the highest grade commercially available.

2.2. Bioinformatic analyses

Alanine scanning mutagenesis, analysis of the interfacial hydrophobic patches and inspection of the AGT structure and interface contacts were performed by the software Molecular Operating Environment (MOE 2015.1001) [12] of the Chemical Computing Group using the crystal structure of human AGT (pdb file: 1H0C). The dimeric structure of human AGT was obtained by means of the PISA web server [13] starting from the available coordinate file of the monomer (PDB id: 1H0C) [2]. In particular, each residue present on the dimerization interface involved in either intrachain or interchain contacts was subjected to alanine scanning mutagenesis using the Unary Quadratic Optimization (UQO) under the LowMode ensemble, which uses the LowModeMD [14] to search the conformational space of the mutants. The conformations that satisfied the required energetic and geometric criteria were saved to the output database. Atoms located at a distance greater than 4.5 Å from the mutation site were marked as inert, iterations were limited to 50, and conformations were limited to ten for each mutated complex. The dStability values (kcal/mol) were calculated with MOE 2015.1001 [12].

2.3. Site-directed mutagenesis

The mutant forms of human AGT-Mi were constructed by the QuikChange™ II kit from Agilent Technologies using the pTrcHis2A vector encoding AGT-Mi (pAGT-His) [1] as template and the oligonucleotides listed in the [Supplementary Table S1](#).

2.4. Expression and purification of AGT-Mi and mutants

E. coli JM109 cells transformed with vectors encoding AGT-Mi or mutated AGT-Mi were grown in 4.5 l of Luria broth at 37 °C to an absorbance at 600 nm of 0.4–0.6. Expression was induced after 6 h with 0.1 mM IPTG for 15 h at 30 °C. Cells were harvested and resuspended in 20 mM sodium phosphate buffer pH 7.4, containing 0.5 M NaCl, 20 mM imidazole and 100 μM PLP. Lysozyme was added to a final concentration of 0.2 $\mu\text{g}/\text{ml}$ and the culture was incubated for 15 min at room temperature. After a freeze-thaw, leupetin (0.5 $\mu\text{g}/\text{ml}$) and pepstatin (0.5 $\mu\text{g}/\text{mL}$) were added and the suspension was centrifuged at 30,000 g for 30 min at 4 °C. The lysate was loaded on a HisPrep FF 16/10 equilibrated with 20 mM sodium phosphate buffer pH 7.4 containing 0.5 M NaCl and 20 mM imidazole. A linear gradient was then applied (0–100% in 240 ml) with the same buffer containing 500 mM imidazole. AGT-Mi and mutants elute between 200 and 300 mM imidazole. After addition of 100 μM PLP, the protein solution was concentrated; imidazole and unbound coenzyme were removed by extensive washing with 100 mM potassium phosphate buffer, pH 7.4, using Amicon Ultra 10 concentrators (Amicon). The protein concentration in the AGT-Mi and mutants samples in the dimeric form was determined using

an extinction coefficient of $9.54 \times 10^4 \text{ M}^{-1} \text{ cm}^{-1}$ at 280 nm [15]. The molar extinction coefficient for the monomeric form of AGT-Mi at 280 nm was determined as described by Pace et al. [16] and was $4.61 \times 10^4 \text{ M}^{-1} \text{ cm}^{-1}$. The PLP content of AGT-Mi and mutant enzymes was determined by releasing the coenzyme in 0.1 M NaOH

dimer) subjected to SEC. The concentration of monomer and dimer was determined by integration the area under the curve and expressed as percent of total area of all protein-related peaks.

According to Manning et al. [17] the $K_{d(\text{dim-mon})}$ value was determined by the following equation:

$$\%D = \left[(8[E] + K_{d(\text{dim-mon})}) - K_{d(\text{dim-mon})}^2 + 16K_{d(\text{dim-mon})}[E]^{\frac{1}{2}} \right] / 0.08[E] \quad (2)$$

and by using an $\epsilon = 6600 \text{ M}^{-1} \text{ cm}^{-1}$ at 388 nm. The apo form of AGT-Mi and mutants were prepared as indicated by Cellini et al. [1].

2.5. Enzymatic activity assays

The kinetic parameters for the overall transamination of the L-alanine/glyoxylate pair of AGT-Mi and mutants was measured in presence of saturating PLP (100 μM) at an enzyme concentration ranging from 0.1 μM to 20 μM . Each species was incubated in the presence of various substrate concentrations at a fixed co-substrate concentration, at 25 °C in 0.1 M potassium phosphate buffer, pH 7.4. The reaction was stopped after 10 min by adding TCA 10% (v/v). The produced pyruvate was measured by a spectrophotometric assay using the coupled lactate dehydrogenase system [1].

2.6. Binding affinity of apomonomer for the PLP cofactor ($K_{d(\text{PLP})}$)

$K_{d(\text{PLP})}$ of the dimeric forms of 0.3 μM AGT-Mi, R118A-Mi, F238S-Mi and F240S-Mi and of monomeric form of 1 μM R118A-Mi/F238S-Mi/F240S-Mi was determined by measuring changes in the ellipticity at 424 nm in 50 mM potassium phosphate buffer, pH 7.4, in the presence of PLP concentrations ranging from 1 to 10 μM for AGT-Mi and the single mutants and from 1 to 50 μM for the triple mutant. The $K_{d(\text{PLP})}$ value was obtained using the following equation:

$$Y = \frac{[E]_t + [\text{PLP}]_t + K_{d(\text{PLP})} - \sqrt{([E]_t + [\text{PLP}]_t + K_{d(\text{PLP})}^2) - 4[E]_t[\text{PLP}]_t}}{2[E]_t} \quad (1)$$

where $[E]_t$ and $[\text{PLP}]_t$ represent the total concentrations of the enzyme expressed as monomer and of PLP, respectively, Y refers to the 424 nm dichroic signal change at the PLP concentration $[\text{PLP}]_t$, and Y_{max} refers to the changes when the total enzyme molecules are complexed with the coenzyme.

2.7. Size exclusion chromatography (SEC)

It has been used to analyze the amount of monomer and dimer present in the protein samples. Analysis was performed on an Akta FPLC system (GE Healthcare) using the Unicorn 5.01 (GE Healthcare) software and a Superdex 200 10/300 GL column at room temperature. The injection volume was 100 μl , the flow rate 0.5 ml/min, and the detection at 280 nm. The mobile phase was 50 mM potassium phosphate buffer, pH 7.4, containing 100 μM PLP. To determine the dimer-monomer equilibrium dissociation constant ($K_{d(\text{dim-mon})}$), a stock solution of enzyme in the apo or holo form was dissolved in 50 mM potassium phosphate buffer at pH 7.4 at different concentrations, and after overnight incubation at 25 °C (a sufficient time to reach the equilibrium between monomer and

where %D is the percentage of dimer to total enzyme, and $[E]$ represents the total enzyme concentration in dimer equivalents. A plot of $\log[\%D/0.04(100 - \%D)^2]$ with respect to $\log[E]$ yields a straight line of slope 1. When $\log[\%D/0.04(100 - \%D)^2] = 1$, $K_{d(\text{dim-mon})} = [E]$.

2.8. Kinetic of dimerization of triple variant

The time course of dimerization $2M \rightarrow D$ induced by exogenous PLP has been fitted to a simple second-order kinetics

$$[D] = \frac{[D]_{\text{eq}}[E]k_{\text{ass}}t}{1 + [E]k_{\text{ass}}t} \quad (3)$$

where $[D]$ and $[D]_{\text{eq}}$ represent the dimer concentrations at time t and at equilibrium, respectively, $[E]$ the enzyme concentration expressed as dimer, and k_{ass} the association rate constant. The equation was derived under the assumption that the reaction of dimerization is irreversible. Although this is never true, at conditions where k_{ass} is $\gg k_{\text{diss}}$ this assumption is valid and will not significantly alter the determined k_{ass} . Eq. (3) has also been used to fit the data of regain of enzyme activity and change in CD signal at 424 nm as a function of time.

On the other hand, to determine the k_{ass} of the reversible association of the apo form, the k_{obs} of dimerization was calculated at different protein concentrations by the linear fit of the decrement of monomer concentration ($1/[M]$) versus time. k_{obs} values as a function of protein concentration were fit to a line whose slope gives the k_{ass} value.

2.9. Spectroscopic measurements

Absorption measurements were made with a Jasco V-550 spectrophotometer. Fluorescence spectra were taken with a Jasco FP-750 spectrofluorometer using 5 nm excitation and emission bandwidths. CD spectra were obtained using a Jasco J-710 spectropolarimeter with a thermostatically controlled compartment at 25 °C. In the near-UV and visible spectra, the protein concentration varied from 1 to 20 μM in a cuvette with a path length of 1 cm. Far-UV measurements were taken at a protein concentration of 0.1 mg/ml using a cuvette with a path length of 0.1 cm. Secondary structure content was calculated from far-UV CD spectra using the "CD deconvolution" software. The thermal unfolding of AGT-Mi and variants was monitored by CD at 222 nm at a concentration of 1 μM in 100 mM potassium phosphate buffer, pH 7.4 with temperature increasing of 0.5 °C/min from 25 to 90 °C. CD signals were fitted either to two or three state unfolding mode using Origin Pro7 software according to the method of Pace [18].

2.10. Dynamic light scattering (DLS) measurements

DLS measurements were made on a Zetasizer Nano S device from Malvern Instruments. The temperature of sample cell was controlled by a thermostating system within ± 0.1 °C and 12.5×45 mm disposable cells with stopper were used. To study the aggregation kinetics, an aliquot of each enzymatic species was diluted to a final concentration of 4 μ M in potassium phosphate buffer 50 mM pH 7.4 at 25 °C. The buffer was filtered immediately before use to eliminate any impurities.

2.11. MD simulations

All MD simulations were carried out by using the software GROMACS 4.5.5 [19]. GROMOS 53A6 united atom force field [20] and the explicit simple point charge (spc/e) water model [21] were used for the simulations. The dimeric structure of human AGT was obtained by means of the PISA web server starting from the available coordinate file of the monomer (PDB id: 1H0C). In the original structure, loop residues 120–123 are missing, so the latter were modelled by a loop modelling script of the Modeller software [22]. We modelled AGT-Mi by introducing the P11L and I340M mutations in the AGT protein using the Chimera software [23]. The latter was also used to introduce the F152I and I244T mutations on AGT-Mi. The molecular topology and atoms parameters for PLP covalently bound to lysine 209 were taken from ATB [24, 25]. The systems were simulated in a triclinic water box, and the minimum distance between any atom of the protein and the box wall was set up to 1.0 nm. The systems were neutralized by adding Na^+ and Cl^- ions using the genion program of the GROMACS 4.5.5 package [19]. Each system was energy minimized in four phases. In the first two phases, 800 steps of steepest descent algorithm followed by 3000 steps of conjugate gradient were performed to gently relax the water molecule around the protein, which was constrained imposing harmonic position restraints of $1000 \text{ kJ mol}^{-1} \text{ nm}^{-2}$. In the third and in fourth phases, the protocol was repeated without using any constraint. Subsequently the minimizations steps, the systems were equilibrated in four steps. In the first stage, the systems were slowly heated up from 0 K to 300 K in 1 ns at 1 atm, followed by two stages of equilibration in isothermal-isobaric (NPT) conditions for 600 ps, in which positional constraints were applied on the solute atoms (force constant of $1000 \text{ J mol}^{-1} \text{ nm}^{-2}$). In the last stage, a 400 ps unrestrained MD simulation was performed at 300 K and 1 atm to assess the stability of the systems. The temperature and pressure were regulated by a Berendsen thermostat and barostat, respectively [26]. The LINCS algorithm [27] was used to constrain all bonds involving hydrogen atoms and the time step was set to 2 fs. Periodic boundary conditions (PBC) were applied. The particle mesh Ewald method (PME) [28] with a cut-off length of 1 nm was used to treat long-range electrostatic interactions, and the same cut-off length was adopted for van der Waals interactions. Finally, all monomer systems were simulated for 170 ns while dimer systems were simulated for 200 ns. For the dimer systems, we decided to carry out longer MD simulations (ca. 200 ns) because the equilibrium state of the two dimer systems was reached at ca. 110 ns. To sum up, the AGT-Mi protein was simulated, in all its mutated forms, totalizing ca. 740 ns of simulation time. For the production runs, a Nosè-Hoover thermostat [29, 30] at 300 K and an Andersen-Parrinello-Rahman barostat [31, 32], at 1 atm were used. The trajectories were analyzed using the standard GROMACS tools. The root mean square deviations (RMSD) and the root mean square fluctuations (RMSF) were performed through GROMACS inbuilt tools. RMSD plots for the AGT-Mi and F152I-Mi mutant were calculated without considering 4–23 region, which it is extremely flexible in the monomeric form and introduces artifacts to RMSD

analysis. Cutoff of 4 Å between N–O atom pairs as a definition of salt bridge formation between Arg118 and Asp243 was used [33]. All the graphical displays were generated using XMGrace program. The molecular graphics shown in this work were created using UCSF Chimera [23].

2.12. Essential dynamics (ED)

ED was performed for AGT-Mi and F152I-Mi MD simulations according to principal component analysis (PCA). ED is a standard technique able to highlight the dominant motions of the investigated systems [34–37]. The principal components (PCs), also called eigenvectors, were calculated by using ED and represent the protein's collective motions. Here, the first eigenvector, that accounts for ca. 50% of the total motions accomplished by the system, was used to understand the dynamical differences between the AGT-Mi and the F152I-Mi systems. Therefore, RMSF along the first eigenvector for the AGT-Mi and F152I-Mi (Fig. S3) were calculated. Covariance matrix was calculated using $\text{C}\alpha$ atoms and the matrix was diagonalized. The PCs were extracted from the covariance matrix. PCA was performed in three steps: i) the covariance matrix was calculated using the $\text{C}\alpha$ atoms; ii) the matrix was diagonalized and iii) a set of eigenvectors and eigenvalues were extracted from the covariance matrix. The eigenvectors correspond to a direction in the multidimensional space while the eigenvalues express the amplitude of the motion of each eigenvectors. PCA was carried out by using the standard GROMACS tool i.e. `g_covar` and `g_anaeig`.

3. Results

3.1. Identification of interface hot-spots

Homodimeric AGT-Mi shows a large monomer-monomer interface (Fig. 1A and B) in comparison with other PLP dependent enzymes. In fact, 48% of the total solvent accessible area (ASA) of the protein is buried upon dimerization. Such surface comprises 110 residues per subunit, many of which are directly involved in inter-chain contacts. In particular, 15 hydrophobic patches, 40 interchain hydrogen bonds and two salt bridges contribute to the monomer-monomer interaction.

Considering the high number and the different type of inter-chain contacts as well as their wide distribution, the identification of possible dimerization hot spot/s could be difficult. Thus, to identify residues or clusters of residues that mainly contribute to the binding free energy at the AGT-Mi dimerization interface, we performed an *in silico* alanine-scanning mutagenesis on the interfacial residues [38–40] using the Molecular Operating Environment software by Chemical Computing Group [12]. In order to find out residues whose substitution should have a minimal impact on the monomer stability, the analysis was carried out on both the dimeric and monomeric AGT-Mi structure.

As shown in Fig. 2, the dStability, representing the relative thermostability of each mutant with respect to AGT-Mi, indicates that among the 15 residues predicted to play a role in stabilizing the dimeric structure (black bars), only Arg118, Phe238 and Phe240 do not significantly change the intrinsic stability of monomeric AGT (red bars). The crystal structure of AGT reveals that these residues are not involved in the binding of the coenzyme and/or the substrate. Such requirements are essential to avoid possible functional effects of the residues substitution. Arg118 forms with Asp243 of the neighbouring chain the unique salt bridge present at the AGT-Mi interface (Fig. 3A). The *in silico* mutagenesis analysis suggests that the R118A substitution could weaken the dimer interface without substantially affecting the monomer structure. Phe238 is engaged in hydrophobic interaction with the same residue of the

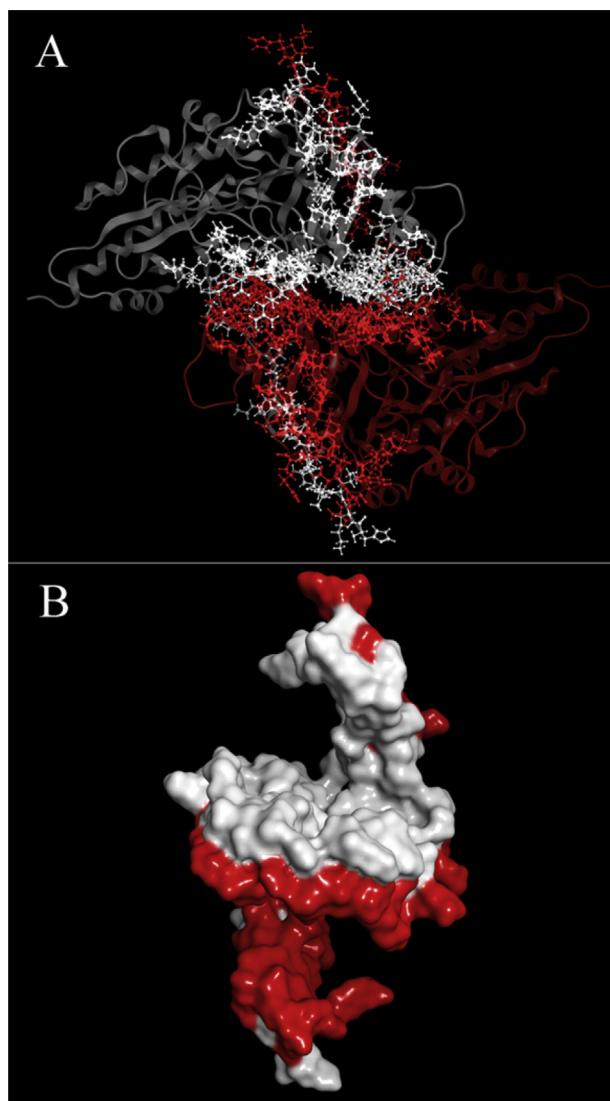


Fig. 1. Representation of the AGT dimer interface. Panel A: structure of AGT highlighting as sticks the interface residues. Panel B: surface representation of the AGT interface residues. The two monomers are coloured red and white.

other subunit, while Phe240 not only interacts with Trp246 of the same subunit but also with Ile115, and possibly with His83, of the adjacent monomer. Thus, unlike R118A and F240S, the F238S mutation could result in only one change at the interface of AGT-Mi. The role of Phe238 and Phe240 in the AGT dimerization was also investigated by the Protein Patch Analyzer tool of MOE 2015. The hydrophobic patches on the dimerization interface of AGT-Mi were ordered from 1 to 15 in the output list on the basis of a decreasing solvent-accessible surface area of the patch (\AA^2). Only patches enumerated as 1, 10, 13 and 14 are shown in Fig. 3B because they are involved in the formation of the main hydrophobic interactions at the dimer interface. In particular, Phe238 (patch 13) and Phe240 (patch 1) are predicted to critically contribute to the hydrophobicity of the interface because both residues show a high ASA value when they become exposed to the solvent upon monomerization. Hydrophobic residues, in particular phenylalanine, tryptophan and isoleucine, and the interactions in which they are involved are critical for stabilizing the core of proteins, native oligomeric assemblies, and aberrant assemblies leading to aggregation [41, 42]. On the basis of these data and observations, the substitution of

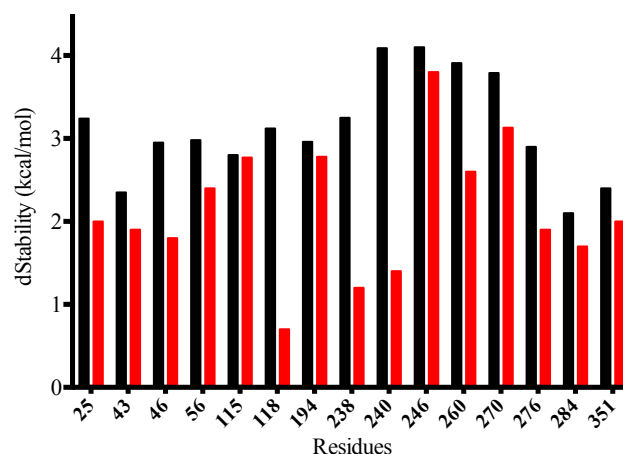


Fig. 2. Plot of the alanine scanning mutagenesis results either on the monomer (red bars) and dimer (black bars) of AGT expressed as dStability (kcal/mol) of each interfacial residue. The dStability (kcal/mol) represents the relative thermostability of each mutant with respect to AGT-Mi. Only residues with a positive value of dStability ≥ 2 kcal/mol are shown.

Phe238 and Phe240 with serine residues could weaken the dimer interface and also enhance the solubility of the monomer.

3.2. Effect of the mutations R118A, F238S and F240S on the structural and functional properties of AGT-Mi

On the basis of the above computational analysis, the construction, expression, purification and characterization of the mutants R118A-Mi, F238S-Mi, and F240S-Mi were first undertaken. Absorbance and CD spectra of the mutants in the visible region are similar to the corresponding ones of AGT-Mi, even if a more pronounced absorbance in the 340 nm region for R118A-Mi and F238S-Mi and a 5-nm blue shift of the 424 nm dichroic band for F240S-Mi are observed (Fig. S1). As shown in Table 1, the mutations R118A, F238S and F240S do not significantly alter the $K_{d(\text{PLP})}$ value of AGT-Mi. The impact of these single mutations on the AGT-Mi dimeric structure was also investigated by SEC at different enzyme concentrations. Analyses of the SEC experiments of R118A-Mi indicate that the holo form elutes as a peak whose elution volume corresponds to that of a dimer and whose total area does not change up to 0.3 μM , while the apo form exhibits a different elution profile consisting in three peaks whose elution volumes correspond to a dimer, a monomer and aggregates at high molecular weight. The integrated area of the dimer decreases and concomitantly that of the monomer and aggregates increases as the enzyme concentration decreases from 10 to 1.25 μM . These data strongly indicate that the apomonomer form is prone to aggregation. The formation of aggregates in this enzymatic species is supported by DLS measurements. The apo form of R118A-Mi at 5 μM concentration exhibits an increase in count rate, typical of a fast aggregation with the count rate stabilizing after about 12 min (data not shown). In an attempt to increase the solubility of the apomonomer R118A-Mi, SEC experiments were carried out in the presence of 10% glycerol. The elution profile, under these experimental conditions, shows that the proportion of the apo monomer increases at the expense of the dimer as the overall enzyme concentration is lowered from 18 to 1 μM . This indicates a slow equilibrium process. A plot of the percent dimer as a function of apoR118A-Mi concentration gives a hyperbolic curve whose linear transformation yields a $K_{d(\text{dim-mon})}$ value of $9.3 \pm 0.1 \mu\text{M}$ (Eq. (2)) (Table S2), a value at least 30-fold higher than that of apoAGT-Mi. The finding that, like AGT-Mi, both apo and holo forms of the mutants F238S-Mi and F240S-Mi

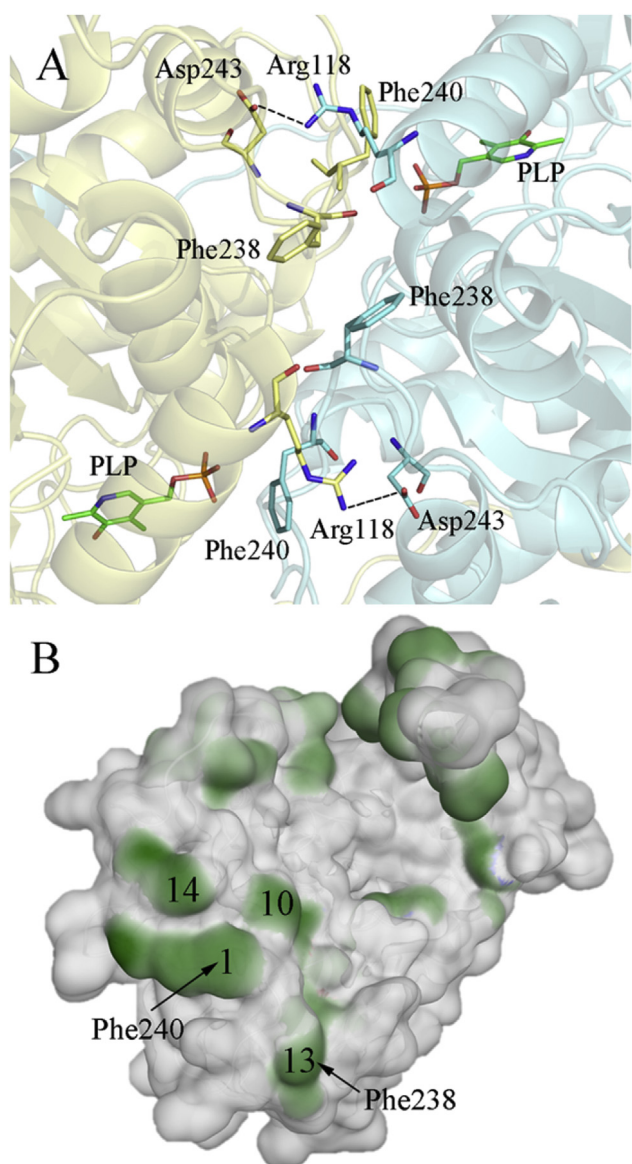


Fig. 3. The main interface hot spot and hydrophobic patches along the dimerization interface. Panel A: Detail of the main interface hotspot. The labelled residues are shown as yellow or cyan sticks on the basis of the colour of the belonging subunit. PLP is shown as green sticks. Panel B: interfacial hydrophobic patches of an AGT monomer shown as green areas on the grey background of AGT. The size and the energy cut-offs of each patch are 75 \AA^2 and 0.25 kcal/mol , respectively.

maintain the dimeric structure up to $0.3 \text{ }\mu\text{M}$ indicates that it is not possible to establish if Phe238 or Phe240 play a role in the dimer formation of AGT-Mi. The steady-state kinetic parameters of the

three mutants were also determined (Table 1). F238S-Mi shows a k_{cat} value comparable to that of AGT-Mi, while R118A-Mi and F240S-Mi display k_{cat} values approximately half that of AGT-Mi. The decrease in k_{cat} of the latter variants could suggest that, although both Arg118 and Phe240 are residues located far from the active site, they are required for the proper conformation of the dimer interface and, as a consequence, for catalysis. Altogether, these data indicate that these mutations slightly affect the PLP binding mode and affinity of AGT-Mi and that the mutated residues Arg118, Phe238, and Phe240 are not essential for the catalytic activity. On the basis of these results and in order to promote monomerization of AGT-Mi, double mutants were subsequently created in the following various combinations: F238S-Mi/F240S-Mi, R118A-Mi/F238S-Mi, and R118A-Mi/F240S-Mi. Since both apo and holo forms of F238S-Mi/F240S-Mi still exist predominantly in the dimeric form up to $0.3 \text{ }\mu\text{M}$ it is not possible to quantify the effect of the combinations of these mutations on the $K_{\text{d(dim-mon)}}$ value of AGT-Mi.

Although Phe238 and Phe240 were changed to Ser to interrupt the hydrophobicity at the dimer interface, different elution profiles on SEC are obtained when each of these mutations was combined with the R118A mutation. The double mutant R118A-Mi/F238S-Mi in the holo form elutes from gel filtration as a dimer up to $0.3 \text{ }\mu\text{M}$, while the apo form has a $K_{\text{d(dim-mon)}}$ value of $7.4 \pm 0.4 \text{ }\mu\text{M}$, a value at least ~ 24 -fold higher than that of apoAGT-Mi, but ~ 1.2 -fold lower than that of apoR118A-Mi (Table S2) (Eq. (2)). Conversely, when both R118A and F240S mutations were added to AGT-Mi, the resulting double mutant demonstrates a significant shift from dimer to monomer both in the apo and holo form. The $K_{\text{d(dim-mon)}}$ value of apo and holo R118A-Mi/F240S-Mi is $24 \pm 1 \text{ }\mu\text{M}$ and $2.4 \pm 0.9 \text{ }\mu\text{M}$, respectively, which are at least ~ 80 - and 8 -fold greater than that of the corresponding ones of AGT-Mi (Table S2) (Eq. (2)). It should be noted that the $K_{\text{d(dim-mon)}}$ values of the mutants R118A-Mi/F238S-Mi and R118A-Mi/F240S-Mi are obtained in the absence of glycerol, thus suggesting that the combination of the mutations F238S and F240S with the R118A mutation prevents the formation of aggregates observed for the R118A-Mi mutant. All together, these data highlight that (i) interacting forces between Arg118 and Asp243 of the other monomer may drive dimer formation in apoAGT-Mi, (ii) a synergic role of the residues Arg118 and Phe240 exist on the formation of the dimer of AGT-Mi, and (iii) substitution of both Phe238 and Phe240 with Ser could be relevant in preventing monomer-monomer aggregation. Therefore, we decided to construct, express, purify, and characterize the triple mutant R118A-Mi/F238S-Mi/F240S-Mi. SEC analyses indicate a slow dimer-monomer equilibrium process for both the apo and holo form of the triple mutant. The $K_{\text{d(dim-mon)}}$ values of triple mutant in the apo and holo forms (Eq. (2)) result to be $80 \pm 1 \text{ }\mu\text{M}$ and $9.4 \pm 0.5 \text{ }\mu\text{M}$, respectively (Table S2). Therefore, since the combination of these three mutations stabilizes both apo and holo forms of AGT-Mi monomer versus dimer we chose the triple mutant as a model to investigate the dimerization process.

Table 1

Steady-state kinetic parameters and $K_{\text{d(PLP)}}$ of AGT-Mi and variants obtained in 50 mM potassium phosphate buffer, $\text{pH } 7.4$ in the presence of $100 \text{ }\mu\text{M}$ PLP.

Enzyme	Substrate	Cosubstrate	$k_{\text{cat}} \text{ (s}^{-1}\text{)}$	$K_{\text{m}} \text{ (mM)}$	$k_{\text{cat}}/K_{\text{m}} \text{ (mM}^{-1}\text{s}^{-1}\text{)}$	$K_{\text{d(PLP)}} \text{ (}\mu\text{M)}$
AGT-Mi	L-alanine	Glyoxylate	35 ± 1	51 ± 7	0.68 ± 0.09	0.10 ± 0.01
	Glyoxylate	L-alanine	39 ± 3	0.20 ± 0.05	195 ± 43	
AGT R118A-Mi ^a	L-alanine	Glyoxylate	21 ± 1	77 ± 10	0.27 ± 0.04	0.20 ± 0.04
	Glyoxylate	L-alanine	19 ± 1	0.18 ± 0.02	106 ± 12	
AGT F238S-Mi	L-alanine	Glyoxylate	36 ± 1	46 ± 1	0.78 ± 0.03	0.25 ± 0.02
	Glyoxylate	L-alanine	35 ± 1	0.71 ± 0.06	49 ± 4	
AGT F240S-Mi	L-alanine	Glyoxylate	22 ± 1	84 ± 7	0.26 ± 0.02	0.19 ± 0.03
	Glyoxylate	L-alanine	20 ± 1	0.28 ± 0.04	71 ± 15	

^a Data obtained in presence of 10% glycerol.

3.3. Spectroscopic features of the monomeric form of the R118A-Mi/F238S-Mi/F240S-Mi and effect of PLP on the dimerization

The far-UV CD spectrum (reflecting the α -helix content) of the apo monomer is comparable with that of apoAGT-Mi in the dimeric form, and the deconvolution reveals that the apomonomer and the apoAGT-Mi have an identical composition of the overall secondary structure. On the other hand, the comparison of near-UV CD spectra and intrinsic fluorescence spectra (both reflecting the microenvironment of the aromatic side chains) as well as ANS fluorescence spectra and thermal stability data of the apo monomer and apoAGT-Mi provides evidence that a different conformation exists between the two forms. In fact, as shown in Fig. 4A and B and inset of Fig. 4B, with respect to AGT-Mi in the apo form, the apo monomer exhibits (i) a consistent decrease in the dichroic signals in the near-UV region, (ii) a ~ 1.3 -fold reduction of the intrinsic fluorescence emission intensity and a 4 nm red-shift of the maximum intensity, and (iii) a ~ 8 -fold increase in ANS emission fluorescence intensity as well as a 4 nm red shift of the emission maximum. Similar features are also observed for the apomonomer of the double mutant R118A-Mi/F240S-Mi. Additionally, unlike apo AGT-Mi which displays a thermal transition curve with an apparent mid-denaturation at 66.1 ± 0.1 °C and 53.8 ± 0.1 °C [43], the triple mutant in the apo form unfolds in a single process with an apparent T_m value equal to 47.5 ± 0.3 °C.

The ability of the apo monomer to bind PLP was first monitored by following changes in the dichroic signal at 424 nm at 2 μ M concentration of the enzyme (expressed per monomer) in the presence of 100 μ M PLP concentration as a function of time. A rapid increase of the magnitude of the dichroic signal at 424 nm due to the formation of the internal aldimine is observed. The kinetics of PLP binding is monophasic and occurs with a rate constant of 2.44 ± 0.08 min⁻¹. At the end of the reaction, the solution has been loaded on a Superdex 200 column. The enzyme elutes as a PLP-bound monomer, as demonstrated by the positive dichroic band at 424 nm whose magnitude is about half that of holoAGT-Mi (data not shown). These data indicate that under these experimental conditions the apo monomer is able to bind PLP remaining in a monomeric state. Nevertheless, when this species at a concentration of 0.1 or 0.2 μ M was incubated with L-alanine and glyoxylate up to 3 h, no pyruvate formation could be detected. The comparison of the features of the holomonomer with the corresponding ones of holoAGT-Mi in the dimeric form also reveals (i) a decrease of the

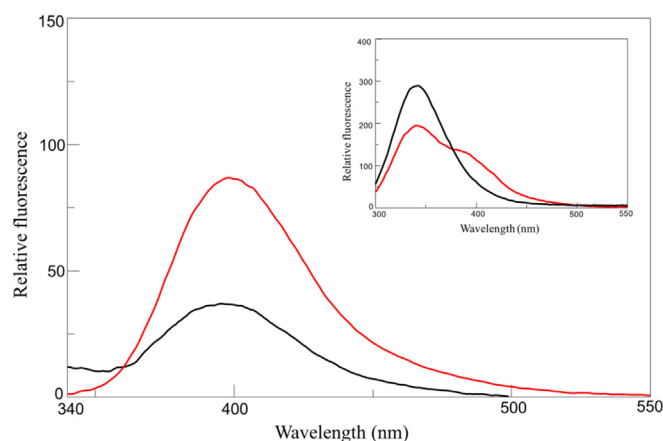


Fig. 5. Fluorescence properties of NaBH₄-reduced R118A-Mi/F238S-Mi/F240S-Mi (red line) and dimeric AGT-Mi (black line). Emission fluorescence spectra upon excitation at 325 nm. The inset show the fluorescence emission upon excitation at 280 nm. Spectra were registered at 1 μ M concentration.

dichroic band in the near-UV region, (ii) an approximately 21-fold increase in the ANS emission intensity with a maximum 9-nm red shifted, and a mid-point denaturation equal to 50.1 ± 0.1 °C, about 23-degrees lower than that of holo AGT-Mi. Moreover, as shown in Fig. 5 the fluorescence emission spectra of the NaBH₄ reduced holomonomer reveal a different PLP binding mode in comparison with that of holo dimeric form of AGT-Mi. When excited at 325 nm, the NaBH₄-reduced holomonomer displays an emission spectrum which, in comparison with that of the reduced holo AGT-Mi, has a 6-nm red shifted maximum and an approximately 2-fold increased emission intensity. We also performed measurements of the intrinsic fluorescence of the reduced holomonomer. Unlike holoAGT-Mi which fluoresces at 341 nm, the holomonomer fluoresces not only at 342 nm but also at 393 nm. This PLP emission is possibly due to the occurrence of an energy transfer from tryptophan(s) to the reduced coenzyme.

When the apomonomer is treated with PLP concentrations ranging from 1 to 40 μ M, the maximal magnitude of the dichroic signal values at 424 nm exhibits a hyperbolic dependence on coenzyme concentration, and the data fitted to Eq. (1) give a $K_{d(PLP)}$ value of 4.4 ± 0.5 μ M per subunit. This value is 17-fold higher than

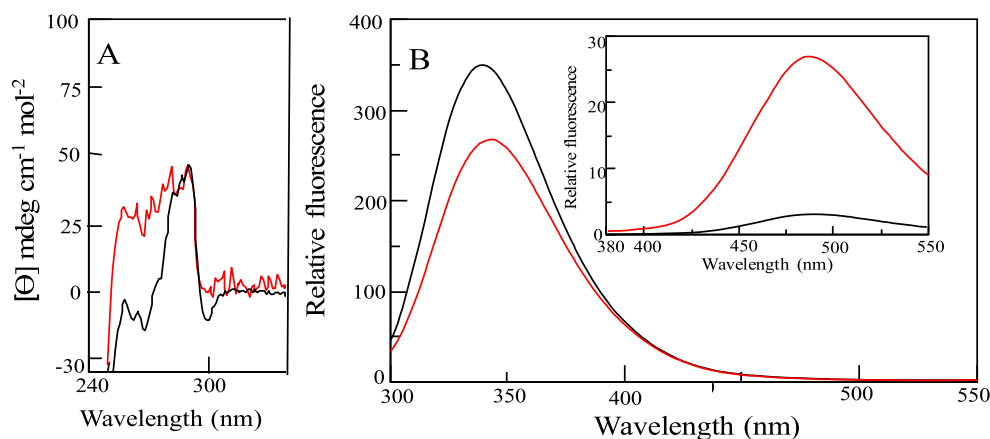


Fig. 4. Spectroscopic features of apo monomer R118A-Mi/F238S-Mi/F240S-Mi (red line) in comparison with apo dimer AGT-Mi (black line). Panel A: near-UV CD spectra at 5 μ M concentration; Panel B: intrinsic fluorescence emission spectra at 1 μ M concentration. Inset of panel B: ANS emission fluorescence spectra at 1 μ M concentration. All measurements were obtained in 50 mM potassium phosphate buffer, pH 7.4.

the $K_{d(PLP)}$ value of AGT-Mi [44] calculated taking into account the monomer concentration. Taken together these data indicate that (i) the monomer is able to bind PLP, even if with an affinity lower than holoAGT-Mi, (ii) unlike AGT-Mi, the holo and apo monomer display a conformation, as revealed by spectroscopic properties and apparent T_m values, similar to each other but different from the corresponding ones of the dimeric forms of AGT-Mi, and (iii) with respect to AGT-Mi, the PLP-bound monomer exhibits local structural alterations of the coenzyme microenvironment leading to exposure to the solvent of the PLP binding site as well as a disturbance of the correct spatial geometry of the functional groups in the PLP microenvironment.

When PLP binding has been monitored as a function of time at 5 μM apomonomer concentration we have observed that the magnitude of the dichroic signal at 424 nm increases in a biphasic way. The fast phase, obtained by fitting the data to a single exponential process, occurs with a rate constant of $2.4 \pm 0.2 \text{ min}^{-1}$, while the slow phase, fitted to Eq. (3), takes place with a rate constant of $0.020 \pm 0.002 \text{ }\mu\text{M}^{-1}\text{min}^{-1}$ (Fig. 6). Thereafter, aliquots were withdrawn from the reaction mixture at various times and subjected to SEC and activity analyses. As shown in the inset of Fig. 6, the dimeric species increases with time at the expense of the monomeric one in a slow equilibrium process. The percentage of the dimeric form as a function of time fits Eq. (3), yielding a rate constant value of dimerization of $0.019 \pm 0.002 \text{ }\mu\text{M}^{-1}\text{min}^{-1}$ (Fig. 6). On the basis of this value and that of $K_{d(\text{dim-mon})}$ of the triple mutant in the holo form, we can estimate a k_{diss} value of $0.18 \pm 0.04 \text{ min}^{-1}$. As shown in Fig. 6, the regain of transaminase activity as a function of time takes place with a rate constant of $0.021 \pm 0.002 \text{ }\mu\text{M}^{-1}\text{min}^{-1}$, a value in excellent agreement with those of dimerization and the slow phase of PLP binding. Thus, it can be claimed that the biphasic process is characterized by a fast phase representing the internal aldimine formation between the apomonomer and the coenzyme followed by a slow phase representing dimerization associated with regain of transaminase activity. To obtain a realistic estimation of the catalytic activity of the triple mutant in the holodimeric form, after incubation of the apomonomer at concentrations ranging from 1.4 to 19 μM with 100 μM PLP, the reaction mixtures were assayed both for transaminase activity and amount of formed dimer. When we plotted the catalytic activity as a function of the

percentage of dimer we noticed a linear relationship between these variables (data not shown). From this plot it can be derived that 1 nmol of the triple mutant in the holo dimeric form reacting with L-Ala and glyoxylate produces pyruvate with an initial rate of 4.8 nmol of pyruvate per sec. Assuming that this value is close to the k_{cat} of the half-transamination, the rate of this reaction is about 9-fold lower than the k_{cat} value of AGT-Mi.

We have also investigated the kinetics of the dimerization of the triple mutant in the apo form. The resulting value of k_{ass} is equal to $7.9 \pm 0.6 \times 10^{-6} \text{ }\mu\text{M}^{-1} \text{ min}^{-1}$ and on the basis of the $K_{d(\text{dim-mon})}$ we estimated a k_{diss} value of $6.4 \pm 0.4 \times 10^{-4} \text{ min}^{-1}$. These data indicate that the apomonomer is able to dimerize even if with a rate of association and of dissociation about 2700- and 280-fold, respectively, lower than the corresponding ones of the PLP-bound monomer.

3.4. Molecular dynamics simulations of F152I-Mi and I244T-Mi variants associated with PH1 and implications in their pathogenicity

The above results indicate Arg118 as a hot-spot interfacial residue playing a relevant role in the dimerization of AGT-Mi. We hypothesized if some PH1-disease causing mutations could be related to mutated residues near to or interacting with Arg118. Thus, a search in this direction has been made. Taken into consideration in the crystal structure of AGT an ideal sphere of 15 Å radius whose center is the $C\alpha$ of Arg118 we noticed the presence of several residues whose mutation is associated with PH1. All of them are located in the large domain of the enzyme. It can be speculated that the pathogenicity of these mutations can be caused by perturbation of the microenvironment of Arg118 and/or Asp243. We focused our attention on the mutations F152I and I244T which are among the most common and the most studied in PH1. Thus, in order to analyze the effect of F152I and I244T pathogenic mutations on AGT-Mi, extensive MD simulations were carried out on the modeled structures of AGT-Mi, I244T-Mi and F152I-Mi in the dimeric form (Material and Methods section). The comparison between AGT-Mi and the I244T-Mi mutant showed that, on the basis of RMSD plots, the simulations reached equilibrium at ca. 110 ns (Fig. S2), thus providing a solid base for further analysis.

By visual inspection, we found that, over 200 ns of simulation, the salt bridge formed by Arg118 and Asp243 is maintained for

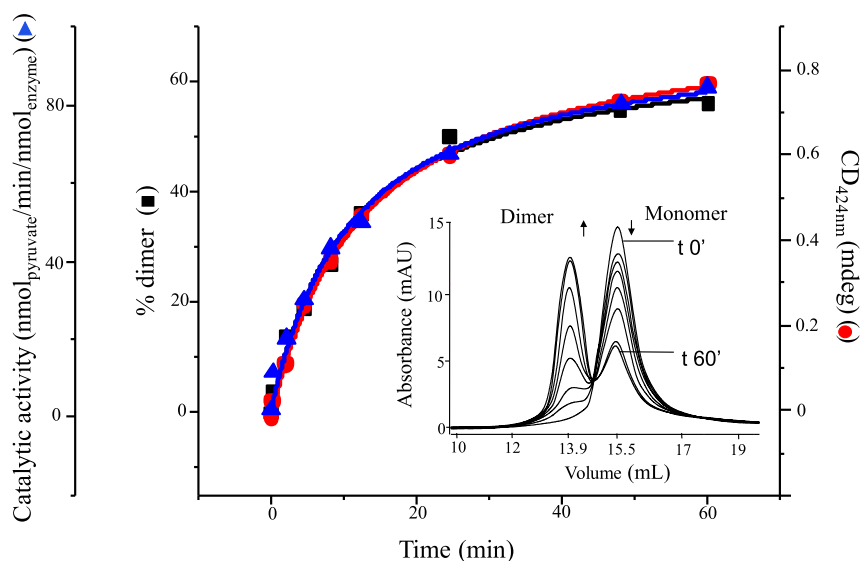


Fig. 6. Second-order kinetic plots for data of dimerization (■), increase of magnitude of the CD signal at 424 nm (●), and catalytic activity (▲) according to Eq. (3). Inset: SEC profiles of the apomonomer after addition of 100 μM PLP at the indicated times.

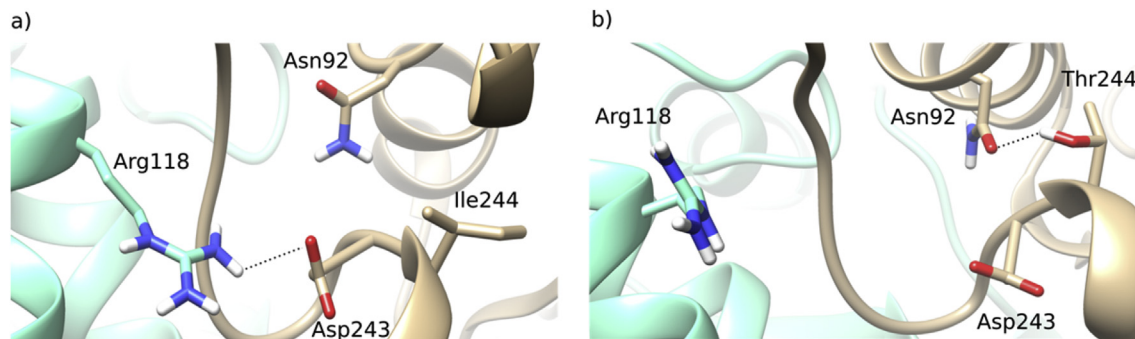


Fig. 7. Perturbation of the microenvironment of Arg118. Panel A: Arg118-Asp243 salt bridge, together without Asn92-Thr244 hydrogen bond interaction. Panel B: breaking of Arg118-Asp243 salt bridge, together with Asn92-Thr244 hydrogen bond interaction; The two monomeric subunits are displayed in aquamarine and brownish. Depicted hydrogen atoms were added within the setup of the simulations.

about 87.3% of the time in AGT-Mi, while it remains stable for only ca. 17.5% of the time in the I244T-Mi mutant. Thus, we hypothesize that the I244T mutation could have a direct influence on the formation of a key interface contact. Indeed, we observed that the breaking of the Arg118-Asp243 salt bridge coincides with the formation of a hydrogen bond between Thr244 and Asp92, which forces a backbone conformational change (Fig. 7 Panel A and B). This is not possible in AGT-Mi because the isoleucine at position 244, which cannot form H-bonds with neighboring residues, guarantees the stability of the Arg118-Asp243 salt-bridge.

Conversely, we did not observe any significant difference between the interface contacts of dimeric AGT-Mi and F152I-Mi

during the simulations. Thus, we conducted MD simulations for 170 ns on the monomeric structure of both AGT-Mi and F152I-Mi. For the two systems we have calculated i) the RMSD to analyze how the systems evolve from the initial structure and ii) the RMSF in order to characterize how flexible they are along the simulations (see Methods section for more details). On the basis of the RMSD of backbone atoms, it can be observed that both systems reached equilibrium after ca. 10 ns to values of about 0.25 nm (Fig. S3). RMSF calculations on both systems showed high fluctuations at the N-terminal and C-terminal loop extremities and in loops far from the dimer interface e.g. 252–255, 280–285 and 355–357 (Fig. S4). However, neither these analyses nor visual inspection revealed significant changes on the dimer interface regions between AGT-Mi and F152I-Mi mutant. Thus, we decided to calculate the ED on the MD simulations. ED technique allows not only to highlight the dominant motions of the system, which are often meaningful and correlated with protein function, but also to reduce the complexity of the data (see Material and Methods section). Fluctuations analysis by ED revealed that the F152I mutation could influence the dynamics of several amino acid stretches of AGT-Mi, i.e., 95–97, 118–121, 141–145, 171–176 and 281–290, with peaks for residues 97, 118, 143, 175 and 281. These results suggest that the latter residues have a different behavior in terms of flexibility in F152I-Mi as compared with AGT-Mi. In particular, it can be appreciated (Fig. 8) that one of the stretches that exhibits different behavior in the mutated system is formed by residues 118–121, located at the dimerization interface. On these bases, we could suggest that the F152I mutation could affect dimer formation by increasing the flexibility of the region 118–121, thus possibly reducing the complementarity between the two monomers. Moreover, approximately 70% of all cumulative protein fluctuations are comprised within the first two principal components (PCs), so the overall motion of the proteins in phase space can be showed as a projection of the first two eigenvectors (PC1, PC2). Our results show (Fig. S5) that F152I mutant covers a larger region of conformational space than AGT-Mi, suggesting an overall escalation in the flexibility of the mutant with respect to AGT-Mi. The values indicating the total variance of the systems for AGT-Mi and F152I-Mi mutant protein were 28.1565 nm² and 52.9434 nm² respectively, validating the hypothesis of the overall increased flexibility of F152I mutant than AGT-Mi.

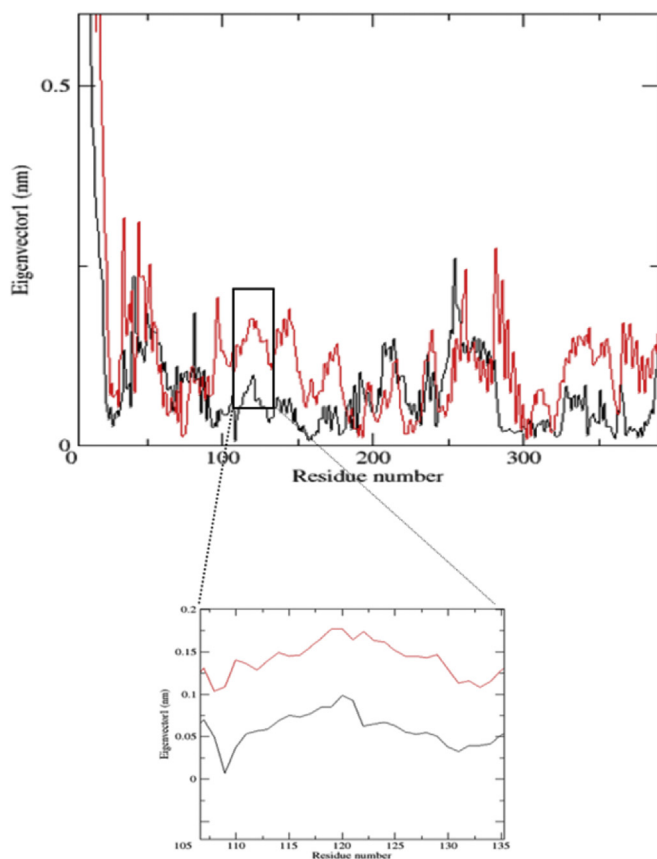


Fig. 8. RMSF of C α atoms along first eigenvector. The simulations were run on AGT-Mi (black) and F152I mutant (red) monomer forms. In the box, we focus our attention on the RMSF value of the residues in the dimer interface.

4. Discussion

The majority of PLP-enzymes exists as dimers, but dimerization was demonstrated to be critical for catalytic activity for only three members of this family, i.e. human ornithine decarboxylase [45], bacterial diaminopimelate decarboxylase [46] and *Treponema*

denticola cystalysin [47]. Mutagenesis targeting residues at their dimer interface followed by analyses of the catalytic activity and the quaternary structure of the generated variants allowed to establish that (i) a sextuple monomeric mutant of ornithine decarboxylase as well as a triple monomeric mutant of cystalysin do not exhibit enzymatic activity, and (ii) two single mutants of diaminopimelate decarboxylase display a loss of decarboxylase activity which correlates with the attenuation in dimerization.

One such example of this approach is reported for AGT-Mi in this study. By means of bioinformatic analyses, we identify Arg118, a hot spot residue at the dimer interface interacting with Asp243 of the opposite subunit, and two other interfacial residues, Phe238 and Phe240, which give a great contribution to the hydrophobic contacts between the two monomers. Thus, these residues at the dimer interface of AGT-Mi should be crucial for monomer self-association. Indeed, the combination of the R118A mutation with both F238S and F240S mutations yields a triple mutant characterized by $K_{d(\text{dim- mon})}$ values of the apo and the holo forms at least ~260- and 31-fold, larger, respectively, than the corresponding ones of AGT-Mi. Moreover, with respect to apo and holo AGT-Mi, the apo and the holo monomer of the triple mutant exhibit changes in the conformation, as indicated by near-UV CD signal, intrinsic fluorescence and markedly low T_m values. Again, a different PLP binding mode and affinity is seen for the apo monomer in comparison with the apo dimeric form of AGT-Mi. The effect of PLP on dimerization of AGT-Mi consists in a fast phase leading to an inactive PLP-bound monomer followed by dimerization paralleling regain of catalytic activity, which reaches an initial velocity about 9-fold lower than the k_{cat} of AGT-Mi. Nevertheless, the apomonomer is also able to dimerize even if with a rate constant of association lower than that of the PLP-bound monomer.

Overall, these data indicate that, although the dimer interface residues Arg118, Phe238 and Phe240 are not critical for transaminase activity of AGT-Mi, they contribute to formation of the dimer, and that dimerization is essential for catalytic activity. This finding, in line with what already reported for the above mentioned PLP-enzymes, is strictly related to the fact that the active site residues of these enzymes are contributed by adjacent subunits. It can be also possible to envisage that dimerization optimizes protein dynamics to support function. The unraveling of the dimerization process of this enzymatic species is not only important to better understand the catalytic mechanism of the enzyme but mainly for the possible relapse in the understanding why some PH1-causing variants encoded on the minor allele, like F152I and I244T, are mistargeted into mitochondria. The import into peroxisomes mainly acts on a fully-folded dimeric state of AGT [5], while that in mitochondria requires a monomeric state of the enzyme provided with a mitochondrial targeting sequence resulting from the P11L polymorphism. Since most of glyoxylate is synthesized in the peroxisomes, only peroxisomal AGT is metabolically efficient. Therefore, the dimerization and the correct subcellular localization of AGT are functionally essential events for this PLP-enzyme. It has been suggested that the combined effect of some mutations with P11L could result in a destabilization of the dimeric structure of AGT-Mi [5]. However, up to now, the effect of these substitutions are not understood in structural terms. Visual inspection of the modelled structure of AGT-Mi indicates that Phe152 and Ile244 are not dimer interfacial residues. However, it cannot be excluded that replacement of Phe152 or Ile244 by Ile and Thr, respectively, could indirectly attenuate the dimerization process. To test this hypothesis, MD simulations were performed on AGT-Mi, F152I-Mi and I244T-Mi. The analyses predict that both mutations interfere with the dimerization process. In particular, replacement of Thr244 with Ile appears to cause the breakage of the ionic bond between Arg118 and Asp243 and the formation of a hydrogen bond between Arg118

and Asp92. On the other hand, in the monomer of F152I-Mi, but not in the dimer, the stretch 118–121 appears more flexible than in the monomer of AGT-Mi. It can be speculated that (i) the buttressing of monomer to form a dimer may prevent increased movement at the dimer interface, and (ii) the flexibility of amino acid residues 118–121 could result in an attenuated monomer in its dimerization process.

Some speculations could be drawn from the data and the MD simulations here presented as well as from previous results [2, 11]. A pathway of AGT folding was already proposed. It foresees the conversion of the unfolded monomer to a partly unfolded monomer, and then to a folded monomer which dimerizes [5]. Here, we advance the proposal that the dimerization will start by means of core dimer interfacial interaction. The large area of the enzyme dimerization interface along with the finding that the 21-N-terminal truncated AGT is able to dimerize [11] support this view. In this dimerization intermediate, the N-terminal extensions, containing the P11L polymorphism in AGT-Mi, should be exposed and flexible, i.e. not tightly bound to the surface of the neighboring subunit (Fig. 9). Following this view, and considering that the dimeric structure of AGT-Mi is less stabilized than that of AGT-Ma, AGT-Ma and AGT-Mi are 100% and 95% peroxisomal, respectively (Fig. 9, pathway 1) Since MD simulations predict that the mutations I244T and F152I interfere with dimerization, the formation of the dimeric structure of the variants I244T-Mi and F152I-Mi should be greatly impaired, while the formation of the partly unfolded and folded monomeric forms could prevail. Thus, the partially unfolded monomers of the variants I244T-Mi and F152I-Mi containing the P11L polymorphism, could be imported into mitochondria, possibly with a rate higher than that of their conversion to the corresponding folded monomers (Fig. 9, pathway 2). Nevertheless, here we have demonstrated that the dimerization of the apomonomer of the triple mutant occurs with k_{ass} and k_{diss} remarkably lower than the corresponding ones of the PLP-bound monomer. These findings indicate that high levels of PLP could shift the equilibrium from the PLP-bound monomer of the variants F152I-Mi and I244T-Mi to the dimeric form, thus preventing their mislocalization. This could explain why the F152I-Mi or I244T-Mi variants have been found to be responsive to pyridoxine administration [44, 48–50]. The proposed model illustrates a putative dimerization process and gives a tentative explanation of the molecular basis of the pathogenicity of

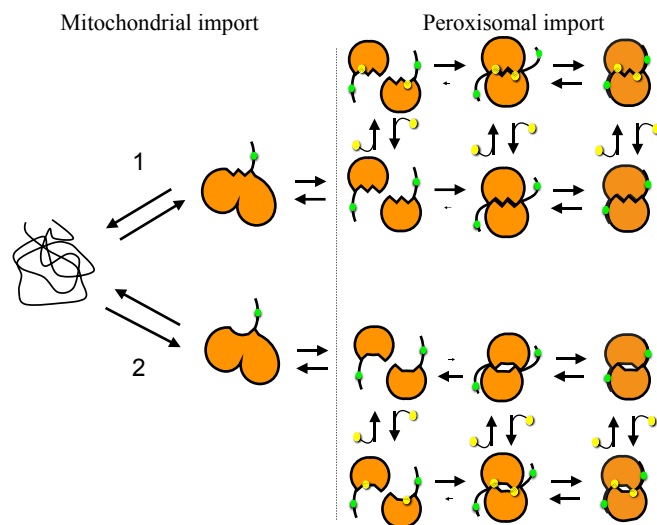


Fig. 9. Proposed folding and dimerization pathway of AGT-Mi (1) and of the I244T-Mi and F152I-Mi variants (2). The green dots indicate the P11L polymorphism. The yellow dots represent the PLP coenzyme.

the variants F152I-Mi and I244T-Mi (Fig. 9).

To conclude, this work allow us to (i) identify interfacial residues, Arg118, Phe238, and Phe240, which are not essential for catalytic activity of AGT-Mi but have a relevant impact on its dimerization process, (ii) engineer and characterize a folded apomonomer and holomonomer, both able to dimerize (iii) demonstrate that dimerization is critical for catalytic activity, and (iv) outline the possible structural basis of the functional synergism between the mutations I244T or F152I and the mutation P11L responsible for the aberrant targeting to mitochondria of the variants I244T-Mi and F152I-Mi associated with PH1.

Conflict of interests

The authors declare no competing financial interests.

Acknowledgements

This work was supported by funding from the Oxalosis and Hyperoxaluria Foundation (OHF2012 to B.C.) and by the University of Verona (F.U.R to B.C.).

Appendix A. Supplementary data

Supplementary data related to this article can be found at <http://dx.doi.org/10.1016/j.biochi.2016.10.001>.

References

- [1] B. Cellini, M. Bertoldi, R. Montioli, A. Paiardini, C. Borri Voltattorni, Human wild-type alanine:glyoxylate aminotransferase and its naturally occurring G82E variant: functional properties and physiological implications, *Biochem. J.* 408 (2007) 39–50.
- [2] X. Zhang, S.M. Roe, Y. Hou, M. Bartlam, Z. Rao, L.H. Pearl, C.J. Danpure, Crystal structure of alanine:glyoxylate aminotransferase and the relationship between genotype and enzymatic phenotype in primary hyperoxaluria type 1, *J. Mol. Biol.* 331 (2003) 643–652.
- [3] C.J. Danpure, Peroxisomal alanine:glyoxylate aminotransferase and prenatal diagnosis of primary hyperoxaluria type 1, *Lancet* 2 (1986) 1168.
- [4] P.E. Purdue, J. Allsop, G. Isaya, L.E. Rosenberg, C.J. Danpure, Mistargeting of peroxisomal L-alanine:glyoxylate aminotransferase to mitochondria in primary hyperoxaluria patients depends upon activation of a cryptic mitochondrial targeting sequence by a point mutation, *Proc. Natl. Acad. Sci. U. S. A.* 88 (1991) 10900–10904.
- [5] B. Cellini, A. Lorenzetto, R. Montioli, E. Oppici, C.B. Voltattorni, Human liver peroxisomal alanine:glyoxylate aminotransferase: different stability under chemical stress of the major allele, the minor allele, and its pathogenic G170R variant, *Biochimie* 92 (2010) 1801–1811.
- [6] A.L. Pey, E. Salido, J.M. Sanchez-Ruiz, Role of low native state kinetic stability and interaction of partially unfolded states with molecular chaperones in the mitochondrial protein mistargeting associated with primary hyperoxaluria, *Amino Acids* 41 (2011) 1233–1245.
- [7] S. Fargue, J. Lewin, G. Rumsby, C.J. Danpure, Four of the most common mutations in primary hyperoxaluria type 1 unmask the cryptic mitochondrial targeting sequence of alanine:glyoxylate aminotransferase encoded by the polymorphic minor allele, *J. Biol. Chem.* 288 (2013) 2475–2484.
- [8] E. Oppici, A. Roncador, R. Montioli, S. Bianconi, B. Cellini, Gly161 mutations associated with Primary Hyperoxaluria Type I induce the cytosolic aggregation and the intracellular degradation of the apo-form of alanine:glyoxylate aminotransferase, *Biochim. Biophys. Acta* 1832 (2013) 2277–2288.
- [9] B. Cellini, R. Montioli, A. Paiardini, A. Lorenzetto, F. Maset, T. Bellini, E. Oppici, C.B. Voltattorni, Molecular defects of the glycine 41 variants of alanine glyoxylate aminotransferase associated with primary hyperoxaluria type I, *Proc. Natl. Acad. Sci. U. S. A.* 107 (2010) 2896–2901.
- [10] E. O. R. Montioli, M. Dindo, A. Roncador, G. Gotte, B. Cellini, C. Borri Voltattorni, Misfolding caused by the pathogenic mutation G47R on the minor allele of alanine:glyoxylate aminotransferase and chaperoning activity of pyridoxine, *Biochim. Biophys. Acta* 1854 (2015) 1280–1289.
- [11] R. Montioli, S. Fargue, J. Lewin, C. Zamparelli, C.J. Danpure, C. Borri Voltattorni, B. Cellini, The N-terminal extension is essential for the formation of the active dimeric structure of liver peroxisomal alanine:glyoxylate aminotransferase, *Int. J. Biochem. Cell Biol.* 44 (2012) 536–546.
- [12] C.C.G.I. CCG, Molecular Operating Environment (MOE), 1010 Sherbooke St. West, Suite #910, Montreal, QC, Canada, H3A 2R7.
- [13] E. Krissinel, K. Henrick, Inference of macromolecular assemblies from crystalline state, *J. Mol. Biol.* 372 (2007) 774–797.
- [14] P. Labute, LowModeMD—implicit low-mode velocity filtering applied to conformational search of macrocycles and protein loops, *J. Chem. Inf. Model* 50 (2010) 92–800.
- [15] B. Cellini, R. Montioli, S. Bianconi, J.P. Lopez-Alonso, C.B. Voltattorni, Construction, purification and characterization of untagged human liver alanine-glyoxylate aminotransferase expressed in *Escherichia coli*, *Protein Pept. Lett.* 15 (2008) 153–159.
- [16] C.N. Pace, F. Vajdos, L. Fee, G. Grimsley, T. Gray, How to measure and predict the molar absorption coefficient of a protein, *Protein Sci.* 4 (1995) 2411–2423.
- [17] L.R. Manning, W.T. Jenkins, J.R. Hess, K. Vandegriff, R.M. Winslow, J.M. Manning, Subunit dissociations in natural and recombinant hemoglobins, *Protein Sci.* 5 (1996) 775–781.
- [18] B.A. S., C.N. Pace, J.T. Thompson, Measuring the conformational stability of a protein, in: T.C. C. (Ed.), *Protein Structure, a Practical Approach*, IRL Press, Oxford, England, 1989, pp. 311–330. Place Published.
- [19] S. Pronk, S. Pall, R. Schulz, P. Larsson, P. Bjelkmar, R. Apostolov, M.R. Shirts, J.C. Smith, P.M. Kasson, D. van der Spoel, B. Hess, E. Lindahl, GROMACS 4.5: a high-throughput and highly parallel open source molecular simulation toolkit, *Bioinformatics* 29 (2013) 845–854.
- [20] C. Oostenbrink, A. Villa, A.E. Mark, W.F. van Gunsteren, A biomolecular force field based on the free enthalpy of hydration and solvation: the GROMOS force-field parameter sets 53A5 and 53A6, *J. Comput. Chem.* 25 (2004) 1656–1676.
- [21] H.J. Berendsen, J.P. Postma, W.F. van Gunsteren, J. Hermans, Interaction models for water in relation to protein hydration, in: *Intermolecular Forces*, Place Published, 1981.
- [22] B. Webb, A. Sali, Comparative protein structure modeling using Modeller, *Curr. Protoc. Bioinforma.* (2014) 5–6.
- [23] E.F. Pettersen, T.D. Goddard, C.C. Huang, G.S. Couch, D.M. Greenblatt, E.C. Meng, T.E. Ferrin, UCSF Chimera—a visualization system for exploratory research and analysis, *J. Comput. Chem.* 25 (2004) 1605–1612.
- [24] I. Kass, D.E. Hoke, M.G. Costa, C.F. Reboul, B.T. Porebski, N.P. Cowieson, H. Leh, E. Pennacchietti, J. McCoy, O. Kleifeld, C. Borri Voltattorni, D. Langley, B. Roome, I.R. Mackay, D. Christ, D. Perahia, M. Buckle, A. Paiardini, D. De Biase, A.M. Buckle, Cofactor-dependent conformational heterogeneity of GAD65 and its role in autoimmunity and neurotransmitter homeostasis, *Proc. Natl. Acad. Sci. U. S. A.* 111 (2014) E2524–E2529.
- [25] A.K. Malde, L. Zuo, M. Breeze, M. Stroet, D. Poger, P.C. Nair, C. Oostenbrink, A.E. Mark, An automated force field topology builder (ATB) and repository: version 1.0, *J. Chem. Theory Comput.* 7 (2011) 4026–4037.
- [26] H.J. Berendsen, J.V. Postma, W.F. van Gunsteren, A.R.H.J. DiNola, J.R. Haak, Molecular dynamics with coupling to an external bath, *J. Chem. Phys.* 81 (8) (1984) 3684–3690.
- [27] B. Hess, H. Bekker, H.J. Berendsen, J.G. Fraaije, LINC: a linear constraint solver for molecular simulations, *J. Comput. Chem.* 18 (12) (1997) 1463–1472.
- [28] D.M. York, A. Wlodawer, L.G. Pedersen, T.A. Darden, Atomic-level accuracy in simulations of large protein crystals, *Proc. Natl. Acad. Sci. U. S. A.* 91 (1994) 8715–8718.
- [29] W.G. Hoover, Canonical dynamics: equilibrium phase-space distributions, *Phys. Rev. A Gen. Phys.* 31 (1985) 1695–1697.
- [30] S.U.I. Nosé, A molecular dynamics method for simulations in the canonical ensemble, *Mol. Phys.* 50 (5) (2002) 1055–1076.
- [31] M. Parrinello, A. Rahman, Polymorphic transitions in single crystals: a new molecular dynamics method, *J. Appl. Phys.* 52 (12) (1981) 7182–7190.
- [32] S. Nosé, M.L. Klein, Constant pressure molecular dynamics for molecular systems, *Mol. Phys.* 50 (5) (1983) 1055–1076.
- [33] J.E. Donald, D.W. Kulp, W.F. DeGrado, Salt bridges: geometrically specific, designable interactions, *Proteins* 79 (2011) 898–915.
- [34] A. Kumar, V. Rajendran, R. Sethumadhavan, R. Purohit, Molecular dynamic simulation reveals damaging impact of RAC1 F28L mutation in the switch I region, *PLoS One* 8 (2013) e77453.
- [35] M. Liu, L. Wang, X. Sun, X. Zhao, Investigating the impact of Asp181 point mutations on interactions between PTP1B and phosphotyrosine substrate, *Sci. Rep.* 4 (2014) 5095.
- [36] N. Nagasundaram, H. Zhu, J. Liu, V. K. C. G.P. C. Chakraborty, L. Chen, Analysing the effect of mutation on protein function and discovering potential inhibitors of CDK4: molecular modelling and dynamics studies, *PLoS One* 10 (2015) e0133969.
- [37] G.P. Doss, B. Rajith, C. Chakraborty, N. NagaSundaram, S.K. Ali, H. Zhu, Structural signature of the G719S-T790M double mutation in the EGFR kinase domain and its response to inhibitors, *Sci. Rep.* 4 (2014) 5868.
- [38] K. T. A.A. Bogan, Anatomy of hot spots in protein interfaces, *J. Mol. Biol.* 280 (1998) 1–9.
- [39] M. U. W.L. DeLano, A.M. de Vos, J.Á. Wells, Convergent solutions to binding at a protein–protein interface, *Science* 287 (2000) 1279–1283.
- [40] C. C. L.L. Conte, J. Janin, The atomic structure of protein–protein recognition sites, *J. Mol. Biol.* 285 (1999).
- [41] E.D. Levy, A simple definition of structural regions in proteins and its use in analyzing interface evolution, *J. Mol. Biol.* 403 (2010) 660–670.
- [42] A.L. Fink, Protein aggregation: folding aggregates, inclusion bodies and amyloid, *Fold. Des.* 3 (1998) R9–R23.
- [43] E. Oppici, R. Montioli, A. Lorenzetto, S. Bianconi, C. Borri Voltattorni, B. Cellini, Biochemical analyses are instrumental in identifying the impact of mutations on holo and/or apo-forms and on the region(s) of alanine:glyoxylate aminotransferase variants associated with primary hyperoxaluria type I, *Mol. Genet.*

- Metab. 105 (2012) 132–140.
- [44] B. Cellini, R. Montioli, A. Paiardini, A. Lorenzetto, C.B. Voltattorni, Molecular insight into the synergism between the minor allele of human liver peroxisomal alanine:glyoxylate aminotransferase and the F152I mutation, *J. Biol. Chem.* 284 (2009) 8349–8358.
- [45] Y.-L. L, C.-Y. Lee, C.-L. Lin, G.-Y. Liu, Hung H-C functional roles of the dimer-interface residues in human ornithine decarboxylase, *PLoS One* 9 (2014).
- [46] M.G. Peverelli, T.P. Soares da Costa, N. Kirby, M.A. Perugini, Dimerization of bacterial diaminopimelate decarboxylase is essential for catalysis, *J. Biol. Chem.* 291 (2016) 9785–9795.
- [47] R. Montioli, B. Cellini, M. Bertoldi, A. Paiardini, C.B. Voltattorni, An engineered folded PLP-bound monomer of *Treponema denticola* cystalysin reveals the effect of the dimeric structure on the catalytic properties of the enzyme, *Proteins* 74 (2009) 304–317.
- [48] H. Hoyer-Kuhn, S. Kohbrok, R. Volland, J. Franklin, B. Hero, B.B. Beck, B. Hoppe, Vitamin b6 in primary hyperoxaluria I: first prospective trial after 40 years of practice, *Clin. J. Am. Soc. Nephrol.* 9 (2014) 468–477.
- [49] S.M. van der Hoeven, C.S. van Woerden, J.W. Groothoff, Primary hyperoxaluria type 1, a too often missed diagnosis and potentially treatable cause of end-stage renal disease in adults: results of the Dutch cohort, *Nephrol. Dial. Transpl.* 27 (2012) 3855–3862.
- [50] C.G. Monico, J.B. Olson, D.S. Milliner, Implications of genotype and enzyme phenotype in pyridoxine response of patients with type I primary hyperoxaluria, *Am. J. Nephrol.* 25 (2005) 183–188.